Multiscale Molecular Approach towards Complex Systems

Dissertation

zur

Erlangung des Doktorgrades (Dr. rer. nat.)

der

Mathematisch-Naturwissenschaftlichen Fakultät

der

Rheinischen Friedrich-Wilhelms-Universität Bonn

vorgelegt von

Friedrich Malberg

aus

Bonn

Bonn 2014

Angefertigt mit Genehmigung der Mathematisch-Naturwissenschaftlichen
Fakultät der Rheinischen Friedrich-Wilhelms-Universität Bonn

1. Gutachter: Prof. Dr. Barbara Kirchner
2. Gutachter: Prof. Dr. Margarida Costa Gomes

Tag der Promotion: 17. Juli 2014
Erscheinungsjahr: 2014

"Any intelligent fool can make things bigger, more complex, and more violent. It takes a touch of genius—and a lot of courage—to move in the opposite direction."

Albert Einstein

This thesis reports on multiscalar studies of two different complex systems, namely ionic liquids and the supramolecular structures rotaxanes. To obtain insights into the complex interactions present in these systems, static quantum chemical calculations, *ab initio* molecular dynamics and classical molecular dynamics simulations were carried out, considering the most sophisticated methods and force fields, which are applicable. The primary goal was to develop a multiscale approach, using a combined set of methods adapted to the characteristic size and time scale of the studied systems, to describe how the complex interactions present influence the physicochemical properties, with a special focus on interactions like hydrogen bonding and dispersion interactions.

For ionic liquids, the formation of ion pairs and the evaporation were the objects of this research. Dynamical probing of the interactions by means of *ab initio* molecular dynamics simulations pointed to a temperature-dependent structural rearrangement of the interactions in the transition from the bulk to the gas phase. With the aid of classical molecular dynamics simulations, applying the same force field, which was shown to be able to reproduce the molecular structure and to describe the surface of ionic liquids properly, a qualitative picture of the formation of an ion pair at the surface as well as of its departure into the vacuum was gained. From this qualitative picture, a multistep evaporation mechanism is proposed. Furthermore, the effect of charge transfer on the formation of ion pairs in ionic liquids has been probed using different population analysis techniques, indicating that the ion pairing in the bulk phase of ionic liquids seems to be less important than thought before.

The object of the rotaxane research was to understand the complexity of their binding patterns. Static quantum chemical calculations were conducted to probe substitution and flexibility effects of the axle in these host-guest complexes. In agreement with experimental data, it was shown that substitution on the diamid axle of Vögtle-type rotaxanes changes the binding properties in several ways and that depending on the substituent the binding is driven either by enthalpic or entropic effects. Increasing the flexibility of the axle increases the binding energy

of Leigh-type rotaxanes independent of the substitution of the axle. Stoppers on the axle, which are attributed a minor role in the binding of rotaxanes, showed an influence on intramolecular interactions, as the trend of hydrogen bonding symmetry observed for different flexibility of axles is reversed in their presence. Including solvent effects through an implicit solvent model, weakens the complex binding for all systems, as the different parts of the host-guest complexes are differently stabilized.

Contents

1 Introduction to Complex Systems **1**

1.1 Ionic Liquids 2

1.1.1 The Complexity of Ionic Liquids 3

1.1.2 Gas Phase of Ionic Liquids 6

1.1.3 Interfaces of Ionic Liquids 9

1.1.4 Ion Pairing in Ionic Liquids 13

1.2 Rotaxanes 15

1.2.1 The Complexity of Rotaxanes 18

1.2.2 Interactions in Rotaxanes from Theory 19

2 Methodology **23**

2.1 Multiscale Molecular Methods 23

2.1.1 Static Quantum Chemistry 24

2.1.2 Cluster Ansatz 31

2.1.3 Ab initio Molecular Dynamics 32

2.1.4 Force Fields 34

2.2 Population Analysis 37

2.3 Topology of Ionic Liquids 43

3 Results and Discussion **45**

3.1 Gas Phase of Ionic Liquids 47

3.1.1 The Bulk and The Gas Phase of 1-Ethyl-3-Methyl-imidazolium Ethylsulfate: Dispersion Interaction makes the Difference. 47

3.1.2 Understanding the Evaporation of Ionic Liquids using the Example of 1-Ethyl-3-Methylimidazolium Ethylsulfate . . . 55
3.2 Interfaces of Ionic Liquids . . . 83
3.2.1 Using Molecular Simulation to Understand the Structure of 1-Ethyl-3-Methylimidazolium Alkylsulfates Ionic Liquids: Bulk and Liquid–Vapor Interfaces . . . 83
3.2.2 Bulk and Liquid–Vapor Interface of Pyrrolidinium-Based Ionic Liquids: A Molecular Simulation Study . . . 111
3.3 Ion Pairing in Ionic Liquids . . . 137
3.3.1 En Route Formation of Ion Pairs at the Ionic Liquid-Vacuum Interface . . . 137
3.3.2 On the Origin of Ionicity in Ionic liquids. Ion Pairing versus Charge Transfer . . . 145
3.4 Rotaxanes . . . 167
3.4.1 Substituent Effects on Axle Binding in Amide Pseudo-rotaxanes: Comparison of NMR Titration and ITC Data with DFT Calculations . . . 167
3.4.2 Substitution Effect and Effect of Axle's Flexibility at (Pseudo-)Rotaxanes . . . 193

4 Conclusion and Outlook **211**

List of Figures **217**

List of Tables **223**

Bibliography **225**

Acknowledgment **268**

List of Publications **271**

Statement of Authorship **273**

1 Introduction to Complex Systems

The term complex systems can be broadly applied to many diverse disciplines, *e. g.* biology, chemistry, physics, economics and sociology. In general, complex systems can be best described by the questions: How do relationships—interactions—between parts of the system initiate collective behavior and how does the system interact with its environment? In order to explain and understand their complex phenomena, scientists seek to find simple rules and subsequently to be able to make predictions.

In chemistry, complex systems are governed by complex interactions between atoms and molecules, which result in unusual properties and interesting behaviors. These unusual properties are then probed from various aspects, relating resulting differences to changes in the interactions. Therefore, when analyzing the complexity of interactions present in these systems, a sensitive choice of the methods and the scale of the method is of high importance in order to provide an accurate description of the system.

In this work, the complex interactions present in two complex systems, namely ionic liquids and the supramolecular structures called rotaxanes, are investigated by means of multiscalar computational methods. In the following, both systems and their complexity are introduced, reflecting the motivation of this work, followed by an outline of the applied methods. Afterwards, the insights gained on the complex interactions are summarized and a global picture of the value of multiscalar methods to describe these systems is drawn.

1.1 Ionic Liquids

"Ionic Liquids are liquids that are entirely composed of ions." [1,2] is probably the most general and most valid definition for ionic liquids (ILs). Apart from that, ionic liquids cannot be generalized. They are composed of organic cations paired with anions that are either organic or inorganic. Cations and anions which are commonly used are shown in Figure 1.1. The number of different ionic liquids is vast and by mixing them an excess of 10^6 binary systems and 10^{18} ternary systems of ionic liquids has been estimated,[3] all with a certain set of physico-

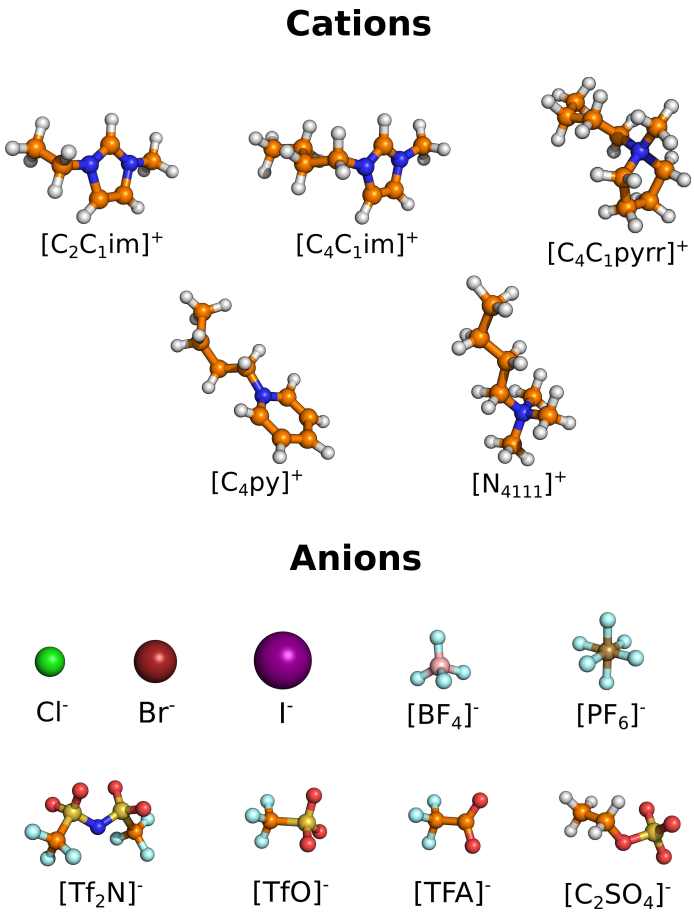

Figure 1.1: Chemical structures of common cations (top) and anions (bottom) used as component for ionic liquids. For ionic liquids, the following coloring code is used here and throughout the work: **C**: orange; **N**: blue; **H**: white; **Cl**: green; **Br**: dark red; **I**: purple; **B**: pink; **F**: turquois; **P**: brown; **O**: red; **S**: yellow.

chemical properties, *e. g.* melting point, conductivity, viscosity, density *etc.* The physicochemical properties of ionic liquids depend on the nature and size of both cation and anion,[4] which allows choosing the ionic liquids best suited for a given application. Due to the variety of ionic liquids and thus the properties, there are different applications of ionic liquids in many areas. They can be used as solvents in synthesis and catalysis,[4–7] for gas storage[8–12] and separation,[13–17] as lubricants,[18,19] in electrochemical applications[20–22] *etc.* Although, the diversity of the combination of cations and anions to form ionic liquids (see Figure 1.1 for a small number of possible combinations) provides an intuitive choice for given tasks, the introduction of special features (*e. g.* functionalization) offers a more efficient way to fit the required performances. Ionic liquids with such incorporated functional groups are nowadays well known as task-specific ionic liquids.[11,23–27] Even though it is possible to tune ionic liquids to specific tasks, systematic classifications of ionic liquids and their properties based on the interplay[28–31] of the ions remains challenging, as already small impurities can have a major effect[32] and because of the large number of different examples with different properties. Also, this interplay itself is already not inconsiderable, as there are several possible interactions between the ions (*e. g.* Coulomb and dispersion interactions[28,29,31]) present in ionic liquids, which all have a certain influence on the properties of the given ionic liquid. This complexity of ionic liquids has been the focus of the research activities of many groups in the last few years, showing the importance of understanding these promising liquids from experiments and theory.

1.1.1 The Complexity of Ionic Liquids

The complexity of ionic liquids can be described from many different points of view. Here, their complexity will be discussed at the example of their hydrogen bonding ability as well as their distillability. The main motivation of the work on ionic liquids is to provide a comprehensive description on the relationship between the different types of interactions present in ionic liquids and their distillability.

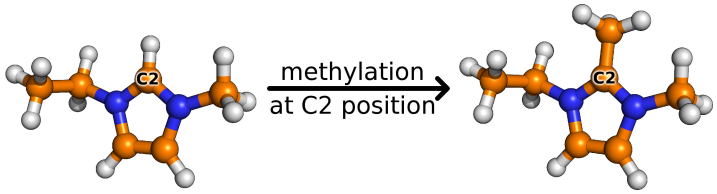

Figure 1.2: Left: C2 position shown at the example of 1-ethyl-3-methylimidazolium; Right: Introduction of a methyl-group at the C2 position.

For ionic liquids, it is uncontested that long-range Coulomb interactions are the strongest interactions between the ions[28,33–39] but even short-range dispersion interaction[29–31] as well as secondary effects like hydrogen bonding[40,41] are not negligible to understand and explain the complex behavior of ionic liquids. Leys *et al.* questioned the linear dependency between the electronic conductivity and the size of various anions for the 1-butyl-3-methylimidazolium-based ionic liquids.[42] They observed an increase in conductivity with increasing ionic radius of an ionic liquid, while it would be expected that the conductivity should decrease because of lower mobility. A possible explanation suggests that secondary effects such as hydrogen bonding[40,41] and charge delocalization play a role in clarifying such unexpected behavior.

Since 1986, the ability of ionic liquids based on the imidazolium cation to form hydrogen bonds is known from the work of Abdul-Sada et al.[43] Since then, understanding the role of hydrogen bonds in ionic liquids is one of the major research areas of ionic liquids.[41,43–50] The effects of hydrogen bonds on thermodynamic properties of ionic liquids are explained in different ways. By introducing the methyl-group at the C2 position of the imidazolium ring (see Figure 1.2), Bonhôte et al.[51] eliminated the effect of hydrogen bonding via the C2-H2 position and observed higher melting points and higher viscosity for these liquids, even though lower melting points and a decrease of viscosity would be expected. Hunt[34] investigated this behavior via density functional methods and was able to explain that the loss of hydrogen bonding in 1-butyl-3-methylimidazolium-based ionic liq-

uids leads to a decrease of possible conformations of the anion around the cation and thus to a decrease of entropy. A different view on the effects of hydrogen bonds is provided by the group of Ludwig.[52–55] They characterize the hydrogen bonds as "defects" in the Coulombic network of ionic liquids. Their influence is described as increasing the dynamics of cations and anions, leading to lower melting points and viscosities, namely fluidizing the ionic liquids. With the aid of far infrared and terahertz spectroscopy they showed from vibrational shifts to higher wavenumbers that the interaction between cation and anion is intensified by the presence of hydrogen bonding, leading to an elongation of the C2-H bond. Noeck *et al.*[56] investigated imidazolium-based ionic liquids, where the C2 position was methylated and nonmethylated, using spectroscopic methods, focusing on describing the interactions between cation and anion. They found changes in position and strength of the interionic interactions and reduced configurational variations. Thus, they connected the entropy explanation of Hunt and the defect explanation of Ludwig *et al.* to describe the effects of hydrogen bonding in ionic liquids properly.

At the beginning, when little was known about ionic liquids, their attractive solvent properties and the negligible vapor pressure led to the suggestion to replace traditional solvents. Clearly, the hope was that the reduction of traditional solvents would diminish the emission of volatile organic compounds into the atmosphere. Thus, ionic liquids were also called "green" solvents, which produced much confusion, because they can be very toxic.[57,58] Also for many years, the negligible vapor pressure of ionic liquids provoked the concept, that they are undistillable, until 2006 when Earle *et al.* showed that ionic liquids can be distilled by applying high temperatures and high-vacuum.[59] This breakthrough lead to more measurements of the vapor pressure and up to now many data were collected and published on different ionic liquids.[60–70] However, this property cannot be generalized for ionic liquids, because there are some ionic liquids known to be distillable (*e. g.* 1,3-dialkylimidazolium ethylsulfates or bis(triflate)amides),[69] while others decompose at any viable pressure before reaching the boiling point.[71] Thus, like

for traditional solvents (nonionic liquid solvents), the molecular structure of the ionic liquid influences the volatility. Several physicochemical properties are the key to understand why some ionic liquids can be distilled, whereas others just decompose. Among those properties, the thermal stability is one of the major driving factors, but also the understanding of the behavior between the molecular structure and properties such as the enthalpy of vaporization, of the composition and structure of the gas phase as well as of the composition and structure of the liquid-vacuum interface are aspects which should be considered when shedding light on the distillability of ionic liquids. In this manuscript, the focus is on understanding the structure of the gas phase of ionic liquids and the liquid-vacuum interface using different theoretical tools.

1.1.2 Gas Phase of Ionic Liquids

The statement "ionic liquids are nonvolatile" opened the door for the use of ionic liquids in a large number of applications, and as potential replacements for organic volatile solvents. Nevertheless, if ionic liquids are nonvolatile, it would not be possible to obtain ionic liquids with high purity if they contain low volatile impurities, as the ionic liquid cannot be distilled. Determining the gas phase behavior of ionic liquids opens up the possibility for new applications, *e. g.* novel synthetic routes or high-temperature crystallization[72], and has a high importance for theoretical investigations as explained in the following. With the accurate identification of vapor pressure, enthalpy and entropy of vaporization, the models (force fields) used to describe ionic liquids in molecular simulations, such as classical molecular dynamics, Monte Carlo methods, or quantum and molecular mechanics, can be properly validated and even help to anchor the parameters of equations of states.[70,73,74] The significance of theoretical investigations in predicting and validating properties of ionic liquids has been demonstrated by Maginn and Marrow, who first indicated the possibility of vapor pressure measurements of ionic liquids from molecular dynamics simulations performed on the ionic liquid 1-butyl-3-methylimidazolium hexaflu-

orophosphate ($[C_4C_1im][PF_6]$).[75] Also Rebelo *et al.* predicted the volatility of ionic liquids from theoretical considerations.[60] With the work of Earle *et al.* in 2006,[59] where they showed that distillation of ionic liquids can be achieved by fine-tuning the thermal stability of the ionic liquids, they stimulated many groups to investigate the volatility of ionic liquids and to accurately determine the vapor pressure and vaporization enthalpy.[61–68,74,76,77] At that point, it was not clear whether the balance of thermal stability and volatility allows the measurement of vapor pressure to evaluate thermodynamic properties of vaporization. The experiments of Zaitsau et al. proved on the example of 1-alkyl-3-methylimidazolium bis[(trifluoromethane)sulfonyl]imide ionic liquids ($[C_nC_1im][Tf_2N]$, n = 2, 4, 6, 8), that thermodynamic properties of vaporization can be evaluated.[61] Several other experimental studies on the same family of ionic liquids applying different direct methods (*e. g.* mass spectrometry,[64,76] thermogravimetry[77]) followed. Although they mainly focused on this one family of ionic liquids, there still remain discrepancies within the reported data, because the experiments have to be performed under rather extreme conditions (moderate-to-high temperature and very low pressure) always preventing the decomposition of the ionic liquid. Most of the systematic errors in these experiments can be related to differences in purity and thermal stability of the measured ionic liquid.[70] With a newly developed technique,[78] Rocha *et al.* were able to perform high-accuracy studies of thermodynamic properties of vaporization on the $[C_nC_1im][Tf_2N]$-family (n = 2, 3, 4, 5, 6, 7, 8, 10, 12).[74] For the first time, trends in the enthalpy of vaporization could be observed and were related to structural modifications throughout this family of ionic liquids using molecular dynamics simulations, allowing for a link between the trends in thermodynamic properties and the nanostructure behavior of ionic liquids to be made.[74]

For the gas phase of ionic liquids, not only the thermodynamic properties are relevant but also the composition of the gas phase itself, as it gives insights into a possible vaporization mechanism for ionic liquids. With the investigation of the vapor pressure and the thermodynamic properties of the ionic liquids, the exis-

tence of isolated ions could be ruled out as the enthalpies of vaporization are only half the size of the binding energy of one ion pair.[61,79] Thus, the gas phase of ionic liquids is composed of neutral species build up by the ions of the ionic liquid. These neutral species can be single ion pairs or even clusters of ion pairs. It was stated by several groups that the gas phase of ionic liquids is composed of isolated ion pairs.[62–67] They were able to provide evidence via photoionization,[62] classical atomistic simulations,[63] mass spectrometric experiments[64,65] and matrix-isolated Fourier transform infrared spectroscopy (FTIR).[66,67] Although clusters of ion pairs were undetected in their measurements, the possibility of clusters in the gas phase could not be ruled out. By utilizing molecular dynamics simulations, a wider range of conditions could be studied and it was found for the ionic liquid 1-butyl-3-methylimidazolium triflate ($[C_4C_1im][TfO]$) that clusters of ion pairs exist at low temperatures and fragment into ion pairs at higher temperature.[80] In addition, a nonnegligible molar fraction of ions exists for very high temperatures, which are still in the chemical stability range of the investigated ionic liquid. Nevertheless, the predominant species constituting the gas phase of ionic liquids remain neutral ion pairs. By comparing the matrix-isolated FTIR-spectra of the vaporized and the pure ionic liquid $[C_2C_1im][Tf_2N]$, Akai *et al.* were able to identify different energetically stable structures of the ion pair via quantum chemical calculations.[66,67] They stated that the geometrical structure of the gas phase is governed by interionic interactions like coulombic interactions. Comparing this picture of ion pair formation in the gas phase to the liquid structure, where the absence of ion pairs was discussed recently,[81,82] it becomes obvious that the association of ions in the ionic liquid have to undergo structural changes prior to entering the gas phase. These structural changes are most likely to occur close to the liquid-vacuum interface. To fully understand the behavior of the ions at the surface during the vaporization process, a deeper understanding of the ion pairs in the gas phase is necessary, not only related to the relative stability of the ion pairs regarding to the liquid phase, but also which conformations and type of interactions are dominant in the gas phase and how they differ from

the liquid phase. Investigation of the liquid-vacuum interface and simulations of the evaporation of an ion pair would finalize the understanding of this complex vaporization process. The insights gained on this process can help to comprehend the liquid-gas interfaces of ionic liquids, especially important for understanding the advantages of using ionic liquids in specific technological applications, like gas sequestration (*e. g.* carbon dioxide) in ionic liquids.[83]

Therefore, one of the main goals of this work is gaining insight on the complex vaporization process of ionic liquids using theoretical tools. The main areas of interest are the structure and dynamics of ion pairs in the gas phase and how these properties compare with those in the bulk liquid phase, as well as an analysis of liquid-vacuum interfaces of ionic liquids. The results are presented and discussed in subsection 3.1.1, 3.1.2 and 3.3.1.

1.1.3 Interfaces of Ionic Liquids

Ionic liquids show an interesting and partly unusual interfacial behavior, which tremendously increased the interface studies involving ionic liquids in the past five years.[84] In fact, even so tremendous, that a special issue of the PCCP-Journal was dedicated solely to ionic liquid surfaces (liquid-solid and liquid-gas) in 2012. The relevance of ionic liquids in solid-liquid interfaces is uncontested as many applications as lubricants, in electrochemistry and heterogenous catalysis are reported up until now.[18,20,22,85–89] However, in this work the focus is on ionic liquid-gas(vacuum) interfaces as they represent an important part in the complexity of the vaporization process of ionic liquids and increase the comprehension from a structural and even dynamic point of view.

There are many successful applications employing the unique properties of the liquid-gas surface, especially those which involve adsorption or desorption, like supported ionic liquid phase (SILP) catalysis,[88,90,91] gas storage,[8–12] gas separation[13–17] and nanoparticle synthesis.[92–94] Understanding the processes of adsorption and desorption requires a detailed knowledge of interactions between ionic liquids and gas phase probes on the liquid-gas interface. But more impor-

tantly, it needs a detailed description of the surface structure, in order to relate these interactions to the surface structure.[83] For imidazolium-based ionic liquids the surface structure dependency on the anion and the alkyl chain of the cation has been described in detail by various experiments.[95–100] Lockett et al. for example used angle-resolved X-ray photoelectron spectroscopy (XPS) to study the surface structure of three different imidazolium-based ionic liquids with a common anion ($[BF_4]^-$). They observed that the longer the alkyl chain of the imidazolium ring, the more carbon atoms are detected at the surface. Thus, the alkyl chain of all investigated ionic liquids are oriented away from the liquid phase.[95] Measurements on the liquid-gas interface of 1-butyl-3-methylimidazolium tetrafluoroborate ($[C_4C_1im][BF_4]$) and 1-octyl-3-methylimidazolium hexafluorophosphate ($[C_8C_1im][PF_6]$) via neutron reflectometry indicated an ordering at the surface.[96] A lamellar structure was formed due to the segregation of tailgroups and headgroups. For a homolog series of 1-alkyl-3-methylimidazolium tetrafluoroborate ($[C_nC_1im][BF_4]$, $n = 6, 8, 10$) ion scattering measurements showed a positive charge at the surface, which decreases as the length of the alkyl chain increases.[97] This decrease results from a larger shift of the imidazolium ring into the bulk with increasing alkyl chain length in contrast to the anions shift. Similar results for the shift of anions into the bulk for a homolog series of 1-alkyl-3-methylimidazolium bis[(trifluoromethane)sulfonyl]imide ($[C_nC_1im][Tf_2N]$, n=2, 4, 6, 8) has been published by Hammer et al.[98] The trend for the shift of the cation however is different. They identified a covering of the anion with the aliphatic chain if the chain length increases, resulting in a shift of the imidazolium ring to the surface. Next to the various experimental works, several theoretical investigations of the liquid-vacuum interface were carried out.[101–104] Lynden-Bell and Del Pópolo simulated the surface of 1-butyl-3-methylimidazolium ionic liquids using molecular dynamics, observing a tendency of the butyl chain to face towards the vacuum. As the butyl chains are not packed densely at the surface, the imidazolium ring and the anions are visible at the surface too.[101] Further molecular dynamics simulations by Bhargava and Balasubramanian on $[C_4C_1im][PF_6]$ showed that the butyl chain

is preferably orientated parallel to the surface normal whereas imidazolium rings close to the surface tend to be perpendicular to the surface normal.[102] The effect of enlarging the alkyl chain of the imidazolium cation on the surface structure was investigated by Jiang *et al.* performing multiscale coarse-grained (MS-CG) molecular dynamics simulations.[103] They observed a change from a monolayer order to a multilayer order as the length of the alkyl chain increases.

In all these works, the role of the alkyl chain of the imidazolium cation on the surface structure has been studied intensively and also influences of different anions were observed. In contrast, little is known about the effect of alkyl chains at the anion on the surface structure. Recently, Martinez *et al.* combined sum-frequency generation spectroscopy, surface potential and surface tension to analyze the ionic liquid-gas interface of 1-alkyl-3-methylimidazolium alkylsulfates ($[C_nC_1im][C_mSO_4]$, $n = 1, 2, 3, 4, 8$; $m = 1, 4, 8$) dependent on the length of alkyl chains at the cation and anion.[99] They observed that the alkyl chains of both ions are oriented towards the gas phase and the polar groups tend towards the liquid, describing a segregation into tailgroups and headgroups. Such a structural segregation not only occurs at the global interface, but also in a smaller scale—in a nanoscopic scale to microscopic scale—forming domains with mesoscopic interfaces.

Mesoscopic Interfaces of Ionic Liquids

The segregation of pure ionic liquids into microphases or domains—polar and nonpolar—forming interfaces in a mesoscopic scale (see Figure 1.3) has been first reported by Wang and Voth in 2005, using MS-CG molecular dynamics simulations on imidazolium-based ionic liquids.[105] Almost simultaneous Canongia Lopes and Pádua also reported such a segregation using all-atom simulations focusing on the ionic liquid family $[C_nC_1im][PF_6]$.[106] The polar domains form a structure similar to a tridimensional network of ionic channels. This network is permeated by nonpolar domains. With increasing alkyl chain length of the imidazolium-based ionic liquids the nonpolar domains formed are getting more

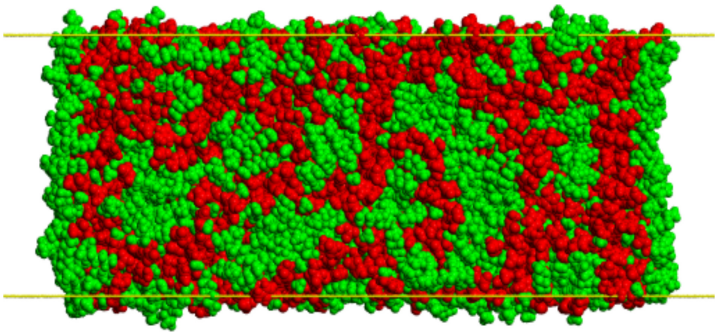

Figure 1.3: Segregation of the pure ionic liquids $[C_2C_1im][C_8SO_4]$ into polar (red) and nonpolar (green) domains, forming mesoscopic interfaces.

continuous.[106] First experimental evidence of the existence of a nanoscale segregation was provided by Triolo *et al.* using X-ray diffraction.[107] The size of the structural heterogeneities (domains) they observed scale linearly with the alkyl chain length of the investigated ionic liquids, suggesting the built up of these domains by the aggregation of alkyl tails surrounded by the charged entities. More experimental evidence on this nanostructure model for the families of the imidazolium-based ionic liquids $[C_nC_1im][BF_4]$, $[C_nC_1im][Cl]$, $[C_nC_1im][Tf_2N]$ and $[C_2C_1im][C_nSO_4]$ was provided too.[108–111] The influence of the alkyl chain at the anion ($[C_2C_1im][C_nSO_4]$) on the nanostructuring of ionic liquids also showed a linear dependency of the nonpolar domain size and the length of the alkyl chain. Interestingly, this structural heterogeneity even occurred for short alkyl chains (ethyl), which was not observed for the other families of ionic liquids so far. Recently, the existence of a third nanostructured domain in ionic liquids has been almost simultaneously suggested by Russina *et al.*[112] and Pereiro *et al.*[113] Considering fluorinated ionic liquids which tend to have an increased aggregation of side chains due to the fluorination,[114] they found evidence for a fluorous domain from experiments and theory.

1.1.4 Ion Pairing in Ionic Liquids

In the previous section, the aggregation of ionic liquids via their alkyl tails to form nanostructured domains was introduced. This aggregation suggests that ionic liquids stick together to some extent. In addition, the formation of ion pairs in the gas phase of ionic liquids has been observed from a variety of experiments (see subsection 1.1.2). In general, the association of oppositely charged ions—ion pairing—which are present in ionic liquids, is a fundamental concept of chemistry.[115] However, ion pairing in neat ionic liquids is a very complex issue, as the solvent—the ionic liquid—itself is composed of oppositely charged ions. Compared to the gas phase of ionic liquids, the identification of ion pairs in the neat ionic liquid is probably the most difficult task, as the ions are surrounded by many oppositely charged ions.[116–120]

From the interactions present in ionic liquids two main association patterns of ions emerge: One where the hydrogen bonding ability of the ionic liquids (see subsection 1.1.1) aligns oppositely charged ions in one plane and another where the ions are stacked. But, choosing specific "pairs" is rather unwarranted,[120] thus, the most general possible definition for ion pairing from a microscopic point of view is to correlate the distance and the time oppositely charged ions travel together. Applying this general definition it was found from molecular dynamics simulations that ion pairs are very short-lived and the ions diffuse rather independently from each other, indicating a lack of ion pairing.[121]

However, macroscopic studies draw a different picture. Watanabe and coworkers[122–125] for example related the ion mobility to the ionic conductivity of ionic liquids according to:

$$I = \frac{\Lambda_{imp}}{\Lambda_{\mathrm{NMR}}} \quad , \tag{1.1}$$

where I is defined as ionicity, Λ_{imp} represents the ion mobility from conductivity measurements and Λ_{NMR} is the ion mobility from NMR measurements calculated according to the Nernst–Einstein equation:

$$\Lambda_{\mathrm{NMR}} = \frac{N_A e^2}{kT}(D^+ + D^-) \quad , \tag{1.2}$$

where N_A is the Avogadro number, e is the electronic charge, k is the Boltzmann factor, T is the temperature, D^+ and D^- are the diffusion constants of the cation and the anion. Watanabe and coworkers showed that the diffusion of the ions measured by NMR is significantly larger than those obtained from conductivity measurements, leading to ionicity values smaller than unity ($I < 1$), which are in agreement with the deviations from ideality in the Walden plot.[126–128] They rationalized these deviations by considering the presence of ion pairs to some extent[123,125] and thus a correlated motion of the oppositely charged ions has been considered.[129]

For ionic liquids, simulations showed that to reproduce dynamical data properly the charge of the ions need to be downscaled,[130] suggesting that charge transfer between ions in ionic liquid is important. Yet, the charge used to calculate the ion mobility via the Nernst–Einstein equation (1.2) was unity and seems to be a simple generalization. Thus, a starting point for exploration of contributions to the concept of ionicity is to investigate the charge transfer in ionic liquids. First results of the charge transfer in different ionic liquids and their influence on the ionicity of these ionic liquids are given in subsection 3.3.2.

1.2 Rotaxanes

Rotaxanes are a class of supramolecular complexes consisting of two mechanically interlocked components, the wheel and the axle. The axle is a linear dumbbell-shaped molecule with two sterically demanding groups at both ends, the so called stoppers. The wheel surrounds the axle but is not connected covalently to it (see Figure 1.4 for a schematic illustration).

A dethreading from the axle is inhibited by the bulky stoppers. If the stoppers are missing at the axle the supramolecular structures are called pseudorotaxanes. Although the two components are not covalently bound to each other, a covalent bond needs to be broken to separate them.[131,132] Otherwise the two components are able to move quite freely with respect to each other. Nevertheless, noncovalent bonds, like hydrogen bonds or π-π interactions, can have a significant influence on the movement of the wheel along the linear axle. They can even be used to control the motions in the interlocked system.[133–149] Thus by utilizing this motion in a clever way, the structure of rotaxanes can work as prototypes for molecular motors, which rotate under energy input, molecular shuttles, which transport molecules or ions from one location to another, molecular switches, which can be reversibly shifted between two or more stable states, and even molecular walkers, which walk directionally along short molecular tracks.[150,151] In general, these motions are triggered by external stimuli such as chemical processes (pH gradient), light, electrical fields or redox processes.[133,135,139,140,143,144,148,149,152,153]

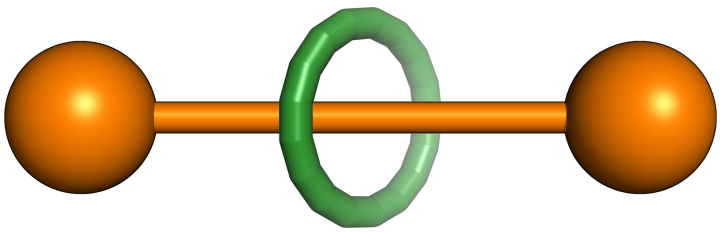

Figure 1.4: Schematic illustration of a rotaxane. Green: Wheel; Orange: Axle with to bulky stoppers at both ends.

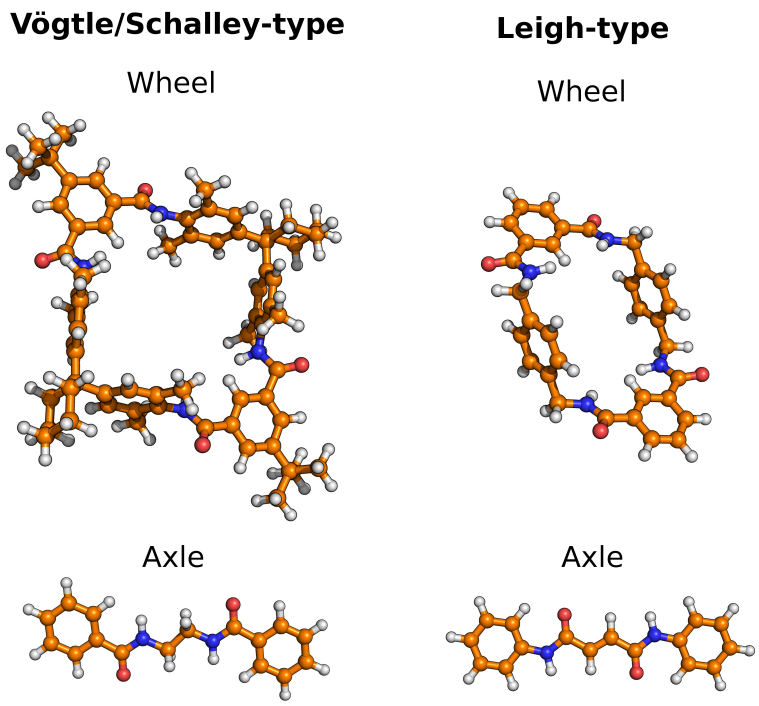

Figure 1.5: Representation of the two different macrocycles (wheel) of the Vögtle/Schalley-type (left) and the Leigh-type (right) and the corresponding axles. For rotaxanes, the following coloring code is used here and throughout the work: **C**: orange; **N**: blue; **H**: white; **O**: red.

Typically, rotaxanes are synthesized from templates, where the axle possesses at least one docking station (*e. g.* hydrogen bonding site) for the wheel.[132,138] The first rotaxane based molecular shuttle was synthesized in 1991 by the Stoddart group.[154] In the last few years, several rotaxane shuttles and switches have been synthesized by the group of Leigh[133,139,144,152,155–160] Most of them are based on a benzylic amide macrocycle with isophtalamide units building up twofold hydrogen bonds to the axle's acceptor site. The same hydrogen bond motif has often been used by Schalley and coworkers for the design of molecular shuttles[140,161–163] based on the Vögtle-Hunter tetralactam macrocycle.[164,165] In the following, the two different types of macrocycles will be denoted as Leigh-type and Vögtle/Schalley-type, for a representation of both macrocycles and their corresponding axles see Figure 1.5.

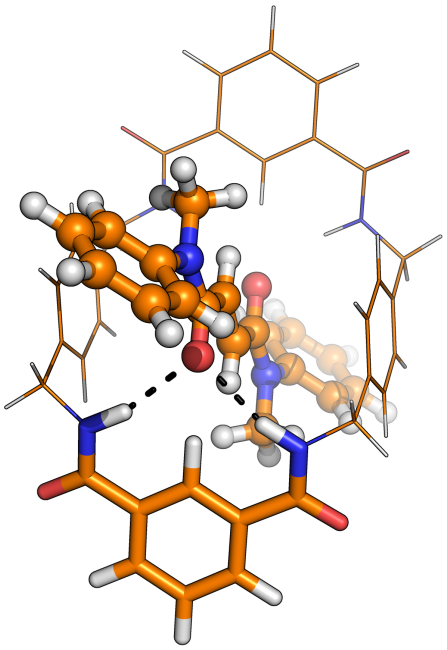

Figure 1.6: Representation of a twofold hydrogen bond (black dashed lines) between the axle (ball and stick) and an isophtalamide unit (sticks) of the wheel (lines) at the example of a Leigh-type rotaxane.

The twofold hydrogen bond motif used in both rotaxanes to form these host-guest complexes is a special type of hydrogen bond.[166] The twofold hydrogen bond (see Figure 1.6) can be described as the formation of two hydrogen bonds between one acceptor at one molecule (axle) and two different donors at another molecule (wheel). Their importance for and influence on the formation of amide-linked rotaxanes like the Vögtle/Schalley-type and Leigh-type have already been investigated in detail.[166,167]

Here, the focus of the research is to explore the complexity of this binding motif by altering the substituents on the axle of both rotaxanes and therefore to understand how these alterations influence possible motions, important for their usage as molecular shuttles or molecular switches. Therefore, the motions as well as the knowledge gained from theory on these systems will be described in more detailed in the following.

1.2.1 The Complexity of Rotaxanes

When describing the complexity of rotaxanes, different possible ways exist. Probably, the two most important ones are the synthesis, as the construction of these host-guest complexes is very challenging, and the possible motions which can occur in these complexes, as their exact characterization as well as the interplay between wheel and axle during these motions are not fully comprehended yet. Here, the complexity of motions in rotaxanes will be used as example to describe the complexity of rotaxanes.

Understanding the important motions enabled by the structure of the rotaxanes on a molecular level is crucial. It helps to improve and to tune the utilization of rotaxanes as molecular shuttles or molecular switches, as modifications in the structure of these host-guest complexes can alter their preferences for existing docking stations—molecular subunits on the axle, which form attractive interactions (*e. g.* hydrogen bonds) with the wheel—within the rotaxanes. Two important movements are the shuttling movement of the wheel along the axle and the pirouetting, where the wheel rotates around the axle. Schematics of the principle of these movements are shown in Figure 1.7. The pirouetting was extensively studied by the group of Sauvage which focused their work on copper-complexed rotaxanes[168–173] They showed that the pirouetting of these rotaxanes can be triggered electrochemically[169–172] or by demetallation.[168] For

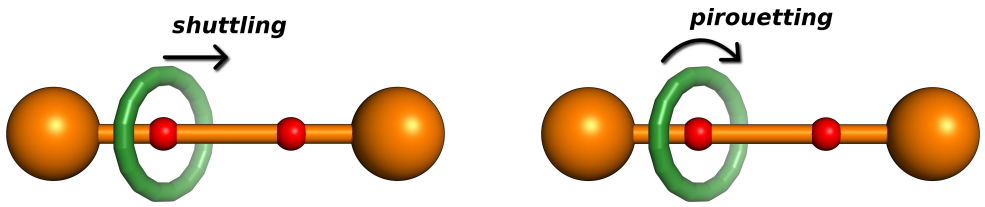

Figure 1.7: Schematic illustration of two important motions present in rotaxanes with two docking stations. Left: Translation of the wheel (green) between different docking stations (red); Right: Pirouetting of the wheel (green) around the axle (orange) at one docking station (red).

the electrochemical-induced oscillation of the wheel, they found huge differences in the rearrangement rate of the wheel for the different oxidization states of copper and attributed it to an easier substitution of the ligand in the coordination sphere of a monovalent complex than in a divalent complex.[173] From density functional theory calculations it was found that this mechanism proceeds in a concerted fashion via a single transition state.[174] The shuttling movement or translation of the wheel has been studied intensively, where the change in attraction of a docking station is introduced by certain external stimuli to initiate this motion.[133,135,139,140,143,144,148,149,152] It was often assumed to be of diffusive nature until recently it was proposed by Baggermann et al.[175] that other possibilities should be considered for this motion. They suggested a harpooning mechanism, which is described by a reduction of a double hydrogen bond at one docking station to a single hydrogen bond while at the second docking station simultaneously a new hydrogen bond between axle and wheel is formed. Therefore, the axle needs to undergo a certain structural rearrangement in order to bring the different docking stations closer together. Understanding the motions in rotaxanes in their full complexity from loosening interaction (*i.e.* hydrogen bonds) at one binding site over moving along/rotating around the axle to binding to the second docking site, needs to be carefully investigated by experiments and theoretical studies. In the following section, the theoretical work in order to understand the complexity of rotaxanes up until now will be described in more detail.

1.2.2 Interactions in Rotaxanes from Theory

Theoretical work on rotaxanes in order to understand their complex binding patterns and motions accompanies the experimental work frequently. Investigations of the shuttling motion, for example, showed that the effective coordinate of the motion can be described as a double-minimum potential, due to a separation of the motion from the other degrees of freedom.[176] Others investigated the shuttling motion of the wheel as a one-dimensional translation in such a simplified double-minimum potential and studied the influence of the Kohn–Sham frontier

orbitals of shuttle and axle upon conductivity and electron tunneling along the rotaxane.[177] Quantum mechanical studies on the shuttling motion of rotaxane-based molecular switches showed that modification of the redox states of the wheel or the axle results in changes of the computational energy profile.[178] In order to gain insights into the energy profile of the shuttling motion, the stability of docking sites of a rotaxane-based molecular shuttle was explored by means of molecular modeling.[179] By applying semiempirical methods, the selectivity of two dibenzo-[24]crown-8 macrocycles to different ammonia binding sites in a [3]rotaxane were studied and hydrogen bond enthalpies in polymeric urethane rotaxanes were estimated.[180] Furthermore, molecular mechanics were used to investigate low-barrier molecular rotary motors with rotaxane architecture.[181]
Next to the investigations of the complex motions and binding preferences, the binding patterns are of large interests,[137,166,167] especially in the group of Kirchner,[167,182–184] as they give insights into the differences in energies due to small variations of wheel and axle and assist in tuning them for desired properties or to lower the energy barrier for the motions. The work of the Kirchner group focused on the main binding motifs of the Vögtle/Schalley- and Leigh-type macrocycles to the corresponding axles (see Figure 1.5). Energetical and vibrational analysis of the twofold hydrogen bonds inhibited by rotaxane mimetics were performed in order to understand their binding patterns. A close relationship between the strength of the hydrogen bonds and the charge of the acceptor oxygen has been found. Substitution with electron withdrawing groups at the axle weakens the twofold hydrogen bonds whereas electron donating groups led to increased interaction energy. The binding energies were correlated to the red shift of the involved stretching modes (N−H stretching and C=O stretching mode). Compared to single hydrogen bonds, the twofold hydrogen bonds showed shorter red shifts for the N−H stretching mode but increased red shifts for the C=O stretching mode.[167] Upon complex-formation of pseudorotaxanes large shifts of N−H stretching modes for wheel and axle were found,[182,184] which reflect trends in individual hydrogen bond energies better than the carbonyl stretch-

ing modes.[184] For pseudorotaxane with a secondary amide axle threaded into the tetralactam macrocycle cavity the most stable conformation consists of three hydrogen bonds between axle and wheel. The known twofold hydrogen bonds between the axles carbonyl group and one isophtalamide group of the wheel and a single hydrogen bond between the amide of the axle and a turned carbonyl group of the wheels amide group, pointing inside the cavity.[182] Substitutions with electron donating and electron withdrawing groups at the axle led to changes in the charge density at the axle's carbonyl oxygen, but had hardly an effect on the total binding energy of this pseudorotaxane system.[183] Analysis of the individual hydrogen bonds based on the shared electron number approach[185] revealed that the effect of the substituents are canceled as the axle simultaneously acts as hydrogen bond donor (single hydrogen bond) and acceptor (twofold hydrogen bond). Comparison of results from different density functional theory calculations, including one functional with an empirical correction for dispersion interaction, to Møller–Plesset second-order perturbation (MP2) calculations showed that the contribution of dispersion interaction to the total binding energy in the gas phase of these systems is of the same magnitude as hydrogen bond interaction.[182] However, the order of stability of different rotaxane co-conformations is quite independent of dispersion interaction. In solution, it can be assumed that the dispersion interaction between the solvent and the wheel is of the same magnitude as the dispersion interaction between axle and wheel. Investigations of the solvent effects suggest that the examined pseudorotaxanes are stable in chloroform but will dethread in water.

The functionality of rotaxanes as molecular shuttles and switches is based on the different interplay of noncovalent interactions between axle, wheel and solvent. To understand the noncovalent interactions on a molecular level in a more detailed way, further systematic probing of effects between wheel, axle and solvent need to be preformed applying different approaches and compared to experimental data. Gaining insights on these different effects was part of this work and will be tackled in section 3.4.

2 Methodology

2.1 Multiscale Molecular Methods

Nowadays, describing the properties and behavior of complex chemical systems is an interdisciplinary challenge. Results obtained from theory need to be combined with and validated by the corresponding experiments and *vice versa*. The development of fast supercomputers opened up the possibility to tackle such systems on different time and size scales from theory, ranging from static quantum chemical methods, where the electronical structure of single molecules is treated, over the cluster ansatz and *ab initio* molecular dynamics covering solvent effects, to force field methods (classical molecular dynamics), where thousands of molecules can be time-dependently simulated up to microseconds. Each of these fields is highly advanced, but still has room for further development. Nevertheless, current developments focus on refining old methods rather than introducing new ones. Thus, the next step towards an accurate description of complex chemical systems from theory lies in the combination of more than one method, utilizing their advantages in multiscale approaches. There are different ways of applying the multiscalar aspect. Probably, the best-known is the hybrid approach, which combines existing methods in a simultaneous calculation and which was recently awarded the Nobel Prize in chemistry.[186] Separate calculations applying different methods on the same system describe another approach, as well as using coarser methods in order to speed up accurate methods. For a detailed description of these approaches the reader is referred to the book by R. Abrol, B. Kirchner and J. Vrabec (see Ref. [187]). In the following, the methods used throughout this

work will be introduced, starting with basic static quantum chemistry, density functional theory and the dispersion correction methods. Then, the cluster ansatz is presented followed by *ab initio* molecular dynamics and the description of force fields. Finally, different population analysis methods will be briefly outlined and a topology to ionic liquids will be introduced.

2.1.1 Static Quantum Chemistry

The focus of static quantum calculations lies in the determination of the structure and energies of molecules. The energy E of the system which is described by the wave function Ψ is given via the time-independent Schrödinger equation

$$\mathbf{H}\Psi = E\Psi \tag{2.1}$$

as eigenvalue of the Hamiltonian

$$\mathbf{H} = \mathbf{T} + \mathbf{V}, \tag{2.2}$$

where $\mathbf{T}$ is the kinetic energy operator and $\mathbf{V}$ the potential energy operator. In this work, the description of relativistic effects is neglected. However, all investigated systems are based on organic molecules without heavy elements. Furthermore, only time-independent phenomena are treated, which reduces the Schrödinger equation to the time-independent Schrödinger equation. Thus, the calculations are based on the nonrelativistic time-independent electronic Schrödinger equation with the electronic Hamilton operator

$$\mathbf{H}_\mathrm{e} = \mathbf{T}_\mathrm{e} + \mathbf{V}_\mathrm{eN} + \mathbf{V}_\mathrm{ee} + \mathbf{V}_\mathrm{NN} \tag{2.3}$$

$$= -\frac{1}{2}\sum_i \Delta_i - \sum_A \sum_i \frac{Z_A}{\mathbf{r}_{iA}} + \sum_i \sum_{i>j} \frac{1}{\mathbf{r}_{ij}} + \sum_A \sum_{A>B} \frac{Z_A Z_B}{\mathbf{R}_{AB}}, \tag{2.4}$$

where $\mathbf{T}_\mathrm{e}$ is the electron's kinetic energy operator, $\mathbf{V}_\mathrm{eN}$ is the electron-nucleus interaction operator, $\mathbf{V}_\mathrm{ee}$ is the electron-electron interaction operator, $\mathbf{V}_\mathrm{NN}$ is the nucleus-nucleus interaction operator, $\mathbf{r}_{ij}$ is the distance between two electrons i and j, $\mathbf{r}_{iA}$ is the distance between electron i and nucleus A, $\mathbf{R}_{AB}$ is the distance between two nuclei A and B, and Z_A and Z_B are the nuclear charges of nucleus

A and B, respectively. Here, the approximation of Born and Oppenheimer was used, which states that the movement of the electrons can be separated from that of the nuclei due to the smaller mass of electrons compared to nuclei. Thus, the kinetic energy operator of the nuclei has no influence on the wave function Ψ_e of the electrons. Equation (2.4) and the following equations are given in atomic units for the sake of simplicity.

In general, the electronic many-particle Schrödinger equation

$$\mathbf{H}_\mathrm{e}\Psi_\mathrm{e} = E_\mathrm{e}\Psi_\mathrm{e} \tag{2.5}$$

cannot be solved analytically due to the electron-electron coupling and further procedures to approximate the solution need to be introduced. One approximation is to describe the electronic wave function Ψ_e as a linear combination of n known basis functions (atomic orbitals) χ_i

$$\Psi_\mathrm{e} = \sum_{i=1}^{n} c_i\chi_i, \tag{2.6}$$

which leads to the matrix representation of the Schrödinger equation:

$$\begin{aligned}\sum_{i=1}^{n} c_i\langle\chi_k|\mathbf{H}_\mathrm{e}|\chi_i\rangle = E_\mathrm{e}\sum_{i=1}^{n} c_i\langle\chi_k|\chi_i\rangle \quad k = 1, 2, \ldots, n \\ \sum_{i=1}^{n} c_i H_{ki} = E_\mathrm{e}\sum_{i=1}^{n} c_i S_{ki} \quad k = 1, 2, \ldots, n \quad .\end{aligned} \tag{2.7}$$

Here, H_{ki} denotes elements of the Hamilton matrix and S_{ki} the elements of the overlap matrix. Exact solutions only exist for the infinite summation over the indices k and i. An approximate solution can be gained with the use of the variational principle, where the energy $\tilde{E}$ of a system described by an approximated wave function $\tilde{\Psi}$ is always larger than the energy E_0 of the system described by the exact wave function Ψ_0:

$$\langle\mathbf{H}_\mathrm{e}\rangle_{\tilde{\Psi}} = \frac{\langle\tilde{\Psi}|\mathbf{H}_\mathrm{e}|\tilde{\Psi}\rangle}{\langle\tilde{\Psi}|\tilde{\Psi}\rangle} = \tilde{E} \geq \langle\mathbf{H}_\mathrm{e}\rangle_{\Psi_0} = E_0 \quad . \tag{2.8}$$

The Hartree–Fock method approximates the wave function by a single Slater determinant of one-particle wave functions $\phi(i)$. The motion of one electron i is

described in the mean-field of the other $n-1$ electrons, leading to an effective one-electron operator—the Fock operator $\mathbf{f}(i)$—which is given by

$$\mathbf{f}(i) = \mathbf{h}(i) + \sum_{b=1}^{n} \left(\mathbf{J}_b(i) - \mathbf{K}_b(i)\right) \quad . \tag{2.9}$$

The one-electron operator $\mathbf{h}(i)$ consists of the kinetic energy operator and the electron-nucleus interaction operator:

$$\mathbf{h}(i) = -\frac{1}{2}\Delta_i - \sum_A \frac{Z_A}{\mathbf{r}_{iA}} \quad , \tag{2.10}$$

and the two-electron operators $\mathbf{J}_b$ and $\mathbf{K}_b$ are denoted as Coulomb and exchange operator:

$$\mathbf{J}_b(i)|\phi_a(i)\rangle = \left\langle \phi_b(j) \left| \frac{1}{\mathbf{r}_{ij}} \right| \phi_b(j) \right\rangle |\phi_a(i)\rangle \quad , \tag{2.11}$$

$$\mathbf{K}_b(i)|\phi_a(i)\rangle = \left\langle \phi_b(j) \left| \frac{1}{\mathbf{r}_{ij}} \right| \phi_a(j) \right\rangle |\phi_b(i)\rangle \quad , \tag{2.12}$$

where $\phi_a(i)$ is a set of one-particle wave function of electron i and $\mathbf{r}_{ij}$ is the distance between electron i and electron j. The Hartree–Fock equation

$$\mathbf{f}(i)\phi_a(i) = \varepsilon_a \phi_a(i) \tag{2.13}$$

can only be solved iteratively, because the Fock operator depends on all the other one-particle wave functions. The generated solution to the Schrödinger equation via the Hartree–Fock method replaces the real electron-electron interaction by an average (mean-field) interaction, reducing the obtainable accuracy. In this ansatz, the correlation between electrons is described insufficiently and the approximation of the wave function as a single Slater determinant provides qualitatively bad results if the states are strongly interacting with each other. Thus, to account for the electron correlation, different methods based on the wave function exist, *e. g.* configuration interaction (CI), coupled cluster (CC) and perturbation theory (*e. g.* MP2). For a detailed description of these methods, the reader is referred to the books of A. Szabo and N. S. Ostlund (see Ref. [188]) and F. Jensen (see Ref. [189]).

Another approach to describe the correlation between electrons, especially for larger systems, is the density functional theory (DFT), which will be briefly outlined here. For a more detailed description of this theory, the reader is referred to the book of R. G. Parr and W. Yang (see Ref. [190] and to the book of W. Koch and M. C. Holthausen (see Ref. [191]). The basis for DFT is the proof by Hohenberg and Kohn, that the ground-state electronic energy, the wave function and further electronic properties are determined completely by the electron density ρ (1st Hohenberg–Kohn theorem).[192] Thus, an n-electron system containing $3n$ coordinates and n spin-coordinates for the electrons can be described by a continuous function $\rho(x, y, z)$ which only depends on three coordinates, independently of the number of electrons. By validating the variational principle (2.8) for the electron density ρ (2nd Hohenberg–Kohn theorem), Hohenberg and Kohn showed that in principle the ground-state energy and the density can be determined. However, both theorems provide no explicit way to calculate the energy from the density.

A solution to this problem has been proposed by Kohn and Sham,[193,194] where they introduced a fictive reference system of noninteracting electrons with the same ground-state density as the system with interacting electrons. The exact solution of the system of noninteracting electrons is one single Slater determinant of n one-electron functions—the Kohn–Sham orbitals ϕ_i^{KS}—which form the electron density according to

$$\rho = \sum_{i=1}^{n} \langle \phi_i^{\mathrm{KS}} | \phi_i^{\mathrm{KS}} \rangle \quad . \tag{2.14}$$

The energy as a functional of the density can then be written as:

$$\begin{aligned} E^{\mathrm{KS}}[\rho] &= T[\rho] + E_{\mathrm{Ne}}[\rho] + E_{\mathrm{ee}}[\rho] \\ &= T_{\mathrm{S}}[\rho] + E_{\mathrm{Ne}}[\rho] + J[\rho] + E_{\mathrm{XC}}[\rho] \\ &= -\frac{1}{2} \sum_{i=1}^{n} \langle \phi_i^{\mathrm{KS}} | \Delta | \phi_i^{\mathrm{KS}} \rangle - \sum_{A=1}^{N} \int \frac{Z_A}{|\mathbf{R}_A - \mathbf{r}|} \rho(\mathbf{r}) d\mathbf{r} \\ &\quad + \frac{1}{2} \iint \frac{\rho(\mathbf{r}) \rho(\mathbf{r}')}{|\mathbf{r} - \mathbf{r}'|} d\mathbf{r} d\mathbf{r}' + E_{\mathrm{XC}}[\rho] \end{aligned} \tag{2.15}$$

with $T_\mathrm{S}[\rho]$ as the functional of the kinetic energy, $E_\mathrm{Ne}[\rho]$ as the functional of the nuclei-electron interaction, $J[\rho]$ as the functional of the Coulomb energy, $E_\mathrm{XC}[\rho]$ as exchange-correlation functional, and $\mathbf{R}_A$ as the coordinates of nucleus A. It has to be noted here that the kinetic energy functional described by the Kohn–Sham formalism $T_\mathrm{S}[\rho]$ is not the exact kinetic energy functional $T[\rho]$ and that the difference is accounted for in the exchange-correlation functional $E_\mathrm{XC}[\rho]$. The Kohn–Sham orbitals ϕ_i^KS are obtained by minimizing the energy with respect to the orbitals, which are required to be orthonormal. This leads to the Kohn–Sham equations

$$\mathbf{h}^\mathrm{KS}\phi_i^\mathrm{KS} = \varepsilon_i^\mathrm{KS}\phi_i^\mathrm{KS} \tag{2.16}$$

with the Kohn–Sham orbital energy $\varepsilon_i^\mathrm{KS}$ and the Kohn–Sham operator

$$\mathbf{h}^\mathrm{KS}(\mathbf{r}_i) = -\frac{1}{2}\Delta_i - \sum_A \frac{Z_A}{|\mathbf{R}_A - \mathbf{r}_i|} + \int \frac{\rho(\mathbf{r}_j)}{|\mathbf{r}_i - \mathbf{r}_j|} d\mathbf{r}_j + v_{xc}(\mathbf{r}_i) \quad , \tag{2.17}$$

where the exchange-correlation potential $v_{xc}(\mathbf{r}_i)$ can equivalently be written as the functional derivative of the exchange-correlation energy:

$$v_\mathrm{xc}(\mathbf{r}) \equiv \frac{\delta E_\mathrm{XC}[\rho(\mathbf{r})]}{\delta\rho(\mathbf{r})} \quad . \tag{2.18}$$

As shown in equation (2.15), all functionals except $E_\mathrm{XC}[\rho]$ can be stated explicitly. The differences in many density functionals lie in the description of the exchange-correlation functional, which also became the major problem of DFT. In general, the exchange-correlation functional is separated in an exchange functional $E_\mathrm{X}[\rho]$ and a correlation functional $E_\mathrm{C}[\rho]$:

$$E_\mathrm{XC}[\rho] = E_\mathrm{X}[\rho] + E_\mathrm{C}[\rho] \quad . \tag{2.19}$$

Local treatment of the density as a uniform electron gas (local density approximation (LDA)) gives the following expression for the exchange functional $E_\mathrm{X}[\rho]$:

$$E_\mathrm{X}^\mathrm{LDA}[\rho] = -c \int \rho(\mathbf{r})^{4/3} d\mathbf{r} \quad , \tag{2.20}$$

where c is a constant, while the correlation functional is interpolated by a method introduced by Vosko, Wilk and Nusair $E_\mathrm{C}^\mathrm{VWN}$.[195] Improvements to the LDA

approach consider a nonuniform electron gas by introducing a dependency of both the exchange and the correlation functional on the derivative of the density. These methods are known as generalized gradient approximations (GGA). In 1988, Becke proposed a widely used correction to the exchange-functional used in the LDA approach,[196] which is fitted to the Hartree–Fock exchange energy of the noble gases up to radon. Lee, Yang and Parr derived a correlation functional $E_{\mathrm{C}}^{\mathrm{LYP}}$ based on wave function calculations of helium atoms.[197] The combination of these two corrections leads to the BLYP functional. Further functionals are the hybrid functionals (*e. g.* B3LYP), which include the Hartree–Fock exchange to a certain amount in the exchange functional, but dependent on empirical parameters. This is one of the drawbacks of these functionals, even though they provide the best results.

One of the most important improvements in accuracy in density functional theory was the introduction of dispersion-corrected functionals. Here, the very straightforward and practical approach by Grimme *et al.*[198–200] will be introduced. The dispersion-corrected total energy $E_{\mathrm{DFT\text{-}D}}$ is defined by

$$E_{\mathrm{DFT\text{-}D}} = E_{\mathrm{DFT}}^{\mathrm{KS}} + E_{\mathrm{disp}} \quad , \tag{2.21}$$

where $E_{\mathrm{DFT}}^{\mathrm{KS}}$ describes the usual self-consistent Kohn–Sham energy and E_{disp} is an empirical dispersion correction given by

$$E_{\mathrm{disp}} = -s_6 \sum_{i=1}^{N-1} \sum_{j=i+1}^{N} \frac{C_6^{ij}}{R_{ij}^6} f_{\mathrm{dmp}}(R_{ij}) \quad , \tag{2.22}$$

where N is the number of atoms in the system, C_6^{ij} denotes the dispersion coefficient for an atom pair (i, j), R_{ij} is the corresponding interatomic distance and s_6 describes a global scaling factor fitted to several benchmarks specific for different functionals.[198] In order to avoid near-singularities for small R_{ij}, the damping function f_{dmp} is introduced:

$$f_{\mathrm{dmp}}(R) = \frac{1}{1 + e^{-\alpha(R/R_0 - 1)}} \quad , \tag{2.23}$$

where R_0 denotes the sum of atomic van der Waals radii and α is a scaling factor, describing the steepness of the damping function. The atomic C_6^i coefficients,

partly taken from literature, are averaged over possible hybridization states of the individual atoms. The dispersion coefficients C_6^{ij} for an atom pair (i, j) are obtained using a simple mixing rule given by:

$$C_6^{ij} = 2\frac{C_6^i C_6^j}{C_6^i + C_6^j} \quad . \tag{2.24}$$

Further improvement of the above described approach could be obtained by a consistent and accurate *ab initio* parameterization for the elements H to Pu. The new approach, also denoted as DFT-D3, applies atom-pairwise specific dispersion coefficients and cutoff radii, which are both calculated from first principle calculations. Even three-body terms have been considered. For more details on the dispersion-corrected density functional theory, see the original references [198–200].

Calculating the electronic structure with density functional theory for large systems ($\sim$ 1000 atoms) is in the standard approach, as described above, still not efficient enough, as the computation of the Hartree (Coulomb) energy $J[\rho]$ and the orthogonalization of the wave functions are not scaling linearly with system size. Therefore, they dominate the computational costs for these large systems. To reduce the computational costs and to treat large condensed systems, an effective hybrid Gaussian and plane wave method (GPW method) has been introduced,[201,202] which is based on the projected augmented wave method introduced by Blöchl,[203] and will be briefly outlined in the following as it was used to calculate the electronic structure during the *ab initio* molecular dynamics simulations. The GPW method, as the name already indicates, uses two representations of the electron density $\rho(\mathbf{r})$ and $\tilde{\rho}(\mathbf{r})$. The first representation $\rho(\mathbf{r})$ is an expansion in atom-centered, contracted Gaussian functions $\varphi_\nu(\mathbf{r})$:

$$\rho(\mathbf{r}) = \sum_{\mu\nu} D_{\mu\nu}\varphi_\mu(\mathbf{r})\varphi_\nu(\mathbf{r}) \quad , \tag{2.25}$$

where $D_{\mu\nu}$ is a density matrix element and

$$\varphi_\nu(\mathbf{r}) = \sum_i k_{i\nu} g_i(\mathbf{r}) \tag{2.26}$$

with $g_i(\mathbf{r})$ as primitive Gaussian functions and the corresponding contraction coefficients $k_{i\nu}$, and the second $\tilde{\rho}(\mathbf{r})$ is represented by an auxiliary basis of plane waves given by

$$\tilde{\rho}(\mathbf{r}) = \frac{1}{\Omega} \sum_{\mathbf{G}} \tilde{\rho}(\mathbf{G}) \exp\left(\mathrm{i}\mathbf{G}\cdot\mathbf{r}\right) \quad , \tag{2.27}$$

where Ω is the unit cell volume and $\mathbf{G}$ are the reciprocal lattice vectors. To ensure the equality on a regular grid in the unit cell between both representations $\tilde{\rho}(\mathbf{r})$ and $\rho(\mathbf{r})$, the coefficients $\tilde{\rho}(\mathbf{G})$ are introduced. With this dual representation, the expensive calculation of the Hartree (Coulomb) energy $J[\rho]$ can be reduced to a single sum and thus, the Kohn–Sham energy expression (2.15) can be rewritten:

$$\begin{aligned} E^{\mathrm{KS}}_{\mathrm{GPW}}[\rho] &= T_{\mathrm{S}}[\rho] + E_{\mathrm{Ne}}[\rho] + J[\rho] + E_{\mathrm{XC}}[\rho] \\ &= -\frac{1}{2} \sum_{\mu\nu} D_{\mu\nu} \langle \varphi_\mu(\mathbf{r}) | \Delta | \varphi_\nu(\mathbf{r}) \rangle \\ &\quad + \sum_{\mu\nu} D_{\mu\nu} \langle \varphi_\mu(\mathbf{r}) | V^{PP}(\mathbf{r},\mathbf{r}') | \varphi_\nu(\mathbf{r}') \rangle \\ &\quad + 2\pi\Omega \sum_{\mathbf{G}} \frac{\tilde{\rho}^*(\mathbf{G})\tilde{\rho}(\mathbf{G})}{\mathbf{G}^2} + E_{\mathrm{XC}}[\rho] \quad , \end{aligned} \tag{2.28}$$

where $\tilde{\rho}^*(\mathbf{G})$ is the complex conjugate of $\tilde{\rho}(\mathbf{G})$, and $V^{PP}(\mathbf{r},\mathbf{r}')$ describes normconserving pseudopotentials, *e. g.* pseudopotentials of Goedecker, Teter and Hutter (GTH).[204,205] To describe a wide range of chemical interesting events, like bond breaking and formation, only an accurate description of the valence electrons is required, which can be obtained by these pseudopotentials. In addition, these pseudopotentials include scalar relativistic corrections because they were optimized based on fully relativistic density functional theory calculations, improving their accuracy for applications involving heavier elements. A more detailed explanation of the implementation and treatment of the single parts of the energy expression (2.28) is given in Ref. [206].

2.1.2 Cluster Ansatz

The cluster ansatz is a method to incorporate solvent effects during *ab initio* calculations. The first appearance of this method was given by Hermansson *et*

al.[207] and Eggenberger *et al.*[208] The idea behind this method is quite simple. Instead of surrounding the system with a continuum representing the solvent, like COSMO,[209] the investigated system is surrounded by a small number of solvent molecules, forming a cluster. The explicit incorporation of these solvent molecules acts as a local representation of the solvent, leading to solvent effects in the system. Certainly, one cluster is not sufficient to be representative for solvent effects, thus a large amount of clusters needs to be generated. The best way to generate these clusters is to perform molecular dynamics or Monte–Carlo simulations, as a large number of particles can be simulated efficiently with a reasonable accuracy. From these simulations, a series of snapshots containing the investigated system can be extracted, providing a large number of different clusters with a variance in the explicit solvation pattern. Utilizing this procedure, two problems need to be addressed: First, the number of snapshots or in this case the number of clusters has to be large enough to guarantee a high variance in the solvation pattern. Second, the number of explicit solvent molecules surrounding the investigated system needs to be carefully evaluated, as they directly contribute to solvent effects and additionally increase computational efforts for the subsequent *ab initio* calculations. In general, it can be stated that the larger the number of clusters, the better the variance, as this increases the statistics of the solvent effect on the investigated system, but it also increases the total computational effort. Further, as the explicit solvent molecules act as local representation of the solvent, at least the first solvent shell surrounding the system should be considered. To incorporate even more solvent molecules and to create not only a local representation of the solvent on the *ab initio* level, *ab initio* molecular dynamics simulations should be performed, whose trajectories can also be used to generate snapshots for the cluster ansatz.

2.1.3 Ab initio Molecular Dynamics

In general, molecular dynamics methods generate a series of time-correlated points in space by propagating the system in time. Therefore, the system (set

of coordinates and velocities) is propagated according to Newton's second law ($F = ma$) using numerical techniques involving a sequence of small finite time steps, *i. e.* Verlet algorithm.

The basic idea underlying every *ab initio* molecular dynamics method is to compute the forces acting on the nuclei from electronic structure calculations "on-the-fly". The electronic variables are considered to be active and explicit degrees of freedom in the simulation. In this way, even systems where the electronic structure changes drastically during the dynamics can be handled easily. There are different approaches to include the electronic structure in molecular dynamics simulations, *e. g.* Ehrenfest, Born–Oppenheimer and Car–Parrinello molecular dynamics. In the following, the essential idea of the Born–Oppenheimer molecular dynamics will be briefly illustrated, as it is used in the program package cp2K, which has been utilized to perform *ab initio* molecular dynamics simulations on the systems investigated here. Readers interested in the theory of the other molecular dynamics methods are referred to the book of Marx and Hutter (see Ref. [210]).

In the Born–Oppenheimer molecular dynamics, the static electronic structure problem is solved for a set of fixed nuclei in each molecular dynamics timestep. Calculating the electronic structure is consequently reduced to the solution of the time-independent Schrödinger equation, while the nuclei are propagated according to classical mechanics, *i. e.* Newton's second law. Thus, the time dependence of the electronic structure is due to the classical motion of the nuclei leading to new sets of fixed nuclei for the electronic structure calculation in every molecular dynamics step. The resulting Born–Oppenheimer molecular dynamics method for the electronic ground-state is defined by:

$$M_I \ddot{R}_I(t) = -\nabla_I \min_{\Psi_0} \{\langle \Psi_0 | \mathbf{H}_\mathrm{e} | \Psi_0 \rangle\} \tag{2.29}$$

$$E_0 \Psi_0 = \mathbf{H}_\mathrm{e} \Psi_0 \quad , \tag{2.30}$$

where M_I is the mass of nucleus I and $\ddot{R}_I(t)$ is the second time-derivative of the nucleus position. For each timestep of the Born–Oppenheimer molecular dynamics propagation, the minimum of $\langle \Psi_0 | \mathbf{H}_\mathrm{e} | \Psi_0 \rangle$ has to be reached. The electronic

part of the equations of motions (2.29) can usefully be reformulated for the special case of effective one-particle Hamiltonians such as the Kohn–Sham operator $\mathbf{h}^{\mathrm{KS}}$ of density functional theory. Thus, the minimum of the Kohn–Sham energy, defined in equation (2.15), represents the electronic ground-state energy of the system with fixed nuclei at positions $\{R_I\}$, leading to:

$$M_I \ddot{R}_I(t) = -\nabla_I \min_{\{\phi_i^{\mathrm{KS}}\}} \{E^{\mathrm{KS}}\} \quad , \tag{2.31}$$

$$\varepsilon_i^{\mathrm{KS}} \phi_i^{\mathrm{KS}} = \mathbf{h}^{\mathrm{KS}} \phi_i^{\mathrm{KS}} \quad . \tag{2.32}$$

In general, it is possible to calculate the electronic ground-state via other methods or to apply all kinds of density functionals, but for efficiency reasons the general gradient approximated functionals are mostly used nowadays. Utilizing density functional theory to calculate the electronic structure greatly improved the prize-performance ratio of all *ab initio* molecular dynamics, leading to an increased popularity in the application next to classical molecular dynamics.

2.1.4 Force Fields

The main advantage of classical molecular dynamics or force field methods is the speed in which calculations of a large number of particles can be performed. This makes this method viable for modeling biological macromolecules, and for simulating solvent effects and interfaces. However, these advantages come with a huge drawback, as the high dependency on parameters of this method leads to good predictions where much is known, while it could fail where little is known. In every classical molecular dynamics simulation, atoms are treated by classical mechanics, while the electrons are totally neglected and their energy is described by a parametric function depending on the nuclear coordinates, which resembles the potential energy of the system. These parameters are fitted to experimental data or data achieved by higher level calculations. The molecules are modeled as atoms covalently bound to each other. The atoms are treated as structurally similar units which have a similar role in different molecules and are called atom types. These atom types depend on the atomic number and the type of chemical bond

they are involved in. Depending on the degree of structural similarity for describing atom types, force fields can be divided into "all-atom" force fields, providing parameterizations for all atoms in a system, including hydrogen atoms, "united-atom" force fields, grouping multiple atoms into a single interacting center, and "coarse-grained" force fields, which provide even less accurate representations of atoms but with increasing computational efficiency. In general, the basic functional form of a force field includes bonded terms for the covalently bound atoms or atom types and nonbonded atom-atom interaction terms. The general form of the total potential energy is given in an additive way:

$$E_{\text{tot}} = E_{\text{bond}} + E_{\text{angle}} + E_{\text{dihedral}} + E_{\text{vdW}} + E_{\text{el}} + E_{\text{cross}} \quad , \tag{2.33}$$

where E_{bond} describes the energy for stretching a bond, E_{angle} the bending energy of an angle, E_{dihedral} the torsion energy of proper or improper dihedrals, E_{vdW} the van der Waals interaction energy, E_{el} the electrostatic interaction energy and E_{cross} the cross-terms between the first three terms. The explicit functional form of every energy term as well as the number of included cross-terms is different for every force field. In this work, the explicit functional form of force fields based on the OPLS-AA[211] and AMBER[212,213] framework will be shortly described, as they were used for performing classical molecular dynamics. For a more detailed description of every energy term and other force fields, the reader is referred to the book of Leach (see Ref. [214]).
The AMBER kind force field is given by:

$$\begin{aligned} E_{\text{tot}}^{\text{AMBER}} = & \sum_{\text{bonds}} K_r(r - r_0)^2 + \sum_{\text{angles}} K_\theta(\theta - \theta_0)^2 \\ & + \sum_{\text{dihedrals}} V_\phi[1 + d\cos(n\phi)] \\ & + \sum_{i<j} \left\{ 4\epsilon_{ij} \left[\left(\frac{\sigma_{ij}}{r_{ij}} \right)^{12} - \left(\frac{\sigma_{ij}}{r_{ij}} \right)^{6} \right] + \frac{q_i q_j}{\varepsilon r_{ij}} \right\} \quad , \end{aligned} \tag{2.34}$$

and the OPLS-AA kind force field is given by:

$$
\begin{aligned}
E_{\text{tot}}^{\text{OPLS-AA}} = & \sum_{\text{bonds}} K_r (r - r_0)^2 + \sum_{\text{angles}} K_\theta (\theta - \theta_0)^2 \\
& + \sum_{\text{dihedrals}} \sum_{n=1}^{4} \frac{V_{\phi,n}}{2} [1 + (-1)^n \cos(n\phi)] \\
& + \sum_{i<j} \left\{ 4\epsilon_{ij} \left[\left(\frac{\sigma_{ij}}{r_{ij}} \right)^{12} - \left(\frac{\sigma_{ij}}{r_{ij}} \right)^{6} \right] + \frac{q_i q_j}{\varepsilon r_{ij}} \right\} \quad . \qquad (2.35)
\end{aligned}
$$

Both frameworks are very similar, as they employ harmonic expressions for the bond stretching and angle bending terms, and describe the nonbonded interactions as a 12-6 Lennard-Jones potential and a Coulomb potential between two point charges. In addition, both frameworks neglect cross-terms of the three bonded terms. The only difference is in the term of the torsion around dihedrals. In the OPLS-AA framework, a combination (Fourier series) of different torsional energy profiles, up to $n = 4$, is possible, while in the AMBER framework only one contributes to the torsion energy. Obviously, for simple torsion energy profiles (no combination), both frameworks provide the same dihedral energy term. The parameters applied in these force fields are the force constants K, the reference values r_0 and θ_0, the Fourier coefficients V, the prefactors d and n, the partial atomic charges q, and the Lennard-Jones radii and well-depths σ and ϵ. To obtain parameters for the interaction of atoms i and j (σ_{ij} and ϵ_{ij}), different mixing rules can be applied *e. g.* Lorentz–Berthelot mixing rules.[215,216] The partial atomic charges q can be obtained by different population analysis methods, which will be described in the next section.

2.2 Population Analysis

Atomic charges are often used to discuss structural and reactivity differences in systems, and they are one of the main parameters needed for an accurate description of atoms in classical molecular dynamics. However, atomic charges cannot be uniquely defined as they are no observables of the system, thus simplified concepts to assign atomic charges to given atoms exist. These concepts use different methods, like partitioning the wave function in terms of basis functions, or they are based on properties of the wave function itself and certain fitting schemes. In the following, a number of different methods assigning atomic partial charges will be described.

The total electron density can be expanded in terms of molecular orbitals $\psi_i(\mathbf{r})$, which again can be expanded in a linear combination of normalized, but nonorthogonal atomic orbitals χ_α leading to the following expression:

$$\rho(\mathbf{r}) = \sum_i n_i \rho_i(\mathbf{r}) = \sum_i n_i \psi_i^*(\mathbf{r})\psi_i(\mathbf{r}) = \sum_i n_i \sum_{\alpha\beta} c_{\alpha i} c_{\beta i} \chi_\alpha^* \chi_\beta \quad , \tag{2.36}$$

where n_i denotes the occupation number and $c_{\alpha i}$ and $c_{\beta i}$ are coefficients. By interchanging the summation indices and integration, this can be rewritten in terms of the overlap matrix elements $S_{\alpha\beta}$ and density matrix elements $D_{\alpha\beta}$:

$$\begin{aligned} N &= \int \rho(\mathbf{r}) d\mathbf{r} = \sum_{\alpha\beta} \sum_i n_i c_{\alpha i} c_{\beta i} \int \chi_\alpha^* \chi_\beta d\mathbf{r} \\ &= \sum_{\alpha\beta} D_{\alpha\beta} \int \chi_\alpha^* \chi_\beta d\mathbf{r} = \sum_{\alpha\beta} D_{\alpha\beta} S_{\alpha\beta} \quad , \end{aligned} \tag{2.37}$$

where N denotes the total number of electrons. In the **DS** matrix, the diagonal elements are the number of electrons in the corresponding atomic orbital. The off-diagonal elements describe the number of electrons shared by two different atomic orbitals. The population analysis based on *Mulliken*[217–221] uses this **DS** matrix to distribute the electrons to the atoms by partitioning the contributions equally between two atoms without taken electronegativity of the atoms into account. The *Mulliken* electron population is thereby defined as:

$$\rho_A = \sum_{\alpha \in A} \sum_\beta D_{\alpha\beta} S_{\alpha\beta} \quad , \tag{2.38}$$

and the atomic partial charge q_A of atom A is the sum of the nuclear and electronic contributions:

$$q_A = Z_A - \rho_A \quad . \tag{2.39}$$

The *Löwdin* population analysis[222] is based on the *Mulliken* population analysis and seeks to improve it, because a violation of the Pauli principle can occur (diagonal elements of the **DS** matrix larger than 2), by transforming the atomic orbitals into a set of orthogonal basis functions. In this orthogonalized basis, all off-diagonal elements are zero and the diagonal elements are restricted to values between 0 and 2, leading to charges that are often closer to chemically intuitive values.

In general, it would be desirable to base the population analysis on the wave function itself instead of a chosen basis set representing the wave function. As the wave function contains all of the information that can be known about a quantum system, also the atomic charges are contained even though there is no quantum mechanical operator associated to it. Defining an atom in the molecule or in the system itself, or otherwise put, dividing the total molecular volume into partial volumes belonging to the different atoms in the system is problematic. Bader proposed a method to divide the molecular volume into atomic volumes named *Atoms in Molecules* (AIM).[223] There, the electron density, given by the absolute square of the wave function Ψ integrated over $N-1$ coordinates (since all electrons are identical it makes no difference over which $N-1$ coordinates),

$$\rho(\mathbf{r}_1) = \int \cdots \int \Psi^*(\mathbf{r}_2, \mathbf{r}_3, \ldots, \mathbf{r}_N)\Psi(\mathbf{r}_2, \mathbf{r}_3, \ldots, \mathbf{r}_N) d\mathbf{r}_2 d\mathbf{r}_3 \ldots d\mathbf{r}_N \quad , \tag{2.40}$$

as a function of three spatial coordinates is analyzed in terms of its topology (maxima, minima and saddle points). The gradient of the electron density points to the strongest attractor, which is usually one of the nuclei and the only maxima in the electron density. By following the direction of the gradient in a series of infinitesimal steps from each point in space until a nucleus (a maximum) is reached, and collecting all the points leading to the same nucleus, the space can be divided into atomic subspaces. The border between these subspaces is a two-

dimensional surface, where the gradient of the electron density is perpendicular to the normal vector of the surface. Once the subspaces are known, integration of the electron density over these subspaces leads to the net atomic charges.
Another way to obtain atomic charges by partitioning the wave function is to let the wave function choose its own optimal orbitals for its description, the so called *natural orbitals*. The natural orbitals are the eigenvectors of the diagonalized first-order density matrix, which is defined as:

$$\Gamma_1(\mathbf{r}_1, \mathbf{r}_1') = N \int \Psi^*(\mathbf{r}_1, \mathbf{r}_2, \ldots, \mathbf{r}_N,)\Psi(\mathbf{r}_1', \mathbf{r}_2, \ldots, \mathbf{r}_N) d\mathbf{r}_2 \ldots d\mathbf{r}_N. \tag{2.41}$$

The eigenvalues of the first-order density matrix $\Gamma_1(\mathbf{r}_1, \mathbf{r}_1')$ are correspondingly the occupation numbers of the natural orbitals. This concept of natural orbitals can be used to distribute electrons into *natural atomic orbitals*, which are localized one-center orbitals and can be described as the effective natural orbitals of one atom in the molecular environment. The idea of natural atomic orbitals was developed by F. Weinhold and coworkers,[224] and it uses the one-electron density matrix for defining the shape of these natural atomic orbitals. Essentially, the construction of the natural atomic orbitals involves two steps. The first step is the diagonalization of subblocks of the density matrix localized on particular atoms, generating orthonormal pre-natural atomic orbitals. The second step is the removal of the interatomic overlap, which is in general the orthogonalization of the complete set of all pre-natural atomic orbitals by preserving the localization on particular atoms. Weinhold and coworkers introduced the occupancy-weighted symmetric orthogonalization for the second step and divided the orthogonalization sequence for strongly occupied and weakly occupied pre-natural atomic orbitals. For a complete mathematical description of this orthogonalization sequence, the reader is referred to the original paper of Weinhold and coworkers.[224] The final set of orthogonal orbitals are the natural atomic orbitals and the diagonal elements of the density matrix in this basis are their populations. Summing all the contributions from natural atomic orbitals belonging to one particular atom produces the electron population of this atom and leads to the atomic charge according to equation (2.39).

Another way to derive partial atomic charges is to find a best fit for the actual *electrostatic potential (ESP)*, as the fundamental electrostatic interaction is between the electrostatic potential generated by one molecule and the charged particles of another. The electrostatic potential at position $\mathbf{r}_i$ is given by:

$$V_{\mathrm{ESP}}(\mathbf{r}_i) = \sum_A \frac{Z_A}{|\mathbf{r}_i - \mathbf{R}_A|} - \int \frac{\Psi^*(\mathbf{r}_j)\Psi(\mathbf{r}_j)}{|\mathbf{r}_i - \mathbf{r}_j|} d\mathbf{r}_j \quad . \tag{2.42}$$

A least squares procedure is used to fit the calculated electrostatic potential

$$\hat{V}(\mathbf{r}_i) = \sum_A \frac{q_A}{|\mathbf{r}_i - \mathbf{R}_A|} \tag{2.43}$$

to a set of points $\{\mathbf{r}_i\}$ in the most important region just beyond the van der Waals distance of each atom A by minimizing the figure of merit χ_{ESP} given by

$$\chi^2_{\mathrm{ESP}} = \sum_i \left[V_{\mathrm{ESP}}(\mathbf{r}_i) - \hat{V}(\mathbf{r}_i) \right]^2 \quad . \tag{2.44}$$

At the minimum, the gradient vanishes:

$$\frac{\partial(\chi^2_{\mathrm{ESP}})}{\partial q_A} = -2 \sum_i \frac{V_{\mathrm{ESP}}(\mathbf{r}_i) - \hat{V}(\mathbf{r}_i)}{|\mathbf{r}_i - \mathbf{R}_A|} = 0 \quad \text{for all atoms } A. \tag{2.45}$$

This forms a system of equations, which can be solved in matrix form with the additional constraint that the total sum of all partial atomic charges resembles the total molecular charge. The major weakness of the ESP-fitting method is that the atomic charges are conformationally dependent and that large charges can occur. To reduce these problems, simple restraints to the fitting procedure were introduced by Kollmann and coworkers,[225] leading to the *restrained electrostatic potential (RESP)* fit method. There, an additional term χ^2_{RSTR} is added to equation (2.44), leading to a new figure of merit to be minimized:

$$\chi^2 = \chi^2_{\mathrm{ESP}} + \chi^2_{\mathrm{RSTR}} \quad , \tag{2.46}$$

for which the gradient still vanishes:

$$\frac{\partial(\chi^2)}{\partial q_A} = \frac{\partial(\chi^2_{\mathrm{ESP}})}{\partial q_A} + \frac{\partial(\chi^2_{\mathrm{RSTR}})}{\partial q_A} = 0 \quad \text{for all atoms } A. \tag{2.47}$$

One possible choice of the restraint is a simple harmonic:

$$\chi^2_{\mathrm{RSTR}} = k \sum_A \left(q_{0_A} - q_A\right)^2 \quad , \tag{2.48}$$

where k determines the strength of the restraint and q_{0_A} is the target charge for the restraint at atom A. The partial charges gained by this method perform well for quantitative aspects of intra- and intermolecular interactions, which is the reason why the RESP charges are usually employed in force field calculations.

Another fitting method is available, introduced by *Blöchl* in 1995,[226] which derives the partial atomic charges based on an analysis of the charge density in the reciprocal space and is thus suitable for obtaining charges from periodic calculations and from calculations utilizing the GPW ansatz (see 2.1.1). The basic idea is that the interaction between two separated charge densities can be expressed entirely through their multipole moments. All multipole moments of a charge density can be expressed by the value and all derivatives of the charge density at the reciprocal lattice vector $\mathbf{G} = 0$. By introducing a model charge density $\tilde{\rho}(\mathbf{r})$ based on Gaussian functions $g_i(\mathbf{r})$, which are centered at atomic sites, representing the original density $\rho(\mathbf{r})$, the assignment of partial atomic charges to the atoms can be performed easily. Therefore, the model charge density $\tilde{\rho}(\mathbf{r})$ given by

$$\tilde{\rho}(\mathbf{r}) = \sum_i q_i g_i(\mathbf{r}) \tag{2.49}$$

needs to reproduce the multipole moments of the original density $\rho(\mathbf{r})$. This is achieved by fitting the reciprocal model density $\tilde{\rho}(\mathbf{G})$ in the surrounding of $\mathbf{G} = 0$ to the original reciprocal density $\rho(\mathbf{G})$. The parameters q_i of the model density are obtained from the extremal condition

$$\begin{aligned} F(q_i, \lambda) = \frac{V}{2} \sum_{\mathbf{G}\neq 0} \omega(\mathbf{G}) \left| \rho(\mathbf{G}) - \sum_i q_i g_i(\mathbf{G}) \right|^2 \\ - \lambda \left[\rho(\mathbf{G}=0)V - \sum_i q_i g_i(\mathbf{G}=0)V \right] \end{aligned} \tag{2.50}$$

where $\omega(\mathbf{G})$ is a weighting function that rapidly decays for increasing $\mathbf{G}$, V is the cell volume and λ is a Lagrangian multiplier. The degree of freedom for the

fitting procedure is introduced by using several different Gaussians with different decay lengths at each atomic site. After the fitting procedure, the partial atomic charge can be obtained by summing up all q_i for a particular atom.
To summarize, the calculation of atomic charges can be performed by different kind of methods, which all have their strengths and drawbacks. Mulliken and Löwdin charges are computationally not demanding but they will not converge to a constant value as the size of the basis set increases. Atomic charges obtained from the natural orbitals on the other hand converge to a well-defined value, while being computationally only slightly more demanding. Calculating atomic charges from the RESP method is computational very demanding, especially when the system is getting larger, still its computational cost is far less than computing the electronic structure which is needed for all methods. However, the RESP charges represent the intra- and intermolecular very well and are subsequently used as charges in force fields. Blöchl charges can on the other hand be calculated from periodic calculations and reproduce the dipole and quadrupole moments very well. Thus, when calculating atomic charges care needs to be taken to what purpose these charges are used and to how much computer time is available.

2.3 Topology of Ionic Liquids

From the interactions present in ionic liquids, two main associations of ions, in-plane and on-top conformation, as briefly introduced in subsection 1.1.4 originate. Defining these conformations in order to investigate structural preferences and dynamical behavior of ionic liquids is a difficult task, because for complex ions the charge can be distributed over several atoms and thus the border between these conformations can become indistinct. Throughout the work on imidazolium-based ionic liquids, the idea of applying conditions to each conformation, building up a topology for imidazolium-based ionic liquids emerged, which will be briefly introduced here.

The in-plane conformation, being a hydrogen bonding conformation between acidic hydrogen atoms of the cation, *e. g.* the hydrogen atom bound to the carbon atom C2 (see Figure 1.2), and the most negatively charged atoms of the anion, can be best described by combining the distance between hydrogen atom (cation) and acceptor atom (anion) and the angle between the vector along the C2–H bond and the vector along the H-acceptor connecting line (see Figure 2.1). To describe the on-top conformation, the imidazolium ring is considered to be contained in a circle, which creates a cylinder above and below the ring plane. If an acceptor atom (anion) resides within this cylinder in a reasonable distance, the corresponding conformation is an on-top conformation (see Figure 2.1).

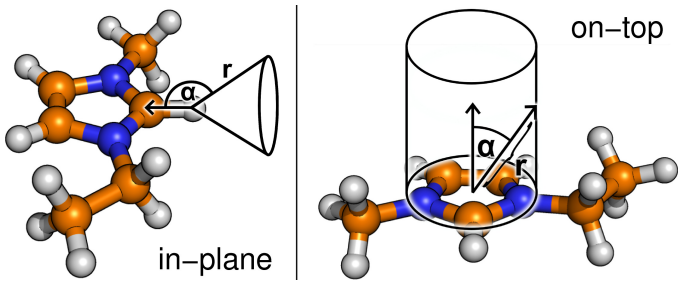

Figure 2.1: Definition of the in-plane (left) conformation and the on-top (right) conformation for complex anions based on distances r and angles α for the example of the cation 1-ethyl-3-methylimidazolium.

With these descriptions of the different conformations, the search for suitable conditions is reduced to distances and angles. For the in-plane conformation, these conditions can be chosen straightforward even for more complex anions, as this conformation is described by hydrogen bonding. For the on-top conformation, the conditions need to be restricted to acceptor atoms (anion) which are contained in the cylinder above or below the ring plane. Therefore, the use of the trigonometric ratio on the right triangle, produced by the two vectors shown in Figure 2.1 (right side), the following relation between the distance r and the angle α can be obtained:

$$r = \frac{r_{im}}{\sin \alpha} \quad , \tag{2.51}$$

where r_{im} is the radius of the circle containing the imidazolium ring. Equation (2.51) describes the boundary of the on-top conformation for imidazolium-based ionic liquids.

3 Results and Discussion

In the following, the results of the investigation of complex interactions present in ionic liquids and rotaxanes gained from the multiscalar methods approach, will be reviewed in form of published or submitted articles.

At first, two published articles describing the gas phase of ionic liquids on the example of 1-ethyl-3-methylimidazolium ethylsulfate compared to its bulk phase and at different temperatures are presented (see section 3.1). These publications offer insights into the variation of the complex interactions from the bulk to the gas phase as well as into the temperature-dependency of stable conformations between cation and anion. Then, the liquid-vacuum interface of ionic liquids on the example of imidazolium-based and pyrrolidinium-based ionic liquids with varying anions is described from classical molecular dynamics. The results are presented in two published articles (see section 3.2), discussing the influence of the interface and the variation of anions on the molecular structure and the morphology of these ionic liquids. Subsequently, the investigation of ion pairing in ionic liquids is discussed in relation to the evaporation of ionic liquids and to the charge transfer present in ionic liquids (see section 3.3), providing new qualitative pictures on the influence and role of ion pairing in ionic liquids.

Finally, the substitution and flexibility effects of the axle in Vögtle-type and Leigh-type rotaxanes, probed by static quantum chemical calculations, are reviewed and compared to experimental data in two published articles (see section 3.4).

3.1 Gas Phase of Ionic Liquids

3.1.1 The Bulk and The Gas Phase of 1-Ethyl-3-Methylimidazolium Ethylsulfate: Dispersion Interaction makes the Difference.

Friedrich Malberg,[a] Alfonso S. Pensado,[a] and Barbara Kirchner*[a]

Received 5th June 2012, Accepted 20th July 2012

DOI: 10.1039/c2cp41878a†

Malberg, F.; Pensado, A. S.; Kirchner, B. *Phys. Chem. Chem. Phys.* **2012**, *14*, 12079–12082 - Reproduced by permission of the PCCP Owner Societies.

Own contributions to this manuscript:

- Conduction and maintenance of simulations for both gas and bulk phase
- Analysis of trajectories
- Interpretation of data
- Writing of the manuscript

[a] *Wilhelm Ostwald Institute for Physical and Theoretical Chemistry, University of Leipzig, Linnéstr. 2, D-04103 Leipzig, Germany. Tel: +49 341 9736401; E-mail: bkirchner@uni-leipzig.de*

† Electronic Supplementary Information (ESI) available: Starting structures, computational details, comparison between global power spectra and experimental spectra. See DOI: 10.1039/c2cp41878a/

Abstract *Ab initio* molecular dynamics simulations were carried out on systems representing the gas and the bulk phase of 1-ethyl-3-methylimidazolium ethylsulfate $[C_2C_1im][C_2SO_4]$. The power spectra and cation-anion spatial distribution revealed different interactions of the anion and cation in the bulk phase *versus* gas phase. In the bulk phase, all oxygen atoms of the anions are involved and interaction *via* the rear hydrogen atoms is possible, forming a closer packed system. The alkyl groups of cation and anion governed by dispersion interaction stick together in the bulk but are relatively free in the gas phase.

In the last few years the interest in ionic liquids (ILs), liquids entirely composed of ions, increased due to their unique properties, such as high electric conductivity, controllable solubility, differences in viscosity and negligible vapor pressure.[1,2,4,5,42,57,58,227]

Since the beginning of the investigation on ILs, the fact that the vapor pressure is negligible, provoked the statement that ILs are undistillable. With the aid of molecular dynamics simulation Maginn and coworkers were the first to estimate the enthalpy of vaporization in ILs.[75,228] They predicted the enthalpy of vaporization to be in the range from 148 to 238 kJ mol^{-1} for ion pairs of different ILs (in good agreement with experimental data)[61,68,229,230] and thus set the state for the nonvolatility of ILs. In 2005, Rebelo *et al.*[60] were able to perform reduced-pressure distillation at moderate temperature of $[C_{12}C_1im][Tf_2N]$. In 2006 the work of Earle *et al.*[59] disproved the statement that ILs are undistillable, inducing other groups to investigate the vapor pressure of ILs. They all stated that the gas phase of ILs is composed of isolated ion pairs and were able to provide evidence *via* photoionization, classical atomistic simulations, mass spectrometric experiments and matrix isolated FTIR.[61–67] It was the group around Akai,[66,67] who found evidence for different structures in the spectra of the vaporized and the bulk IL $[C_2C_1im][Tf_2N]$. Questions that follow from their observations include, understanding how do these structures look like for ILs in general, which one is preferred in which phase and, if they are different, how does the transition occur? In this communication, we focus on the comparison of one ion pair of

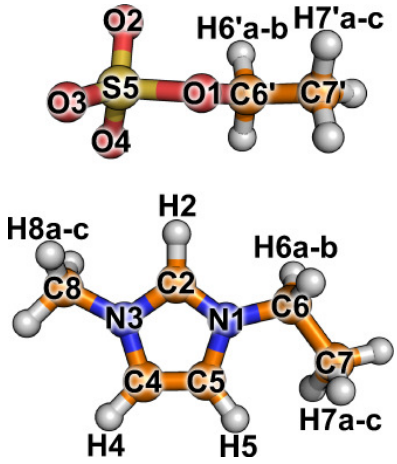

Figure 3.1: Labeling of $[C_2C_1im][C_2SO_4]$ used throughout the communication. C: brown; N: blue; H: white; O: red and S: yellow.

$[C_2C_1im][C_2SO_4]$ (gas phase) and the bulk phase of $[C_2C_1im][C_2SO_4]$, to investigate structural differences between both phases. The evaporation temperature of this IL was found[69] to be around 390 K. Thus, we simulate the gas phase (1 ion pair) and the bulk phase (27 ion pairs with periodic boundary conditions) from *ab initio* molecular dynamics simulations at 400 K (Figure 3.1).

All starting structures and the computational details are provided in the ESI†, and we wantto mention here that we work with dispersion corrected functionals.[31,198,199] The structural functions were calculated with our analyzing software TRAVIS.[231]

The power spectra, that are known to be the sum of all the peaks of Raman- and IR-spectra and even motions which are not active in either of them,[231] are shown for both investigated systems in Figure 3.2. In general, the global spectra of our investigated bulk phase fit the experimental data quite well (see ESI†, Figure S2). The spectra are split into the contributions of the cation $[C_2C_1im]^+$ and the anion $[C_2SO_4]^-$ to identify changes in the vibrational density of states of the particular ion more easily. The observed results for the gas (black) and bulk (red) phase contain some differences for both, cation and anion (see Figure 3.2). Comparison of the cation spectra reveals a shift towards lower wavenumbers in

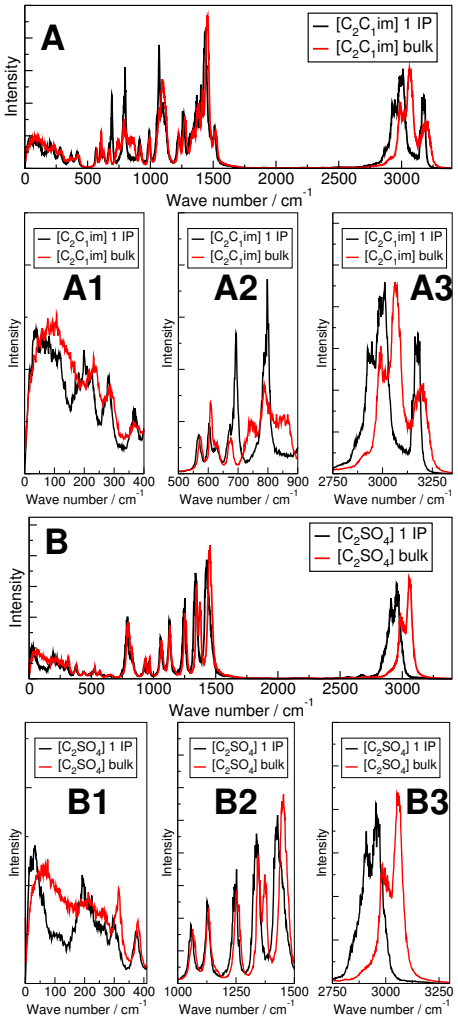

Figure 3.2: Comparison of the power spectrum obtained from the calculations with one ion pair (black curves) and of the bulk (red curves). Top panel: $[C_2C_1im]^+$; Bottom panel: $[C_2SO_4]^-$

the gas phase, more evident in the region between 2800 and 3300 cm^{-1} (see Panel A3 of Figure 3.2). The peak at ∼3200 cm^{-1} originates from the C−H stretching modes of the imidazolium ring protons and is only slightly shifted, whereas the peaks between 2800 and 3100 cm^{-1}, originated from the stretching vibration of the CH_2 and CH_3 groups, are strongly shifted in both cases (see Panel A3 and B3 of Figure 3.2). These redshifts indicate free movement and stretching of the apolar parts of the cation and the anion in the gas phase in contrast to the bulk phase, where the apolar parts are hindered due to sterical reasons, but more im-

portantly they stick together due to alkyl chain aggregation. Further differences for the cation are the distinct peaks at ∼700 cm^{-1} and ∼800 cm^{-1} in the gas phase spectrum, originated from the waging of the two rear hydrogen atoms H4 and H5 (∼700 cm^{-1}) and from the waging of the CH_2-group (H6a-b).[232,233] These peaks are less evident in the bulk phase spectrum, where two broad peaks, shifted to higher wave numbers, can be found (see Panel A2 of Figure 3.2). Identifying the two broad bands (∼750 cm^{-1} and ∼850 cm^{-1} in Panel A2 of Figure 3.2) present in the bulk phase to be the two distinct peaks of the gas phase, the blueshift describes a weaker waging of the rear hydrogen atoms H4 and H5 and of the CH_2-group (H6a-b) and thus a more directed interaction cation-anion: in the direct environment of the hydrogen atoms H4, H5 and H6a-b an anion can be found, interacting strongly with them. Thus in the bulk phase, the broadening of the former distinct peak (∼750 cm^{-1}) describes a strong cation-anion interaction *via* the rear hydrogen atoms H4 and H5.

The spectra of the anion for the gas and bulk phase are quite similar in the region between ∼1000 cm^{-1} and ∼1500 cm^{-1} except that we observe a split at the distinct peak at ∼1350 cm^{-1} of the gas phase spectrum in the bulk phase spectrum (see Panel B2 of Figure 3.2): this is another marked difference between gas and bulk phase. The vibrational mode attributed to this peak is the rocking of the hydrogen atoms of the anion.[233] A blueshift of this vibrational mode or even its split means that the environment of the anion is different and thus also the interactions of the ethyl-group change. Low frequency vibrational modes that correspond to the low wave number region of the global spectra (see ESI†, Figure S1), are dominated by vibrations of intermolecular hydrogen bonds between the anion and the cation[234–236] and short-range interionic interactions.[237] We observe a blueshift of the bulk phase spectrum, but we also see a strong enhancement of the area between 50 and 150 cm^{-1} (see ESI†, Figure S1), which describe the interaction of the cation and the anion *via* hydrogen bonds.[234–236] The enhanced area describes hydrogen bond interaction between the cation and anion not only *via* C2–H2 but also *via* C4–H4 and C5–H5. Going a step further the spectra

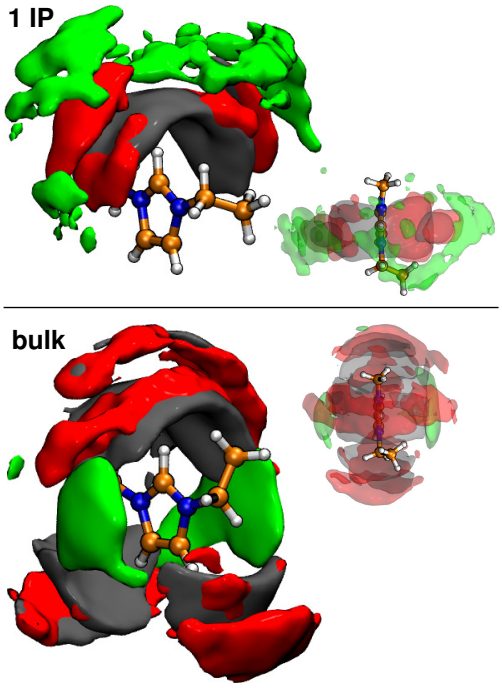

Figure 3.3: Spatial distribution function of the oxygen atoms (grey: O2-O4 (terminal); red: O1 (bridging)) and the carbon atom C7' (green) around the cation in the gas phase (top panel) and the bulk phase (bottom panel).

of the anion (see Panel B1 of Figure 3.2) show a significant difference between one ion pair and the bulk phase, explained by the permanent contribution of all oxygen atoms (terminal and bridging) to the hydrogen bonds in the bulk phase. The difference in the spectra of the cation (see Panel A1 of Figure 3.2) between 50 and 150 cm^{-1} is small, indicating that the contribution of the hydrogen bond interactions *via* C4–H4 and C5–H5 are less intense than of the hydrogen bond interaction *via* C2–H2. We also started calculations in the gas phase, where the anion is coordinated *via* C4 and C5, which revealed an immediate movement (∼3–4 ps) of the anion to the C2 coordination.

To support the results of the power spectra analysis, we consider the spatial distribution functions (SDF) of the oxygen atoms (red and grey) and the carbon atom C7' (green) of the anion around the cation in the gas and bulk phase (see Figure 3.3). The visualization of the environment of the cation clearly displays

interaction of the anion in the bulk phase *via* the rear hydrogen atoms H4 and H5, which is in agreement with previous works.[30,238,239] The interaction takes place *via* the bridging oxygen atom O1 (red) and the terminal oxygen atoms O2-O4 (grey). The interaction of the carbon atom C7' (green) with the cation in the bulk phase (see Figure 3.3, bottom panel) is directed towards the imidazolium ring from above (below) the ring plane, whereas in the gas phase the side chain of the anion moves freely almost not interacting with the cation. We also investigated the distribution of the terminal carbon atom C7' of such anions, which in addition interacts with the cation *via* the ring hydrogen atoms H2, H4 and H5. There, the main coordination of the terminal carbon atom C7' is also above the imidazolium plane (see ESI†, Figure S3). The distribution in the bulk phase is driven by the anions, which interact with the cation *via* the ring hydrogen atoms and in addition by other anions in the neighborhood and not by other cations. Considering the behavior of the side chains in the gas and bulk phase, we can state that on the liquid/vacuum surface[83] of the investigated IL, the side chains point towards the vacuum, in agreement with several experimental works.[240,241] In the bulk phase, the apolar part of the anion interacts with the aromatic ring and thus is not driven by Coulomb interactions, which are the strongest interactions between ions in ionic liquids,[28,33–39] or secondary effects, like hydrogen bonding.[40,41,43–50] The driving force for this interaction, next to the sterical hindrance in the bulk phase, is the dispersion interaction, *i.e.*, the dispersion correction should always be taken into account even though one might falsely assume that these interactions are unimportant due to their "weakness" compared to the Coulombic forces.[30,31] We should also point out that the blueshift in the spectrum of bulk phase of the anion (Panel B3 of Figure 3.2) also originates from the interaction of the side chain with the imidazolium ring and thus shows a stronger blue shift than the spectrum of the bulk phase of the cation (see Panel A3 of Figure 3.2).

In conclusion, by revealing the differences in the power spectra of the example of $[C_2C_1im][C_2SO_4]$, we can state that the conformations taken in the gas phase

resemble only conformations in the bulk phase where the anion is coordinated to the cation *via* the most acidic hydrogen atom H2. Additional interactions between the cation and the anion *via* the rear hydrogen atoms H4 and H5 are present in the bulk phase. With the aid of the SDFs, we confirm the existence of interactions of the apolar part of the anion with the imidazolium ring of the cation, which influences the spectrum of the bulk phase and is mainly caused by dispersion interactions. We prove that the anion also interacts with the cation *via* the bridging oxygen atom O1 and not just with the terminal oxygen atoms O2-O4.

Acknowledgment This work was supported by the DFG, in particular by the projects KI-768/5-1, KI-768/5-2, KI-768/5-3 and KI-768/7-1. We thank Prof. Ralf Ludwig for helpful discussions.

3.1.2 Understanding the Evaporation of Ionic Liquids using the Example of 1-Ethyl-3-Methylimidazolium Ethylsulfate

Friedrich Malberg,[a] Martin Brehm,[b] Oldamur Hollóczki,[a] Alfonso S. Pensado,[a] and Barbara Kirchner*[a]

Received 16th July 2013, Accepted 2nd September 2013

DOI: 10.1039/c3cp52966e

Malberg, F.; Brehm, M.; Hollóczki, O; Pensado, A. S.; Kirchner, B. *Phys. Chem. Chem. Phys.* **2013**, *15*, 18424–18436 - Reproduced by permission of the PCCP Owner Societies.

Own contributions to this manuscript:

- Conduction and maintenance of simulations
- Analysis of trajectories
- Calculation of free energy surface
- Interpretation of data
- Writing of the manuscript

[a] *Mulliken Center for Theoretical Chemistry, Institut für Physikalische und Theoretische Chemie, Universität Bonn, Beringstr. 4+6, D-53115 Bonn, Germany. E-mail: kirchner@thch.uni-bonn.de*

[b] *Wilhelm Ostwald Institute for Physical and Theoretical Chemistry, University of Leipzig, Linnéstr. 2, D-04103 Leipzig, Germany.*

Abstract In this work we present a comprehensive temperature-dependence analysis on both the structural and the dynamic properties of a vaporized ionic liquid (1-ethyl-3-methylimidazolium ethylsulfate). This particular ionic liquid is known to be distillable from experimental studies and thus enables us to deepen the understanding of the evaporation mechanism of ionic liquids. We have used *ab initio* molecular dynamics of one ion pair at three different temperatures to accurately describe the interactions present in this model ionic liquid. By means of radial and spatial distribution functions a large impact on the coordination pattern at 400 K is shown which could explain the transfer of one ion pair from the bulk to the gas phase. Comparison of the free energy surfaces at 300 K and 600 K supports the idea of bulk phase-like and gas phase-like ion pairs. The different coordination patterns caused by the temperature, describing a loosening of the anion side chains, are also well reflected in the power spectra. The lifetime analysis of typical conformations for ionic liquids shows a characteristic behavior at 400 K (temperature close to the experimental evaporation temperature), indicating that conformational changes occur when the ionic liquid is evaporated.

Introduction

Ionic liquids (ILs)[1,2,5,227,242] were often regarded as "nonvolatile" replacements of organic molecular solvents, and hence often even labeled as "green" solvents.[57,58] However, for the processes, in which ILs are applied to exploit their other advantageous properties,[19,86,243–249] their low vaporizability has rather become a limiting obstacle that prevents the efficient purification by distillation. This barrier has lately been overcome by Earle et al.,[59] who showed that by applying high vacuum and high temperatures ILs can be distilled, despite the general belief that they are "nonvolatile".[227] This breakthrough facilitated the already existing vapor pressure measurements for ILs, and since then many data has been collected and published on different ILs.[60–70] Similarly to molecular solvents (*viz.* non-IL liquids), the molecular structure influences volatility; hence there are some ILs that are known to be distillable (*e. g.* 1,3-dialkylimidazolium ethylsulfates or

bis(triflate)amides),[69] while others decompose before reaching the boiling point under any viable pressures.[71] Obviously, thermal stability of ILs is required for distillability, and therefore it has been studied extensively, but it is only one side of the problem, and the mechanism and energetics of vaporization should also be fully understood to predict distillability.

Presenting the vaporazibility of ILs has also initiated a number of subsequent studies that discussed the structure of IL vapors, in order to understand the mechanism of vaporization.[66,67,70] The strong Coulomb-type interactions between the particles prohibit the full dissociation of the liquid to free ions at the temperatures applied in the distillation process, and therefore the gas phase should be composed of neutral units.[66,67,70] In the case of imidazolium-based ILs the formation of free carbenes and acids by a proton transfer from the cation to the anion—*via* a similar mechanism to that observed for protic ILs—has been considered in the very beginning,[250–252] but it has also been excluded based on the fact that not only 1,3-dialkylimidazolium-based ILs could be evaporated.[59] It is worth mentioning here that later this mechanism has been observed by theoretical and experimental investigations to occur in 1,3-dialkylimidazolium salts possessing basic ions (*e. g.* acetate), and has been surmised also for other basic derivatives as well.[253–258]

Apart from these special cases the presence of single, neutral ion pairs has been suggested, which has been evidenced by line-of-sight mass spectroscopic and photoelectron spectroscopic measurements.[62,64,65] Comparing this picture to the liquid structure, where recently the lack of associations *via* "ion pairing" (long-living ion pairs) has been suggested[121] or in other words were described as "melange",[81,82] it is clear that the vaporization itself is not as simple as in case of molecular solvents, and significant changes have to occur prior to entering the gas phase. Accordingly, it is reasonable to assume the vaporization is a multistep process, starting by an initial formation of vaporizable "ion pairs" by the association of the otherwise independently diffusing ions of the liquid. In full agreement with this phenomenon, it has been observed that those ionic liquids,

which have a somewhat higher association between the cations and the anions, possess higher vapor pressure.[61,114]

For vaporizable ion pairs important changes have to occur, as they are a association of two molecular units, which possess great flexibility, especially when they are considered in the gas phase. From a comparison of power spectrum of the gas and the bulk phase for $[C_2C_1im][C_2SO_4]$ different structural rearrangements were emphasized, which support the idea of vaporizable ion pairs.[259] As a first approach in understanding the vaporization of ionic liquids the behavior of the ion pairs in the gas phase needs to be considered for different aspects like temperature-dependence or differences to bulk ion pairs. Investigation of the vacuum-liquid interface should give even further insight on the special bearings for ion pairs at the surface during the vaporization process[83] and exploit similarities/differences to both gas and bulk phase ion pairs. The process of an ion pair actually being evaporated would finalize the understanding, but experimentally this is not possible and theoretically it would be an induced event. Yet, it could give important insights and therefore help tuning ionic liquids to all the applications where vaporizability is a key factor.

In this study we provide the first insight into the complex vaporization of ILs, by investigating the gas phase behavior and temperature-dependence of $[C_2C_1im][C_2SO_4]$ in the vapor. We provide a short overview on the investigated system and the methods we used, our study being focused on the structural differences caused by the different temperatures. In addition, we compare the power spectra obtained at different temperatures to identify the structural differences in special contributions. Next, we investigate some dynamical behaviors by focusing on different conformations that are present for the ion pairs and investigate the free energy differences between the different temperatures.

Systems investigated

We investigated one ion pair of $[C_2C_1im][C_2SO_4]$ to understand the structural and dynamical behavior between the cation and the anion in the gas phase.

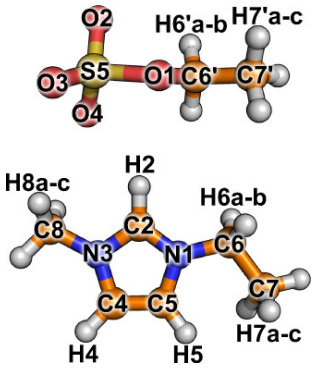

Figure 3.4: Adoptive labeling of $[C_2C_1im][C_2SO_4]$ used throughout the article. C: brown; N: blue; H: white; O: red and S: yellow.

$[C_2C_1im][C_2SO_4]$ is a colorless, hygroscopic room temperature IL with a melting point[260] of 236.29 K. The decomposition temperature is around 500 K, which is about 100 K lower compared to alkylsulfonates, indicating a lower stability of alkylsulfates when compared to alkylsulfonates.[261] In 2010, Lovelock *et al.* were able to detect vapor pressure of the investigated IL at 390 K under ultrahigh-vacuum conditions (5×10^{-8} Pa).[69] By extrapolation, they estimated the normal boiling temperature to be around 950 K, which is 100 K higher than the one of $[C_2C_1im][Tf_2N]$. Extensive investigations of the heat capacity of $[C_2C_1im][C_2SO_4]$ were made during the past years.[260,262–264] In 2010, a review on all different heat capacities and their uncertainties was published by Paulechka *et al.*[265,266] The surface tension of $[C_2C_1im][C_2SO_4]$ was found to be between 46.9×10^3 N m^{-1} and 48×10^3 N m^{-1} at room-temperature.[227,267] Increasing the length of the alkyl chain of the cation leads to a decrease in surface tension.[227,267] Compared to ILs with different anions, like $[PF_6]^-$, $[BF_4]^-$ or $[Tf_2N]^-$, and the same cation, the surface tension of the investigated IL $[C_2C_1im][C_2SO_4]$ is higher.[227] The viscosity was found to be between 97 mPa s and 108 mPa s at room-temperature.[227,268,269] When increasing the length of the alkyl chain of either the cation or the anion the viscosity increases.[261]

Based on the evaporating temperature (390 K) that Lovelock *et al.*[69] determined for $[C_2C_1im][C_2SO_4]$, we simulated the ion pair (see Fig. 3.4) with *ab initio* molec-

ular dynamics simulations at three different temperatures, a temperature, where the ion pair is normally in the bulk phase (300 K), one close to the evaporation temperature (400 K) and a temperature, where the ion pair is definitly in the gas phase (600 K).

Computational details

The gas phase simulations were performed in a cubic box with a cell vector of 1800 pm and periodic boundary conditions. We used the Quickstep module[206] of the program package CP2k[202,270] for our AIMD simulations, where the electronic structure was calculated by DFT[193,194] using the BLYP-D functional,[196,197] which includes the semi-empirical pair potential developed by Grimme[199] to effectively account for dispersion effects (D2). GTH pseudopotentials[204,205] and basis sets of the type TZVP-MOLOPT-GTH[271] were applied. The temperature was controlled by massive Nosé–Hoover chain thermostats[272–274] for 5 ps and by global thermostats afterwards. All simulations were carried out in a NVT ensemble with a time step of 0.5 fs and an SCF convergence criterion of 10^{-6}. The ion pair $[C_2C_1im][C_2SO_4]$ was simulated at 300 K, 400 K and 600 K and the lengths of the trajectories were between 295 ps and 340 ps, see Table 3.1. The computational details of the bulk phase simulation, which is used for comparison, can be found in ref. [259].

For the thermodynamic integration the C2–S distance was constrained every 10 pm between 300 pm to 400 pm. The initial structures for each thermodynamic integration point were optimized with a restraint on the distance between C2–S using CP2k.[202,270] Each point was then equilibrated with global Nosé–Hoover chain thermostats for 10 ps. To obtain the constrained forces further 10 ps simulations with constrained distances were conducted. We followed the calculation of the free energy as laid out by Brüssel et al.[275] based on the work of Sprik and Ciccotti.[276]

The analysis of the obtained trajectories was preformed with our software TRAVIS.[231] To visualize the isosurfaces of the 3D pictures, we used the VMD

Table 3.1: Comparison of average temperature $\langle T \rangle$, average Kohn–Sham energy $\langle E^{\mathrm{KS}} \rangle$ and standard deviation σ of the conserved quantity for the three investigated systems. The total simulation time t is given in last column.

T/K	$\langle T \rangle$/K	$\langle E^{\mathrm{KS}} \rangle$/a.u.	σ/a.u.	t/ps
300	301.3	−148.6487	0.0002	337
400	401.8	−148.6349	0.0003	325
600	599.9	−148.6079	0.0021	297

1.9[277] program package and for rendering we used the Tachyon library.[278] All isosurfaces were plotted at 50 ppm. The grace program[279] was used to plot the 2D diagrams. The contour plots were created with Wolfram Mathematica.[280]

Results

Structural Investigation On the left side of Figure 3.5, the distance distribution functions (DDFs) of the acidic hydrogen atom H2 with the bridging oxygen atom O1 (red curve) and the terminal oxygen atoms O2-O4 (black curve) are illustrated for the three investigated temperatures 300, 400 and 600 K. The terminal oxygen atoms are located closer to the acidic hydrogen atom H2 than the bridging oxygen atom. The distribution of the terminal oxygen atoms (black curve) shows two distinct peaks for all temperatures, which can be explained by the molecular structure of the anion. Either one or two oxygen atoms coordinate to the cation and the other two or one is close by. However, the distribution of the bridging oxygen atom (red curve) changes with increasing temperature. At 300 K, the distribution resembles the distribution of the terminal oxygen atoms with two distinct peaks, indicating a coordination of the anion to the cation *via* the bridging oxygen atom O1.

At 400 K, the contribution to the first, closer peak decreases and moves to the second peak (further distances), which means that the coordination *via* the bridging oxygen atom O1 is less favorable at this temperature. At 600 K, only

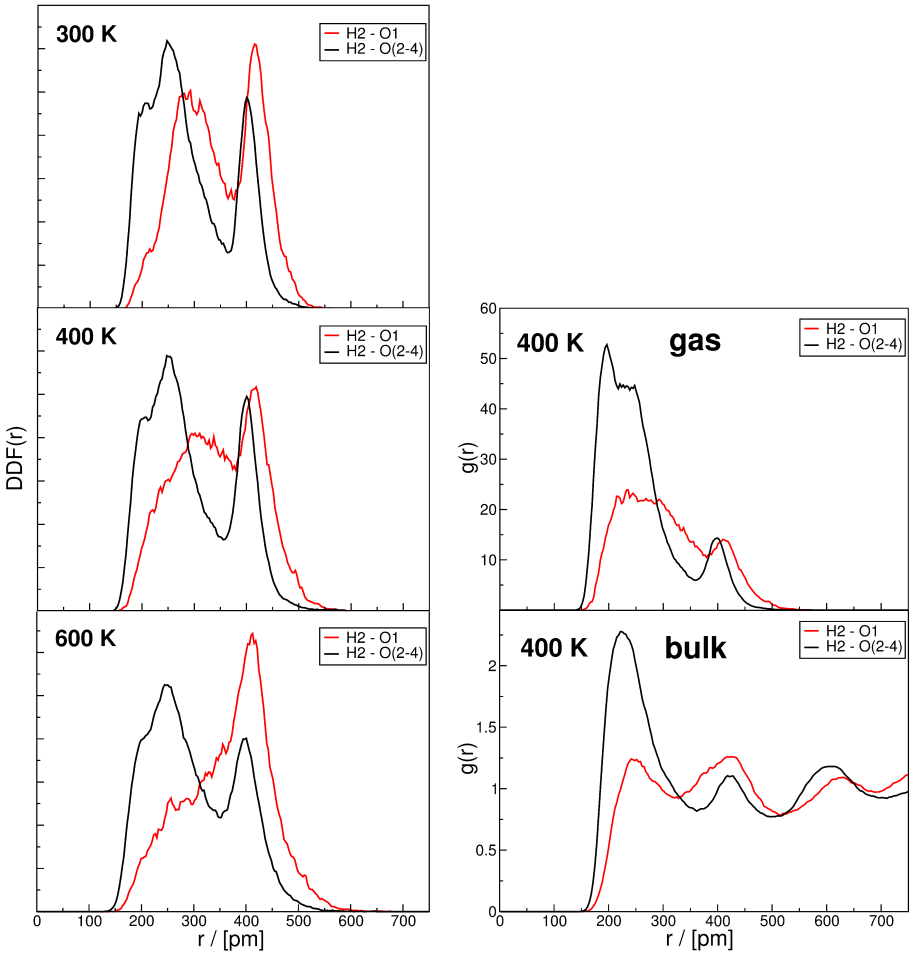

Figure 3.5: Left: Distance distribution functions (DDFs) of the anion's terminal oxygen atoms O2-O4 (black curve) and the bridging oxygen atom O1 (red curve) to the acidic hydrogen atom H2 of the cation, see Fig 3.4 for labeling; **right:** radial distribution functions (RDFs) between the same atoms of the gas phase and bulk phase at 400 K.

the distinct peak at large distances is left for the distribution of the bridging oxygen atom (red curve). Thus, the coordination *via* the bridging oxygen atom is almost suppressed during the simulation at 600 K. Overall, the coordination of the oxygen atoms at room temperature (300 K) is well structured and shows two distinct peaks for both, the terminal and bridging oxygen atoms. With increasing temperature the structure of the ion pair changes so that the terminal oxygen atoms O2-O4 almost exclusively coordinate around the acidic hydrogen atom H2.

On the right side of Figure 3.5, the radial distribution functions (RDFs) between the same oxygen atoms of the gas phase and the bulk phase at 400 K are illustrated. The position of the coordination peaks in the RDFs and DDFs of the gas phase are equal, only the shape of the peaks differ, because the DDFs are not normalized. As we focus on structural changes concerning only one ion pair, the use of DDFs to represent positions of specific atoms is sufficient. Comparing the RDFs of gas and bulk phase at 400 K, the positions of the first two peaks are very similar for both terminal and bridging oxygen atoms. As the positions of the peaks in the DDFs at different temperatures do not change significantly, it is justified to conclude that the positions of the first two peaks at 300 K and 600 K are also very similar for both terminal and bridging oxygen atoms.

We combined the DDF between the acidic hydrogen atom H2 and the bridging oxygen atom O1 with the DDF between the acidic hydrogen atom H2 and the terminal oxygen atoms O2-O4 at each investigated temperature in Figure 3.6. At 300 K, we see three highly populated areas (A, B, C). The upper area (A) displays the coordination of the bridging oxygen atom O1 to the acidic hydrogen atom H2 and due to the molecular structure of the anion, the resulting long distance of, at least, one terminal oxygen atom. The lower-left area (B) is populated by the other terminal oxygen atoms of the coordination described for area (A). The area in the right (C), shows the coordination *via* the terminal oxygen atoms whereby the bridging atom is located at long distances (∼425 pm). The situation at 400 K is similar. We still observe three areas (A, B, C) of high population, but compared to the areas at 300 K they are less populated. In addition, we see a shift from area (B) to area (C), in agreement with the results on the DDFs. At 600 K, the situation is different. Only one highly populated area (C), reflecting the coordination of the anion to the cation *via* the terminal oxygen atoms O2-O4 is left.

As mentioned before, coordination of the anion around the cation changes with increasing temperature. While at room temperature anion coordinations *via* the bridging (O1) as well as *via* the terminal oxygen atoms (O2-O4) occur around

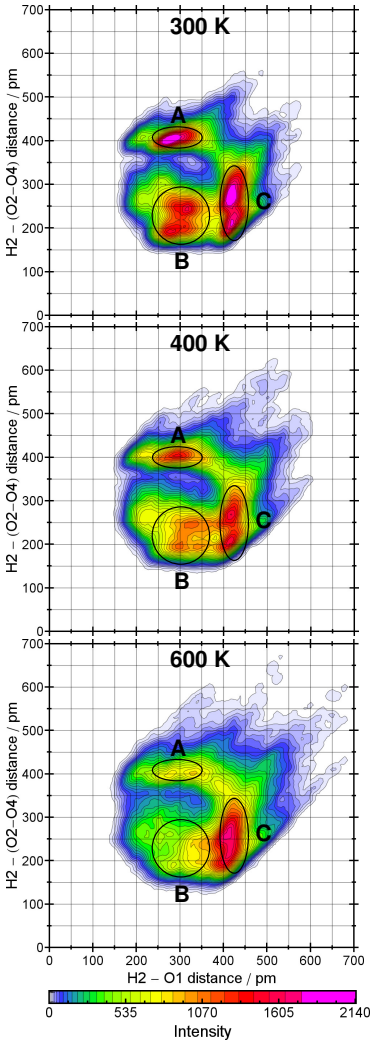

Figure 3.6: Combined distribution functions (CDFs) of the DDFs between the hydrogen atom H2 and the terminal oxygen atoms O2-O4 and the bridging oxygen atom O1 at the investigated temperatures. The color scheme and intensity are displayed at the bottom and are the same for all CDFs.

the acidic hydrogen atom H2, the preferred coordination at 600 K is almost exclusively *via* the terminal oxygen atoms O2-O4.

To obtain further information on the structure, we now explore the spatial distribution of the oxygen atoms around the cation. These results are depicted in Figure 3.7, where the distribution of the terminal carbon atom C7' of the anion is also included. The bridging (red) and terminal (grey) oxygen atoms only coordinate around the acidic hydrogen atom H2 of the cation. At 300 K, we observe

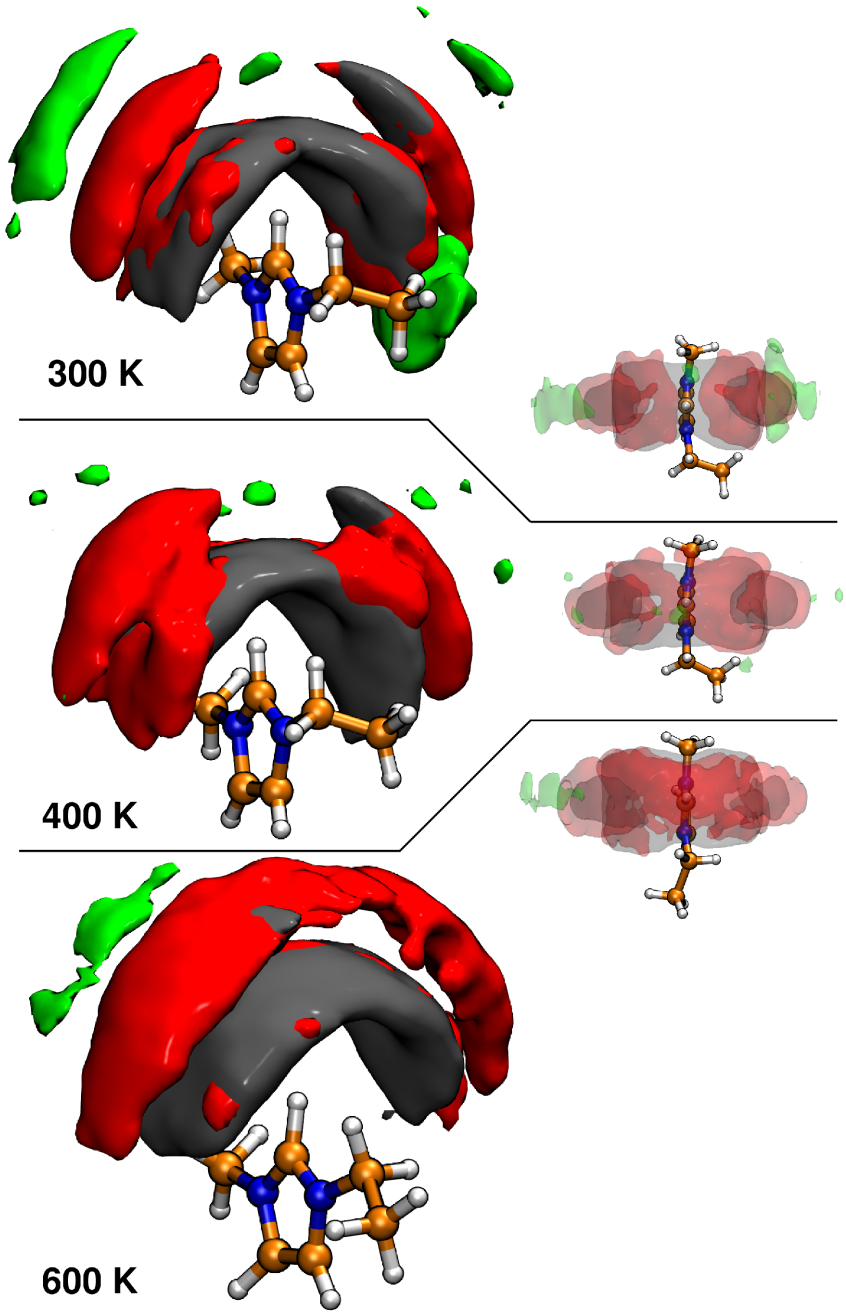

Figure 3.7: Spatial distribution functions (SDFs) of the terminal oxygen atoms O2-O4 (grey), the bridging oxygen atom O1 (red) and the terminal carbon atom C7' (green) of the anion around the cation at the investigated temperatures. All isosurfaces were plotted at 50 ppm to ensure a comparability between the SDFs at different temperatures.

no population of the bridging oxygen atom O1 (red) in the first and second shell directly in the plane of the cation. In contrast, only the terminal oxygen atoms O2-O4 (grey) can be found in the first shell in plane. The shifts mentioned in the results on the DDFs and CDFs, where the coordination of the anion to the cation changes from a coordination *via* the bridging oxygen atom O1 to a coordination *via* the three terminal oxygen atoms O2-O4, can be identified in between the first and second shell at the most populated region around the cation. At 400 K, the shifts occur more often, which can be identified through the enhanced red areas between the first and the second shells compared to the SDFs at 300 K. In addition, a coordination of the anion around the cation, where the bridging oxygen atom O1 is located in plane of the imidazolium ring interacting with the hydrogen atom H2 (see Fig. 3.7, 400 K transparent illustration), can now be identified. Increasing the temperature to 600 K leads to an increased occupation of the second shell of the in-plane coordination by the bridging oxygen atom O1. Therefore, the shifts between the first and second shell are reduced (no areas in between the two shells). The second shell of the oxygen atoms is now even populated directly above the acidic hydrogen atom H2, which was not detectable at the other temperatures.

The terminal carbon atom C7' (green) shows a very diverse behavior with increasing temperature. At 300 K, the ethyl chain of the anion is rigid and thus the terminal carbon atom C7' populates only specific areas around the cation. Especially worth mentioning is the area directly on-top of the imidazolium ring. For higher temperatures, this on-top area is not populated. In contrast, the bulk phase of this IL shows a significant population of this area at 400 K, as we observed in a previous work.[259] Since the evaporating temperature is ∼390 K and structural similarities between gas phase at 300 K and the bulk phase are observed (see right panel Figure 3.5 and its discussion and ref. [259]), the system at 300 K can be characterized as a "bulk phase-like" system. At 400 K, the distribution of the terminal carbon atom C7' is very diffuse, showing no highly populated areas just small spots. Thus, the ethyl-chain of the anion is less rigid

and is moving freely around the cation. This behavior of the anion describes the structural change from a "bulk phase-like" ion pair to a more gaseous ion pair. The plot at 600 K shows just one populated area for the terminal carbon atom C7' (green), which supports the picture of an anion facing the cation mostly *via* the terminal oxygen atoms O2-O4, describing a more stretched conformation.
The three dimensional view on the structure of an ion pair in the gas phase revealed a very interesting information: with increasing temperature, the anion shifts its coordination to the cation from a "bulk phase-like" coordination to a more free, gas-like coordination. Even though no ionic liquid/gas surface was considered here, this structural change of just one ion pair in the gas phase at different temperatures might describe the structural change and the change in the specific interactions between the cation and anion that occur during the evaporation process.

Power spectra are known to be a useful tool to analyze changes related to the strength of hydrogen bonding.[281] They are sensitive to structural changes and can be compared to experimental IR and Raman spectra. They are the sum of all the peaks in a IR and Raman spectra and even motions that are not active in either of them.[231,282] We have calculated the power spectra at 300 K, 400 K and 600 K (see Figure 3.8). We splitted the contributions to the power spectrum into the contributions of the cation $[C_2C_1im]^+$ (top panels of Figure 3.8) and the anion $[C_2SO_4]^-$ (bottom panels of Figure 3.8), to easily identify changes related to the anion and cation.
With increasing temperature, the power spectra for the cation and anion (panels A and B of Figure 3.8) are slightly shifted towards lower wavenumbers, more evident in the region 2800-3300 cm^{-1} (panels A3 and B3 of Figure 3.8). But more interestingly, the double peak of the stretching vibration of the CH_2 and CH_3 groups between 2800 cm^{-1} and 3000 cm^{-1} at 300 K and 400 K is reduced to a single peak at 600 K for both the cation and the anion (panels A3 and B3 of Figure 3.8). Thus, the structural change from a liquid phase-like ion pair at 300 K to a gas phase-like ion pair at 600 K has a explicit influence on the

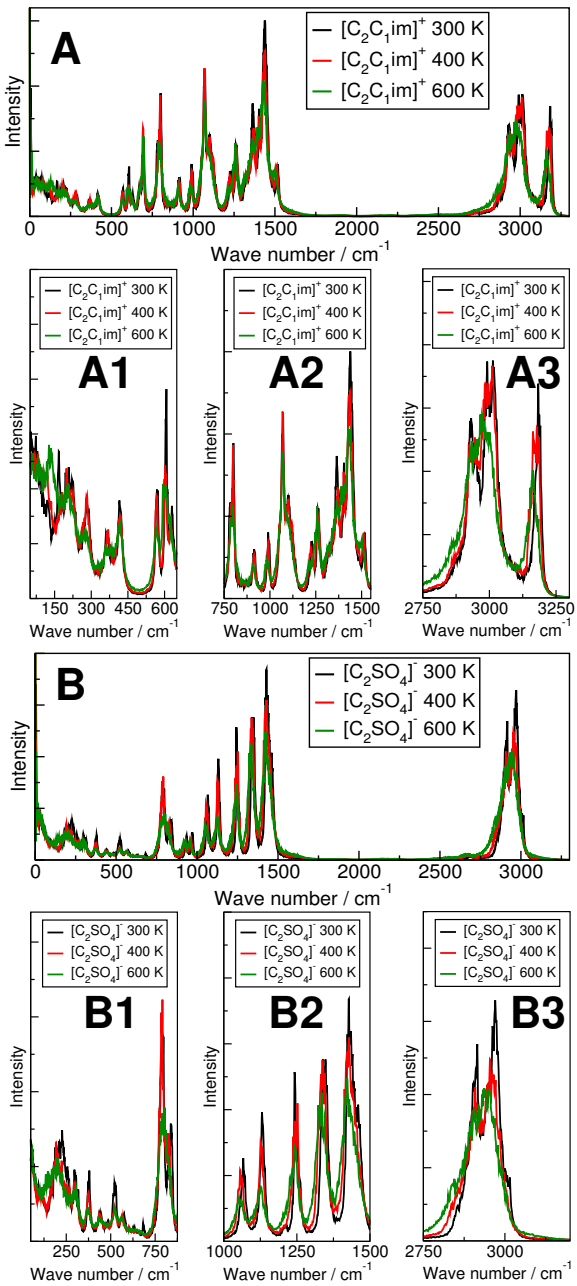

Figure 3.8: Comparison of the power spectrum obtained from the calculations at 300 K (black curve), 400 K (red curve) and 600 K (green curve). Top panels: $[C_2C_1im]^+$; bottom panels: $[C_2SO_4]^-$

stretching vibrations of the apolar groups. The double peak in the 2800 cm^{-1} and 3000 cm^{-1} region obviously resembles the liquid phase-like ion pair in the gas phase and is also part of the power spectrum of the bulk phase.[259] Further influence on the cation can be found at ∼1100 cm^{-1} and ∼1400 cm^{-1} (panel A2 of Figure 3.8), where the twisting (∼1100 cm^{-1}) and the rocking (∼1400 cm^{-1}) of the CH_2 and CH_3 groups can be found. At 600 K, the small peaks, that are present at 300 K and 400 K, are absent, indicating a uniform interaction with the anion and thus a steady coordination of the anion around the cation at high temperatures. Another strong influence on the cation can be found at ∼125 cm^{-1} (panel A1 of Figure 3.8), where a peak is present in the spectrum at 600 K but not at 300 K and 400 K. According to Fumino *et al.*,[52] this peak represents the bending of the ethyl chain and is therefore another evidence of the different structural coordination of the anion around the cation at 600 K.

The spectra of the anion for the three different temperatures are quite similar. Next to the major influence on the stretching vibrations of the apolar groups, there is a change in the structure of the peak at ∼780 cm^{-1} (panel B1 of Figure 3.8). The two peaks present at 300 K and 400 K collapse into a single peak at 600 K. This peak is slightly blue-shifted, which is different to the general small red-shift of the spectrum. Thus, the large peak, which is present at 300 K and 400 K, is missing in the spectrum of the anion at 600 K. This peak was identified by Dhumal *et al.*[233] as S5–O1 stretching vibration. Considering the structural differences at the different temperatures, the missing large peak points to a missing conformation at 600 K, where the anion side chain interacts with the cation and thus influences the shape of the peak.

We were able to identify the structural change of the ion pair, which occurs with increasing temperature, in the vibrational modes of the cation and the anion. It should be noted that some changes on the vibrational modes could also occur due general temperature effects.[282] The structural change especially influences the vibrational modes of the apolar parts (side chains) of the cation and anion. The vibrations of the polar parts of the cation (imidazolium ring) and the anion

([SO_4]-group) are nearly unaffected. Thus, the structural change is mostly based on the loosening of the side chain interactions between the cation and the anion. A weaker interaction of the side chains of the cation and the anion leads to a minor role of dispersion in the overall coordination of the counter ions, but only when an ion pair in the gas phase at high temperatures is considered. In contrast, at lower temperature (300 K), the dispersion interactions play an important role to the overall coordination of the counter ions, leading to bulk phase-like coordinations. In general, dispersion interactions can be understood as alterations of the coulombic interaction network and are necessary for the accurate description of the ions interplay in the ionic liquids.[28]

Dynamical Investigation After exploring the structural features, we are now investigating the dynamical behavior of the ion pair [C_2C_1im][C_2SO_4]. For simple and uncomplex anions like chloride, imidazolium-based ILs are known to have stable structures, *i.e.* conformations. They are defined as in-plane and on-top conformation with respect to the imidazolium ring. We illustrated these stable conformations in Figure 3.9 and for clarity we neglected the hydrogen atoms.

For more complex anions, where the negative charge is distributed over several atoms, the definition of the in-plane and on-top conformation is a difficult task. This is not only because the anions are able to build multiple hydrogen bonds with different acceptor atoms but also because of van der Waals interactions be-

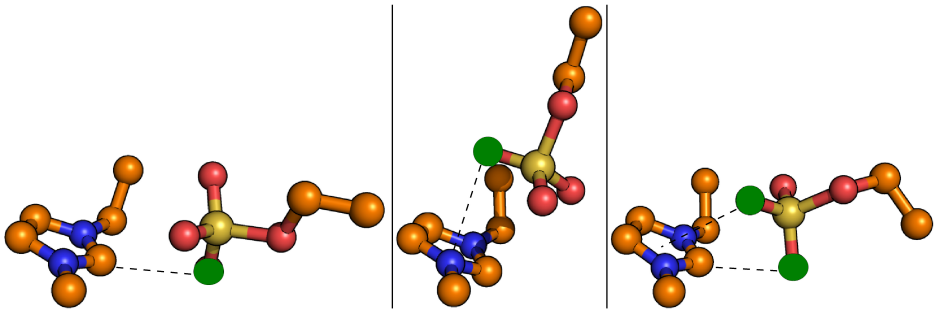

Figure 3.9: Illustrations of the in-plane (left), on-top (middle) and multiple interaction (right) conformation. Green atoms mark the coordination sites.

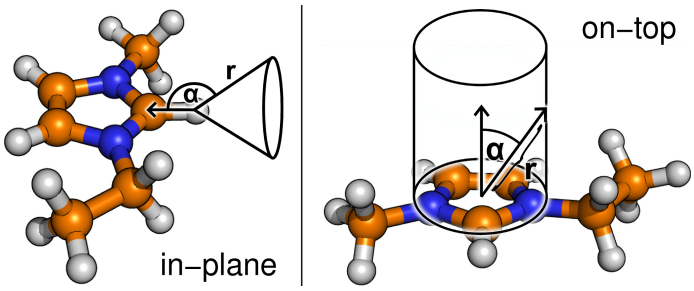

Figure 3.10: Ideas of how to define the in-plane (left) conformation and the on-top (right) conformation for complex anions based on distances r and angles α.

tween uncharged parts of the anion and the cation, which stabilize the ion pair in conformations different from those two. In Figure 3.9, the general idea of each conformation is illustrated by the interaction of the green-colored oxygen atoms. On the left, we see the in-plane conformation, in the middle the on-top one and on the right there is a conformation with a multiple interaction depicted (in-plane and on-top).

To distinguish the different conformations, we need to define conditions for each of them. The in-plane conformation can be seen as hydrogen bonding conformation between the acidic hydrogen atom H2 and the oxygen atoms O1-O4 and thus the best way to define conditions is to combine the angle between the vector H2–C2 and the vector H2–(O1-O4) and the distance between the hydrogen atom H2 and the oxygen atoms O1-O4 (see Figure 3.10).

To describe the on-top condition, we consider the imidazolium ring to be contained in a circle, which creates a cylinder above and below the ring plane. Thus, if a oxygen atom enters the cylinder, it should be counted as on-top conformation (see Figure 3.10). The same conditions for the on-top conformations were already used by us to describe the different conformations in a mixture of ionic liquids.[116]

We need to limit the distance so that only coordinations with the closest oxygen atoms are considered, due to the complex molecular structure of the anion. For the in-plane conformation, we just need to define a maximum distance and an angle interval, but for the on-top conformations this is still not straightforward,

because we need to restrict the counting to the oxygen atoms, which are inside of the cylinder. Using the trigonometric ratios on the right triangle, produced by the two vectors on the right side of Figure 3.10, we get the following relation between the distance r and the angle α:

$$r = \frac{120 \text{ pm}}{\sin \alpha} \tag{3.1}$$

The equation (3.1) describes the boundary of the on-top conformation, depending on the distance r and the angle α. Considering the combined distribution functions (CDFs) of the described distances r and angles α for the two different conformations presented in Figure 3.10, we can now define the boundaries for the different conformations displayed in Figure 3.11.

On the left side of Figure 3.11, the inside of the red rectangle describes all the coordinations that are counted as in-plane conformation. On the right side of Figure 3.11, the black curve displays the boundary (equation (3.1)). Everything below this black curve is inside of the cylinder, describing the on-top conforma-

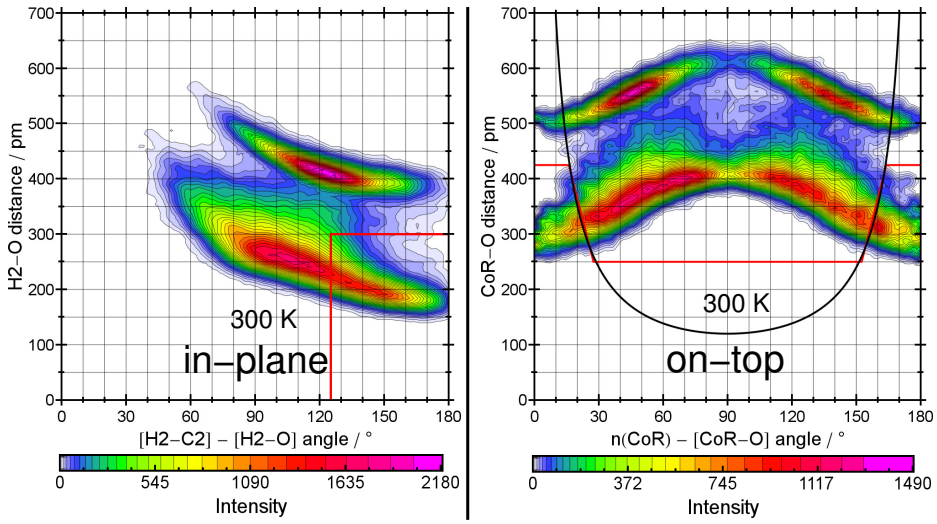

Figure 3.11: Boundaries for the in-plane conformation (left) and on-top conformation (right) shown exemplarily at room temperature (300 K). In case of the in-plane conformation, events placed inside the rectangle are counted. In case of the on-top conformation, events placed below the red line are counted. The black line describes the relation between distance and angle evaluated in equation (3.1).

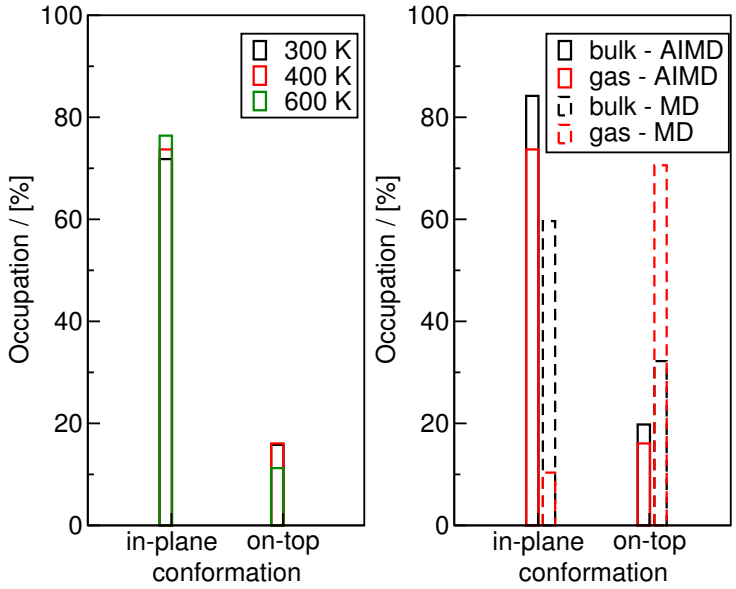

Figure 3.12: Left: Histogram of the occupation of both in-plane and on-top conformations for all three temperatures; **right:** comparison between the occupation of both in-plane and on-top conformation from gas and bulk phase AIMD and MD simulations. Computational details of the MD simulations can be found in ref. [283], the AIMD simulation of the bulk phase was already published in ref. [259].

tion. The red curve restricts the counting to the coordinations, where the oxygen atoms are close to the imidazolium ring, thus interacting with the cation from above or below the ring plane. Taking a look at the areas which fulfill the in-plane and on-top conditions, we already can state, that the in-plane conformation is more preferred, in agreement with the results of Figure 3.7.
To actually have a number of the preference, we provide in Figure 3.12 a histogram of the occupation of both conformations for all temperatures.

The occupation of the in-plane conformation increases slightly with increasing temperature, while the occupation of the on-top conformation slightly increases from 300 K to 400 K and decreases for 600 K. In general, the in-plane conformation is more preferred than the on-top conformation for all temperatures. On the right side of Figure 3.12, a comparison between the occupation of both in-plane and on-top conformation from gas and bulk phase AIMD and MD simulations

are shown. This comparison will not be discussed in detail, but highlights a very interesting phenomenon, when comparing the AIMD simulations to the MD simulations. For the bulk phase simulations, the MD simulation overpopulates the on-top conformation, while the in-plane conformation is underpopulated, but the trend that in-plane conformation should be higher occupied than the on-top conformation is correct. Turning to the gas phase simulations, this trend is completely reversed. As most of the force fields are fitted to bulk properties of ionic liquids, they fail to describe the gas phase of ionic liquids and MD simulations of gas-bulk interfaces of one ionic liquid need to be adjusted to the special properties of the gas phase as well.

To further investigate the temperature-dependence of the ion pair in these conformations, we take a look at the continuous correlation function. The continuous correlation function calculates the lifetime of an ion pair under certain conditions. The function is "1" as long as the ion pair satisfies the chosen conditions. As soon as the condition is not fulfilled, the correlation functions drops to "0", thus the function is able to depict the longest lifetime of an ion pair under these conditions. The functions, we provide in Figure 3.13, are the average over all these events and were computed under the in-plane and on-top conditions (see Figure 3.11).

On the left side of Figure 3.13, we see the continuous correlation function for the in-plane condition and on the right side for the on-top condition for all investigated temperatures. We added the continuous correlation functions on a logarithmic scale to easily compare the lifetimes and the differences between the correlation functions (bottom panel of Figure 3.13). Compared to each other, we can see that the lifetime of an on-top conformation is shorter than the lifetime of an in-plane conformation by ∼1-2 ps, for all temperatures.

A detailed description of the preferred conformations of different fluorinated aprotic ionic liquids (FAILs) was given recently.[114] At 400 K, we see a special behavior for the in-plane conformation. There, the longest lifetime of the ion pair is about 0.5 ps longer than at 300 K (bottom, left panel of Figure 3.13) which is surpris-

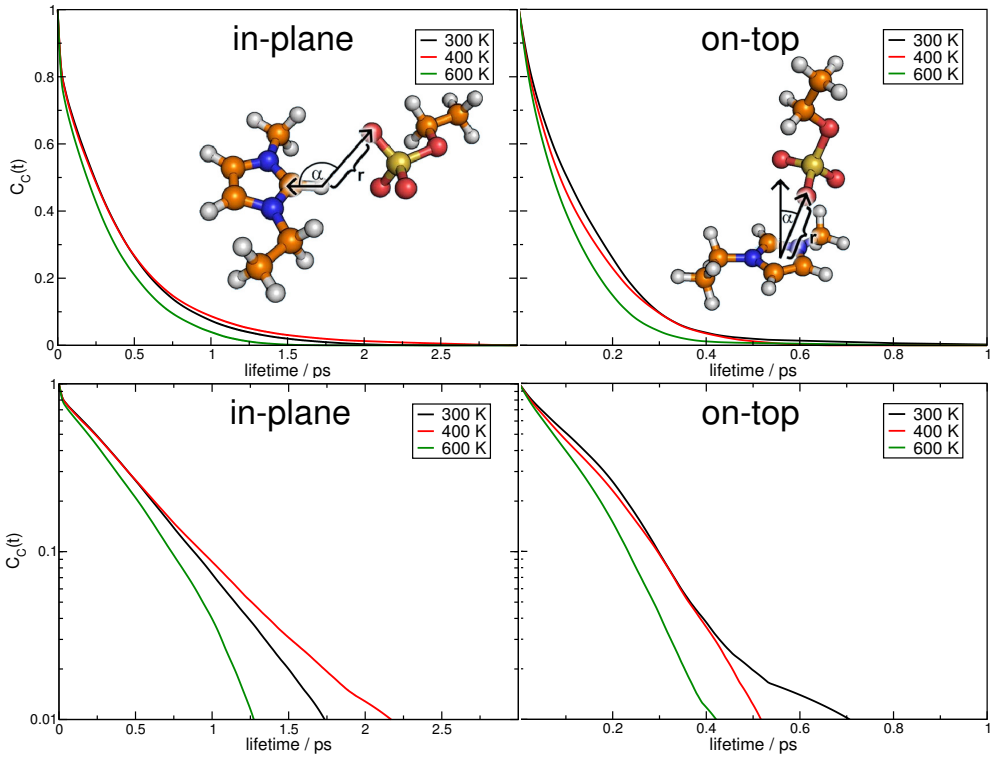

Figure 3.13: Continuous correlation functions of the in-plane conditions (left) and on-top conditions (right) at 300 K (black), 400 K (red) and 600 K (green). The top panel: linear scale; the bottom panel: logarithmic scale.

ing, considering that the atoms move faster at higher temperatures and are not sterically hindered (*e. g.* other ion pairs). In contrast, the lifetime of the on-top conformation shows the temperature-dependence one would expect. There, the ion pairs live the longest at 300 K and the shortest at 600 K. If we think of the in-plane conformation as a hydrogen bond-like conformation, then this special behavior at 400 K (longer lifetime of in-plane conformation) can be explained as an enhanced hydrogen bond affinity. An enhanced hydrogen bond affinity leads to a greater distortion of the coulombic network and thus, as discussed by the group of Ludwig,[52–55] fluidizes the ionic liquid even more. Considering the evaporation temperature of the investigated IL (390 K), we can state, that in our case the distortion of the coulombic network could explain the evaporation of the ionic liquid. As previously mentioned in the structural investigation (see para-

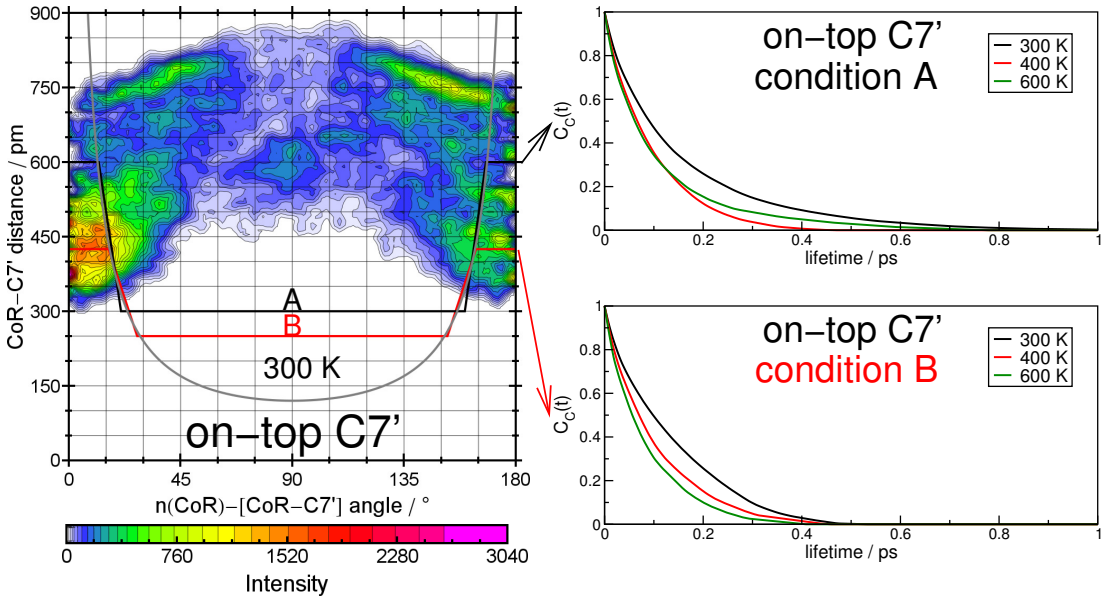

Figure 3.14: Left: CDF of the distance between the center of the ring (CoR) and the terminal carbon atom of the anion C7' and the angle between the normal vector to the ring plane n(CoR) to the vector between the CoR and the terminal carbon atom C7' containing two different boundaries A and B. Events below the black line are counted for condition A and events below the red line are counted for condition B. The gray line describes the relation between distance and angle evaluated in equation (3.1); **right:** continuous correlation function of the on-top coordination *via* carbon atom C7' under condition A (top) and condition B (bottom).

graph Structural Investigation) the anion experiences a structural rearrangement at 400 K. The shift of the oxygen atoms between the first and second shell around the cation causes the anion to stay in a hydrogen bond supported conformation: the in-plane conformation. With the increase of temperature the role of the hydrogen bonded conformation (distortion of the coulombic network) becomes less relevant as the system is in the most fluidizable state, the gas phase.

As we already pointed out in the discussion of the SDFs, the terminal carbon atom C7' of the anion populates a large spot directly on-top of the imidazolium ring. We are now interested in the dynamics of this coordination. Therefore, we choose the same definition as for the on-top coordination of the oxygen atoms,

with the same boundary (B) and also extended the boundary (A), because the interaction *via* the terminal carbon atom C7' is weaker as *via* the oxygen atoms. In Figure 3.14, we presented these boundaries in a CDF on the left side and on the right side, we displayed the continuous correlation functions for both boundaries (A and B).

The continuous correlation functions under condition A and condition B show a very different temperature-dependence. Considering the functions under condition B (see Figure 3.14, right side, bottom) we see that at 300 K the lifetimes between 0.05 ps and 0.4 ps durates longer than at 400 K or 600 K. The correlation functions at 400 K in condition B are a little bit more pronounced than at 600 K, which leads to the conclusion that in the bulk phase-like state of the ion pair the interaction between the imidazolium ring and the carbon atom C7' of the anion is more important than in the gas phase. Extending the condition we choose for the oxygen atoms (condition B) to count also coordinations at higher distances (condition A), we observe a clear change. At 600 K, the ion pair lives up to 0.3 ps longer under condition A than at 400 K, but still lives shorter than the ion pair at 300 K. Comparing the correlation function at 400 K for both conditions A and B, we observe no change in the behavior of the correlation function. Thus, we conclude that the similar behavior of the correlation functions represents a weak interaction between the terminal carbon atom C7' of the anion and the imidazolium ring under both conditions at 400 K. This weak interactions therefore supports the evaporating process (∼390 K) for the ion pair $[C_2C_1im][C_2SO_4]$.

Free Energy Surface We calculated the free energy surface of the ion pair at 300 K and 600 K with respect to the distance between C2 and S *via* thermodynamic integration. We set the reaction coordinate to this distance because we were interested in the free energy surface change with increasing temperature. In the structural investigation, we already pointed to a structural change of the ion pair from 300 K to 600 K. The change is governed by the disengagement of the anions side chain from the imidazolium ring and the resulting further distance between anion and cation. We identified the change as a change from a bulk

phase-like coordination to a gas phase-like coordination. Thus, the calculated free energy surface at 300 K represents the bulk phase-like free energy surface without the contributions of interacting ion pairs and the one at 600 K the gas-phase like free energy surface.

In Figure 3.15, we compare the distance distribution function of C2–S at 300 K and 600 K to the calculated free energy surfaces at these temperatures. In the distribution function (see Figure 3.15, top panel), we see a shift of the maximum to further distances and an extending of the peak-width with increasing temper-

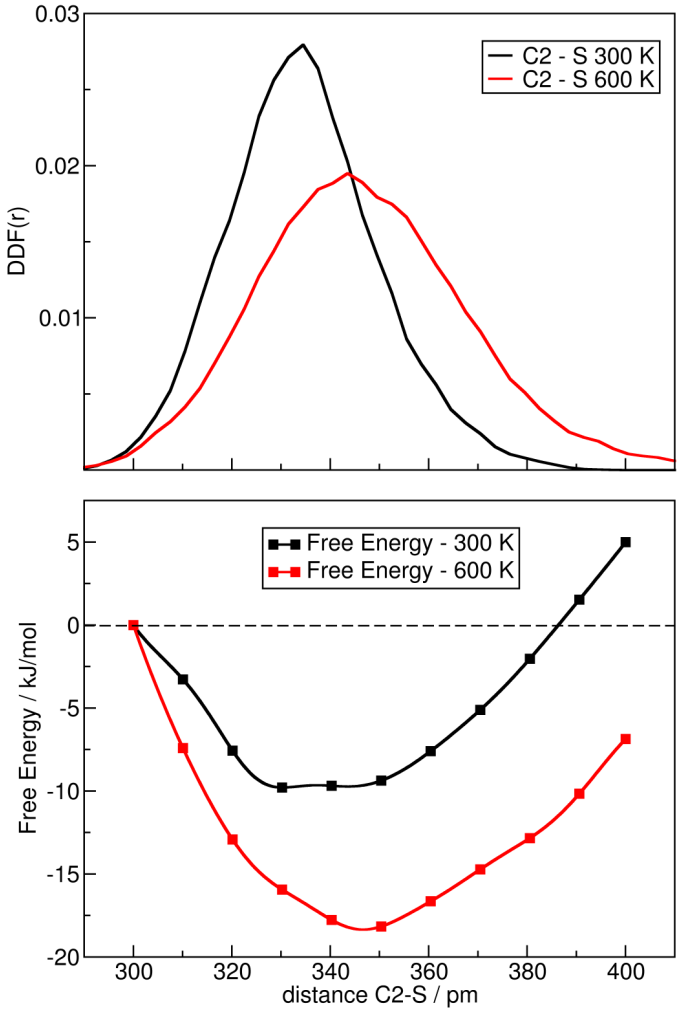

Figure 3.15: Comparison of the distance distribution function of C2–S at 300 K and 600 K (top) to the calculated free energy surface with respect to this distance(bottom).

ature. Comparing these maxima with the free energies (see Figure 3.15, bottom panel), both reside with the minimum of the free energy surface at the respective temperature. At 300 K, the minimum of the free energy surface is situated at ∼330 pm and at 600 K, it is shifted to ∼345 pm. In addition, the minimum of the free energy surface at 600 K can be found at lower values, which describes the temperature-dependence of the free energy. It also explains why the peak-width of the distance distribution function is extended at 600 K. At 300 K, the free energy takes positive values at ∼385 pm, which are close to the position, where the DDF drops to zero. The free energy surface around the minima at 300 K is very flat, allowing the anion to switch easily between positions, where the sulfur atom changes from distances between 330 pm and 345 pm. In Figure 3.6, two different coordinations of the anion to the cation were already discussed. We identified them as a coordination *via* the three terminal oxygen atoms and a coordination where the bridging oxygen atom also interacts with the cation. Thus, the possible distances of the sulfur atom are in accord with the two known coordinations of the anions oxygen atoms around the cation at 300 K. At 600 K, we describe the interaction of the anion to only take place *via* the terminal oxygen atoms. With the minima of the free energy surface, we can identify this coordination with the C2–S distance of 345 pm.

The different shapes of the free energy surfaces explain the structural change of the ion pair with increasing temperature. Even though we calculated the free energy surface with respect to the C2–S distance, the shape is in accord with the observations made in the structural investigation based on the coordination of the oxygen atoms to the cation. Considering the free energy surface at 300 K to be the bulk phase-like free energy surface, it is possible to describe why the system is more packed in the bulk phase, next to sterical reasons. When compared to the free energy surface at 600 K—the gas phase-like free energy surface—the difference in the coordination at 300 K and 600 K with respect to the C2–S distance becomes obvious and can be used to explain the structural change during the evaporation process.

Conclusion

We presented an *ab initio* molecular dynamics study on an ion pair of the ionic liquid 1-ethyl-3-methylimidazolium ethylsulfate $[C_2C_1im][C_2SO_4]$ at three different temperatures 300 K, 400 K and 600 K. From comparison to previous studies, we could observe that 300 K resembles ion pairs in the bulk, while at 400 K another behavior is detected. By investigating the temperature-dependence of the structure of the ion pair, we were able to point out, that the coordination of the anion to the cation around the most acidic hydrogen atoms H2 changes with increasing temperature. At 300 K, a mixed coordination of the anion to the cation *via* the terminal oxygen atoms O2-O4 and bridging oxygen atom O1 is preferred. At 400 K, the temperature close to the evaporation temperature, a structural change occurs, where the bridging atom moves to further distances, and at 600 K, the anion interacts with the cation only *via* the terminal oxygen atoms O2-O4, *i.e.* being in a more hydrogen bond-like state. This structural change corresponds to a shift from a bulk phase-like coordination to a more free, gas phase-like coordination, which can be used to describe the evaporation process of the investigated ionic liquid. The different shapes of the free energy surface with respect to the C2–S distance explain the structural change from 300 K to 600 K and support the idea of a bulk phase-like and gas phase-like coordination. We were interested in the influence of this change on the vibrational density of states. Only the vibrational modes of the apolar parts of both ions changed, whereas the vibrational modes of the polar parts remained nearly unchanged. From the three dimensional picture of the anion around the cation a loosening of the side chains is indicated from the interionic interactions and the conclusion follows that the role of the dispersion interaction at high temperatures, in contrast to low temperatures, is less marked.

Analyzing the dynamics of the system, we observed that the longest lifetime in the in-plane conformation was at 400 K, which pointed to an enhanced hydrogen bond affinity to support the structural change. The lifetimes of the ethyl chain of the anion in on-top conformation under different conditions, revealed

that the evaporating process is also triggered by a weak interaction between the ethyl chain and the imidazolium ring. Even if coulombic interactions in ILs are important and responsible for the behavior of different properties, dispersion interactions (weaker than Coulombic) play an important role for the vaporization process. The dispersion interactions present in the liquid phase are much weaker in the gas phase.

Acknowledgment

This work was supported by the DFG, in particular by the projects KI-768/5-1, KI-768/5-2, KI-768/5-3 and KI-768/7-1. Computer time from the RZ Leipzig, the NIC Jülich, and the DEISA supercomputer center are gratefully acknowledged. We would like to thank Frank Uhlig for helpful discussions.

3.2 Interfaces of Ionic Liquids

3.2.1 Using Molecular Simulation to Understand the Structure of 1-Ethyl-3-Methylimidazolium Alkylsulfates Ionic Liquids: Bulk and Liquid–Vapor Interfaces

Xavier Paredes,[†] Josefa Fernández,[†] Agílio A. H. Pádua,[‡] Patrice Malfreyt,[*,‡] Friedrich Malberg,[§] Barbara Kirchner[§] and Alfonso S. Pensado[*,‡,§]

Received 25th September 2012, Revised 22th October 2012

Published 12th November 2012

DOI: 10.1021/jp309532t

Own contributions to this manuscript:

- Analysis of trajectories
- Critical evaluation of the results
- Discussion of the results
- Co-writing of the manuscript

[†] *Laboratorio de Propiedades Termofísicas, Departamento de Física Aplicada, Universidade de Santiago de Compostela, E-15782 Santiago de Compostela, Spain*

[‡] *Institut de Chimie de Clermont-Ferrand, Equipe Thermodynamique et Interactions Moléculaires, Clermont Université, Université Blaise Pascal, BP 80026, 63171 Aubiere, France and CNRS, UMR6296 ICCF, BP 80026, F-63171 Aubiere, France, E-Mail: patrice.malfreyt@univ-bpclermont.fr*

[§] *Wilhelm Ostwald Institute für Physikalische and Theoretische Chemie, Universität Leipzig, Linnéstr. 2, D-04103 Leipzig, Germany, E-Mail: alfonso.pensado@uni-leipzig.de*

Abstract Using molecular dynamics simulations we have studied the structure of alkylsulfate-based ionic liquids: 1-ethyl-3-methylimidazolium n-alkylsulfate $[C_2C_1im][C_nSO_4]$ (n = 2, 4, 6 and 8). The structure of the different ionic liquids have been interpreted taking into account radial and spatial distribution functions, and structure factors, that allowed us to characterize the morphology of the polar and nonpolar domains present in this family of liquids. The size of the nonpolar regions depends linearly on the anion alkyl chain length. Furthermore, properties of the surface of ionic liquids, such as surface tension, ordering, and charge and density profiles, were studied using molecular simulation. We were able to reproduce the experimental values of the surface tension with a maximum deviation of 10 %, and it was possible to relate the values of the surface tension with the structure of the liquid-vacuum interfaces. Microscopic structural analysis of orientational ordering at the interface and density profiles along the direction normal to the interface suggest that the alkyl chains of the anions tend to protrude toward the vacuum, and the presence of the interface leads to a strong organization of the liquid phase in the region close to the interface, stronger when the side chain length of the anions increases.

Introduction

The most accurate definition of ionic liquids (ILs) has been proposed by Hallet and Welton[284] quite recently: "Ionic liquids are compounds constituted entirely of ions, with melting points lower than 373 K". No more general comments hold for ionic liquids, in addition the nature of the interactions present in this media are complex.[28,39,40,44,256] Both cations and anions, usually voluminous and characterized by complex molecular structures, flexibility, highly asymmetric and with delocalization of the electrostatic charge, can be selected to tune the physicochemical properties of the ILs. One of the most common statements on ionic liquids was that ionic liquids are nonvolatile, even though in 2002 Morrow and Maginn,[75] with the aid of molecular simulation, predicted enthalpies of vaporization for ionic liquids in the range of 150–240 $kJ{\cdot}mol^{-1}$. Then, Rebelo, Magee

and coworkers[59,60] provided experimental evidence of the ability of ionic liquids to be distillable, opening intense research into the vapor phase of ionic liquids. Advances in the field of ionic liquids technology will strongly benefit a comprehensive understanding of both their bulk and surface properties. A wide range of chemical reactions takes place mainly at interfaces.[284] The use of ionic liquids in electrochemical applications[20–22] and gas-storage techniques[9–12] or gas separation[14–17] requires also an accurate description at the molecular level of the gas-liquid interfaces. Applications such as the synthesis of metallic nanoparticles[92,285–287] will depend upon both surface and bulk properties. The size distributions of the nanoparticles[288] synthesized in different ionic liquids are related to the heterogeneous structure of the particular IL, which may contain polar and non polar regions.

Alkylsulfate-based ILs with a cation derived from imidazolium[289,290] can be considered as some of the most promising ILs for the application in industrial processes. In general, they can be easily synthesized in an atom-efficient and halide-free way, at a reasonable cost. They show low melting points,[260] relatively low viscosities,[291,292] and high biodegradability. Thus, Deng *et al.*[27] performed several toxicity and biodegradability studies on a large set of ionic liquids, observing that the ionic liquid $[C_1COOC_5C_1im][C_8SO_4]$ was completely degraded within 5 days; therefore, this IL can be considered "readily biodegradable" with the "CO_2 headspace test". Wilfred *et al.*[293] analyzed the performance of several ILs to efficiently remove sulfur compounds in oil refining. These authors investigated the effect of mass ratio between ILs and dodecane (model oil), extraction temperature, and extraction time on dibenzothiophene (DBT) removal efficiency. A total of 18 different ILs were used to extract DBT from dodecane respectively, observing that the ionic liquids $[C_4C_1im][SCN]$, $[C_4C_1im][N(CN)_2]$, $[C_4C_1im][C_8SO_4]$, and $[N_{4441}][CH_3CO_3]$ were the top four ILs with desulfurization efficiency ranging from 66 % to 62 %. Pereiro *et al.*[294] studied the performance of the ionic liquid $[C_2C_1im][C_2SO_4]$ to separate azeotropic mixtures. This IL showed a high ability to act as an extraction solvent, that allows purifying alkanes from their azeotropic

mixtures with ethanol. Therefore, the development of new industrial applications of this family of ionic liquids will strongly benefit from a deep knowledge of both bulk and surface properties.

Russina *et al.*[108] have performed X-ray diffraction measurements on a range of ionic liquids based on the alkylsulfate anion, namely $[C_2C_1im][C_nSO_4]$, with n = 2, 4, 6, and 8, that show the existence of nanoscale structural heterogeneities for all the ILs, with the size depending linearly on the anion alkyl chain length. Martinez *et al.*[99] combined sum-frequency generation spectroscopy, surface potential and surface tension measurements to analyze the ionic liquid-gas interface for 1-alkyl-3-methylimidazolium alkylsulfate ionic liquids, showing an increase on the surface potential of the IL when the length of the alkyl chain on the cation or anion increases. They also conclude that the imidazolium ring and the sulfate group are found at the same distance from the surface for all the studied ILs.

In this work, we present results of MD simulations for the bulk phase of the ionic liquids 1-ethyl-3-methylimidazolium ethylsulfate $[C_2C_1im][C_2SO_4]$, 1-ethyl-3-methylimidazolium butylsulfate $[C_2C_1im][C_4SO_4]$, 1-ethyl-3-methylimidazolium hexylsulfate $[C_2C_1im][C_6SO_4]$ and 1-ethyl-3-methylimidazolium octylsulfate $[C_2C_1im][C_8SO_4]$, together with the study of the liquid-gas interface of the $[C_2C_1im][C_2SO_4]$ and $[C_2C_1im][C_8SO_4]$ ILs to assess the surface tension and the structure of the surface. This set of ionic liquids was chosen in order to rationalize the effect of increasing the side chain length of the anion in the bulk phase structure, the structure at the surface and the surface tension.

Simulation Methodology

Potential model. Ionic liquids were represented by an all-atom force field,[295,296] which is based on the AMBER/OPLS_AA framework[211,212] but was developed specifically for ionic liquids. This model contains all the parameters required to simulate the alkylsulfate anions $[C_2SO_4]^-$, $[C_4SO_4]^-$, $[C_6SO_4]^-$ and $[C_8SO_4]^-$, and the 1-ethyl-3-methylimidazolium cation $[C_2C_1im]^+$ (Figure 3.16). The functional form of the force field contains four kinds of potential energy: stretching

of covalent bonds, bending of valence angles, torsion around dihedral angles, and nonbonded interactions. Nonbonded interactions occur between atoms of the same molecule separated by more than three bonds and between atoms of different molecules. The potential energy associated with bonds and angles is described by harmonic terms, dihedral torsion energy is represented by series of cosines, and nonbonded interactions are given by the Lennard-Jones sites and by Coulomb interactions (calculated using the Ewald summation method) between partial point charges placed on the atomic sites.

Computational procedures. The bulk phase of the ionic liquids $[C_2C_1im][C_2SO_4]$, $[C_2C_1im][C_4SO_4]$, $[C_2C_1im][C_6SO_4]$ and $[C_2C_1im][C_8SO_4]$ were simulated in periodic cubic boxes containing 512 ion pairs using the molecular dynamics method implemented in the DL_POLY package.[297] The initial configurations were lattices with low-density. Equilibrations starting from the low density arrangement of ions took 1 ns, at constant NpT and T =423 K, with a timestep of 2 fs. Once the equilibrium density was obtained, simulation runs of 2 ns were performed. At the final densities of the ionic liquid state, the lengths of the sides of the simulation boxes range from approximately 54 Å to 63 Å for the ionic liquids with the $[C_2SO_4]^-$ and $[C_8SO_4]^-$ anion, respectively. Additionally, for the analysis of the free surfaces of the ionic liquid, we have considered rectangular parallelepiped simulation boxes of dimensions $L_xL_yL_z$ (with $L_x = L_y$) containing between 1024 ion pairs of the ionic liquids $[C_2C_1im][C_2SO_4]$ and $[C_2C_1im][C_8SO_4]$, for a total of around 30000 ($[C_2C_1im][C_2SO_4]$) and 50000 ($[C_2C_1im][C_8SO_4]$) atoms in the simulated systems. Periodic boundary conditions were applied in the three directions of space. The direction normal to the surface of the ionic liquid was elongated (300 Å) so that the liquid slab occupies ∼120 Å ($[C_2C_1im][C_2SO_4]$) and ∼150 Å ($[C_2C_1im][C_8SO_4]$) in the middle with two equivalent interfaces. The systems were simulated via molecular dynamics using the DL_POLY program[297] at 423 K. The system was coupled to a Nosé–Hoover thermostat (constant NVT). The integration time step was 2 fs. Initial configurations were constructed by placing together two cubic boxes considered

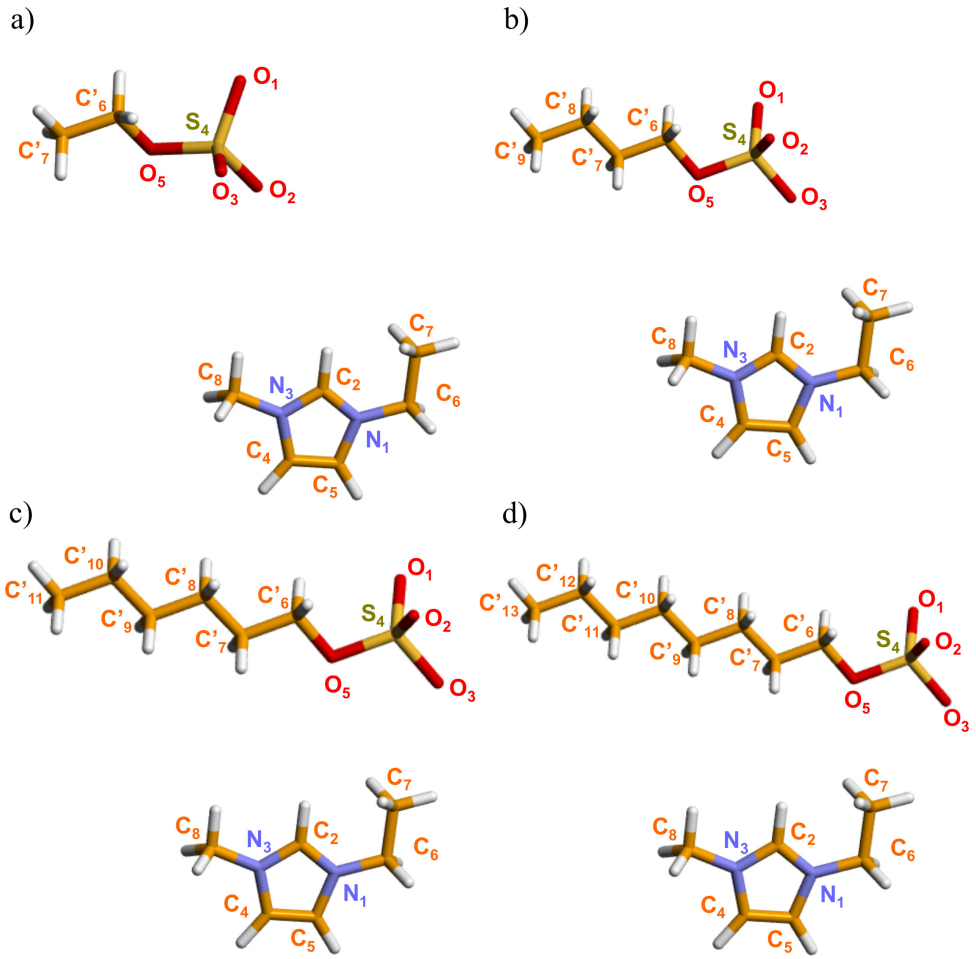

Figure 3.16: Adopted nomenclature for the sites of the studied ionic liquids. (a) 1-Ethyl-3-methylimidazolium ethylsulfate $[C_2C_1im][C_2SO_4]$, (b) 1-ethyl-3-methylimidazolium butylsulfate $[C_2C_1im][C_4SO_4]$, (c) 1-ethyl-3-methylimidazolium hexylsulfate $[C_2C_1im][C_6SO_4]$ and (d) 1-ethyl-3-methylimidazolium octylsulfate $[C_2C_1im][C_8SO_4]$.

in the previous step. Equilibrations starting from this arrangement of ions took 1 ns (NpT), after which the systems were run for 1 ns to allow the interface to equilibrate. Then, a production run of 2 ns was executed. As expected, no detectable vapor phase was observed during the simulations. We calculated profiles of typical properties as a function of z (as the geometry of the system shows heterogeneity along the axis normal to the interface, z axis) by splitting the cell into slabs of width δz.

The methods used most frequently to calculate the surface tension[298–300] consider the mechanical route definition and express the surface tension through the components of the pressure tensor. The Kirkwood and Buff expression[300] evaluates the components of the pressure tensor as a function of the derivative of the intermolecular potential. The definition of Irving and Kirkwood[299] is based upon the notion of the force across a unit area and profit of expressing the local components of the pressure tensor along the direction normal to the interface. Gloor *et al.*[298] have established a method based upon the thermodynamic definition of the surface tension allowing the calculation of this quantity through a perturbation of the cross-sectional area of the system containing the interface. In previous works, we have shown the equivalence of the three methods to assess the performance of the different routes to calculate the surface tension of ionic liquids.[104,301] Full details of the calculation methods, including the treatment of long-range corrections, can be found elsewhere.[104]

Results and Discussion

Bulk phase. Using molecular dynamics simulation, and almost simultaneously, Wang and Voth,[105] employing a multiscale coarse-graining (MS-CG) method, and Canongia Lopes and Pádua,[106] using an all-atom potential model, reported the existence of a nanometer-scale structuring in imidazolium-based ionic liquids (from $[C_2C_1im]^+$ to $[C_{12}C_1im]^+$) corresponding to a segregation of polar and nonpolar domains. Ester-functionalized imidazolium-based ionic liquids[302] also present this characteristic nanosegregation in polar and nonpolar regions. Triolo and coworkers,[107–111] using X-ray diffraction, provided experimental evidence of a nanoscale organization in the ionic liquids of the families $[C_nC_1im][PF_6]$, $[C_nC_1im][BF_4]$, $[C_nC_1im][Cl]$, $[C_nC_1im][Tf_2N]$, and $[C_2C_1im][C_nSO_4]$. The importance of this segregation of the ionic liquids into polar (or ionic) and nonpolar spatial domains is a key issue to define their solvation characteristics, mainly due to distinctive effects of this dual structure and also through the existence of different types of interaction with both polar and nonpolar solutes.[303]

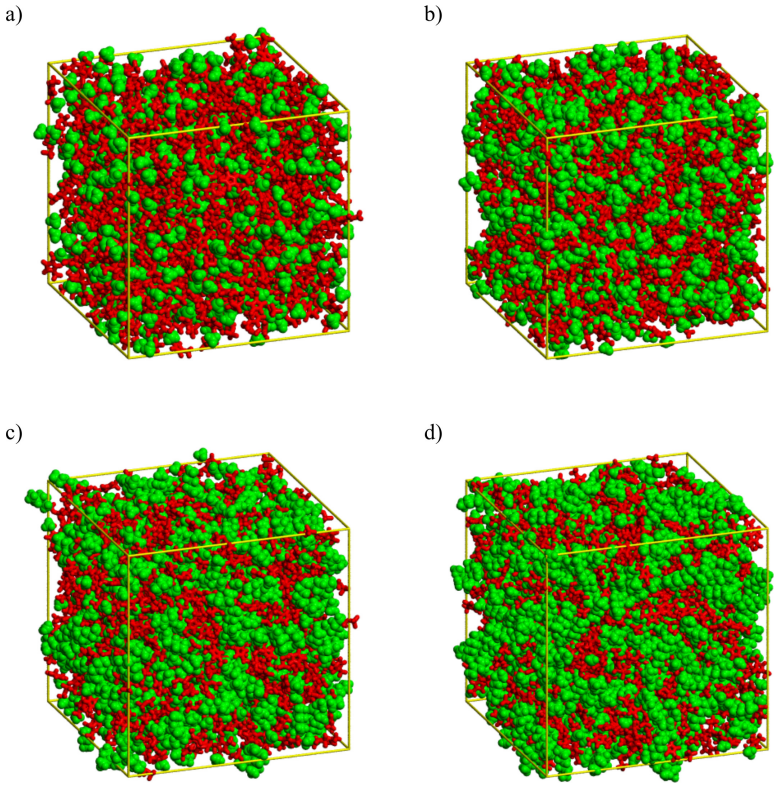

Figure 3.17: Snapshots of simulation boxes containing 512 ions of $[C_2C_1im][C_nSO_4]$, using a coloring code to identify the charged (polar) and nonpolar domains that form in ionic liquids. The lengths of the box sides are given: (a) $[C_2C_1im][C_2SO_4]$ l = 54.7 Å, (b) $[C_2C_1im][C_4SO_4]$ l = 57.8 Å, (c) $[[C_2C_1im][C_6SO_4]$ l = 60.4 Å and (d) $[C_2C_1im][C_8SO_4]$ l = 63.0 Å.

Figure 3.17 depicts the morphology of the polar and nonpolar regions for the studied alkylsulfate-based ionic liquids, using the same color code proposed by Canongia Lopes and Pádua[106] to identify high charge (red) and low charge density (green) regions. The polar regions considered to be of high charge density consist of the atoms of the imidazolium ring of the cation plus the atoms directly bonded to them (including the hydrogen atoms directly bonded to the first carbon of the alkyl chain), the sulfur and oxygen atoms of the alkylsulfate anions, together with the carbon atom bonded to the bridging oxygen atom, and the hydrogen atoms bonded to it. The terminal CH_3 group of the ethyl side chain of the cation, and the remaining atoms of the side chain of the anions constitute

the regions considered to be of low charge density (green). The distribution of the charged domains is not homogeneous but it has the form of a continuous tridimensional network of ionic channels that coexist with the nonpolar domains. The nonpolar domains form a dispersed phase in the case of the ionic liquid with the $[C_2SO_4]^-$ anion, whereas in the case of the IL with the $[C_8SO_4]^-$ anion, the nonpolar domains form a continuous and complex tridimensional structure.

The snapshots of the simulation boxes depicted in 3.17 present a qualitative (visual) description of the nanostructure of the considered ionic liquids; a more quantitative analysis can be performed by means of the radial distribution functions (RDFs), and the static structure factors, which can be directly compared with X-ray measurements. Figure 3.18 shows the site–site radial distribution functions between several representative atoms of the anions and cations of the studied ionic liquids. A prominent feature of the RDFs is the strong correlation between the terminal oxygen atoms of the alkylsulfate anions and the atoms of the imidazolium ring of the $[C_2C_1im]^+$ cation. We observe larger peaks in the C_2–$O_{1,2,3}$ radial distribution functions when increasing the side chain of the anion, reflecting a more structured liquid phase. We also observe a strong peak in the S–S RDF (panel c, Figure 3.18) at distances around 7.5 Å, that correspond to conformations where two anions are linked to the same cation. For the ionic liquid $[C_2C_1im][C_2SO_4]$ the terminal atom of the side chain of the anion is also located close to the imidazolium ring (see panel b of Figure 3.18). Panels d-f of Figure 3.18 show the radial distribution functions between the terminal atoms of the cations and anions. The most remarkable feature is that the terminal atoms of both cations and anions tend to stick together, being the origin of the polar and nonpolar segregation present on the ionic liquids. Canongia Lopes and Pádua[106] observed for the family of ionic liquids $[C_nC_1im][PF_6]$ clear differences between the RDFs of the terminal atoms of the cations with the increase of the side chain, whereas in this work, the differences on the radial distribution functions of the terminal atoms of the investigated anions show small differences, highlighting how the molecular structure of the IL affects the structure of the liquid phase.

We observe a shift of the first minimum of the RDFs, but the position of the first maximum, as well as its value is only slightly affected. We observe that the peak of the RDF between the terminal atom of the cation and the terminal atom of the anion decreases with the side-chain length. The structural features are better depicted in the three-dimensional spatial distribution functions, shown in Figure 3.19.

We observe a high probability of finding the oxygen atoms of the anions close to the imidazolium ring of the cation. The anion interacts with the cation mainly via the terminal oxygen atoms of the sulfate head, and the coordination occurs via the most acidic hydrogen atom in position C_2, but also through the hydrogen atoms in positions C_4 and C_5. We observe that the coordination of the anion is stronger when the length of the side chain of the anion increases, in good agreement with the results presented in the radial distribution functions depicted in Figure 3.18. Recently, Malberg *et al.*[259] using dispersion corrected *ab initio* Molecular Dynamics, have simulated the bulk and gas phase of the ionic liquid $[C_2C_1im][C_2SO_4]$. These authors observed that in the bulk phase the terminal atom of the anion interacts with the imidazolium ring of the cation, being situated above (below) of the ring: this establishes the dispersion interaction as the driving forces. This interaction is not present in the gas phase. We observe in panel a of Figure 3.19 the same feature: The terminal atom of the $[C_2SO_4]^-$ anion can be found with high probability above (below) the imidazolium ring. Increasing the length of the side chain of the anion makes this interaction weaker (the green regions in the SDFs decrease in size), but it is still present in the IL. The good agreement between the results obtained in this work, using classical molecular simulations, and a nonpolarizable force field for the ionic liquids and the results of Malberg *et al.*[259] using dispersion corrected *ab initio* Molecular Dynamics (a technique where the electronic structure of the atoms is explicitly considered, and the interactions between the different atoms present on the simulation are calculated on the fly by means of a density functional theory calculation) allows us to validate the performance of the classical force field employed in this work.

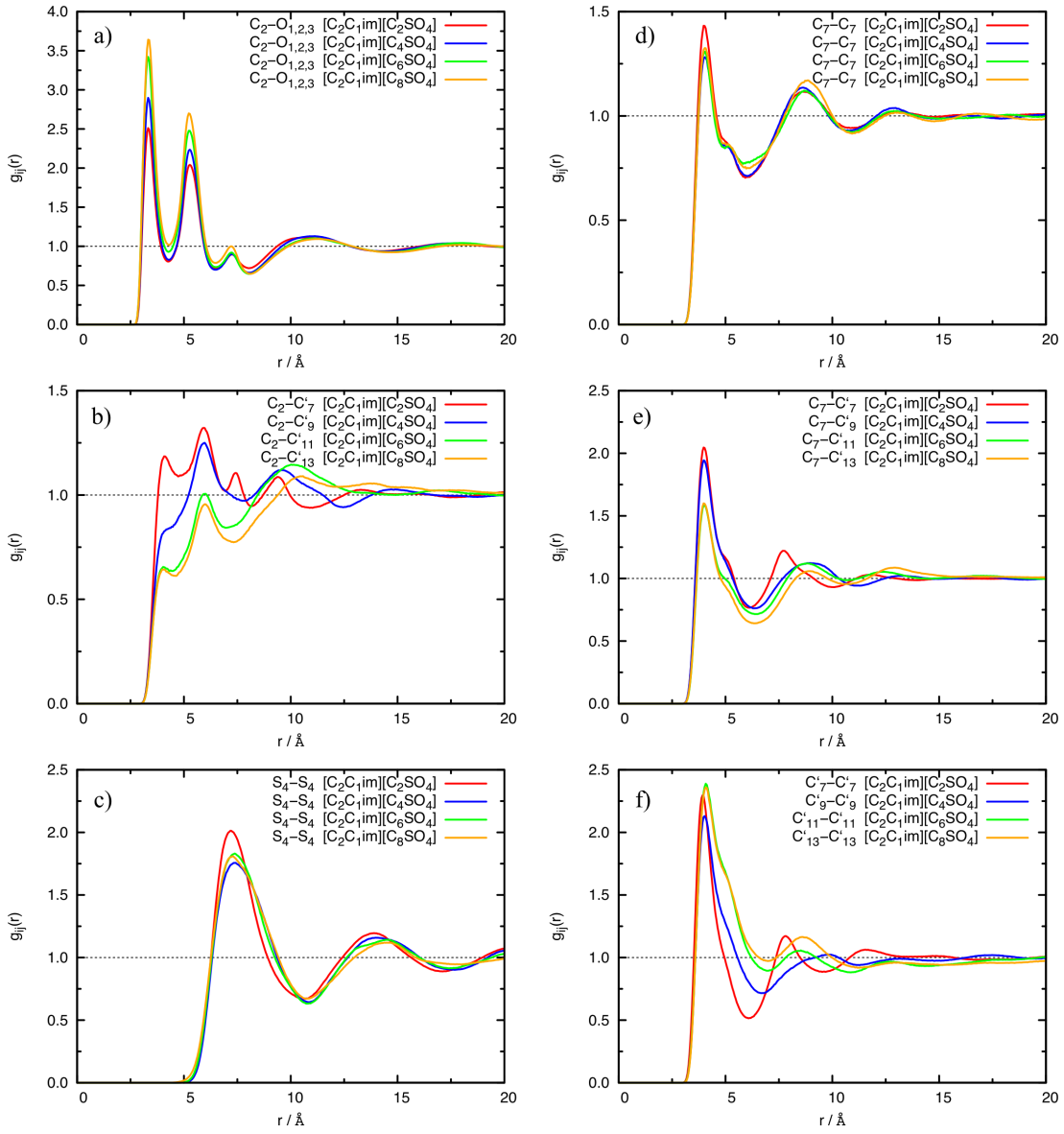

Figure 3.18: Cation-anion site–site radial distribution functions. (a) Oxygen atoms of the $[C_nSO_4]^-$ anions around the $[C_2C_1im]^+$ cation. (b) Terminal carbon atom of the $[C_nSO_4]^-$ anions around the $[C_2C_1im]^+$ cation. (c) Sulfur atom of the $[C_nSO_4]^-$ anions. (d) Terminal carbon atom of the $[C_2C_1im]^+$ cation. (e) Terminal carbon atom of the $[C_2C_1im]^+$ cation and terminal carbon atom of the $[C_nSO_4]^-$ anions. (f) Terminal carbon atom of the $[C_nSO_4]^-$ anions.

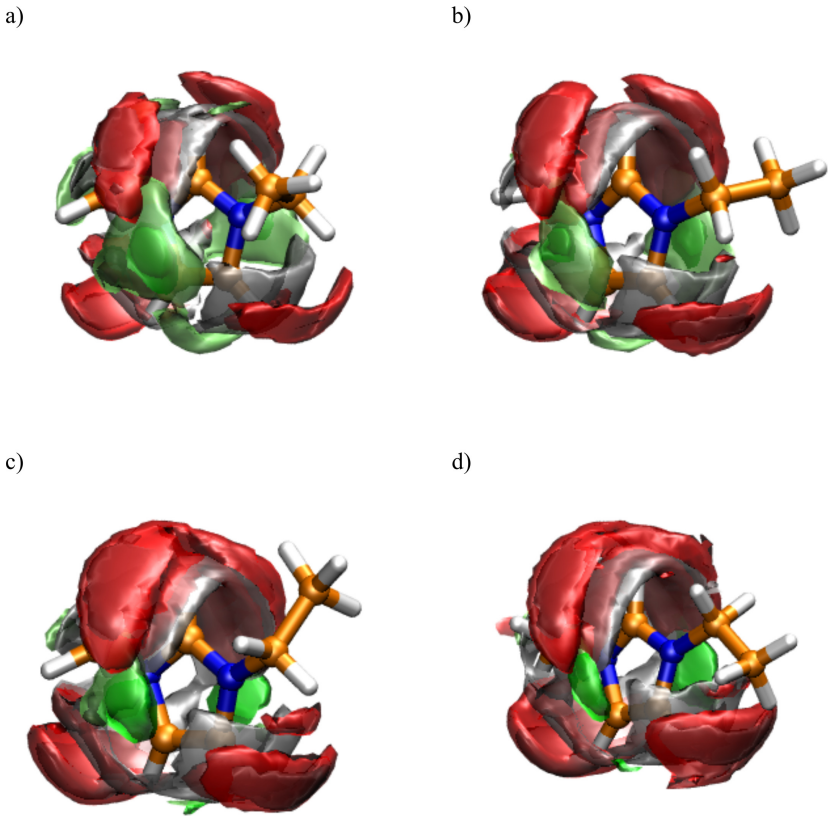

Figure 3.19: Spatial distribution functions of the oxygen atoms (gray: $O_{1,2,3}$, red: O_5), terminal atom of the anion (green) around the $[C_2C_1im]^+$ cation. (a) $[C_2C_1im][C_2SO_4]$, (b) $[C_2C_1im][C_4SO_4]$, (c) $[C_2C_1im][C_6SO_4]$ and (d) $[C_2C_1im][C_8SO_4]$. The isosurfaces represent 3 times the average density.

To characterize the length scales of the polar and nonpolar regions, we use the static partial structure factors, $s_{ij}(k)$, corresponding to the partial RDFs, $g_{ij}(r)$, defined by Fourier transform according to equation (3.2), where ρ is the number density of the atomic sites considered.

$$s_{ij}(k) = 1 + \frac{4\pi\rho}{k} \int_0^\infty [g_{ij}(r) - 1] r \sin(rk) dr \tag{3.2}$$

Recently, Bodo *et al.*[304] and Macchiagodena *et al.*[305] were able to calculate the X-ray diffraction patterns of several imidazolium-based ionic liquids using molecular simulations, using the Debye scattering equations where the atomic scattering factors for each atom contained in the system is accounted. Therefore, the structure factors obtained from equation (3.2) differ quantitatively from the

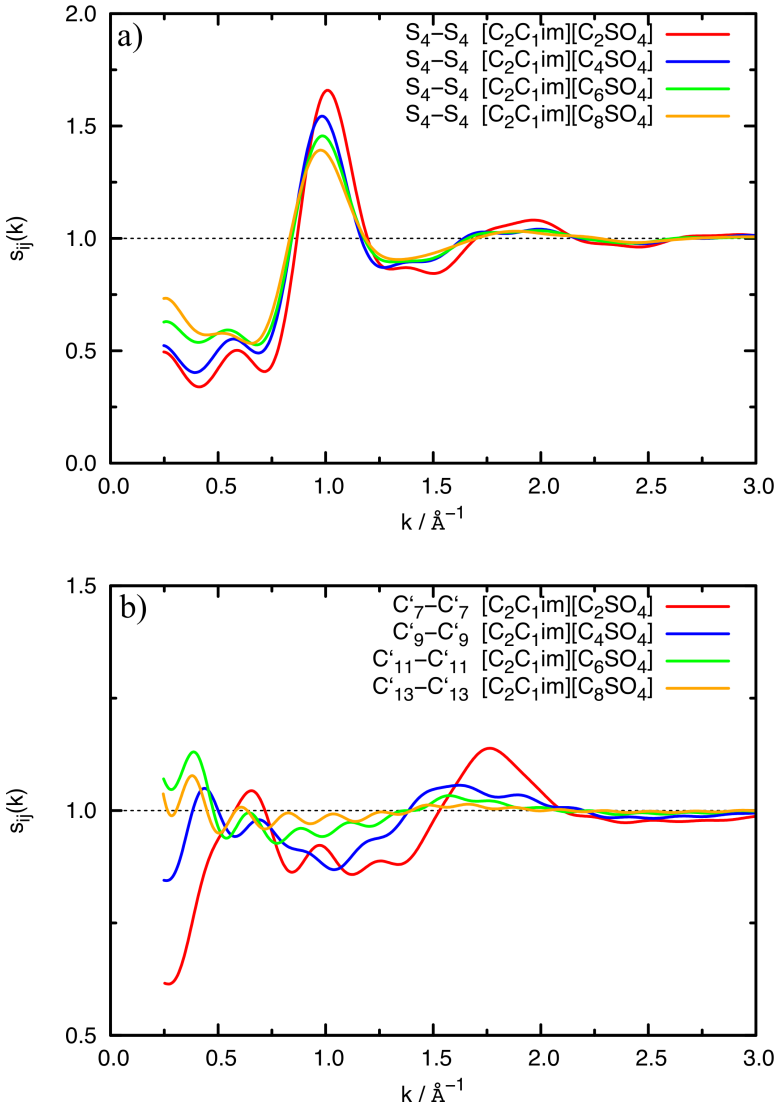

Figure 3.20: Static structure factors of representative atoms of the polar and nonpolar regions calculated from their radial distribution functions.

experimental X-ray diffraction patterns. Nevertheless, it is possible to directly compare qualitatively the result of our simulations with the experimental data obtained from X-ray measurements by Russina *et al.*[108] The results for the partial structure factors of several representative sites of the polar and nonpolar regions are presented in Figure 3.20.

Table 3.2: Length scales of the polar/nonpolar domains obtained from analysis of the static structure factors.

ionic liquid	peak wavenumber/Å^{-1}	length scale/Å
Polar Domains		
$[C_2C_1im][C_2SO_4]$	0.59	10.6
$[C_2C_1im][C_4SO_4]$	0.57	11.0
$[C_2C_1im][C_6SO_4]$	0.56	11.2
$[C_2C_1im][C_8SO_4]$	0.54	11.6
Nonpolar Domains		
$[C_2C_1im][C_2SO_4]$	0.47	13.4
$[C_2C_1im][C_4SO_4]$	0.44	14.3
$[C_2C_1im][C_6SO_4]$	0.40	15.7
$[C_2C_1im][C_8SO_4]$	0.48	16.5

It is important to point out that the features observed at the very low k range are unreliable due to the limited box size. Peaks in the structure factors at values of $k \approx 1$ Å^{-1} correspond to a wavelength of around $2\pi/1 = 6.2$ Å, *i.e.*, to the distances between successive neighbor shells in the liquid structure. The existence of prepeaks in the structure factors indicates the presence of characteristic lengths that are larger than first-neighbor ion–ion contacts. Several works using both molecular simulation[106,302] and experiments[107–110] have highlighted the existence of such prepeaks in ionic liquids with alkyl side chains of intermediate length (in both cations and anions), indicating aggregation of the chains into nonpolar domains, while the charged head groups of the ions keep in close contact. The partial structure factors concerning the sulfur atoms of the alkylsulfate anions show small peaks at about 0.54–0.60 Å^{-1}. The peak wavenumbers correspond to the length scales are presented in Table 3.2. The results suggest that the size of the polar regions are only slightly affected by the increase of the side chain of the

anion. Coulomb interactions are dominant on ionic liquids and their magnitude is only slightly dependent on the nonpolar part of the ions.[306] A slightly more interesting picture can be observed if we represent the partial structure factors of the terminal carbon atoms of the side chain of the alkylsulfate $[C_nSO_4]^-$ anion, that provide an indication of the size of the nonpolar domains. We observe the existence of a small shoulder in the structure factor of the $[C_2SO_4]^-$ at values of $k \approx 0.47$ Å^{-1}. With increasing side chains of the anion, a distinct peak appears at values of $k \approx 0.44$ Å^{-1}, for the IL with the $[C_4SO_4]^-$ anion (Table 3.2). This peak shifts to lower k values for the ILs with the $[C_6SO_4]^-$ and $[C_8SO_4]^-$ anions respectively, reflecting the size increase of the nonpolar regions in agreement with the snapshots presented in Figure 3.17. The results of our simulations are in good agreement with the experimental results obtained by Russina et al.[108] from X-ray measurements. These authors observe indications of nano-segregation for the IL $[C_2C_1im][C_2SO_4]$, in contrast with the results for different ionic liquids constituted by the same cation but different anions such as $[PF_6]^-$ or $[Tf_2N]^-$. Russina et al.[108] estimated that the size increase on the nonpolar domains was 2.03 Å/CH_2 unit. This value was comparable to the corresponding one obtained for other ILs, where the alkyl chain was bonded to the imidazolium ring of the cation.[108] The authors conclude that those values for the alkyl chain length dependence of the structural heterogeneities sizes reflect a characteristic organization of the nonpolar domains, with the alkyl chains stretching and not showing interdigitation. We observe a lower increase of the nonpolar domains size with the number of CH_2 units for the studied alkylsulfate-based ionic liquids. A similar result was observed by Canongia Lopes and Pádua[106] for the family $[C_nC_1im][PF_6]$. To better understand the morphology of the nonpolar domains, we present in Figure S1 of the Supplementary Information the radial distribution functions between the terminal carbon atoms of the anion and the other carbon atoms of the anion. We observe important peaks in the different RDFs, suggesting a complex situation. The ILs studied here do not form a clear laminar structure. These results, together with those of the X-ray experiments suggest that further investigations

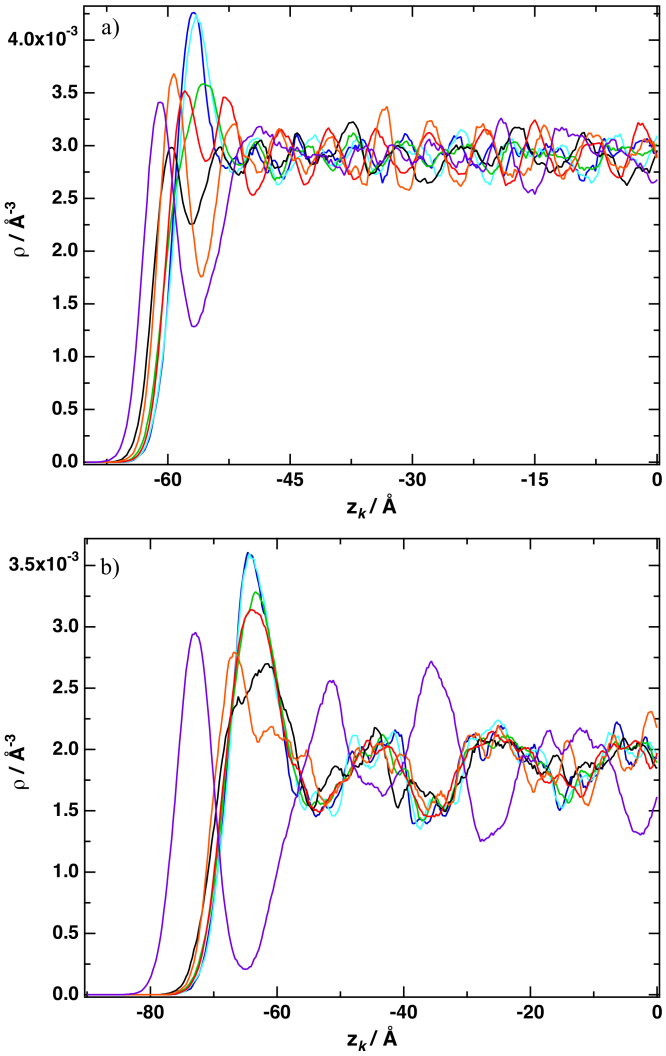

Figure 3.21: Number density profile of $[C_2C_1im][C_2SO_4]$ (upper panel) and $[C_2C_1im][C_8SO_4]$ (lower panel): blue line: C_2; cyan line: $C_{4,5}$; black line: C_7; green line: C_8; red line: $O_{1,2,3}$; orange line: O_5; purple line: C'$_7$ (panel a), C'$_1$3 (panel b).

on the structure of alkylsulfate-based ionic liquids are needed to clearly elucidate the structure of the nonpolar regions of the ILs. Computing the X-ray diffraction pattern from molecular simulation,[304,305] will allow a quantitative comparison with the experimental X-ray data to be performed; nevertheless, this aspect is beyond the scope of the present article.

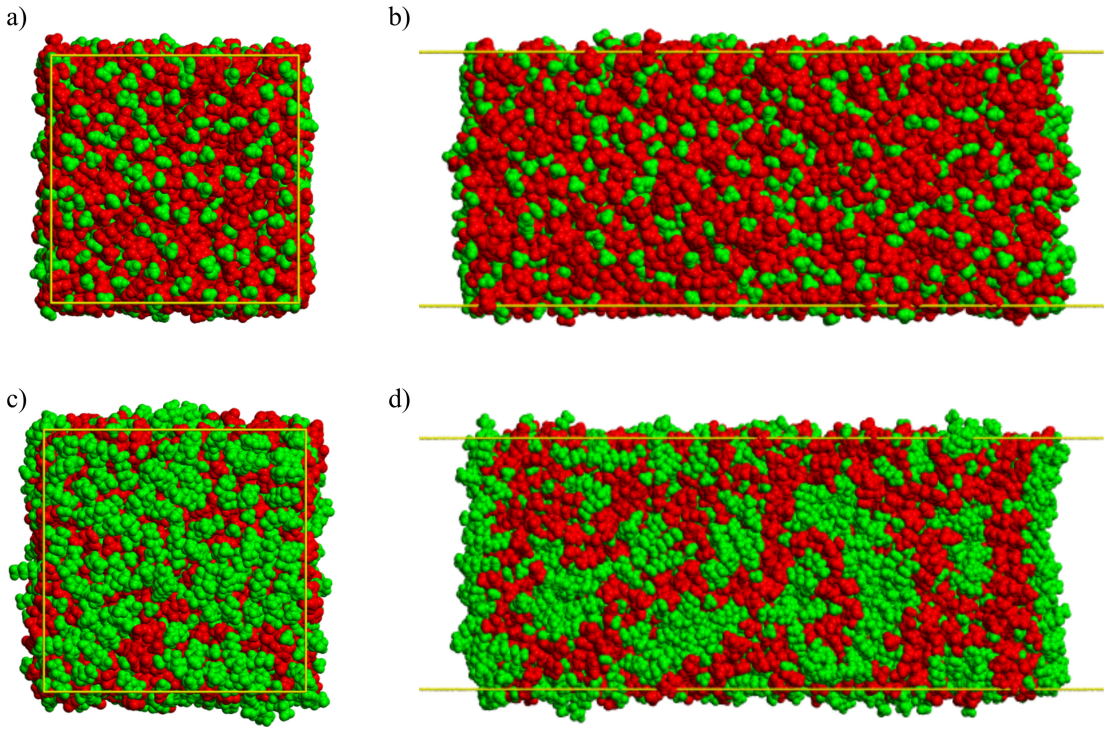

Figure 3.22: Snapshots of the simulation boxes. a) and b) $[C_2C_1im][C_2SO_4]$, c) and d) $[C_2C_1im][C_8SO_4]$.

Ionic liquid–gas interface. We present in Figure 3.21 the number density profile of the most representative atoms of the cation and anions. The alkyl side chains of both cations and anions tend to protrude toward the vacuum. An interesting feature is observed for the IL $[C_2C_1im][C_2SO_4]$, the terminal CH_3 group of the anion is found closer to the vacuum phase than that of the cation, which is found close to the bridging oxygen atom (O_5) of the anion. Low minima for the atoms of the side chain of the anion can be seen in the denser region (purple lines on panels a and b of Figure 3.21), where there is a maximum in the density of the atoms of the imidazolium rings of cation. The terminal oxygen atoms ($O_{1,2,3}$) of the anion are closer to the vacuum phase than the imidazolium ring of the cation. The increase of the side chain of the anion leads to interesting features in the liquid–vacuum interface of the IL. Thus, for $[C_2C_1im][C_8SO_4]$ we observe the existence of a layering in the ionic liquid below the surface, with significant fluctuations of the probability to find atoms belonging to the alkyl chain and to the imidazolium

ring. A similar effect was observed previously[301] for $[C_8C_1im][BF_4]$. The side chains of the $[C_8SO_4]^-$ anion protrude toward the vacuum phase, leaving the oxygen atoms of the anion and those of the $[C_2C_1im]^+$ cation in an innermost region. The different atoms of the cation are found with high probability in the same region, suggesting a flat orientation of the cation with respect to the interface. The simulation snapshot of Figure 3.22 shows a view looking down on the surface of the ionic liquids $[C_2C_1im][C_2SO_4]$ and $[C_2C_1im][C_8SO_4]$. It can be seen in panels a and c of Figure 3.22, that the alkyl chains do not cover totally the surface, for both ionic liquids, therefore, implying that the polar part of the ionic liquids are accessible from above the surface. The structures of the polar and nonpolar regions of the ionic liquid are not strongly affected by the presence of a free surface, so the ionic liquid keeps its characteristic nanoscale heterogeneity.

We present in Figure 3.23 plots of the orientational ordering parameter, defined as the average of the second Legendre polynomial:

$$\langle P_2(\theta)\rangle = \left\langle \frac{1}{2}(3cos^2\theta - 1) \right\rangle \tag{3.3}$$

In Eq. (3.3), θ is taken as the angle between a specific direction vector in the molecule-fixed frame and the surface normal z. The Legendre polynomial functions enable us to investigate the range and extent of orientation preferences at the interface. P2(θ) ranges from 1 to -0.5. A value of 1 implies that the two considered vectors are parallel, whereas a value of -0.5 indicates that they are perpendicular. We observe for both ionic liquids, $[C_2C_1im][C_2SO_4]$ and $[C_2C_1im][C_8SO_4]$, the imidazolium ring tends to adopt an orientation parallel to the interface, in agreement with the density profiles of Figure 3.21, where the different atoms of the imidazolium rings were present in the same region of the simulation box. For the IL $[C_2C_1im][C_2SO_4]$, the side chains of the cations tend to align themselves with the normal direction to the interface (the angle is lower than 30°). The side chains of the anion form, in average, an angle between 30° and 45° with the normal to the interface. For the IL $[C_2C_1im][C_8SO_4]$, the side chain of the anion forms preferentially angles lower than 30° with the normal to the interface, whereas the side chain of the cation is found preferentially forming angles around 45° with the

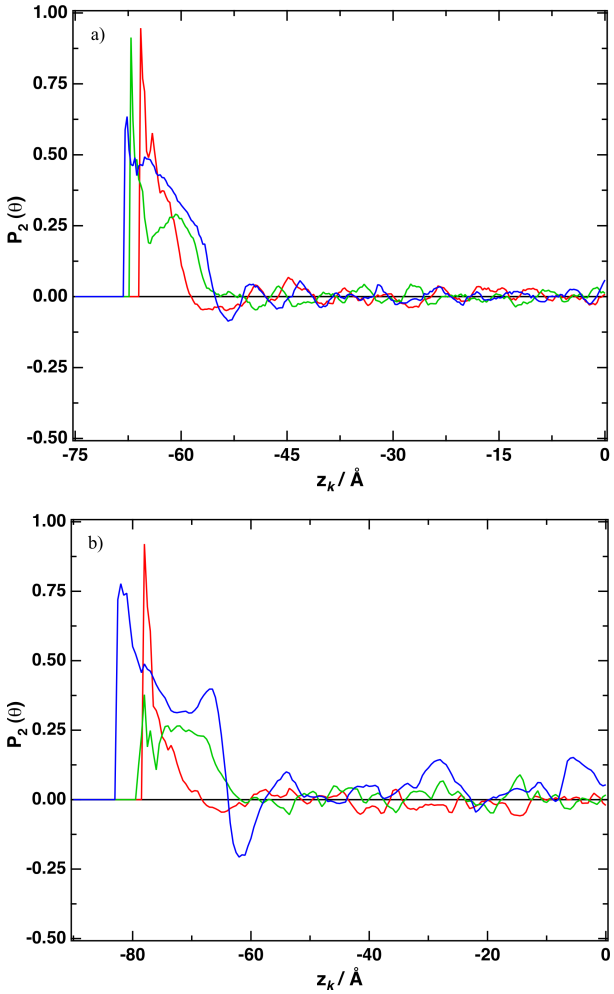

Figure 3.23: Orientational ordering parameter. θ is defined by the angle between the direction vectors and the surface normal. Red line: normal vector to the imidazolium ring; green line: N_1C_7 vector on $[C_2C_1im]^+$; blue line, upper panel: O_5C_7' vector on the $[C_2SO_4]^-$ anion; and blue line, lower panel: O_5C_{13}' vector on the $[C_8SO_4]^-$ anion.

z direction, in agreement with the density profiles presented in Figure 3.21.

From the density profiles of the different atoms of the cations and anions, it is possible to assess the charge distribution in the direction normal to the interface. Panel a of Figure 3.24 depicts the charge profile for the IL $[C_2C_1im][C_2SO_4]$ along the direction normal to the interface. We observe an excess of positive charge in the liquid phase close to the interface, followed by a region of slightly negative charge. Strong oscillations of the charge profiles are observed indicating the or-

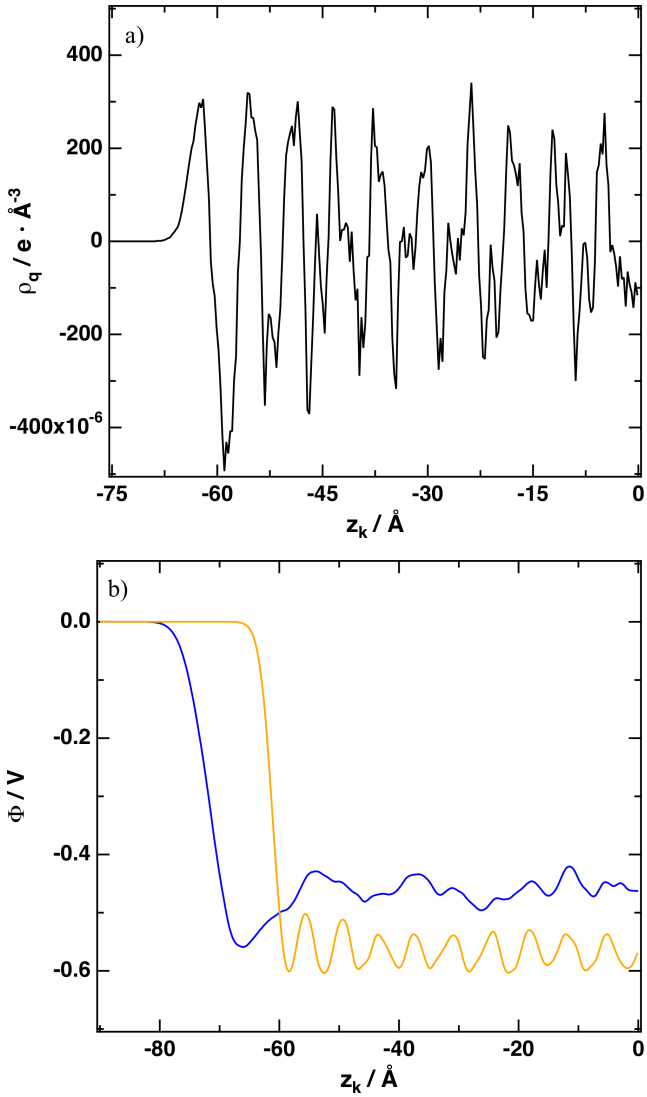

Figure 3.24: (a) Variation of the charge density for $[C_2C_1im][C_2SO_4]$. (b) Electrostatic potential for $[C_2C_1im][C_2SO_4]$: orange line and $[C_2C_1im][C_8SO_4]$: blue line.

dering effect of the interface. The fluctuations of the charge density profiles near to the interface occur in characteristic sizes smaller than the size of the single ions, showing that there is no clear electrical double layer on the liquid–vacuum interface of the ionic liquid.

According to the results of Figure 3.21, we observe that both cations and anions are present close to the surface; a weak segregation between cations and anions occurs but there is not an electrical double layer. The electrostatic potential

changes when crossing the surface of a liquid containing polar or charged entities. From the charge density profiles it is possible to evaluate the electrostatic potential Φ using the Gauss' theorem:

$$\frac{d\Phi}{dz_k} = -\frac{1}{\varepsilon_0}\int_{-\infty}^{z_k} \rho_q(z')dz' \tag{3.4}$$

where $\rho_q(z')$ is the charge density at the position z'. Panel b of Figure 3.24 shows the variation of the potential across the direction normal to the interface. Relative to the vacuum, the potential for the two considered ILs is negative, in agreement with previous results[301] for imidazolium-based ionic liquids with alkyl and hydroxyl functionalized side chains. By analyzing the dependence of the potential in the liquid with the molecular structure, we can observe in panel b of Figure 3.24 that increasing the length of the side chain leads to less negative values of the potential. Bresme *et al.*[307] considered an ionic liquid consisting of spherical rigid ions interacting through the so-called "soft primitive model" (SPM), and they observed that ion size asymmetry results in charge separation at the liquid–vapor interface and therefore in a local violation of the electroneutrality condition. The authors observed that an increase in size asymmetry results in an increase of the potential. Pensado *et al.*[301] observed in a previous work that increasing the side chain of the cation for ILs based on the $[BF_4]^-$ anion, leads to more negative values of the potential, whereas for the ILs considered in this work, increasing the side chain of the alkylsulfate anion leads to less negative values of the potential, highlighting that not only the size of the ions but also the local ordering in the interfacial region plays a major role. The local ordering of the ions at the surface, the effective packing of the anion and cation in the interfacial region, together with the molecular structure of the ions are key parameters that control the values of the electrostatic potential at the surface. Thus, it is complex to predict the behavior of the potential considering only geometrical factors such as the shape of the ions and the effective packing at the interface (how the ions are structured in the interfacial region) can play also a major role. This aspect highlights the intrinsic complexity of ionic liquids and the difficulty to rationalize their properties in terms of the molecular structure.[261]

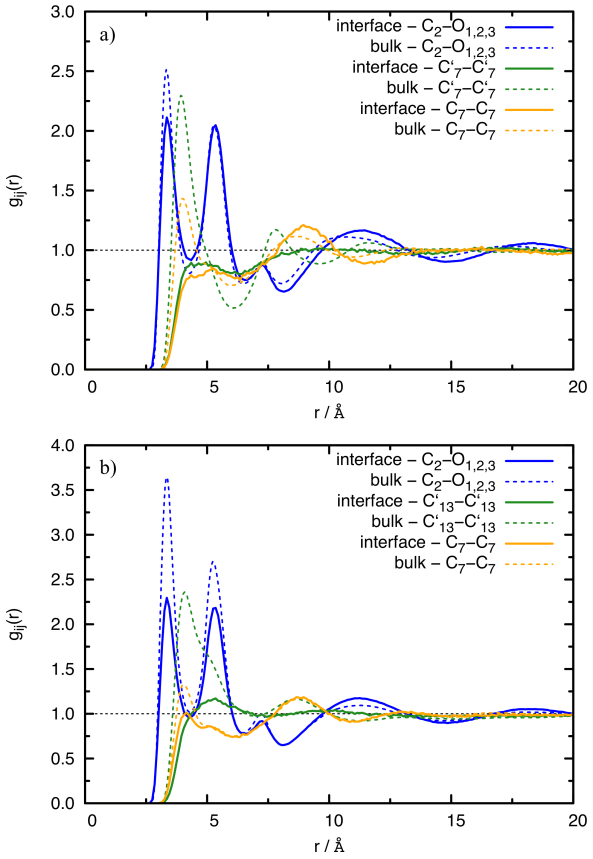

Figure 3.25: Tangential radial distribution functions (TRDF) of individual regions for several representative pairs of atoms in the interfacial (solid lines) and bulk regions (dashed lines): (a) $[C_2C_1im][C_2SO_4]$: blue line: C_2–$O_{1,2,3}$; green line: C'$_7$–C'$_7$; orange line: C_7–C_7. (b) $[C_2C_1im][C_8SO_4]$: blue line: C_2–$O_{1,2,3}$; green line: C'$_{13}$–C'$_{13}$; orange line: C_7–C_7

To analyze the effect of the explicit interface on the structure of the ionic liquids, we calculated zone-resolved tangential pair distribution functions (TRDF) that will allow us to analyze the lateral structure of the interface. The TRDFs are defined by:

$$g_{ij}(r) = \frac{\sum_{i,j} \delta(r - r_{ij})}{2\pi r dr \rho_{\text{region}} \Delta z}; \qquad z_{ij} < \Delta z \tag{3.5}$$

where ρ_{region} is the average number density in each region which normalizes the corresponding TRDF to unity at infinite distance, and $r_{ij} = (x_{ij}^2 + y_{ij}^2)^{1/2}$ is a two-dimensional distance, parallel to the plane of the surface. $\Delta z = 5$ Å is chosen to achieve significant statistical averages.

Table 3.3: Surface tension ($mN \cdot m^{-1}$) for the studied ionic liquids calculated from MD simulations using the different operational expressions at $T = 423$ K[a]

	$[C_2C_1im][C_2SO_4]$	$[C_2C_1im][C_8SO_4]$
γ_{KB}	36.6 ± 3.9	20.1 ± 2.2
γ_{IK}	34.6 ± 3.9	22.3 ± 2.4
γ_{LRC}	2.4	1.8
$\langle\gamma\rangle$	38.0 ± 3.9	23.0 ± 2.4

[a] $\langle\gamma\rangle$ is averaged over KB and IK methods

Figure 3.25 shows the TRDFs between several representative atoms of each ionic liquid. The TRDFs between the carbon atom C_2 of the imidazolium ring and the terminal oxygen atoms $O_{1,2,3}$ of the two anions are lower in the interfacial region than in the bulk region; this effect is more intense for the IL $[C_2C_1im][C_8SO_4]$. The presence of a discontinuity on the local density leads to a less ordered liquid phase near to the interface, resulting in less efficient packing of cations and anions in the interfacial region. The most remarkable feature is the loss of the correlation between the terminal carbon atoms of the alkyl chains of both cations and anions in the interfacial region. The TRDFs between the terminal atoms of the $[C_2C_1im]^+$ cations and $[C_2SO_4]^-$ anions are, in the interfacial region, lower than 1, showing the lack of correlation of the side chains, in agreement with the snapshots of the simulation box presented in Figure 3.22. For the IL $[C_2C_1im][C_8SO_4]$, we observe that the TRDF between the terminal atoms of the $[C_8SO_4]^-$ anion shows in the interfacial region a small peak at distances around 5 Å, but much lower than that observed in the bulk. The outer region of the interface is composed mainly of the side chains of the anions, but their correlation is weak.

We present in Table 3.3 the values of the surface tension for the two ionic liquids studied, using the Kirkwood–Buff and Irving–Kirkwood expressions. A good agreement between both methods is observed.

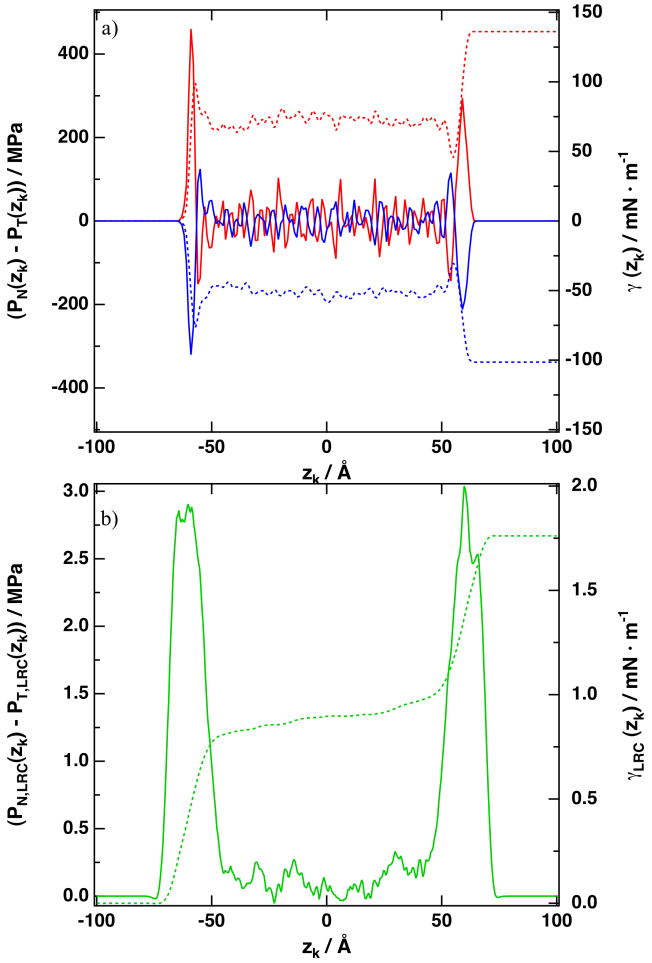

Figure 3.26: (a) $p_N(z_k) - p_T(z_k)$ for the Lennard-Jones (red curve) and the electrostatic part of the potential (blue curve) as a function of z_k for $[C_2C_1im][C_2SO_4]$. The dashed lines correspond to the integral of as a function of z (right axis); (b) $p_N(z_k) - p_T(z_k)$ for the long-range corrections as a function of z_k for $[C_8C_1im][C_8SO_4]$. The dashed lines correspond to the integral of as a function of z_k (right axis).

Panel a of Figure 3.26 shows the profiles of the surface tension for the ionic liquid $[C_2C_1im][C_2SO_4]$ across the direction normal to the interface; similar behavior is observed for the ionic liquid $[C_2C_1im][C_8SO_4]$. The contributions to the surface tension for a system in mechanical equilibrium should come from the interfacial regions and not from the isotropic bulk region, as it is pointed out in a number of molecular simulation[308–311] studies on surface tension, concerning different systems. The profiles of pseudolocal surface tension should increase in

a similar way in the two interfacial regions, and remain constant in the bulk phases, as required for a system in mechanical equilibrium. As it was observed previously for different ionic liquids,[104,301] the dispersion–repulsion contribution to the surface tension (calculated from the Irving–Kirkwood approach) is negative, whereas the electrostatic contribution is positive. Panel b of Figure 3.26 depicts the contribution of the long-range correction to the surface tension for $[C_2C_1im][C_8SO_4]$. Again, there is no contribution of the long-range correction to the surface tension coming from the bulk, since the integral of $\gamma_z(z_k)$ is flat in this region. The long-range corrections, γ_{LRC}, to the surface tension account for around 10 % of the total (see Table 3.3) and this underlines the need of considering this correction carefully. It is possible to relate the surface tension of the ionic liquids to the structure at the free surface. The ionic liquids behave as surfactants, so when the length of the alkyl side chain is increased, the more favorable configurations correspond to alkyl chains in the vacuum side, leading to a decrease in the surface tension, as observed in this work.

The force field used in this work was not adjusted to surface properties; therefore, the calculation of surface tension is also a test of the transferability of the force field. Restolho *et al.*[312] investigated the surface tension of the IL $[C_2C_1im][C_2SO_4]$ from 298 to 453 K, using the pending drop method. Yang *et al.*[313] measured the surface tension of this IL from 278.15 to 328.15 K, using the maximum bubble pressure method. Gómez *et al.*,[269] using the drop weight method, reported surface tension data for the same IL in the range of 283.15–313.15 K. Wandschneider *et al.*,[314] using the drop pending method, measured the surface tension of $[C_2C_1im][C_2SO_4]$ from 278.75 to 328.15 K, Fernández *et al.*,[315] using the drop weight method, reported values of the surface tension of this IL from 303.15 to 333.15 K. Finally, Nieto de Castro *et al.*[267] measured the surface tension from 293.15 to 332.15 K, using the Wilhelmy plate method. The results of our simulations agree with the extrapolated data with deviations of 1 %, −7 %, 2 %, 2 %, −9 % and −7 %, respectively. Hasse *et al.*[316] measured the surface tension of the $[C_2C_1im][C_8SO_4]$ at 293 K, finding a value of 31

$mN{\cdot}m^{-1}$. It is therefore not possible to compare the experimental value of the surface tension for this IL with the results of our simulations. Nevertheless, the experiments[317] show that, at constant temperature, increasing the side-chain length (anion) of the alkylsulfate-based ionic liquids based on the IL $[C_2C_1im]^+$ cation leads to a decrease of the values of the surface tension, in good agreement with our simulations. The comparison of the surface tension values calculated from molecular simulations and the experimental values allow us to conclude that the atomistic force field and the simulation techniques used in the present work are able to predict the surface tension of ionic liquids within a maximum deviation of ± 10 %.

Conclusions

Using molecular simulation we were able to explore the relation between the molecular structure of several imidazolium ionic liquids, linked with alkylsulfate anions (with different side-chain lengths) and the structure of the polar and nonpolar regions present in these ILs. The results of our simulations concerning the characteristic size of the nonpolar regions agree qualitatively with the experimental data of Russina et al.[108] using X-ray measurements. We observe that dispersion forces, correctly described with the classical force field used in this work, explain the presence of the side chain of the anion close to the imidazolium ring of the cation, this effect being less evident when the side chain of the anion increases. Using molecular simulation it is also possible to explore the structure of the ionic liquid–gas interface. We observe that the ionic liquid with long side chains behaves like a surfactant, with the side chains pointing toward the vacuum, whereas the cations adopt orientations with the imidazolium ring parallel to the surface. The values of the surface tension obtained from the simulations are in good agreement with the experimental data, and the trend of this property with the molecular structure of the ions is well reproduced. Molecular simulation can be used to assist the design of ionic liquids with specific surface properties.

Acknowledgment

This work was supported by the Spanish Science and Technology Ministry (CTQ2008-6498-C02-01 and CTQ2011-23925 projects) and the DFG, in particular by the projects KI-768/7-1 and KI-768/5-3 from the SPP-IL program. The participation of A.S.P. was made possible by a postdoctoral fellowship granted by the DFG through the SPP-IL program. Computer time from the "Centro de Supercomputación de Galicia" (CESGA) is acknowledged gratefully.

3.2.2 Bulk and Liquid–Vapor Interface of Pyrrolidinium-Based Ionic Liquids: A Molecular Simulation Study

Xavier Paredes,[†] Josefa Fernández,[†] Agílio A. H. Pádua,[‡,§] Patrice Malfreyt,[*,‡,§] Friedrich Malberg,[⊥] Barbara Kirchner[⊥] and Alfonso S. Pensado[*,†,⊥]

Received 5th July 2013, Revised 30th December 2013, Published 2nd January 2014
DOI: 10.1021/jp406651f

Own contributions to this manuscript:

- Analysis of trajectories
- Critical evaluation of the results
- Discussion of the results
- Co-writing of the manuscript

[†] *Laboratorio de Propiedades Termofísicas, Departamento de Física Aplicada, Universidade de Santiago de Compostela, E-15782 Santiago de Compostela, Spain*
[‡] *Institut de Chimie de Clermont-Ferrand, Equipe Thermodynamique et Interactions Moléculaires, Clermont Université, Université Blaise Pascal, BP 80026, 63171 Aubiere, France and CNRS, UMR6296 ICCF, BP 80026, F-63171 Aubiere, France*
[§] *CNRS, UMR6296 ICCF, BP 80026, F-63171 Aubiere, France, E-Mail: patrice.malfreyt@univ-bpclermont.fr*
[⊥] *Mulliken Center for Theoretical Chemistry, Institut für Physikalische und Theoretische Chemie, Universität Bonn, Beringstr. 4+6, D-53115 Bonn, Germany, E-Mail: alfonso.pensado@uni-leipzig.de*

Abstract Using molecular dynamics simulations we have studied the structure of three 1-butyl-1-methylpyrrolidinium ionic liquids whose anions are triflate, bis(trifluoromethanesulfonyl)imide and tris(pentafluoroethyl)trifluorophosphate. The structure of the bulk phase of the three ionic liquids has been interpreted using radial and spatial distribution functions and structure factors that allows us to characterize the morphology of the polar and nonpolar domains present in this family of liquids. The size of the polar regions depends on the anion size, whereas the morphology of the nonpolar domains is anion-independent. Furthermore, the surface ordering properties of the ionic liquids and charge and density profiles were also studied using molecular simulations. The surface tension of the liquid–vapor interfaces of these ionic liquids was also predicted from our molecular simulations. In addition, microscopic structural analysis of orientational ordering at the interface and density profiles along the direction normal to the interface suggest that the alkyl chains of the cation tend to protrude toward the vacuum, and the presence of the interface leads to a strong organization of the liquid phase in the region close to the interface. In the interfacial area, the polar regions of the ionic liquids are more structured than those in the bulk phase, whereas the opposite behavior is observed for the nonpolar regions.

Introduction

Room-temperature ionic liquids (RTILs) are defined[284] as compounds constituted solely of ions with melting points lower than 373 K. The research on ionic liquids (ILs) in its early stage was predominantly focused on their use as solvents; nowadays, their perception within the scientific community has evolved, and they are considered as tunable multipurpose materials with a great variety of applications rather than just solvents.[3–5] Many ILs present unique physicochemical properties, like very low volatility,[59–61] high electrochemical stability,[318,319] wide liquids range,[4,320] good electrical conductivity,[129,321] and excellent ability to selectively dissolve different types of compounds.[322,323] ILs can be tailored to specific applications by fine-tuning the functional groups of the weakly coordi-

nating organic cations and the inorganic/organic anion. There are many possible applications of ILs that depend upon not only the bulk properties, but also upon the IL/gas surface. The use of ILs as a medium for the synthesis of metallic nanoparticles,[93,324] electrochemical applications,[22,325] gas-storage,[326,327] lubricants[85–87] or reaction media[284,328] will be strongly influenced by a better understanding of their bulk and interfacial properties. Thus, in his recent review, Lovelock[83] emphasizes that the applications, for which there is dependence upon the interaction of different species with the IL/gas surface, cannot achieve the full extent of their potential without a profound understanding of the surface structure and properties.

A large number of studies appeared in the last years referring to imidazolium-based ILs, just because these are the materials more used by synthetic chemists. In the last years, interest on pyrrolidinium-based ILs has grown particularly amongst electrochemists due to their wider electrochemical windows[329–331] and higher electrochemical stability when compared to imidazolium-based ILs. Santos *et al.*[332] have performed a X-ray scattering study to analyze the bulk structure of the ILs $[C_nC_1pyrr][Tf_2N]$, (n = 4, 6, 8 and 10). First, sharp diffraction peaks were found for the ILs with n larger than 6; a similar behavior was observed by Russina et al.[110] for the family $[C_nC_1im][Tf_2N]$. Even if the imidazolium cation is planar and aromatic whereas the pyrrolidinium cation is nonplanar and nonaromatic, both families of ILs display remarkably similar scattering patterns. Li *et al.*[333] performed a combined study, using X-ray scattering and molecular simulation to analyze the bulk structure (and its dependence on the temperature) of the ILs $[C_nC_1pyrr][Tf_2N]$, (n = 3−10). The authors observed good agreement between the experiments and the molecular simulation. MD results highlight the existence of a first (weak) diffraction peak for n =4. Men *et al.*[334] investigated the bulk phase of seven $[C_nC_1pyrr][X]$ ILs using X-ray photoelectron spectroscopy (XPS), to elucidate the binding energy for each IL. These authors related the fact that the pyrrolidinium–based ILs have a wider electrochemical window than their imidazolium-based counterparts with the observation that the carbon atom

in position C2 of the imidazolium is more electropositive than any of the carbon atoms in the pyrrolidinium cation.

Men *et al.*[335] studied the surface chemistry of a series of four pyrrolidinium-based ILs, $[C_nC_1pyrr][Tf_2N]$ where n = 4−10, by angle resolved X-ray photoelectron spectroscopy (ARXPS), observing that as n increases, the surface composition becomes increasingly enriched with contributions from the linear alkyl substituents of the cation, which are significantly greater than those expected from the nominal stoichiometries. From inspection of this small homologous series of pyrrolidinium-based ILs, it seems that the surface structure is analogous to that of $[C_nC_1im][Tf_2N]$ samples.[98,241,336,337]

Molecular simulations have shown their ability to explore the structure of the bulk phase and the liquid–vacuum interface of ionic liquids.[104,106,283,301,302,305,338] Therefore, in this work, we present MD studies of the bulk phase and the liquid–vacuum interface of the ILs 1-butyl-1-methylpyrrolidinium triflate $[C_4C_1pyrr][CF_3SO_3]$, 1-butyl-1-methylpyrrolidinium bis(trifluoromethanesulfonyl)imide $[C_4C_1pyrr][Tf_2N]$ and 1-butyl-1-methylpyrrolidinium tris(pentafluoroethyl)trifluorophosphate $[C_4C_1pyrr][FAP]$. This set of ILs was chosen in order to understand the effect of changing the anion in the bulk phase structure, in the structure at the surface and the surface tension.

Simulation Methodology

Potential model. The ILs $[C_4C_1pyrr][CF_3SO_3]$, $[C_4C_1pyrr][Tf_2N]$ and $[C_4C_1pyrr][FAP]$ were represented by an all-atom force field,[296,306] based on the OPLS_AA framework[211,212] but developed specifically for describing ILs, the Canongia Lopes–Pádua force field (CL&P). The force field model contains the parameters required to simulate the 1-butyl-1-methylpyrrolidinium cation and the $[CF_3SO_3]$, $[Tf_2N]$ and [FAP] anions (Figure 3.27). The functional form of the force field contains four kinds of potential energy: stretching of covalent bonds, bending of valence angles, torsion around dihedral angles, and nonbonded interactions. We consider that the nonbonded interactions are active between atoms

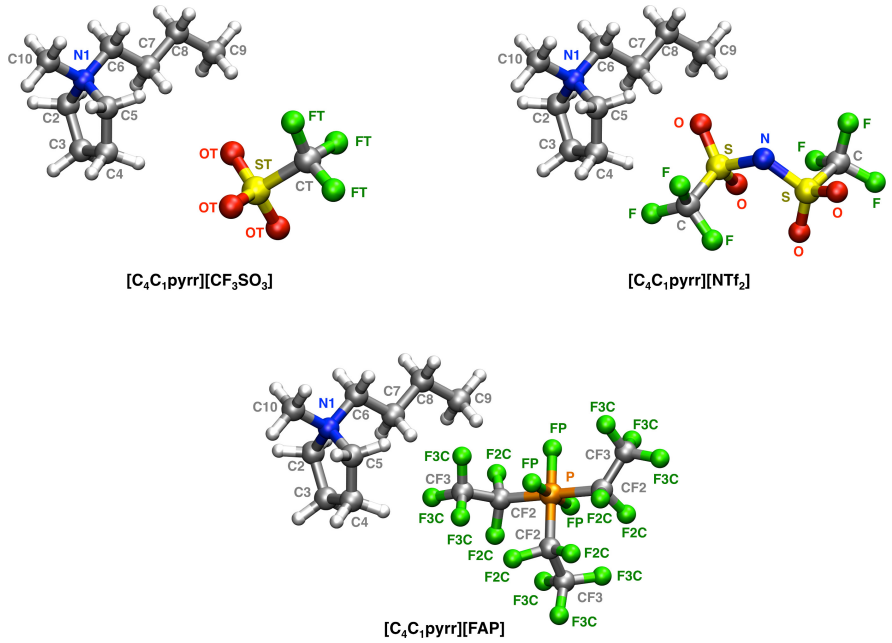

Figure 3.27: Adopted nomenclature for the sites of the ILs 1-butyl-1-methylpyrrolidinium triflate, 1-butyl-1-methylpyrrolidinium bis(trifluoromethanesulfonyl)imide and 1-butyl-1-methylpyrrolidinium tris(pentafluoroethyl)trifluorophosphate.

of the same molecule separated by more than three bonds and between atoms of different molecules. The potential energy associated with bonds and angles is described by harmonic terms, dihedral torsion energy is represented by series of cosines, and nonbonded interactions are given by the Lennard-Jones sites and by Coulomb interactions (calculated using the Ewald summation method) between partial point charges placed on the atomic sites. Further details about the description of the force field can be found elsewhere.[339] The choice of the force field is a question of paramount importance when molecular dynamics (MD) simulations are performed. The CL&P force field[339] used here was successfully used to simulate a large number of ILs, where the structure and thermodynamic properties were, in general, well-represented. Triolo and coworkers[305,338] demonstrate recently the performance of this particular force field to represent accurately the X-ray spectra of several imidazolium-based ILs; also, we have shown in previous

works[104,283,302] that the surface tension is predicted within an uncertainty of 10 % using this force field. Additionally, experimental work analyzing the structure of ILs at the liquid–vacuum interface (see the outstanding review of Lovelock[83]) shows good agreement with the simulations performed using the CL&P force field. We can conclude that there are a large number of molecular simulations using this particular force field that provide a good description of the structure and thermodynamic properties ILs, being therefore our choice fully justified.

Computational procedures. The bulk phases of the ILs $[C_4C_1pyrr][CF_3SO_3]$, $[C_4C_1pyrr][Tf_2N]$ and $[C_4C_1pyrr][FAP]$ were simulated in periodic cubic boxes containing 330, 280 and 230 ion pairs, respectively, using the MD method implemented in the DL_POLY package.[297] The initial configurations were lattices with low density. Equilibrations starting from the low-density arrangement of ions took around 2 ns, at constant NpT and T =423 K, with a timestep of 2 fs. Simulation runs of 2 ns were performed once the equilibrium density was obtained. The lengths of the sides of the simulation boxes at the final densities are around 52 Å. Additionally, for the analysis of the free surfaces of the IL, we have considered rectangular parallelepiped simulation boxes of dimensions $L_xL_yL_z$ (with $L_x = L_y$) containing 660 ion pairs of the IL $[C_4C_1pyrr][CF_3SO_3]$, 560 ion pairs of the IL $[C_4C_1pyrr][Tf_2N]$ and 460 ion pairs of the IL $[C_4C_1pyrr][FAP]$ for a total of around 25000 atoms in the simulated systems. Periodic boundary conditions were applied in the three directions of space. The direction normal to the surface of the IL was elongated (300 Å) so that the liquid slab occupies ∼120 Å in the middle of the simulation box with two equivalent liquid–vacuum interfaces. The systems were simulated via MD using the DL_POLY program[297] at 423 K. The system was coupled to Nosé–Hoover thermostats (constant NVT). The integration time step was 2 fs. Initial configurations were constructed by placing together two cubic boxes from the previous step. Equilibrations starting from this arrangement of ions took around 1 ns (NpT), after which the systems were run for 1 ns allowing the interface to equilibrate. Then, a production run of 2 ns was executed. As expected, no detectable vapor phase was observed during the

simulations. We calculated profiles of typical properties as a function of z (as the geometry of the system shows heterogeneity along the axis normal to the interface, z axis) by splitting the cell into slabs of width Δz.

Several methods can be used to compute the surface tension from molecular simulations. The methods[298–300] used most frequently consider the mechanical route definition and relate the surface tension to the components of the pressure tensor. The Kirkwood and Buff[300] (KB) expression evaluates the components of the pressure tensor as a function of the derivative of the intermolecular potential. The method proposed by Irving and Kirkwood[299] (IK) is based upon the notion of the force across a unit area and profits of expressing the local components of the pressure tensor along the direction normal to the interface. The IK approach allows us to check that the interfaces are well-stabilized and exhibit features in line with the mechanical equilibrium of planar interfaces. Full details of the calculation methods, including the treatment of long-range corrections, can be found elsewhere.[104,301]

Results and Discussion

Bulk phase. Wang and Voth,[105] using a multiscale coarse-graining (MS-CG) method, and Canongia Lopes and Pádua,[106] using an all-atom potential model, reported the existence of a nanometer-scale structuring in imidazolium-based ILs (from $[C_2C_1im]^+$ to $[C_{12}C_1im]^+$) corresponding to a segregation of polar and nonpolar domains. Triolo and coworkers[107,109–111,338,340] provided experimental evidence, using X-ray diffraction, of the existence of a nanoscale organization in the ILs of five families based in $[C_nC_1im]^+$ cations and $[PF_6]^-$, $[BF_4]^-$, $[Cl]^-$, $[Tf_2N]^-$ or $[C_mSO_4]^-$ anions. Recently, Paredes *et al.*[283] using molecular simulation have found that nanosegregation also occurs in the family $[C_2C_1im][C_nSO_4]$ (n = 2, 4, 6 and 8). This segregation into polar (ionic) and nonpolar spatial domains is important to define the solvation characteristics of ILs,[288,303] through effects of this dual structure and also through the types of interaction with polar and nonpolar solutes. Recent experimental[341] and molecular simulation investiga-

tions[302] have shown that the presence of specific functionalities in the side chain of the imidazolium cations modifies the morphology of the polar and nonpolar domains, but the characteristic nanosegregation is kept. X-ray scattering studies and molecular simulations have indicated[333] that the IL $[C_4C_1pyrr][Tf_2N]$ also presents a nanosegregation between polar and nonpolar domains. We analyze here the influence of the anion in the microscopic structure for three ILs based on the $[C_4C_1pyrr]^+$ cation. The three carbon atoms at the end of the alkyl chains of the cations, together with their bonded hydrogen atoms, constitute the regions considered to be of low charge density, whereas the atoms of the pyrrolidinium cycle plus the atoms bound to these, including the hydrogen atoms bonded to the first carbon of the alkyl chain and all the atoms of the anions, constitute the regions considered to be of high charge density. The justification for such a division is illustrated in the electrostatic surface potential plot depicted by Figure 3.28.

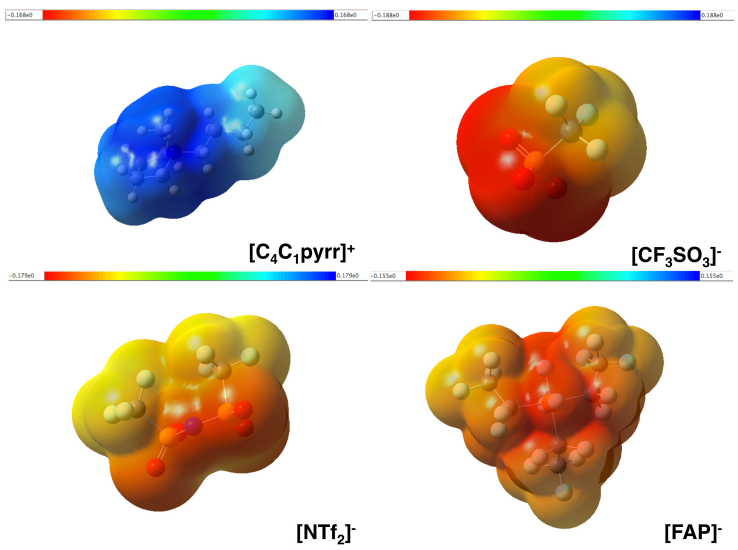

Figure 3.28: Mapping of the electrostatic potential onto an isoelectronic density surface obtained *ab initio* at the MP2 level (darker blue shades represent more positive regions, and darker red colors indicate more negative regions) in the $[C_4C_1pyrr]^+$ cation and $[CF_3SO_3]^-$, $[Tf_2N]^-$ and $[FAP]^-$ anions. Details of the calculations can be found in the literature.[296]

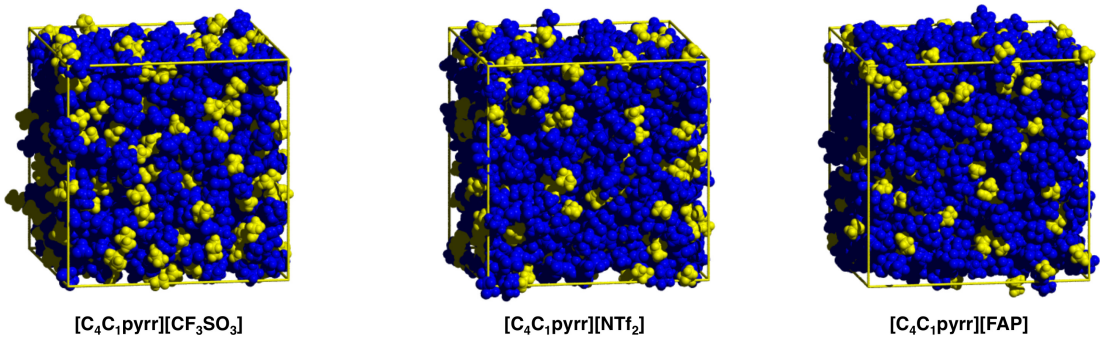

Figure 3.29: Snapshots of simulation boxes depicted using a coloring code to identify the polar (charged, depicted in blue) and nonpolar (depicted in yellow) domains that are formed in the ILs. The lengths of the boxes' sides are given: (a) $[C_4C_1pyrr][CF_3SO_3]$ $l = 51.6$ Å, (b) $[C_4C_1pyrr][Tf_2N]$ $l = 52.2$ Å, (c) $[C_4C_1pyrr][FAP]$ $l = 54.1$ Å.

The morphology of the polar and nonpolar regions for the studied pyrrolidinium-based ILs is illustrated in Figure 3.29, where the high charged regions are colored in blue and low-charge density regions are yellow. It is clear that the tail groups aggregate and form several spatially heterogeneous domains. The relative sizes of the nonpolar domains in the three ILs analyzed remain unchanged, whereas the size of the polar domains is strongly affected by the anion (Figure 3.29). A quantitative description of the nanostructure of the studied ILs can be performed by means of the radial distribution functions (RDFs) and static structure factors. Figure 3.30 depicts the RDFs between several representative atoms of the anions and cations, which show several remarkable features. We observe a strong correlation between the nitrogen atom of the pyrrolidinium cation and the anions, especially with $[CF_3SO_3]^-$ and $[Tf_2N]^-$, for which the coordination to the cation (see panels a-d of Figure 3.30) occurs preferentially via the oxygen atoms of the anions (these atoms carry the most negative charge).

The situation is slightly more complex in the case of the $[FAP]^-$ anion, for which the coordination occurs preferentially via the fluoride atoms directly bonded to the phosphorus and also via the terminal fluoride atoms of the perfluoroethyl chains. The peaks in the RDFs are more intense in the case of the IL

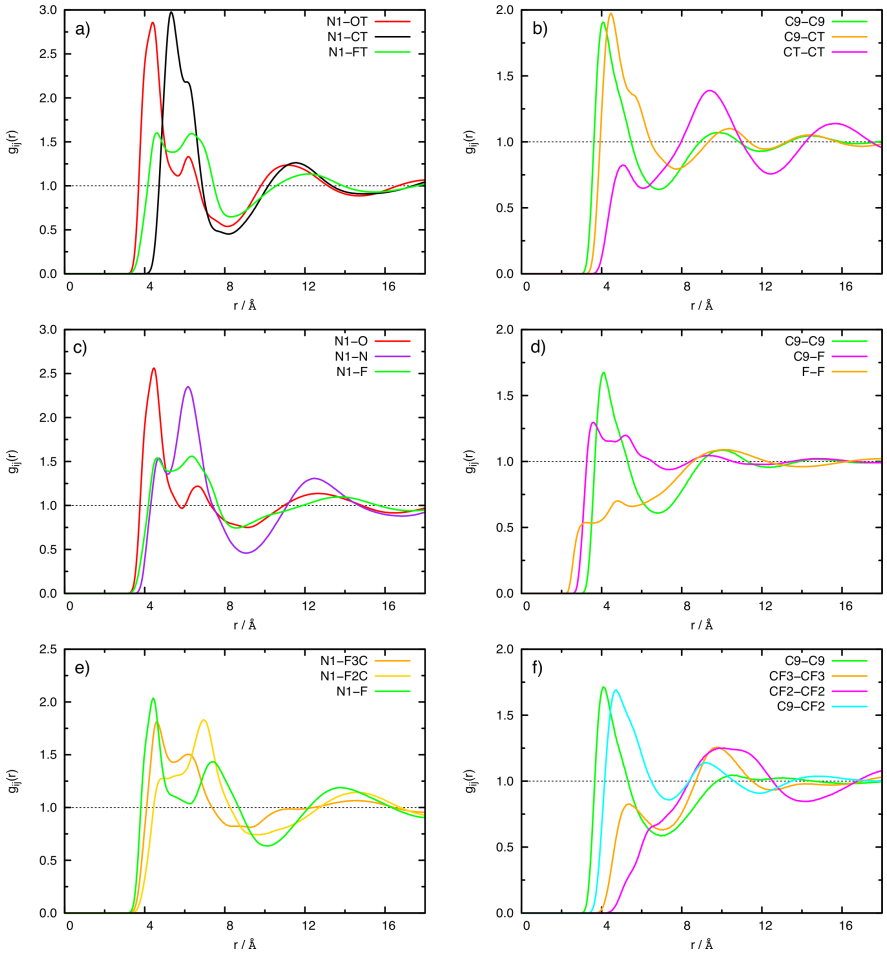

Figure 3.30: Site–site RDFs between several representative atoms of the cations and anions: (a,b) 1-butyl-1-methylpyrrolidinium triflate, (c,d) 1-butyl-1-methylpyrrolidinium bis(trifluoromethanesulfonyl)imide and (e,f) 1-butyl-1-methylpyrrolidinium tris(pentafluoroethyl)trifluorophosphate. For nomenclature, please refer to Figure 3.27.

$[C_4C_1pyrr][CF_3SO_3]$; the small size of the anions makes them easier to be closely packed in the neighborhood of the cation. Nevertheless, an interesting feature appears when the second solvation shell is observed, namely, the position of the second peak in the RDFs is shifted toward larger distances when the size of the anion is increased. Another interesting feature is that the terminal atoms of the $[C_4C_1pyrr]^+$ cations are found with a high probability at close distances from each other, which is a sign of alkyl chain aggregation. The position of the peak

Table 3.4: Length scales of the polar/nonpolar domains obtained from analysis of the static structure factors.

IL	peak wavenumber/Å^{-1}	length scale/Å
Polar Domains		
$[C_4C_1pyrr][CF_3SO_3]$	0.95	6.6
	0.50	12.6
$[C_4C_1pyrr][Tf_2N]$	0.84	7.5
	0.43	15.1
$[C_4C_1pyrr][FAP]$	0.78	8.1
	0.32	19.6
Nonpolar Domains		
$[C_4C_1pyrr][CF_3SO_3]$	0.56	11.2
$[C_4C_1pyrr][Tf_2N]$	0.64	9.8
$[C_4C_1pyrr][FAP]$	0.61	10.3

is almost unaffected when the size of the anion increases; its intensity follows the trend $[C_4C_1pyrr][CF_3SO_3] > [C_4C_1pyrr][Tf_2N] \approx [C_4C_1pyrr][FAP]$. Even in the case of the voluminous $[FAP]^-$ anion the nonpolar chains of the cations stick together, forming the nonpolar domains visualized in the snapshots of Figure 3.29.

To characterize the length scales of the polar and nonpolar regions, we can use the static partial structure factors, $s_{ij}(k)$ corresponding to the partial RDFs, $g_{ij}(r)$, that are defined by a Fourier transform according to equation (3.6), where ρ is the number density of the atomic sites considered.

$$s_{ij}(k) = 1 + \frac{4\pi\rho}{k} \int_0^\infty [g_{ij}(r) - 1] r \sin(rk) dr \tag{3.6}$$

The results for the partial structure factors of several representative sites of the polar and nonpolar regions are presented in Figure 3.31. Concerning the structure factors of the terminal carbon atom of the side chain, the most remarkable

features are the strong peaks in the region between 0.56 and 0.64 $Å^{-1}$. The peak wavenumbers corresponding to the length scales are presented in Table 1. The results suggest that the sizes of the nonpolar regions are only slightly affected by the increase of the size of the anion. A slightly more interesting picture can be observed if we represent the partial structure factors of the nitrogen atom of the pyrrolidinium cation. We observe the existence of a first peak at 0.95 $Å^{-1}$ corresponding to a wavelength $\lambda = 6.6$ Å for the IL $[C_4C_1pyrr][CF_3SO_3]$, at 0.84 $Å^{-1}$ ($\lambda = 7.5$ Å) for the IL $[C_4C_1pyrr][Tf_2N]$ and at 0.78 $Å^{-1}$ ($\lambda = 8.1$ Å) for the IL $[C_4C_1pyrr][FAP]$, reflecting the characteristic distances between successive neighboring shells in the liquid structure, which depend on the type of anion, as previously was pointed out experimentally by Russina *et al.*[110] The existence of prepeaks in the structure factors indicates the presence of characteristic lengths that are larger than first-neighbor ion–ion contacts. ILs with alkyl side chains of intermediate length show the presence of such prepeaks, as it was previously observed[107,109–111,305,338,340–349] using both experiments and molecular simulation. Such prepeaks, whose origin has been analyzed recently in great detail,[346,347] indicate the aggregation of the chains into nonpolar domains, while the charged head groups of the ions keep in close contact. Margulis and coworkers have extensively studied the origin of such prepeaks.

Panel (a) of Figure 3.31 shows secondary peaks at 0.5 $Å^{-1}$ corresponding to a wavelength of around 12.6 Å for the IL $[C_4C_1pyrr][CF_3SO_3]$, peaks at 0.43 $Å^{-1}$ ($\lambda = 15.1$ Å) for the IL $[C_4C_1pyrr][Tf_2N]$ and peaks at 0.32 $Å^{-1}$ ($\lambda = 19.6$ Å) for the IL $[C_4C_1pyrr][FAP]$. The polar domain length scales in the investigated ILs are quantitatively different, as can be visualized by comparing the results of Figure 3.31 with the snapshots of Figure 3.29. The different morphology of the nanoscale domains in these ILs can influence the solvation of different species and, therefore, probably also the performance of these liquids as reaction or separation media. The results for the IL $[C_4C_1pyrr][Tf_2N]$ presented here agree quantitatively with the molecular simulation results of Li *et al.*[333]

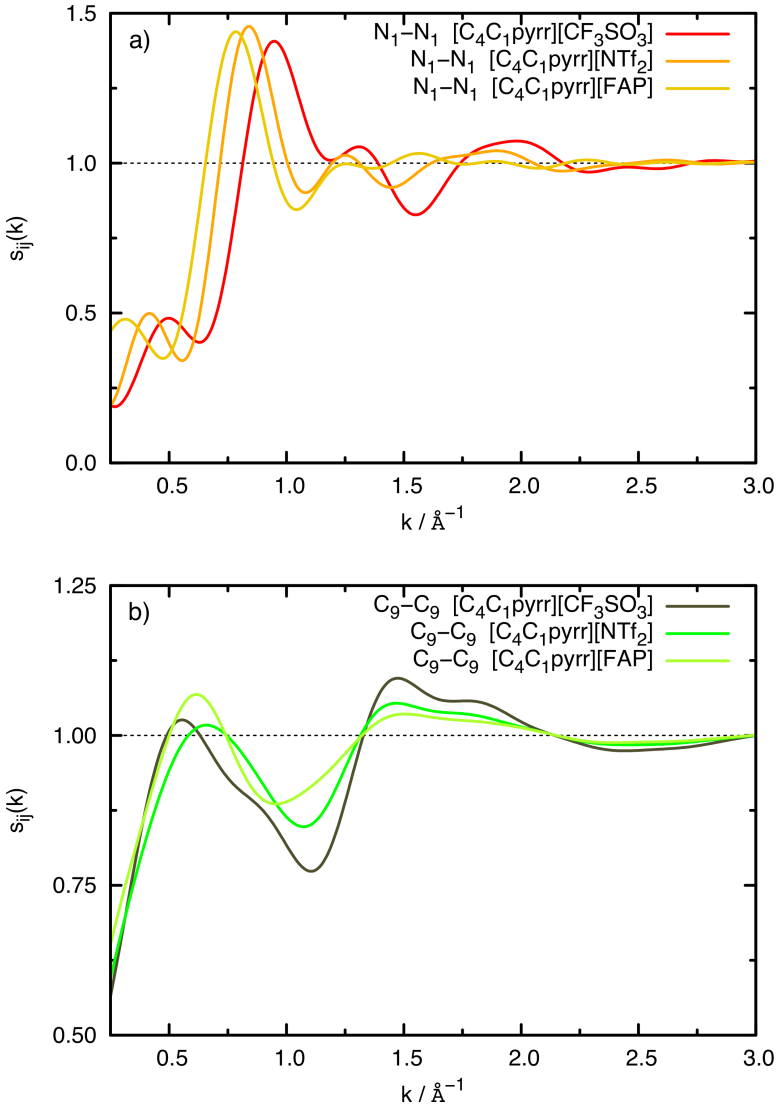

Figure 3.31: Static structure factors of representative atoms of the (a) polar and (b) nonpolar regions calculated from RDFs.

IL–Gas interface. Figure 3.32 depicts the number density profile of the most representative atoms of the cation and anions. The alkyl side chains of the cations tend to protrude toward the vacuum, in agreement with experimental results.[335,350,351] Deep minima for the number density of the atoms of the side chain are observed in the denser region (this aspect is less marked in the case of the IL $[C_4C_1pyrr][FAP]$). The oxygen atoms of the $[CF_3SO_3]^-$ and $[Tf_2N]^-$ anions (those atoms carry the most negative charge on the anion) are found in the same

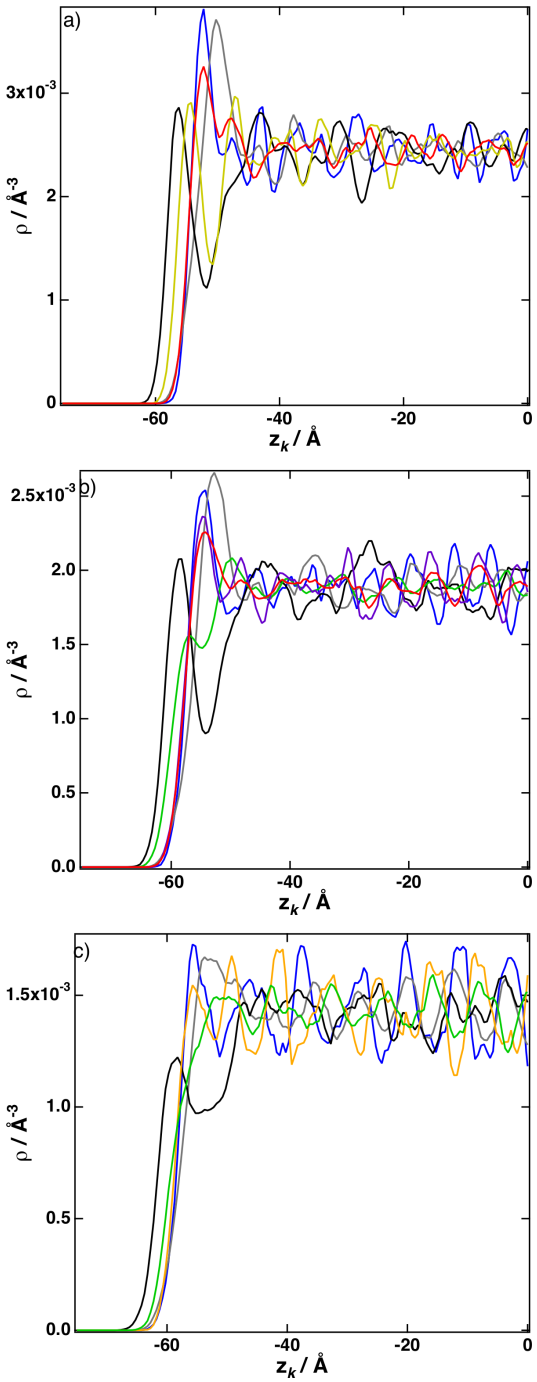

Figure 3.32: Number density profile of (a) $[C_4C_1pyrr][CF_3SO_3]$: blue line: N1; gray line: C3,4; black line: C9; yellow line: CT; red line: OT; (b) $[C_4C_1pyrr][Tf_2N]$: blue line: N1; gray line: C3,4; black line: C9; green line: F; purple line: N; red line: O; and (c) $[C_4C_1pyrr][FAP]$: blue line: N1; grey line: C3,4; black line: C9; green line: CF3; orange line: P.

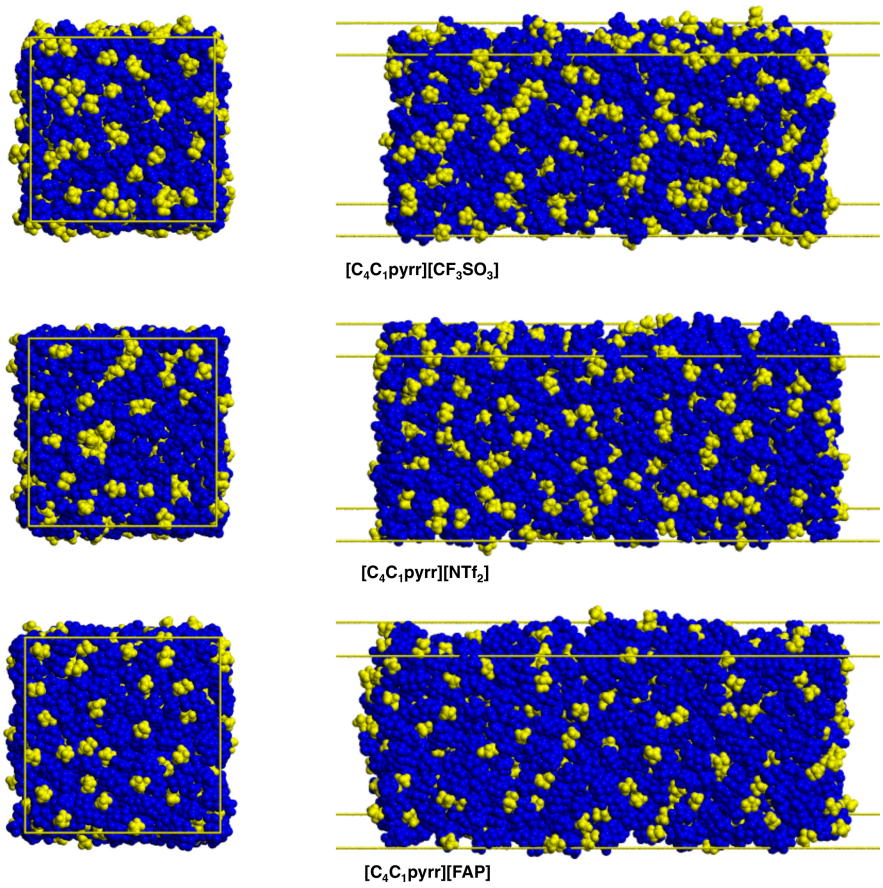

Figure 3.33: Snapshots of the simulation boxes. The high-charged regions are represented in blue and the low-charged regions in yellow.

region as the pyrrolidinium ring. The terminal CF_3 groups of the $[CF_3SO_3]^-$ point also toward the vacuum. Concerning the $[Tf_2N]^-$ anion, the fluorine atoms are the outermost ones, whereas the nitrogen atoms are placed deeper into the liquid. Some remarkable features are observed for the IL $[C_4C_1pyrr][FAP]$: (i) The local density of the side chains of the cation in the most outer region is much lower than for the other studied ILs. (ii) A denser subsurface region as clearly appears in the case of the ILs $[C_4C_1pyrr][CF_3SO_3]$ and $[C_4C_1pyrr][Tf_2N]$ is not observed for the IL based on the $[FAP]^-$ anion. (iii) The different atoms of the bulk $[FAP]^-$ anion are present in the interfacial region. This can be related to the hydrophobic character of the anion and to the difficulty to compactly pack such voluminous anion at the interface. The simulation snapshot of the left side of Figure 3.33

shows a view looking onto the surface of the studied ILs. It can be seen that the alkyl chains do not cover the surface completely for the three ILs. This implies, therefore, that the polar parts of the ILs are accessible from above the surface, with this effect being more intense when the size of the anion increases. The structure of the polar and nonpolar regions of the IL is not strongly affected by the presence of a free surface;[104,283,301] therfore, the IL keeps its characteristic nanoscale heterogeneity.

Figure 3.34 depicts the plots of the orientational ordering parameter, defined as the average of the second Legendre polynomial

$$\langle P_2(\theta) \rangle = \left\langle \frac{1}{2}(3cos^2\theta - 1) \right\rangle \tag{3.7}$$

In eq (3.7), θ is taken as the angle between a specific direction vector in the molecule-fixed frame and the surface normal z. The Legendre polynomial functions enable us to investigate the range and extent of orientation preferences at the interface. $P_2(\theta)$ ranges from 1 to -0.5. A value of 1 implies that the two considered vectors are parallel, whereas a value of -0.5 indicates that they are perpendicular. We observe that the pyrrolidinium ring adopts in the three investigated ILs preferential orientations perpendicular to the interface, confirming the results presented in the density profiles in Figure 3.32 (the nitrogen atom N1 is located closer to the vacuum–liquid surface than the atoms C3,4). Nevertheless, for the IL $[C_4C_1pyrr][FAP]$, the structure at the vacuum–liquid interface is less ordered than that for the other two investigated ILs, in agreement with the previous results for the density profiles. The presence of a bulky, voluminous anion strongly distorts the ordering in the IL caused by the presence of an explicit interface. The side chains of the cations form, on average, an angle between 25 and 40° with the normal to the interface, in good agreement with the observations of Aliaga et al.[351] using sum frequency generation experiments. The analysis of the preferential orientation of the different anions shows several remarkable features. The ST–CT vector of the $[CF_3SO_3]^-$ forms an angle of around 30° with the normal vector to the surface.

The S–S vector of the $[Tf_2N]^-$ anion is orientated forming an angle of 60° with

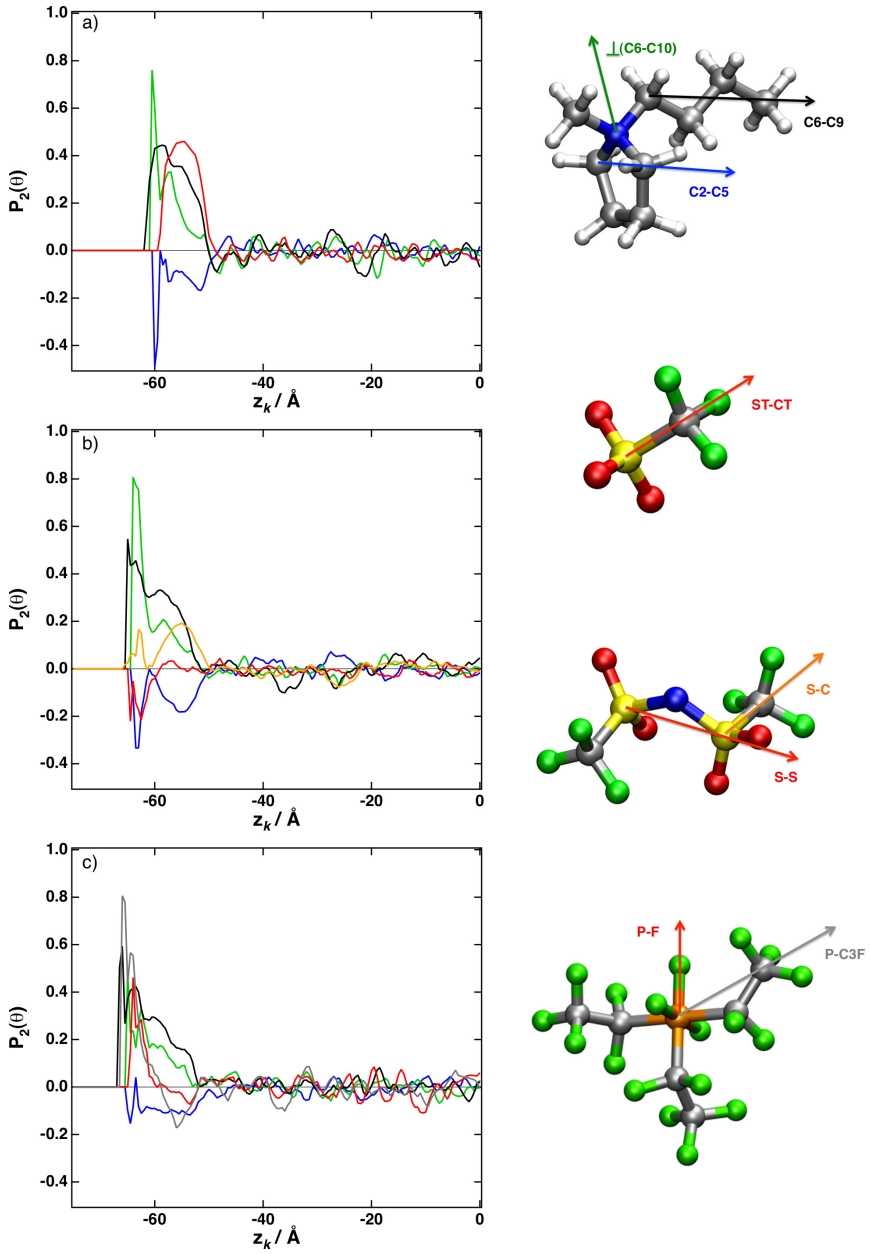

Figure 3.34: Orientational ordering parameter. θ is defined by the angle between the directional vectors and the surface normal. Blue line, C2–C5 vector of the $[C_4C_1pyrr]^+$ cation; green line, vector perpendicular to (C6–C10) pointing in the direction of N1 of the $[C_4C_1pyrr]^+$ cation; black line, C6–C9 vector of the $[C_4C_1pyrr]^+$ cation. (a) $[C_4C_1pyrr][CF_3SO_3]$: red line, ST–CT vector of the $[CF_3SO_3]^-$. (b) $[C_4C_1pyrr][Tf_2N]$: red line, S–S of the $[Tf_2N]^-$ anion; orange line, S–C of the $[Tf_2N]^-$ anion. (c) $[C_4C_1pyrr][FAP]$: red line, P–F vector of the $[FAP]^-$ anion; gray line, P–C3F vector of the $[FAP]^-$ anion.

the normal vector to the surface, in good agreement with previous results[352] for several ILs linked to the $[Tf_2N]^-$ anion. For the $[FAP]^-$ anion, the vector connecting the phosphorous and the fluoride atoms, and the vector P–C3F show preferential orientations with angles between 20 and 40° with the normal vector to the surface, highlighting that different orientations of the anion are present, which results on a more disordered structure at the vacuum–liquid surface.

The charge density profiles for $[C_4C_1pyrr][CF_3SO_3]$ (Figure 3.35a) and $[C_4C_1pyrr][Tf_2N]$ (Figure 3.35b) exhibit a high peak at the interface for both ions, which indicates that the charge for both the cation and anion is enhanced at the interfacial region. This peak in the interfacial region is lower for the IL $[C_4C_1pyrr][FAP]$. For all the studied ILs, there is a small excess of negative charge in the outermost interfacial region. The fluctuations of the charge density profiles in the interfacial region occur in typical sizes smaller than the size of the single ions, showing that there is no electrical double layer of the size of the ions on the liquid–vacuum interface of the IL; just a weak segregation between cations and anions occurs at the interface. The electrostatic potential changes when crossing the surface of a liquid containing polar or charged entities. From the charge density profiles it is possible to evaluate the electrostatic potential Φ using the Gauss theorem:

$$\frac{d\Phi}{dz_k} = -\frac{1}{\varepsilon_0}\int_{-\infty}^{z_k} \rho_q(z')dz' \tag{3.8}$$

where $\rho_q(z')$ is the charge density at the position z'. Panel (d) of Figure 9 shows the variation of the potential across the direction normal to the interface. Bresme *et al.*[307] considered an IL consisting of spherical rigid ions interacting through the so-called "soft primitive model" (SPM), and they observed that ion size asymmetry results in charge separation at the liquid–vapor interface and therefore in a local violation of the electroneutrality condition. The authors observed that an increase in size asymmetry results in an increase of the potential. The electrostatic potential[104] for $[C_6C_1im][Tf_2N]$ is ∼0.2 V. For $[C_2C_1im][BF_4]$, $[C_2OHC_1im][BF_4]$, $[C_2C_1im][BF_4]$ and $[C_2OHC_1im][BF_4]$ the potential[301] ranges from −0.15 to −0.35 V. For $[C_2C_1im][C_2SO_4]$ the electrostatic potential[283] is around −0.45 V whereas for $[C_2C_1im][C_8SO_4]$ is around −0.55 V. Relative to

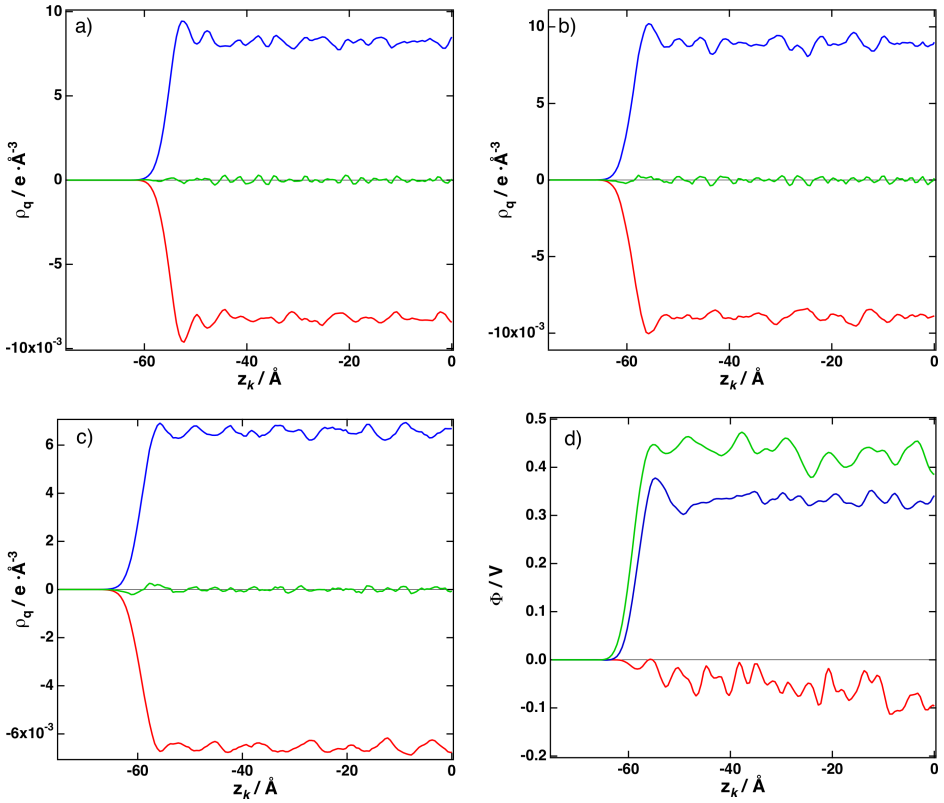

Figure 3.35: Charge density profiles for (a) $[C_4C_1pyrr][CF_3SO_3]$, (b) $[C_4C_1pyrr][Tf_2N]$ and (c) $[C_4C_1pyrr][FAP]$. Blue curves correspond to the cation, red curves to the anions, and green curves to the sum of these two contributions. (d) Electrostatic potential for $[C_4C_1pyrr][CF_3SO_3]$: red line; $[C_4C_1pyrr][Tf_2N]$: blue line; $[C_4C_1pyrr][FAP]$: green line.

the vacuum, the potential for $[C_4C_1pyrr][Tf_2N]$ and $[C_4C_1pyrr][FAP]$ is positive, whereas for $[C_4C_1pyrr][CF_3SO_3]$ the potential is compatible with zero. The results presented here, together with those previously obtained for other ILs, suggest that the electrostatic potential can be adjusted by selecting a combination of cation and anion, the influence of the selected anion being larger. It is clear that the local ordering of the ions at the surface, the effective packing of the anion and cation in the interfacial region, together with the molecular structure of the ions are key parameters that control the values of the electrostatic potential at the surface.

To analyze the effect of the explicit interface on the structure of the ionic liquids, we calculated zone-resolved tangential pair distribution functions (TRDF) that will allow us to analyze the lateral structure of the interface. The TRDFs are defined by

$$g_{ij}(r) = \frac{\sum_{i,j} \delta(r - r_{ij})}{2\pi r dr \rho_{\text{region}} \Delta z}; \qquad z_{ij} < \Delta z \tag{3.9}$$

where ρ_{region} is the average number density in each region which normalizes the corresponding TRDF to unity at infinite distance, and $r_{ij} = (x_{ij}^2 + y_{ij}^2)^{1/2}$ is a two-dimensional distance, parallel to the plane of the surface. $\Delta z = 5$ Å is chosen to achieve significant statistical averages.

Figure 3.36 depicts the TRDFs between several representative atoms of the investigated IL. The TRDFs between the nitrogen atom N1 of the pyrrolidinium ring and the oxygen atoms of the $[CF_3SO_3]^-$ anion are quite similar in the interfacial region and in the bulk; just the second peak in the TRDF at the interface is larger than in the bulk. We observe that the TRDFs between the nitrogen atom N1 of the pyrrolidinium ring and the oxygen atoms of the $[Tf_2N]^-$ anion and the fluorine atom and the terminal carbon atom of the perfluoroethyl chain of the $[FAP]^-$ anion present higher peaks in the interfacial region compared with the bulk, suggesting a more ordered liquid phase in the interfacial region. The most remarkable feature is the loss of the correlation in the interfacial region between the terminal carbon atoms of the alkyl side chains of the cations and also between the perfluoroalkyl chains of the anions. The outer region of the interface is composed mainly of the side chains of the anions, but their correlation is weak, as can be also observed in the snapshots of the simulation boxes presented in Figure 3.33.

The values of the surface tension for the three considered ILs are presented in Table 3.5 and are calculated using the KB[300] and IK[299] expressions. Both methods provide results that are in quite good agreement. Panel (a) of Figure 3.37 shows the profiles of the surface tension for the IL $[C_4C_1pyrr][Tf_2N]$ across the direction normal to the interface; similar behavior is observed for the other two ILs. The contributions to the surface tension for a system in mechanical equi-

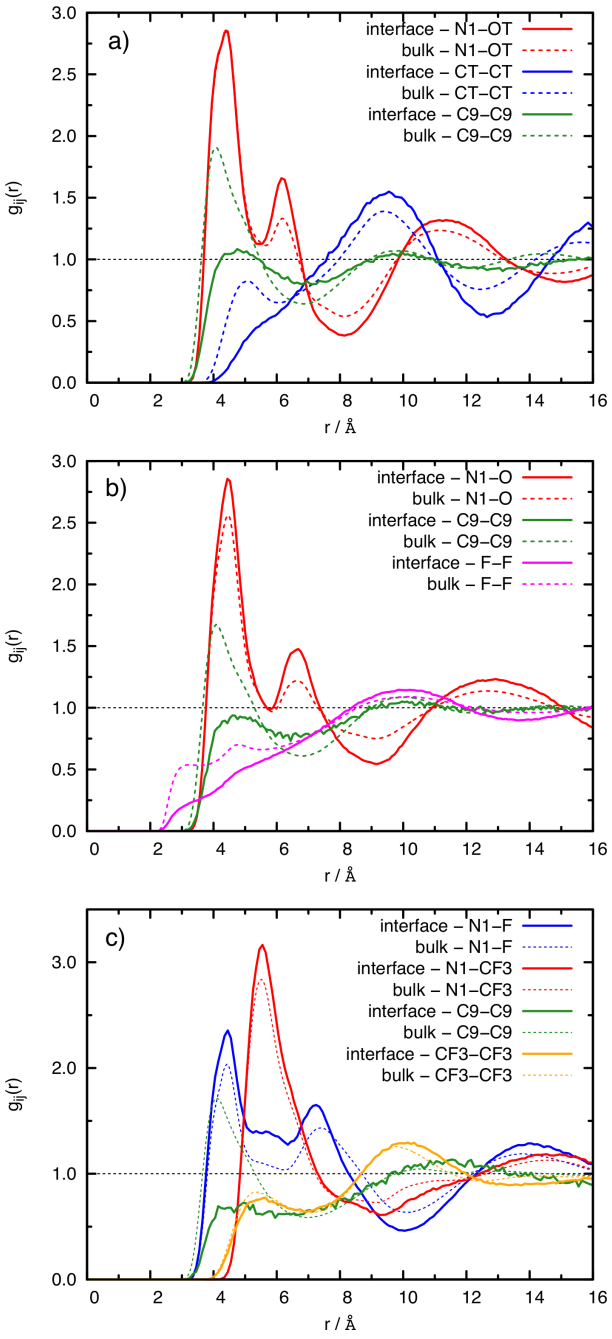

Figure 3.36: Tangential radial distribution functions (TRDFs) of individual regions for several representative pairs of atoms in the interfacial (solid lines) and bulk regions (dashed lines). (a) $[C_4C_1pyrr][CF_3SO_3]$: red line, N1–OT; green line, C9–C9; blue line, CT–CT. (b) $[C_4C_1pyrr][Tf_2N]$: red line, N1–OT; green line, C9–C9; magenta line, F–F. (c) $[C_4C_1pyrr][Tf_2N]$: red line, N1–CF3; blue line, N1–F; green line, C9–C9; orange line, CF3–CF3.

Table 3.5: Surface tension ($mN \cdot m^{-1}$) for the studied ILs calculated from MD simulations using the different operational expressions at $T = 423$ K[a]

	$[C_4C_1pyrr][CF_3SO_3]$	$[C_4C_1pyrr][Tf_2N]$	$[C_4C_1pyrr][FAP]$
γ_{KB}	29.1 ± 3.5	30.3 ± 3.6	30.6 ± 3.7
γ_{IK}	27.5 ± 3.3	28.9 ± 3.5	30.2 ± 3.6
γ_{LRC}	1.95	1.9	1.87
$\langle\gamma\rangle$	30.3 ± 3.5	31.5 ± 3.6	32.3 ± 3.7

[a] $\langle\gamma\rangle$ is averaged over KB and IK methods

librium should come from the interfacial regions and not from the isotropic bulk region.[308–311] As is required for a system in mechanical equilibrium, the profiles of pseudolocal surface tension should increase in a similar way in the two interfacial regions and remain constant in the bulk phase. The dispersion–repulsion contribution to the surface tension (calculated from the IK approach) is negative, whereas the electrostatic contribution is positive, a common behavior of ILs. We present in panel (b) of Figure 3.37 the contribution of the long-range correction to the surface tension for $[C_4C_1pyrr][CF_3SO_3]$. Again, there is no contribution of the long-range correction to the surface tension coming from the bulk because the integral of $\gamma_z(z_k)$ is flat in this region. The long-range corrections,[353] γ_{LRC}, to the surface tension account for around 10 % of the total value (see Table 3.5), and this underlines the need of considering this correction carefully. It is possible to relate the surface tension of the ILs to the structure at the free surface. The force field used in this work was not adjusted to surface properties; therefore, the calculation of surface tension is also a test of the transferability of the force field.

Fletcher *et al.*[354] have measured the surface tension of the IL $[C_4C_1pyrr][FAP]$ at 293 K using the Du Noüy ring, finding a value of 38 $mN \cdot m^{-1}$. Kolbeck *et al.*[355] investigated the surface tension of the IL $[C_4C_1pyrr][Tf_2N]$ from 293 to 298 K using the pending drop method, obtaining values in the range 32.7–32.3 $mN \cdot m^{-1}$.

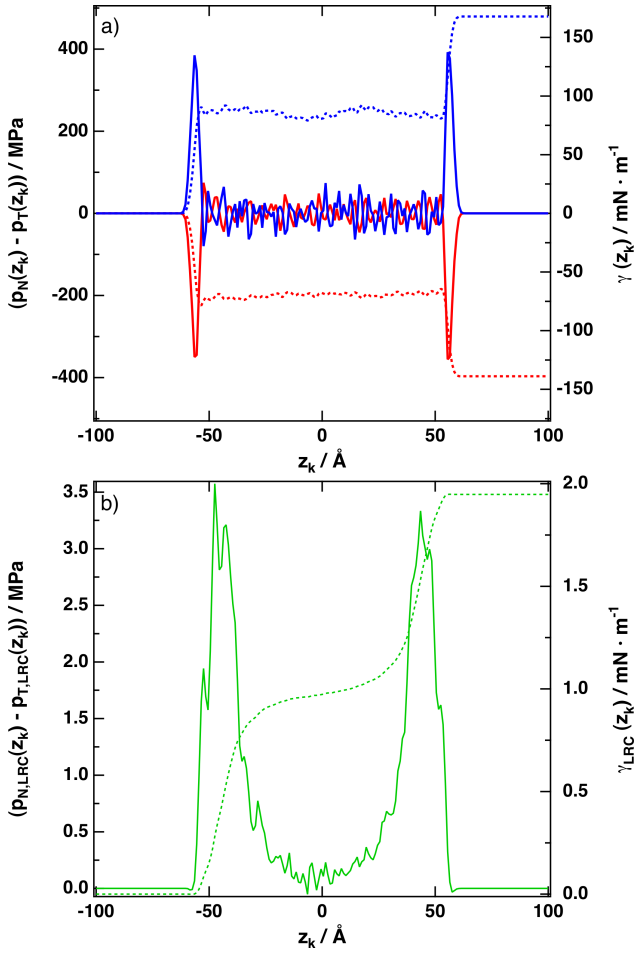

Figure 3.37: a) $p_N(z_k) - p_T(z_k)$ for the Lennard-Jones (red curve) and the electrostatic part of the potential (blue curve) as a function of z_k for $[C_4C_1pyrr][Tf_2N]$. The dashed lines correspond to the integral as a function of z (right axis); (b) $p_N(z_k) - p_T(z_k)$ for the long-range corrections as a function of z_k for $[C_4C_1pyrr][CF_3SO_3]$. The dashed lines correspond to the integral as a function of z_k (right axis).

Jin *et al.*[356] obtained for this IL a value of the surface tension of 33 mN·m^{-1} at 293 K. Shamsipur *et al.*,[357] using the Du Noüy ring method, report experimental values of the surface tension for the IL $[C_4C_1pyrr][Tf_2N]$ from 283 to 363 K in the range from 34.5 to 33 mN·m^{-1}. Using the same method, Carvalho *et al.*[358] have obtained surface tensions for the same IL from 293 to 343 K ranges from 34.9 to 32 mN·m^{-1}. No surface tension data is available in the literature for the IL $[C_4C_1pyrr][CF_3SO_3]$, nevertheless for imidazolium-based ILs, with a common

cation, the surface tension values of the IL based on the $[CF_3SO_3]^-$ and $[Tf_2N]^-$ anions are quite similar.[317] As the temperature range of the experimental measurements and the simulations performed here do not overlap, it is difficult to perform comparisons between the data; nevertheless, we can roughly conclude that the atomistic force field and the simulation techniques used in the present work are able to predict the surface tension of ILs within a deviation of ±10 %. According to the Langmuir principle, only the parts of the ions that are at the outer surface will primarily contribute to the surface tension values.[359] The similar structure at the liquid–vacuum interface for the ILs with the $[CF_3SO_3]^-$ and $[Tf_2N]^-$ anions presented here is in agreement with the trends of the surface tension observed from the molecular simulations. For the IL $[C_4C_1pyrr][FAP]$, the presence of a voluminous anion incites a lack of ordering at the surface, which is enriched with the most charged part of the ions, as can be observed in the density profiles depicted in Figure 3.32, leading to larger values of the surface tension (see Table 3.5). Pensado *et al.*[301] demonstrate that the inclusion of a terminal hydroxyl group at the end of the side chain of imidazolium-based ILs distorts the structure at the liquid–vacuum interface, leading to larger values of the surface tension, a similar behavior as that observed here for the IL $[C_4C_1pyrr][FAP]$.

Conclusions

The structure of the bulk phase and the vacuum–liquid interface of three pyrrolidinium-based ILs, with a common cation, have been studied using molecular simulations. The studied liquids show segregation between polar and nonpolar domains, where the morphology of the nonpolar regions is independent of the specific anion. Increasing the size of the anion leads to an increase of the characteristic sizes of the polar domains. The analysis of the vacuum–liquid interface shows an enrichment of the surface composition with the alkyl side chains of the cations. The presence of a discontinuity in the local density leads to a small charge segregation at the surface, this effect being less intense for the IL with the $[FAP]^-$ anion as this voluminous anion incites a lack of ordering at the

surface. From the charge distribution, it is possible to determine the electrostatic potential, observing a clear dependence of this magnitude on the anion. The analysis of the tangential pair distribution functions shows that in the interfacial area, the polar regions of the ILs are more structured than those in the bulk phase, whereas the opposite behavior is observed for the nonpolar regions.

Acknowledgment

This work was supported by the Spanish Science and Technology Ministry (CTQ2008-6498-C02-01 and CTQ2011-23925 projects) and the DFG, in particular, by the Projects KI-768/7-1 and KI-768/5-3 from the SPP-IL program. The participation of A.S.P. was made possible by a postdoctoral fellowship granted by the DFG through the SPP-IL program. Computer time from the "Centro de Supercomputación de Galicia" (CESGA) is acknowledged gratefully.

3.3 Ion Pairing in Ionic Liquids

3.3.1 En Route Formation of Ion Pairs at the Ionic Liquid-Vacuum Interface

Friedrich Malberg,[a] Oldamur Hollóczki,[a] Martin Thomas,[a], Alfonso S. Pensado[a] and Barbara Kirchner[a,*]

Received 7th March 2014

Malberg, F.; Hollóczki, O.; Thomas, M.; Pensado, A. S.; Kirchner, B. *ChemPhysChem* **2014**, submitted. Unpublished work.

Own contributions to this manuscript:

- Conduction and maintenance of simulations
- Analysis of trajectories
- Interpretation of data
- Writing of the manuscript

[a] *Mulliken Center for Theoretical Chemistry, Institut für Physikalische und Theoretische Chemie, Universität Bonn, Beringstr. 4+6, D-53115 Bonn, Germany, E-Mail: kirchner@thch.uni-bonn.de*

Abstract The suggestion of the shortage of ion pairing in ionic liquids is opposed to the sole ion pair structure of their vapor phase. Structural rearrangement has to occur en route from the liquid to the vapor. In this study, we propose a detailed four step evaporation mechanism for ionic liquids, providing a novel and sophisticated perspective on the theory of this process based on the connection between ion pairing and volatility. The process involves diffusion of ions from the bulk to the surface, where they drift around at the surface until a well-defined ion pair is formed with a counter-ion, leading to the departure from the surface into the vacuum. To assess the validity of this scheme, we performed a series of classical and *ab initio* molecular dynamics simulations based on the most sophisticated methods and force fields available for ionic liquids.

Ionic liquids (ILs) had been often described as "nonvolatile" replacement for organic solvents,[5] however, in processes where other possible advantageous properties of ILs are utilized, the low vaporizability became a limiting obstacle in the effective purification via distillation. As a real breakthrough in this issue, Earle *et al.* showed that under rather harsh conditions ILs can be distilled.[59] Accordingly, many subsequent studies aimed to understand the vapor and the vapor-liquid interface of ILs,[61,64,69,70,83] to have a better insight into the mechanism of vaporization. Based on line-of-sight mass spectroscopy and photo-electron spectroscopy, the vapor phase consisting solely of single ion pairs was evidenced. On the other hand, within the liquid the lack of single cation-anion associations,[81] thus, the lack of "ion pairing" was suggested, or at least a certain ion pairing deficiency due to structural mixture of ion-pairing with nonassociative behavior, *i.e.* scale of ionicity,[122,123] as opposed to the vapor structure consisting of solely ion pairs. Considering these important structural differences, the process of vaporization is apparently not as trivial as for molecular solvents, and significant structural rearrangement has to occur *en route* from the bulk to the vapor. The vaporization process, therefore, should involve not only the diffusion to the surface, but also the formation of the vaporizable entity, and—since it consist of

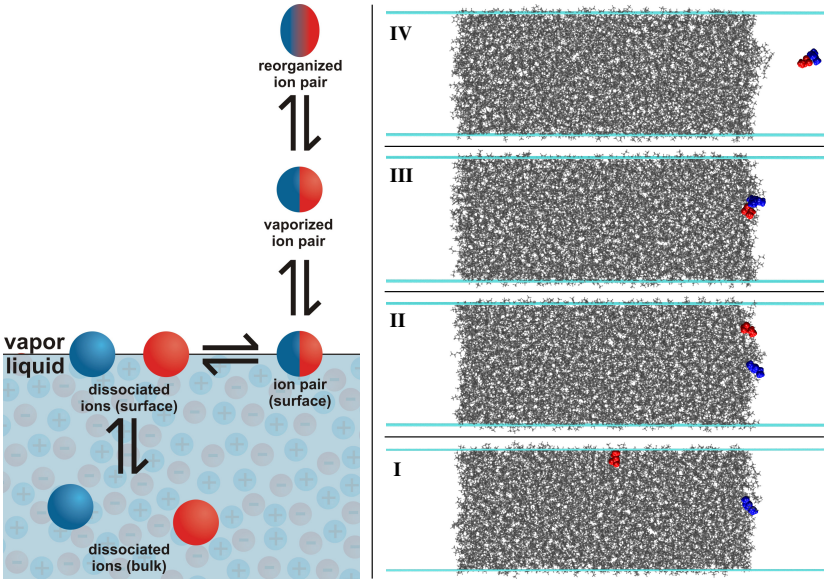

Figure 3.38: Left: Multistep mechanism describing the complex evaporation process of ionic liquids, from the "melange" [81] of ions in the bulk, via the formation of an ion pair at the surface and the subsequent evaporation, to the rearranged and stabilized vapor.[82] Right: Snapshots of MD simulations, reproducing the mechanism; Blue: cation, red: anion.

two molecules, and hence it is more flexible than the molecular solvents—also its rearrangement in the gas phase may be of great importance.[360] Thus, we propose here a detailed, multistep evaporation mechanism for ILs (see Fig.3.38), providing a novel and sophisticated perspective for the theory of this process. To assess the validity of this scheme, we performed a series of classical and *ab initio* molecular dynamics simulations on the 1-ethyl-3-methylimidazolium ethylsulfate ionic liquid. First, to obtain a qualitative picture, in an ensemble that contains an IL surface (described elsewhere[283]) a chosen ion was dragged out of the liquid through the interface by applying a constant force to it. The resulting trajectory was in very good agreement with the general picture. The ion first diffuses to the surface, where it is drifting for a certain time at the surface, and after forming a well-defined ion pair with a counter-ion, both depart together from the surface to the vacuum together, see scheme in Fig. 3.38.

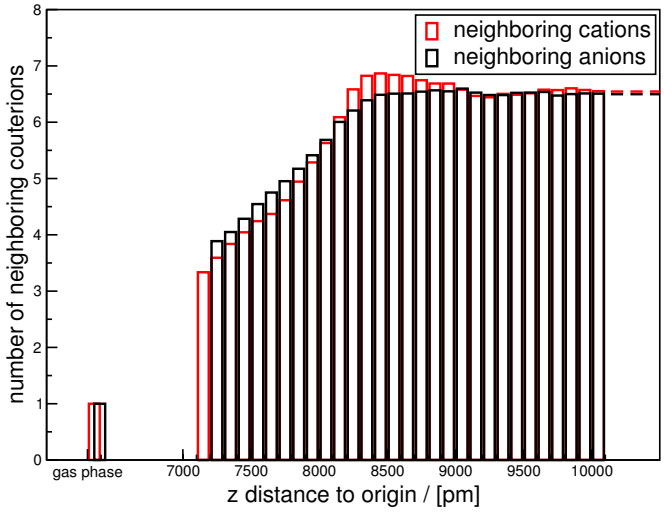

Figure 3.39: Histogram of neighboring counter-ions; black: neighboring anions to reference cations; red: neighboring cations to reference anions. To obtain the number of neighboring counter-ions, we determined the radial distribution functions of the center of mass of the reference ion to the center of mass of the observed ions and integrated these functions to the first minimum in the bulk, which is ∼800 pm. The x-axis show the explicitly chosen reference ions from regions with a width of 100 pm in the normal direction to the interface. The slab of the ionic liquid extends over 12000 pm in z-direction, while the whole box is 27500 pm wide. Therefore at approximately 7000 pm measured from the box origin the surface of the slab is expected.

The cornerstone of the above described mechanistic picture is the formation of the ion pairs, which should occur either at the surface, or very close to it. Accordingly, at the interface region of the IL there should be more ion pair-like structures (IPs), than in the bulk phase. Since one of the reasons that there are no (long-lived) ion pairs in the bulk is that there are several counter-ions surrounding one particle,[117,343,361,362] this change in ion pairing can be tracked indirectly by monitoring the coordination number from the bulk to the surface (Fig. 3.39).

Indeed, the bulk and the interface region can clearly be distinguished in Fig. 3.39. In the bulk region both the cations and anions have ∼6.5 counter-ions in their first solvation shell, which at a distant of ca. 1100 pm from the surface starts

to drop, and reaches ∼3.5 at the surface. As has been observed before,[283] the cations and the anions are not homogeneously distributed at the interface. The surface is mainly covered by the anions, and until ca. 1000 pm below that there are somewhat less cations in the liquid. This shortage on cations is made up for by their slight excess in the following 1000 pm, which afterwards flattens into the completely equal coordination number of both ions. Interestingly, according to these results the surface region of the IL is rather thin, after ca. 1000 pm its effect on the coordination number is small, and after 2000 pm it is not observable at all. It is also worth to point out, that beyond this "layering" of the different ions, the anion and cation have other microscopic properties that show clear differences. For example, it has been shown that the cations possess larger mobilities in ILs compared to the anions,[122,123] even if the latter particle is significantly smaller in size. Ion pairing, however, can also be defined via considering dynamical criteria, as has been proposed by Zhao *et al.*[121] The two descriptors that may aid assessing the presence of IPs are how far and for how long two neighboring oppositely charged particles travel together in the solution. If the above described changes in ion pairing are valid, then these dynamic criteria should also exhibit significant changes for the bulk and for the surface. In Fig. 3.40 it can be seen, that while the distribution of the IPs' lifetime is almost identical in these two regions, their path that they move together is considerably elongated at the surface (bottom) compared to the bulk (top). In other words, although they remain neighbors for the same time at both the surface and in the bulk of the IL, during this time they move more, thus, they "survive" more collisions with the surrounding particles. Hence, also these findings can be interpreted as increased ion pairing at the surface of ILs, similarly to the picture achieved via the other approach above.

Beyond the mere fact that the ion pairing is different at these two regions, being important in the evaporation process, this more restrictive association should also have structural consequences. In Figure 3.41 averages of three characteristic distances are shown as approaching the surface from the bulk, and for the single (gas phase) ion pair. Similarly to the coordination numbers, a gradual change can

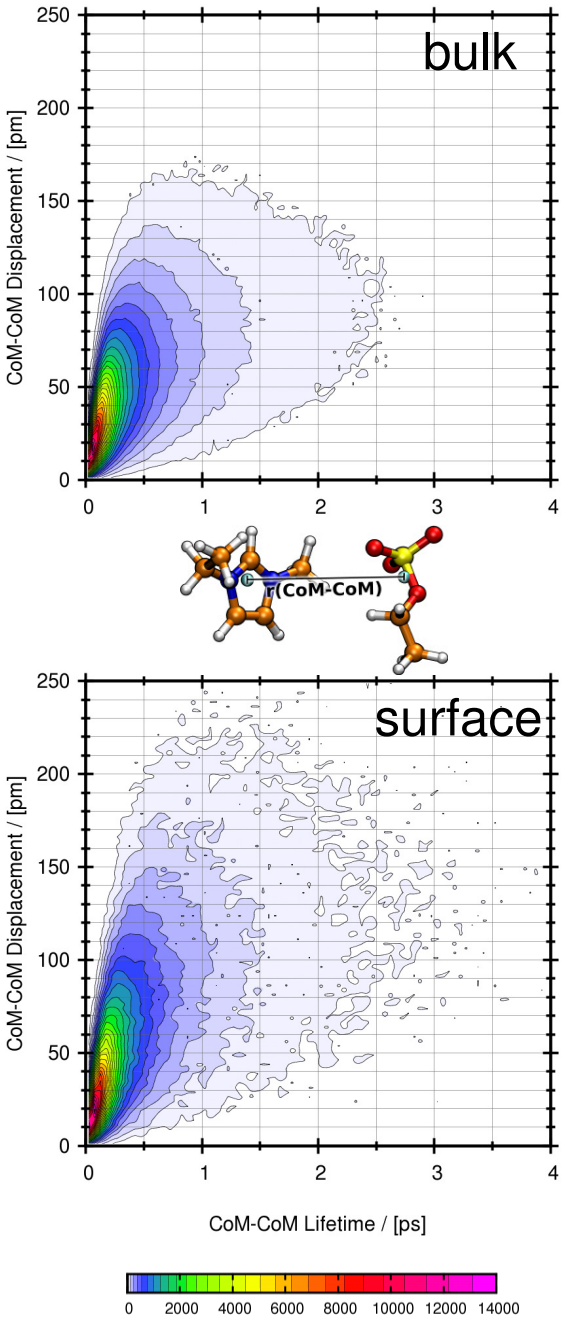

Figure 3.40: Combined distribution function (CDF) plotting the CoM-CoM displacement of an ion pair during its lifetime calculated for being next neighbors with respect to the CoM. Top: CDF calculated for ions of the bulk region, without ions of the surface region (7000 pm to 8200 pm). Bottom: CDF calculated only for ions situated in the surface region.

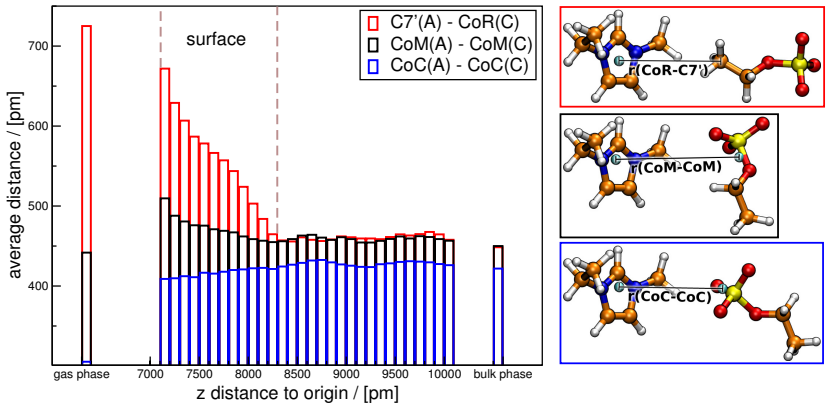

Figure 3.41: Histogram of the average distance between the terminal carbon atom of the anion C7' to the center of the imidazolium-ring (CoR), between the center of mass (CoM) of the anion (A) and cation (C) and between the center of charges (CoC) of anion (A) and cation (C). To obtain the average distance, we determined the distance distribution between next neighboring observed atoms and calculated their average distance, depending on the specific regions.

be observed in the average conformation, from about 1200 pm below the surface. Throughout this interval, the C7'(A)-CoR distances increase, which means that the anion's ethyl group moves away from the cation's ring, which is even more extremely elongated in the gas phase.[259] This displacement is in accordance with the slight decrease in the distances between the centers of charge (CoC); thus, the charged, and therefore more interacting sulfate oxygen atoms turn to face the cationic ring, while the anionic side chain is moving away from it. In the gas phase, where no other ions are present to provide further interactions, the CoC(A)-CoC(C) distance is minimized, which also brings the centers of mass closer, seemingly breaking the increasing trend in their distance from the bulk to the surface. In compliance with the above data it is obvious that the arrangement of the IL ions changes from the bulk to the surface gradually more similar to that in the gas phase, preparing the ion pair for departure, thus, evaporation. This involves the formation of ion pairs in the surface, and also the conformational alignment of the two ions within these ion pairs. In accordance to this, it was

pointed out recently by Austen Angell *et al.*, that ionic liquids indicating pairing up of ions in the liquid, were the ones observed to distill easily.[126] After evaporation these changes are consummated by further, more extreme rearrangement. Hence, these data completely underpin the multistep mechanism shown in Fig. 3.38, providing a novel viewpoint in the theory of vaporization in general. We believe this scheme is necessary for the proper description of the corresponding process, and thus, enhances the advance in the field of IL design.

Acknowledgment

The financial support from the Humboldt foundation for O. Hollóczki is gratefully acknowledged. Furthermore, we would like to thank the SPP 1708.

Computational Details

We investigated 1024 ion pairs of $[C_2C_1im][C_2SO_4]$ in a periodic box, where the normal direction to the surface was extended to 27500 pm so the liquid slab occupies $\sim$ 12000 pm in the middle with two equivalent liquid-vacuum interfaces. The initial configuration was constructed by placing together two cubic boxes with 512 ion pairs, which were equilibrated for 1 ns at constant NPT and T=423 K with a time step of 2 fs to obtain the final density of this liquid. Equilibration of the initial configuration took 1 ns with a time step of 2 fs in the NPT ensemble, after which the system was run for 1 ns to allow the interface to equilibrate. The production run was 2 ns with periodic boundary conditions coupled to Nosé–Hoover thermostats[272,273] to keep the temperature constant at 423 K (constant NVT). Afterwards, a constant force in opposite z-directions (normal to the surfaces) was put on arbitrary choosen cation and anion to obtain a qualitative picture of the mechanism at the surface. The systems were simulated via molecular dynamics using the DL_POLY package.[297]

3.3.2 On the Origin of Ionicity in Ionic liquids. Ion Pairing versus Charge Transfer

Oldamur Hollóczki,[a] Friedrich Malberg,[a] Tom Welton[b] and Barbara Kirchner[a,*]

Received 18th March 2014

Hollóczki, O.; Malberg, F.; Welton, T.; Kirchner, B. *Phys. Chem. Chem. Phys.* **2014**, submitted - Reproduced by permission of the PCCP Owner Societies.

Own contributions to this manuscript:

- Conduction of charge transfer calculations
- Analysis and interpretation of charges transfer data
- Discussion of the results
- Co-writing of the manuscript

[a] *Mulliken Center for Theoretical Chemistry, Institut für Physikalische und Theoretische Chemie, Universität Bonn, Beringstr. 4+6, D-53115 Bonn, Germany, E-Mail: kirchner@thch.uni-bonn.de*

[b] *Department of Chemistry, Imperial College London, London, SW7 2AZ, U.K.*

Abstract In this paper we show by using static DFT calculations and classical molecular dynamics simulations that the charge transfer between ionic liquid ions plays a major role in the observed discrepancies between the overall mobility of the ions and the observed conductivities of the corresponding ionic liquids, while it also directly suppresses the association of oppositely charged ions, thus the ion pairing. Accordingly, in electrochemical applications of these materials it is important to consider this reduction of the total charges on the ions, which can greatly affect the performance of the given process or device in which the ionic liquid is used. By slightly shifting from the salt-like to a molecular liquid-like system via the decreased charges, the charge transfer also fluidizes the IL. We believe that this vital information on the molecular level structure of ILs offers a better understanding of these materials, and allows us to improve the *a priori* design of ILs for any given purpose.

Introduction

Association of oppositely charged ions, thus ion pairing,[115] is a fundamental concept for electrolyte systems, that governs many of their physicochemical properties such as viscosity, conductivity and osmotic pressure; therefore affecting greatly the design and application of batteries, solar cells, and fuel cells. Ion pairing, however, can also have a considerable, albeit more complex role in synthetic approaches, since via selectively oriented associations of ionic reactants/catalysts control over regio- or stereoselectivity can be achieved,[363,364] increasing the effectiveness of the corresponding applications, or even enabling reaction paths that are otherwise not favored.[115,363,365] Due to these very diverse effects of this very basic elementary behavior, it has been in the focus of physical chemical research for many decades.[115,363,364,366–370]

Ion pairing is an especially intriguing issue in ionic liquids (ILs),[4,5,58,371,372] where the solvent itself is composed of ions. ILs are used in an extremely wide variety of applications, as *e. g.* electrolytes for electrochemical purposes,[126,373–382]

or tunable media for synthesis.[5,58,372,383] Due to the aforementioned connection between the physicochemical properties of the electrolytes and ion pairing, and since many of the potential beneficial properties of ILs are related to their ionic nature,[4,5,58,81,371–373] there is a substantial overlap between the fields ion pairing and ionic liquids, and the possible formation of ion pairs and other neutral subunits[253,254,384] in these materials is of great current interest.[81,82,121,123,125,385]

There have been different ways of approaching this issue, somewhat related to the electrochemical and synthetic points of view in the applications of ILs in general. On one hand, the pure IL can be investigated in terms of ion pairing, while on the other hand ionic solutes can also be considered. In pure IL systems however, not only observing, but also defining an ion pair is difficult, since one cation is surrounded by many anions and *vice versa*,[116–120,385,386] and unless there is a distinct interaction with one of the neighboring particles, choosing any specific "pair" seems rather unwarranted.[120] From the microscopic point of view a possible way to look at ion pairing in pure ILs is to define it via a distance and time scale; thus, how far and for how long do the oppositely charged, neighboring ions travel together in the liquid.[121] By applying this definition it has been shown by molecular dynamics simulations that ion pairs are very short lived in ionic liquids and that the ions are generally diffusing rather independently from one another,[121] inferring a lack of ion pairing. In good agreement, the stabilization of ion pairs against separation has also been found low in a follow-up study.[387]

From certain macroscopic studies, however, a somewhat different picture was obtained. Watanabe and coworkers have compared[123,125] the mobility of the ILs' ions to the conductivity of the IL itself for a wide variety of ILs according to

$$\Lambda_{\mathrm{NMR}} = \frac{N_A e^2}{kT}(D^+ + D^-) \tag{3.10}$$

and

$$\mathrm{I} = \frac{\Lambda_{\mathrm{imp}}}{\Lambda_{\mathrm{NMR}}}\ , \tag{3.11}$$

where N_A is the Avogadro number, e is the charge of the electron, k is the Boltzmann factor, T is the temperature, D^+ and D^- are the diffusion constants of the

cation and the anion, Λ_{NMR} is the ion mobility from the NMR measurements, Λ_{imp} is the ion mobility from the conductivity measurements, while I is defined as the very helpful ionicity scale. It was shown by Watanabe and coworkers[123,125]—in agreement with the deviations from ideality in the Walden plot[127,128,382,388]—that for all ILs the actual mobilities of the IL ions (measured by NMR) are significantly larger than those what one can obtain from the conductivity measurements; thus, the ionicity values (eq. (3.11)) are lower than one. In other words, ILs conduct worse than expected according to the diffusion coefficients of the IL particles. Assuming that eq. (3.10) holds, this discrepancy could only be rationalized by considering a correlated motion[129] of the oppositely charged ions, hence—in contrast to the molecular dynamics results above—the presence of ion pairs to some extent,[123,125] or other, low-charge aggregates was concluded. Accordingly, the ionicity value was interpreted as the ratio of the "effective concentration of charged species" and the total concentration of the ionic liquid.[125]

Unlike in the case of neat ILs, ionic solutes can clearly be distinguished from the IL solvent, therefore their ion pairing can be observed directly. Although in a strict meaning these measurements concern only the behavior of the solute in the IL, and not the solvent itself, IL-like solutes can also be considered as probes, which are incorporated into the IL in a way that they are not distinguishable from the solvent, and therefore they nevertheless hold some information on the association processes of the IL solvent. As a pioneering study in this field, the kinetics of the S_N2 reaction shown in Figure 3.42 was investigated,[81] and a different reaction mechanism was suggested in ILs compared to molecular solvents. Instead of a two-step mechanism, involving an intermediate step of a contact ion pair formation, a direct, one-step mechanism could be observed.[81] Similar conclusions could be deduced from spectroscopic measurements for Kosower's salt in different ILs,[82] that no preferential ion pairing is present in IL solutions. Thus, these results—in agreement with molecular dynamics simulations, and in contrast to the conductivity measurements—suggest the lack of ion pairing in ionic liquids.

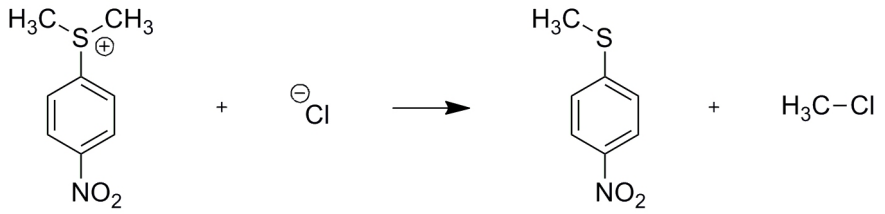

Figure 3.42: Reaction between charged species in ionic liquids, which—unlike in molecular solvents—was shown to occur in one step, without the initial ion pair formation of the substrates.

Again in contrast to these observations, a theoretical study on the NaCl ion pair in 1-butyl-3-methylimidazolium bis(trifluoromethanesulfonyl)imide ($[C_4C_1im][Tf_2N]$) ionic liquids by classical molecular dynamics simulations showed[389] that separating the Na^+ and the Cl^- ions is *endothermic* with a reaction free energy of 38 kJ/mol, thus, the ion pair formation is that much favored over dissociation. It is important to note here that NaCl is rather poorly soluble in ionic liquids[390] due to the very stable ionic lattice of this salt, which hence forms larger aggregates in the form of precipitation, as was also shown by the authors of this study.[389] Nevertheless, these two extreme cases of different behaviors for this classical salt-like structure or the IL-like solutes, together with the contradicting findings described above show, that the problem of ion pairing in ionic liquids is a very complex matter and still further efforts are needed to understand this aspect of the ILs' microscopic structures.

In order to establish a bridge between the dissonant results from these thorough measurements performed by very different experimental[81,82,123,125] and theoretical[121] techniques on the association processes of the ions in ionic liquids, it is worth starting from the molecular structure of ionic liquid ions within the IL. Although the total charges of independent, isolated ions or molecules clearly must be integers, in ionic liquids these ions are not isolated from each other at all, but they form an extensive hydrogen bonding network.[40,119,120,256,391–395] Since hydrogen bonding involves orbital interactions[40,119,391] that can result in a partial

charge transfer,[40] it is, in principle, possible to have fractional charges on each ion. Recently it has been shown by theoretical methods that this is indeed the case.[40,79,394,396] Static calculations on a linear cluster of 1,3-dimethylimidazolium chloride ion pairs showed a charge of ca. ± 0.8 on the ions,[79] which was later also found to be the best total charge on similar IL ions to reproduce the orientational and dynamic properties of these materials in classical molecular dynamics simulations.[130,394,396,397] If the charges are lower than one, however, less charge is carried by the transport of a particle and accordingly a drop of the conductivity can be expected, as it would with the aggregation of ions (see eq. (3.10)). In the light of these considerations, all experimental results based on charge transport and the assumption that the charge at the ions is $\pm e$ should be revisited; and since Coulombic interactions are of high importance in ILs, how much the presence of charge transfer influences our general picture of both microscopic and macroscopic structures of ionic liquids with respect to ion pairing should be evaluated in each case.

In this study we evaluate the extent of charge transfer for single ion pairs of several commonly used ionic liquids, and consider its possible contribution to the previously defined ionicity values. Via artificially induced charge transfer within a probe ion pair we also evaluate the structural effects of the obtained lower charges on the ionic liquid itself, including ion pairing.

Applied methods

To estimate the extent of charge transfer in general, a variety of ionic liquids were chosen. The labeling of the ions is shown in Figure 3.43. To calculate the charges on the ionic liquid ions, two conformations of a single ion pair (see Supp. Inf.) of each investigated ILs has been optimized in a COSMO[209,398] ensemble ($\epsilon = 15$; distance between the solvent and the atomic van der Waals radii was 2.5 Å), using the BLYP-D3 GGA-type density functional that contains Grimme's dispersion correction D3,[31,200] with a def2-TZVP basis set, by the Turbomole 6.5 program package.[399]

The charges were calculated with different localization techniques (Blöchl,[226] Mulliken,[217] AIM, RESP[225]) for both considered conformers, and then were averaged. Blöchl and RESP charges were calculated by the CP2K program package[270] at the BLYP-D3/TZVP-MOLOPT-GTH level with type GTH pseudopotentials, while the AIM charges were produced by the AIMAll program package using the BLYP-D3/def2-TZVP electron density.[400] In the paper only the Blöchl and RESP charges are shown, for the rest of the data, see the Supp. Inf. It should be stressed here that due to the fact that partial charges at the atoms are not observable properties, their calculation is very dependent on the method. On the other hand, although there are reasons and examples for and against the different localization techniques for certain problems, there is, nevertheless, no clear hierarchy among them, and therefore, by such calculations only a qualitative picture[401] can be obtained.

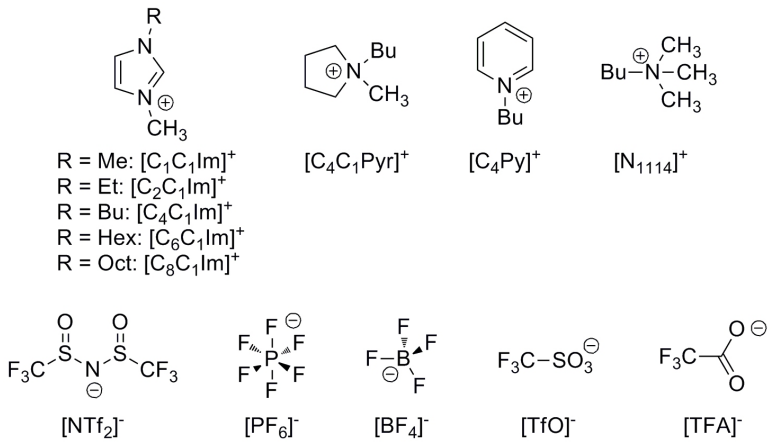

Figure 3.43: The IL ions considered in this study, and their abbreviations.

Classical molecular dynamics simulations were performed by using the LAMMPS program package,[402,403] applying the usual Lorentz–Berthelot mixing rules with previously fitted potentials for the ionic liquid,[296,404] for the Na^+,[405] and for the Cl^-.[404] The total charges of the ionic liquid ions were ± 0.8, which was obtained by scaling the RESP fitted charges of the single ions, as described previously.[114] The charge of the sodium and chloride ions was set to ± 0.5, ± 0.8,

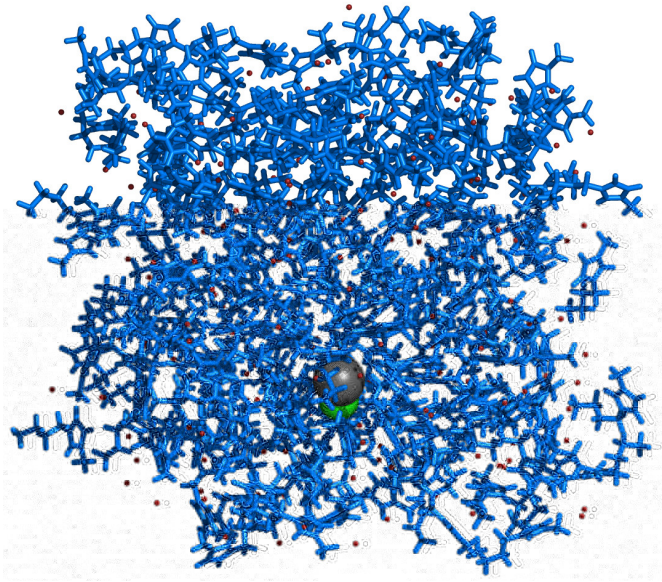

Figure 3.44: Example for the simulation boxes of $[C_4C_1im]Br$ with an ion pair of NaCl. $[C_4C_1im]^+$: blue; Br^-: red; Na^+: grey; Cl^-: green.

± 1.0, ± 1.5, ± 2.0, ± 3.0 in a series of different simulations. For the ± 0.8 charge setup, the effect of the sodium ion's size was also investigated, which was varied by different σ values in the Lennard–Jones potential (for the potential form, see Supp. Inf.), being 1.5 and 2 times larger than the originally fitted parameter. The cut-off for nonbonding interactions was chosen as somewhat larger than 2.5 times the biggest σ value present in the force field (for details, see Supp. Inf.). The simulation box (for a representative snapshot see Figure 3.44) contained 200 1-butyl-3-methylimidazolium bromide ion pairs, and a single sodium chloride contact ion pair. Each initial box had a density of 1 g cm^{-3}, which was simulated in an NPT ensemble for 1 ns, in order to achieve the equilibrium density. The average cell vector of the last 0.5 ns was used in the further simulations. 1 ns of equilibration of the obtained box in the NVT ensemble was followed by the production run of 10 ns, again in the NVT ensemble. The timestep of 1 fs was chosen, and the trajectory was saved throughout the whole 10 ns in every 1000 steps (in every 1 ps).

To investigate the free energy profile of the NaCl ion pair's dissociation process, thermodynamic integration was performed for all systems along increasing Na-Cl distance. In these simulations the box was prepared analogously to the equilibrium simulations described above, but during the production run an extra potential was applied at the Na-Cl distance, and the corresponding forces were collected in each step. The system was equilibrated in an NVT ensemble for an extra 0.1 ns at each distance, which was followed by a 0.25 ns production run in the same NVT ensemble.

For the analysis of the classical molecular dynamics results the TRAVIS program[231] was applied. The labeling of the $[C_4C_1im]^+$ cation is shown in Figure 3.45 as used throughout the article.

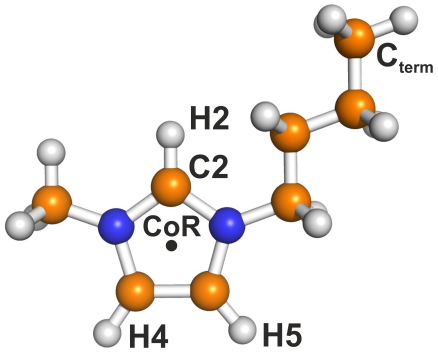

Figure 3.45: Labeling of the $[C_4C_1im]^+$ cation used throughout the paper. CoR = Center of Ring; H: white; C: brown; N: blue.

Results and Discussion

Charge transfer in ionic liquid ions, and its effect on ionicity First we performed static quantum chemical calculations on a series of ILs to acquire a rough estimate of the charge transfer, and to evaluate its effect on the ionicity values. Thus, we selected a set of highly investigated ionic liquids (Table 3.6), and calculated the charges on the ions in an ion pair of each kind within a continuum solvent model. The obtained charges, together with the originally published[123,125] and the hereby recalculated ionicities are shown in Table 3.6.

Table 3.6: Calculated absolute charges on the ions within a single ion pair in a COSMO ensemble. For the Lewis structural formula of the considered ions, see Figure 3.43. I: ionicity (see eq. (3.11)); $|q_{Bl}|$: absolute charges at the ions, based on the Blöchl partial charges; I'_{Bl}: ionicities recalculated by using $|q_{Bl}|$; $|q_{RESP}|$: absolute charges at the ions, based on the RESP fitted charges; I'_{RESP}: ionicities recalculated by using $|q_{RESP}|$.

IL	I	$\|q_{Bl}\|$	I'_{Bl}	$\|q_{RESP}\|$	I'_{RESP}
$[C_4C_1im][Tf_2N]$	0.61[a]	0.82	0.90	0.74	1.11
$[C_4C_1im][PF_6]$	0.68[a]	0.91	0.82	0.88	0.88
$[C_4C_1im][BF_4]$	0.64[a]	0.88	0.83	0.87	0.85
$[C_4C_1im][TfO]$	0.57[a]	0.84	0.80	0.88	0.74
$[C_4C_1im][TFA]$	0.52[a]	0.84	0.73	0.84	0.75
$[C_1C_1im][Tf_2N]$	0.76[a]	0.83	1.09	0.81	1.16
$[C_2C_1im][Tf_2N]$	0.75[a]	0.85	1.04	0.78	1.23
$[C_4C_1im][Tf_2N]$	0.61[a]	0.82	0.90	0.74	1.11
$[C_6C_1im][Tf_2N]$	0.57[a]	0.78	0.93	0.77	0.97
$[C_8C_1im][Tf_2N]$	0.54[a]	0.72	1.04	0.66	1.26
$[C_4C_1im][Tf_2N]$	0.61[a]	0.82	0.90	0.74	1.11
$[C_4C_1pyrr][Tf_2N]$	0.70[a]	0.75	1.26	0.77	1.18
$[C_4py][Tf_2N]$	0.63[a]	0.75	1.12	0.78	1.04
$[N_{1114}][Tf_2N]$	0.65[a]	0.79	1.04	0.79	1.04

[a] values taken from literature[123,125]

As can be seen from the data (Table 3.6), the absolute values of the charges at the ions are indeed significantly lower than unity, which shows the presence of a large charge transfer between the anion and the cation within all the ion pairs. The charge transfer varies by altering the anion (upper third of Table 3.6), the length of the side chain (middle third of Table 3.6), and the cationic head group as well (lower third of Table 3.6), but also by the localization method that is used for the calculation of the charges (see Supp. Inf.). Generally, the more spherical inorganic anions ($[PF_6]^-$ and $[BF_4]^-$) have the smallest deviation from unit charges, while the large and flexible $[Tf_2N]^-$ anion has the largest charge transfer. The increasing length of the cation's side chain induces an increase of the deviation from the unit charges, while the cationic head groups also show different charge transfers, although the order depends on the localization technique. According to the large charge transfer values obtained, and to eqs. (3.10)–(3.11) (note that the square of the charge is used in eq. (3.10)!), the reduction of mobile charge can originate both from ion pairing and from the charge transfer; thus, the latter effect is also reflected in the ionicity values. It is, however, possible to use these charges as the charge of the ions instead of the originally applied unit charges in eq. (3.10), and hence eliminate the effect of the charge transfer from the ionicity values reported[123,125] previously. As can be seen in Table 3.6, the recalculated ionicity values (I′) are remarkably higher, demonstrating that the original values are indeed significantly influenced by the charge transfer between the ions and that the long-term association of ions into neutral subunits plays a smaller role than previously inferred from the corresponding conductivity measurements.[123,125] It is important to point out that there are some cases, in which the obtained I′ values are larger than one. This is in clear contrast to chemical intuition, since it would mean that the ions carry more charge than expected from their total charges (calculated here), and their measured mobilities (published previously[123,125]). This might be explained by the limitations of the simple model applied, such as considering one single ion pair with an implicit solvent without temperature effects and fluctuations. Accordingly, we are planning

to perform a subsequent study with a more systematic approach to this specific matter, but the difficulties of the electron localization during the charge calculations makes this issue very complicated, especially considering that the square of the charge is applied in eq. (3.10), which enlarges any slight error. It is, however, clear already according to these crude values that considering the observed slight changes in the total charges at the ions is important when analyzing ILs' ionicities, since these can alter the physical picture of IL systems.

While the most important aspect of these findings is to show that ILs are, in general, less prone to ion pairing than was previously thought based on conductivity measurements, there are some interesting details that should also be pointed out. With these estimated values the trends in the ionicities are altered at some points, to reflect a ranking that corresponds more to the general chemical picture of the considered materials. The more salt-like, small and spherical $[[PF_6]^-$ and $[BF_4]^-$ derivatives seem oddly less associated in the original data set than those with the more flexible, less hydrogen-bonding $[Tf_2N]^-$, which is completely corrected by considering the effect of charge transfer. Similarly, as has been pointed out by Pádua *et al.*,[106] for longer side chains one can anticipate that the contribution of the stronger, associative Coulombic interactions decreases, leading to less ion pairing, although from the original ionicity values the opposite trend was observed. Taking the charge transfer into consideration, however, this trend is partly corrected. Although it is tempting to explain the amount of charge transfer in the different ion pairs simply by the strength of the hydrogen bonds, comparing our charge transfer results to experimental data[395] did not provide any clear correlation.

Structural Effects of the Charge Transfer: Ion Paring and More After having seen that the charge transfer plays a major role in the deviations between the conductivities and particle mobilities, it is also important to discuss the structural changes that it induces. To observe such differences, we placed a single probe ion pair of sodium chloride in 1-butyl-3-methylimidazolium bromide and performed a series of molecular dynamics simulations with varying charges on

the sodium and the chloride anions. With these manually varied charges we represent the different states of charge transfer within the ion pair, showing how it influences the interactions between these two ions, or with the solvent. While the simplicity of the solute ion pair makes it easier to interpret the changes in intermolecular interactions, the relatively small bromide anion of the ionic liquid avoids artifacts of size differences between the solute and solvent anions [cf. chloride and bis(trifluoromethanesulfonyl)imide]. Moreover, due to the similar sizes of the bromide and chloride anions, the dissociation-association processes of the ion pair can be spontaneous according to the very simple hypothetical NaCl + Br^- → NaBr + Cl^- substitution reaction, which also holds valuable information on the system.

The observable attractive interactions within these systems are Na^+-Cl^-, Na^+-Br^-, and Cl^--$[C_4C_1im]^+$, where the latter generally takes effect via the ring hydrogen atoms, especially via the H2 (for labeling see Figure 3.45.[40,119,120,256,391–394] The characteristic distances that we focused on were those between Na^+ and Cl^-, Na^+ and Br^-, Cl^- and the Center of Ring in the $[C_4C_1im]^+$ cation, Cl^- and H2 of the $[C_4C_1im]^+$ cation, and finally between the Na^+ and the C_{term} of $[C_4C_1im]^+$. In Table 3.7 the location of the first peak in each corresponding radial distribution function is presented. While with |q| = 0.5 the NaCl ion pair spontaneously, and irreversibly dissociates, for |q| = 0.8 such dissociation occurs for a few ps period of time, and then the solute ion pair is regenerated (Figure 3.46). For the even higher charges no dissociation is observed at all. The Na-Cl distance exhibits high dependency on the charge, as it drops from 265.5 pm (|q| = 0.8) to 193.2 pm (|q| = 3), showing that the ion pair formation is more probable in the cases of the high charges, while decreasing the charge—via *e. g.* charge transfer—makes ion pair formation less probable.

Due to the aforementioned spontaneous dissociation, in the |q| = 0.5 case the whole of both surfaces of the solute ions are available for solvation, and therefore upon increasing the charge to |q| = 0.8 the average coordination number of bromide anions around the sodium cation decreases (Table 3.7). In the rest

Table 3.7: Characteristic distances (in pm units) in the simulations of a single NaCl ion pair in $[C_4C_1im]Br$ ionic liquid, with different charges on the Na^+ and Cl^- ions. For the numbering of the atoms in the $[C_4C_1im]^+$ cation, see Figure 3.45. N_{Br}^{Na}: average number of coordinating Br^- anions around the sodium ion within the first solvation shell; $N_{[C_4C_1im]}^{Cl}$: average number of $[C_4C_1im]^+$ cations around the Cl^- anion; Ex_{Br}^{Na}: observed number of exchanges of Br^- anions between the bulk and the first solvent shell of the Na^+ cation throughout the simulation; $\tau_{[C_4C_1im]}^{Cl}$: mean lifetime of $[C_4C_1im]^+$–Cl^- interactions.

$\|\mathbf{q}\|$	$\mathbf{d}_{Na-Cl}$	$\mathbf{d}_{Na-Br}$	$\mathbf{d}_{Cl-H2}$	$\mathbf{d}_{Na-C_{term}}$	$\mathbf{N}_{Br}^{Na}$	$\mathbf{N}_{[C_4C_1im]}^{Cl}$	Ex_{Br}^{Na}	$\tau_{[C_4C_1im]}^{Cl}$
e	pm	pm	pm	pm	-	-	-	ps
0.5	–[a]	281.8	294.5	478.2	2.99	4.38	55[b]	45
0.8	256.5	275.4	275.5	642.2	2.64	4.62	11[b]	79
1.0	250.1	269.2	269.2	661.8	3.00	4.67	0[b]	124
1.5	224.8	256.5	262.9	655.7	3.00	4.58	0[b]	240
2.0	212.2	250.2	256.5	661.8	3.00	4.67	0[b]	534
3.0	193.2	243.8	250.2	611.3	3.00	4.63	0[b]	913

[a] spontaneous dissociation occurs

[b] due to the rarity of the exchange event, mean lifetimes cannot be given

of the structural properties in Table 3.7 the increasing strength of solute-solvent interactions are clearly indicated throughout the whole range (Table 3.7). Interestingly, nevertheless, the average number of coordinating bromide anions does not exceed three, while the average number of $[C_4C_1im]^+$ cations around the chloride also shows only a fluctuating trend between four and five. The lack of any clear increasing trend can be explained by the repulsive forces between the alike solvating IL ions, and also by the gradually increasing Na^+-$[C_4C_1im]^+$ and Cl^--Br^- interactions.

In the $|q| = 0.5$ case—note the aforementioned dissociation— the three coordinating bromide anions are arranged in a loose, often distorted planar triangular

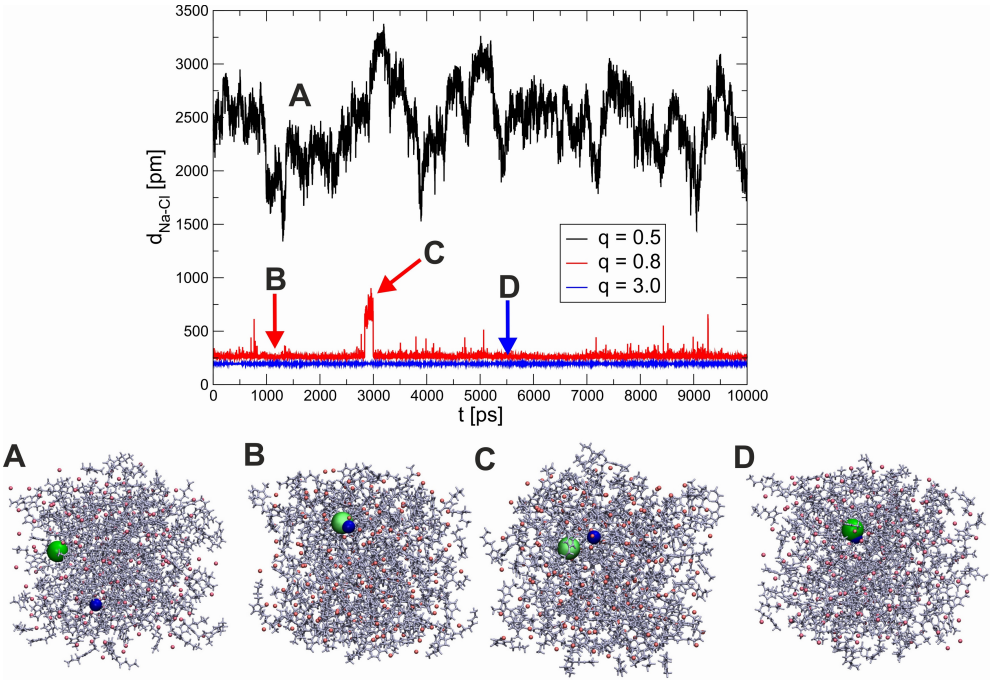

Figure 3.46: Development of the Na-Cl distances over time in three simulations, with 0.5, 0.8 and 3.0 e absolute charges on the ions. Below four snapshots are shown from these trajectories, taken from the points marked by arrows ($[C_4C_1im]^+$: grey; $[Br]^+$: red; Cl^-: green; Na^+: blue).

shape around the sodium ion. In the rest of the cases where the NaCl does not dissociate, however, the IL anions around the sodium cation are generally arranged in a fashion, so that they form a tetrahedron together with the chloride (Figure 3.47). Interestingly, this not only allows the longest possible Br^--Br^- and Cl^--Br^- distances, but also creates Br^--$[C_4C_1im]^+$ interactions within the solvent shell, around the midpoint of the Na-Cl axis (cf. regions A and E in Figure 3.48). The exchange of IL ions between the bulk and the first solvent shell dramatically decreases by increasing charge (cf. Ex^{Na}_{Br} or $\tau^{Cl}_{[C_4C_1im]}$ data for different |q| values in Table 3.7), which means that the solvent ions spend more time around the solute ion pair. Accordingly, the Br^--$[C_4C_1im]^+$ interaction within the first solvent shell becomes more static, thus, it is apparent that the presence of highly charged ion pairs in the solution induces the formation of further, static ion pair-like structures in the surrounding ions. Furthermore, it is also worth mentioning that in

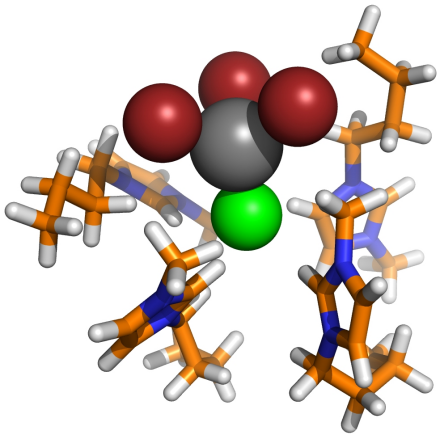

Figure 3.47: A representative snapshot of the NaCl ($|q| = 2$) ion pair's solvation shell in $[C_4C_1im]^+$.

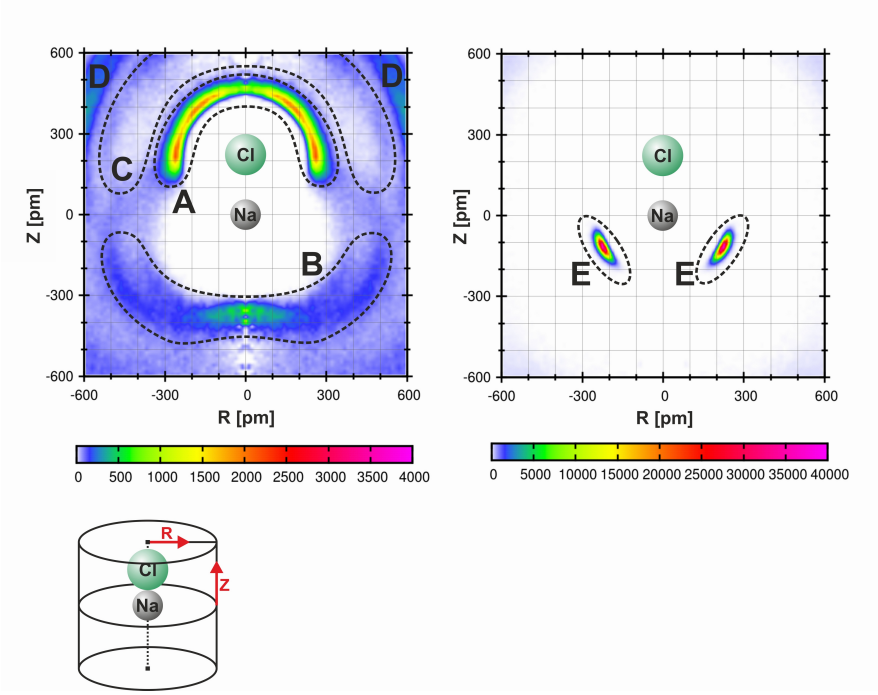

Figure 3.48: Pseudo-spatial distribution of the $[C_4C_1im]^+$ cation's ring hydrogen atoms (left), and the bromide anions (right) around the NaCl ion pair ($|q| = 2$).

Table 3.8: Free energy barrier and free energy of dissociation (in kJ mol^{-1} units) of the NaCl ion pair with different charges at the Na^+ and Cl^- ions.

|q|	**0.5**	**0.8**	**1.0**	**1.5**	**2.0**	**3.0**
$\Delta A^{\ddagger}$	13	29	84	247	573	1588
ΔA	−8	8	50	205	518	1547

the pseudo-spatial distribution of the $[C_4C_1im]^+$ cation around the NaCl ion pair (Figure 3.48, left) also shows a structure inducing effect in the longer range: approaching the bulk from the chloride anion, after the first solvate shell with high occurrences of the IL cation (regions A, Figure 3.48) there is a region, where the charged moieties are rare (region C, Figure 3.48), followed by a second solvate shell (region D, Figure 3.48). Also, some cations are apparently interacting with the bromide anions around the sodium ion, providing some occurrences in the lower half of Figure 3.48 (region B). After this second solvate shell, however, the effect of the increased ion-ion interactions are screened by the ion network of the IL, as has been shown before.[387]

Although some of these results represent extreme cases, the observed trends by the changes in charge are gradual, therefore they are very helpful in describing and understanding the effects of smaller fluctuations in the charges, such as the charge transfer described in the previous section. Accordingly, if there is a charge transfer between two neighboring ions in the solution, which decreases the total charge of each ion involved, it helps the dissociation of the two species and breaks the static aggregation of the surrounding ions as well, thus, locally fluidizing the liquid. This can also be described as the charge transfer changes the IL into a more molecular liquid-like assembly, influencing its physicochemical properties to a great extent.

The energetics of the dissociation process is in agreement with all the trends in the interactions established above, viz. the dissociation free energies and the corresponding free energy barriers (Table 3.8) are gradually, and steeply increasing.

Table 3.9: Characteristic distances (in pm units) in the simulations of a single NaCl ion pair in $[C_4C_1im]Br$ ionic liquid, with different sizes of the sodium anion ($|q| = 0.8$). The size is given as the percentage of that in the original force field, in terms of σ value in the corresponding Lennard–Jones potential. For the numbering of the atoms in the $[C_4C_1im]^+$ cation, see Figure 3.45. N_{Br}^{Na}: average number of coordinating Br^- anions around the sodium ion within the first solvation shell during the simulations; $N_{[C_4C_1im]}^{Cl}$: average number of $[C_4C_1im]^+$ cations around the Cl^- anion; Ex_{Br}^{Na}: observed number of exchanges of Br^- anions between the bulk and the first solvent shell of the Na^+ cation throughout the simulation; $\tau_{[C_4C_1im]}^{Cl}$: mean lifetime of $[C_4C_1im]^+$–Cl^- interactions.

$\mathbf{size}_{Na}$	$\mathbf{d}_{Na-Cl}$	$\mathbf{d}_{Na-Br}$	$\mathbf{d}_{Cl-H2}$	$\mathbf{d}_{Na-C_{term}}$	$\mathbf{N}_{Br}^{Na}$	$\mathbf{N}_{[C_4C_1im]}^{Cl}$	Ex_{Br}^{Na}	$\tau_{[C_4C_1im]}^{Cl}$
%	pm	pm	pm	pm	-	-	-	ps
100	256.5	275.4	275.5	642.2	2.64	4.62	11[b]	79
150	–[a]	338.8	275.5	503.1	4.01	5.07	35[b]	136
200	–[a]	408.5	269.2	490.5	4.72	5.20	99[b]	126

[a] spontaneous dissociation occurs

[b] due to the rarity of the exchange event, mean lifetimes cannot be given

For the $|q| = 0.5$ case the free energy is a low negative value, indicating a favored dissociation, in clear accordance with the spontaneous dissociation observed in this system, as described above; while for the $|q| = 3.0$ value it is almost 1600 kJ mol^{-1}. The barriers are generally by ca. 20-40 kJ mol^{-1} higher, than the dissociation free energies, thus, the barrier of the reverse process is, interestingly, hardly changing at all. Since the disparity in ion size has also been reported to have an impact on the structure of ionic liquids,[406,407] while the size itself has been shown to have an effect on the association behavior,[129] the Lennard–Jones parameters of the sodium ion have also been varied at $|q| = 0.8$ charges, shifting the location of the potential minimum closer to or farther away from the sodium ion, thus practically changing the size of this ion. As it is shown in Table 3.9, the

Table 3.10: Free energy barrier and free energy of dissociation of the NaCl ion pair (in kJ mol^{-1} units) with different sizes of the Na^+ ion.

	50 %	**100 %**	**150 %**	**200 %**
$\Delta A^{\ddagger}$	54	29	33	12
ΔA	29	8	26	−4

Na^+-Cl^- and Na^+-Br^- distances are, as expected, significantly increased by the change of the sodium ion's size, while those distances involving only the chloride anion remain mostly in the same range. The increased size of the sodium cation reduces the charge density at its surface, and therefore the attractive Coulombic interactions with the chloride and bromide anions are decreased. Accordingly, with increased sizes (150 % and 200 %) similar spontaneous dissociation of the NaCl ion pair occurs, as it has been shown for the $|q| = 0.5$ case above, and also the dissociation free energies and free energy barriers show a generally decreasing, albeit somewhat scattering trend (Table 3.10). Similarly, the solute-solvent interactions are weakened by enlarging the sodium, as shown by the more frequent exchange of the Br^- anions in the solvent shell of the Na^+ cation.

However, while the strength of each Na^+-Br^- interplay is decreased by the increasing size of the Na^+, the number of interactions is also increased, and the average number of bromide anions around the sodium cation grows from 2.64 to 4.72 (Table 3.9), although the dissociation of the NaCl ion pair also takes a major role in this increase, as described above. Interestingly, not only the size and the composition of the solvent shell changes, but also the solute-solvent interaction modes: while in Table 3.7 it can be seen that by approaching higher charges the weaker, dispersion-like Na-butyl interplay becomes less significant (see $d_{Na-C_{term}}$ values), the larger size and the corresponding smaller charge density allows this interaction to take a somewhat larger part in the solvation (Table 3.9). This is shown by the Na-C_{term} distances, which are decreasing with the increasing size of the ion, unlike any other distances involving the Na^+. This has some resemblance

to the so-called microheterogeneity in ILs with long alkyl groups, where the non-polar side chains aggregate and form a microstructure within the IL.[105,106,408]

Summary and Conclusion

In the present paper we showed that considering the charge transfer has a dramatic effect on the ion pairing behavior of ionic liquids, and resolves many discrepancies in earlier literature. We found large charge transfer values—viz. the decrease of the total charge on the ions—between the cation and the anion of a series of ionic liquid ion pairs, which is in agreement with previous *ab initio* data,[79] and also with the general behavior of force fields for ionic liquids by charge alteration.[130,394,396,397] Since the comparison of the conductivity values and the ions' mobilities[123,125]—defining the term "ionicity"—must include the charge that is transported by the movement of the ions, the observed decrease of the charges affects greatly the interpretation of the observed ionicity values. Apparently, the originally published values involve not only the association processes, but also the charge transfer; in other words, while the neutralization of the mobile particles indeed occurs, it is not or not only via ion pair formation, but also via charge transfer. The charge-corrected values show, accordingly, a much more independent movement of the ions, and although the association of ions is still observable after correction, ion pairing seems less important than thought before based on conductivity measurements.

After having seen the importance of the charge transfer in ionic liquids, we focused on the structural effects of the differently separated charges within a probe ion pair in an ionic liquid, by using molecular dynamics simulations. The solvation of the NaCl probe ion pair showed large changes upon altering the charge on the sodium and on the chloride. By increasing the charge on the ions, the Na-Cl and the solute-solvent interactions become stronger, and the association of the ion pair is favored, while the solvent shell becomes more static and concomitant ion pair formation in the IL itself is induced in the solvent shell. The decrease of the charge has the opposite effect, and one may assume that by

the charge transfer the structure of the ionic liquid changes, and by becoming somewhat similar to a molecular liquid rather than a salt, it is becoming more fluid. This is in clear agreement with, and may explain the previous rule of thumb in molecular dynamics simulations of ionic liquids that the viscosities and other dynamic properties become more realistic, and more liquid-like if the charges are scaled by a factor of ca. 0.8.[130,394,396,397]

In summary, the importance of charge transfer is clearly indicated, which does not only explain, at least in part, the previously observed discrepancies between conductivity measurements and other approaches aiming to understand ion pairing in ionic liquids, but also that the structure is highly affected by it. The more molecular liquid-like structure of ILs, which is achieved by the charge transfer between the ions, may also serve as a significant contribution to answer the question, why are ionic liquids liquid?

Acknowledgments This work has been financially supported by DFG project SPP 1708. The support for O. Hollóczki by the Alexander von Humboldt-Stiftung is gratefully acknowledged.

3.4 Rotaxanes

3.4.1 Substituent Effects on Axle Binding in Amide Pseudorotaxanes: Comparison of NMR Titration and ITC Data with DFT Calculations

Lena Kaufmann,[a] Egor V. Dzyuba,[a] Friedrich Malberg,[b], Nora L. Löw,[a] Matthias Groschke,[a] Boris Brusilowskij,[a] Juhani Huuskonen,[c] Kari Rissanen,[c] Barbara Kirchner*[b] and Christoph A. Schalley*[a]

Received 26th January 2012, Accepted 23th March 2012

DOI: 10.1039/c2ob25196e†‡

Kaufmann, L.; Dzyuba, E. V.; Malberg, F.; Löw, N. L.; Groschke, M.; Brusilowskij, B.; Huuskonen, J.; Rissanen, K.; Kirchner, B.; Schalley, C. A. *Org. Biomol. Chem.* **2012**, *10*, 5954–5964 - Reproduced by permission of The Royal Society of Chemistry.

Own contributions to this manuscript:

- Static quantum chemical calculations
- Frequency calculations
- Interpretation of data
- Co-writing of the manuscript (theoretical part)

[a] *Institut für Chemie und Biochemie, Freie Universität Berlin, Takustraße 3, 14195 Berlin, Germany. E-mail: christoph@schalley-lab.de; Fax: (+49) 30-838-55817*

[b] *Wilhelm-Ostwald-Institut für Physikalische und Theoretische Chemie Universität Leipzig, Linnéstraße 2, 04103 Leipzig, Germany. E-mail: bkirchner@uni-leipzig.de; Fax: (+49)341-9736399*

[c] *Department of Chemistry, Nanoscience Center, University of Jyväskylä, P.O. Box 35, 40014 Jyväskylä, Finland*

† This article is part of the *Organic & Biomolecular Chemistry* 10th Anniversary issue.

‡ Electronic supplementary information (ESI) available: Results from NMR titrations and ITC measurements, crystallographic data, and theoretical calculations. CCDC 853879 and 853880. For ESI and crystallographic data in CIF or other electronic format see DOI: 10.1039/c2ob25196e

Abstract The binding behavior of differently substituted diamide axle molecules to Hunter/Vögtle tetralactam macrocycles was studied with a combination of NMR titration, isothermal titration calorimetry (ITC) experiments and calculations employing density functional theory (DFT), along with dispersion-corrected exchange-correlation functionals. Guests with alkyl or alkenyl chains attached to the diamide carbonyl groups have a significantly higher binding affinity to the macrocycle than guests with benzoyl amides and their substituted analogues. While the binding of the benzoyl and alkenyl substituted axles is enthalpically driven, the alkyl-substituted guest binds mainly because of a positive binding entropy. The electronic effects of *para*-substituents at the benzoyl moieties have an influence on the binding affinities. Electron donating substituents increase, while electron-withdrawing substituents decrease the binding energies. The binding affinities obtained from both NMR titration and ITC experiments correlate well with each other. The substituent effects observed in the experimental data are reflected in adiabatic interaction energies calculated with density functional methods. The calculated structures also agree well with pseudorotaxane crystal structures.

Introduction

Pseudorotaxanes are weakly bound host–guest complexes bearing a thread-like linear axle that penetrates the cavity of a macrocyclic host.[132,409–419] They are the precursors of their mechanically interlocked siblings, *i.e.* rotaxanes and catenanes, and therefore play a pivotal role in the construction of molecular machines based on interlocked molecules.[161,173,420–434] Understanding the binding properties of pseudorotaxanes has thus an important impact on the development of template effects for rotaxane and catenane synthesis which can be, for example, based on metal complexation,[421,432,435–449] charge transfer interactions,[450–465] or hydrogen bonding to neutral amides,[138,143,164,165,466–468] secondary ammonium ions,[469–477] or anions.[145,162,478–487] Multiply interlocked supramolecular architectures have been synthesized[147,488–490] and were analyzed with respect to multi-

valent binding.[491–494] Other, squaraine-based, fluorescent rotaxanes have been used as long-term stable dyes in biological research.[495–498]

Tetralactam macrocycles (TLM) of the Hunter/Vögtle-type are well-known as host molecules and as rotaxane or catenane wheels. They bear four converging amide groups, which can form hydrogen bonds to suitable axle molecules. This property has not only been utilized for rotaxane and catenane synthesis, but also for the construction of quartz microbalance sensors that can detect carbonyl compounds[499–501] and for STM investigations of pseudorotaxane formation in TLM monolayers on gold surfaces.[502–504] The processes that occur during pseudorotaxane and rotaxane formation are known to be quite sensitive to structure and electronic environment. Therefore, small changes can cause unexpectedly large effects as investigated earlier by kinetic studies on the reverse reaction, *i.e.* the deslipping of axles with stopper groups of intermediate sizes.[134,505–507]

Jeong and co-workers[508] have examined the binding of a dicarbonyl guest to TLMs similar to **1a** (Scheme 3.1). In this study, both hemispheres of the macrocycle were pyridine-2,6-dicarboxamides. Substituents at the position *para* to the pyridine nitrogen atom cause strong electronic effects on the binding behavior of the TLM. This was rationalized by secondary effects[509–512] and perturbations of the intramolecular hydrogen bonds between the amide NH hydrogen atoms and the pyridine nitrogen. Therefore, a nitro group attached to the pyridine ring increases the binding strength significantly, while electron-donating groups reduce it.

A recent theoretical study[183] systematically varied the substituents on a *mono*-amide axle which is known to bind to Hunter/Vögtle TLMs by three hydrogen bonds. Two wheel amides donate one hydrogen bond each to the axle carbonyl group, which in turn donates its amide NH hydrogen to bind to a third amide carbonyl incorporated in the wheel. No significant substituent effects were observed, because the substituents alter the binding properties of the three hydrogen bonds in a counterbalancing way. When the (axle)C=O···H−N(wheel) hydrogen bonds are strengthened, the (axle)N−H···O=C(wheel) hydrogen bond

is weakened and *vice versa*. Thus, the substituents affect the individual hydrogen bonding strengths, but overall the effects more or less cancel each other. In marked contrast, a second theoretical paper[184] on pseudorotaxanes with different diamide axles reported strong substituent effects on the total interactions energies. Here, the binding situation is different, since the TLM (in this case the smaller Leigh-type TLM)[513,514] binds with all four amide NH groups to the two carbonyl groups of the diamide axle and thus excludes a similar compensation effect. Although the individual hydrogen bonds of the diamide pseudorotaxanes are somewhat weaker than those of the monoamide pseudorotaxanes, the calculations predict differences in the total interaction energies of 20 kJ mol^{-1} between the strongest and the weakest axle investigated. The individual hydrogen bonding energies correlate nicely with N−H stretch vibrational frequencies. Good linear correlations between these frequencies and Hammett's substituent constants[515] were found. So far, however, no experimental data supporting these calculations have been reported.

This has encouraged us to investigate the structural and electronic effects of different substituents on the binding of diamide axles to the unsymmetrically substituted TLM **1a** (Scheme 3.1). In order to obtain reliable data, NMR titrations were combined with isothermal titration calorimetry (ITC) experiments. Sessler *et al.*[516,517] compared both methods for calix[4]pyrrole, which binds ammonium salts in an ion-pair binding motif. They obtained comparable K_a values as long as the binding constants are within the dynamic ranges of both methods. This combination of methods provides structural information on the binding motifs from NMR experiments with detailed thermodynamic data from ITC measurements and therefore is of great benefit for a complete characterization of the pseudorotaxanes under study.[518] The experimental data are again accompanied with theoretical calculations employing density functional theory (DFT), along with dispersion-corrected exchange-correlation functionals which reflect the substituent effects and show similar trends as experimentally observed.

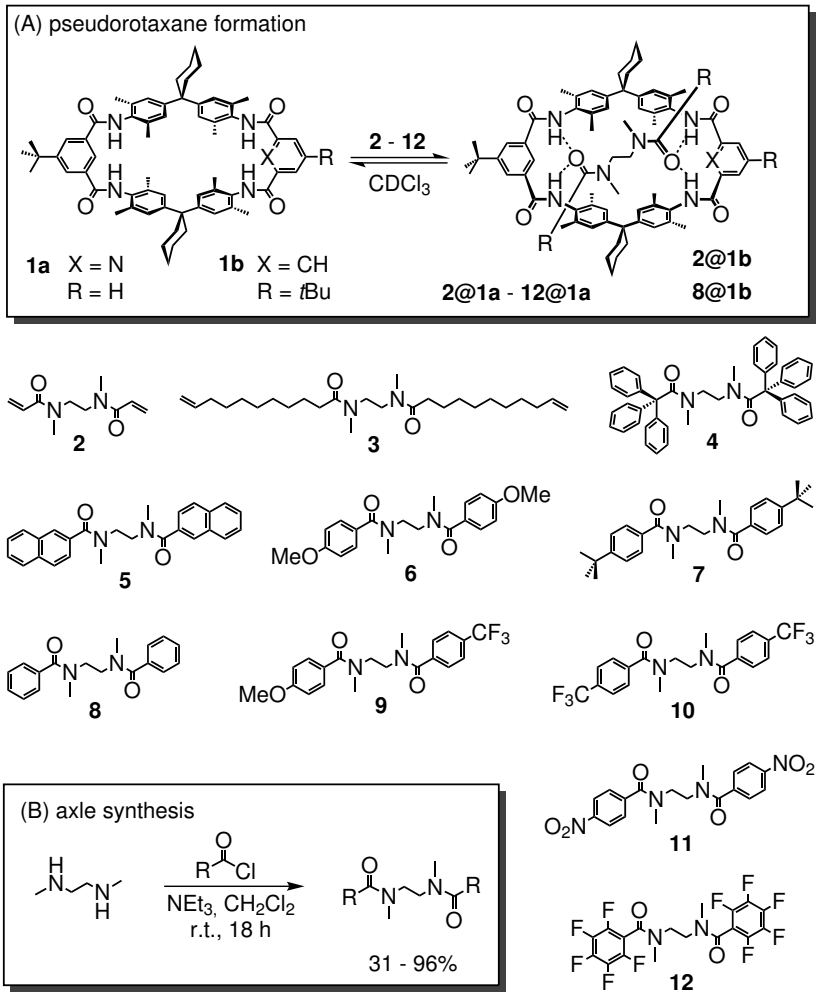

Scheme 3.1: (A) Binding motif of the pseudorotaxanes based on tetralactam macrocycles **1a** and **1b**; (B) synthesis of axles **2**–**12** with different R substituents and overview of diamide axles

Results and Discussion

TLMs **1a,b** (Scheme 3.1) were synthesized by an established literature procedure.[519] Macrocycle **1a** contains a pyridine-2,6-dicarboxamide on one side whose N atom points into the cavity and forms two intramolecular (pyridine)N···HN(amide) hydrogen bonds. They force the amide NH atoms to converge into the cavity and thus provide preorganization for a better binding of the axle's carbonyl groups.[520–523] The opposite hemisphere of **1a** contains an

isophthaloyl diamide substituted with a solubility-enhancing *t*-butyl group. On this side, one of the amide NH groups can rotate outwards so that one wheel carbonyl group can point into the cavity, if required by a guest. This conformational change neither has a significant barrier nor causes any substantial energy difference.[137,166,524]

The differently substituted diamide guest molecules **2**–**12** (Scheme 3.1) are available from simple one-step syntheses in good to excellent yields. Starting from *N,N'*-dimethyl ethylene diamine and the appropriately substituted acid chlorides, the desired products are obtained in separate reactions after stirring at room temperature in dichloromethane for 18 hours with NEt_3 as the base. An exception is guest **9**, which was synthesized in a step-by-step approach (see Experimental section). These diamide guests are known to bind noncovalently inside the cavity of **1a**—usually by forming four hydrogen bonds between the carbonyl groups of the guest and the amide hydrogen atoms of **1a,b**.[140,163] Consequently, a threaded geometry results. Because no bulky stopper groups terminate the axles, the association is reversible on a fast time scale. Since diamide axles are insoluble in organic solvents, when secondary amides are incorporated, their tertiary amide analogues were used for this study. The better solubility, however, comes at the price of higher conformational freedom, because the *cis*- and *trans*-amide isomers equilibrate. The *trans*, *trans*-isomer is the major isomer for the axles under study, but a significant contribution from the *trans*, *cis*- and a minor amount of the *cis*, *cis*-isomer is clearly visible in the axle NMR spectra.[525] Peak broadening at room temperature points to an interconversion of these isomers slow on the NMR time scale, but close to the coalescence temperature. The binding constants determined here thus are apparent binding constants. Single crystals of pseudorotaxanes **2@1b** and **8@1b** suitable for X-ray crystallography could be grown and their crystal structures were solved (Fig. 3.49 and ESI‡). In contrast to the other pseudorotaxanes under study here, these pseudorotaxanes bear the symmetrical wheel **1b** with two *t*-butyl-substituted isophthaloyl diamide moieties in the two hemispheres. Nevertheless, the two structures are quite instructive with respect

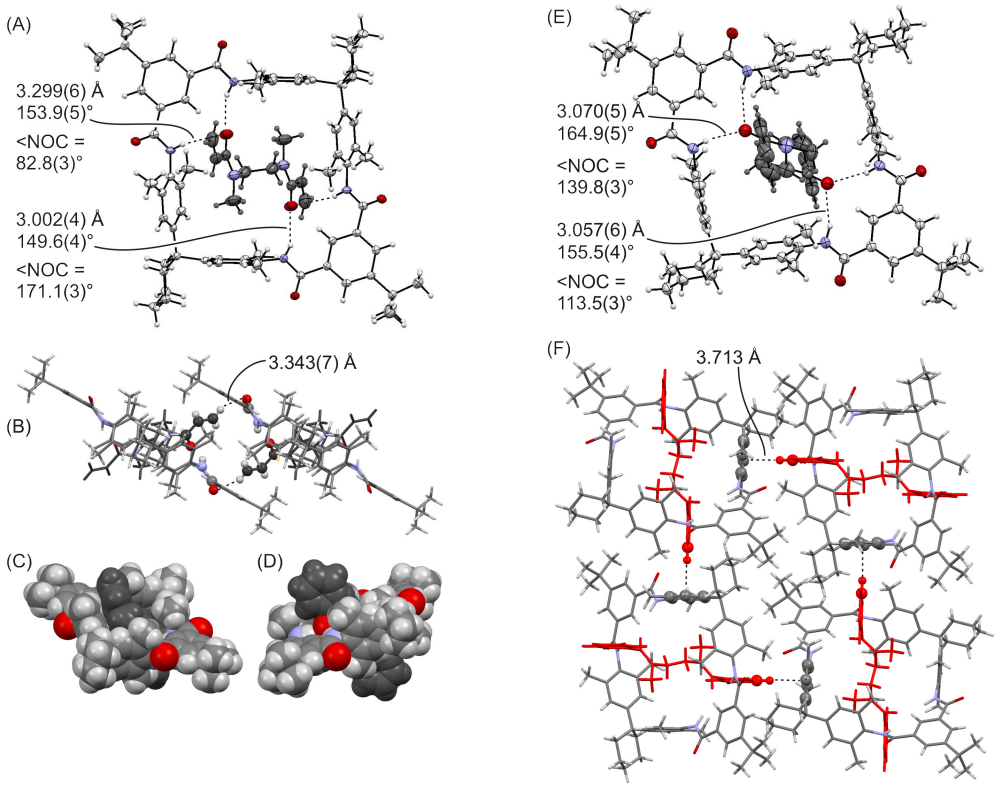

Figure 3.49: (A) Ortep plot of the crystal structure of **2@1b** (50 % probability level). (B) Packing of **2@1b** highlighting short C−H···O contacts between a vinyl H atom and a carbonyl O of the neighbor's wheel. (C, D) Space filling representations of **2@1b** and **8@1b**, respectively. (E) Ortep plot of the crystal structure of **8@1b** (50 % probability level). (F) Crystal packing of **8@1b** highlighting C−H···π contacts between the axle phenyl group and one of the wheel aromatic rings of a neighboring pseudorotaxane.

to the hydrogen bonding connecting the wheel with the diamide stations of the two axles. For **8@1b**, four hydrogen bonds connect axle and wheel (Fig. 3.49E). The N−O distances of 3.057 and 3.070 Å are in a normal range as found earlier in crystal structures[140,526–528] of rotaxanes and catenanes based on Hunter/Vögtle TLMs as well as in theoretical calculations.[137,166,524] Because of the zig-zag conformation of the ethylene diamide spacer connecting the two axle amide groups, the two axle carbonyl groups are unable to position themselves exactly in the mirror plane through the two isophthaloyl diamide groups of the macrocycle. Consequently, the N−H···O hydrogen bond angles differ by about 10°. The de-

viation of the carbonyl groups from the mirror plane is also reflected in the (wheel)N−O=C(axle) angles that are 113.5° and 139.8°. Thus, the structure of **8@1b** is in good agreement with expectation from earlier studies. The structure of **2@1b** (Fig. 3.49A) exhibits some contrasting features: The two (wheel)N−H···O=C(axle) hydrogen bonds in each hemisphere are very different in length (3.002 *vs.* 3.299 Å). Consequently, the axle forms two stronger and two weaker hydrogen bonds with the wheel. While the N−H···O angles are not much smaller than those of **8@1b**, the two (wheel)N−O=C(axle) angles describing the tilt of the axle carbonyls out of the wheel's mirror plane are drastically different. The shorter hydrogen bond corresponds to an almost linear arrangement (<NOC = 171.1°), while the longer one relates to an NOC angle of only 82.8°. The tilt of the carbonyl group out of the plane is thus much larger in **2@1b** as compared to **8@1b**. The packing of the two pseudorotaxanes exhibits C−H···O and C−H···π interactions, respectively: one of the vinyl hydrogen atoms at the terminal carbon atom of the axle in **2@1b** directly points towards a carbonyl oxygen atom of the next neighbor's wheel (Fig. 3.49B). With a value of 3.343 Å, the C−O distance is quite short for a C−H···O hydrogen bond. Instead, each of the phenyl rings of the axle in **8@1b** has a C−H···π contact with one of the aromatic rings in the wheel of the next neighbor pseudorotaxane. The distance between the C−H carbon atom and the centroid of the wheel's aromatic ring is 3.713 Å (Fig. 3.49F). Fig. 3.50 shows the results of a typical ^{1}H NMR titration experiment. Upon stepwise addition of axle **2** to **1a**, the two signals for the four wheel amide NH protons shift upfield by 1.46 ppm (py-NH) and 1.34 ppm (isoph-NH). Similarly, the proton at C(6) of the isophthaloyl moiety feels the presence of the axle inside the cavity of the wheel and shifts by 0.53 ppm to lower field.[529] The 1:1 stoichiometry of the axle–wheel complex is confirmed by the intersection of two lines fitted to the first and last four data points of the titration curve, respectively. They cross at a 1:1 host–guest ratio. In contrast, the signals for the diamide axle binding site, *i.e.* the axle NCH_3 and NCH_2 protons, shift to higher field, because they feel the anisotropy of the aromatic rings incorporated in the

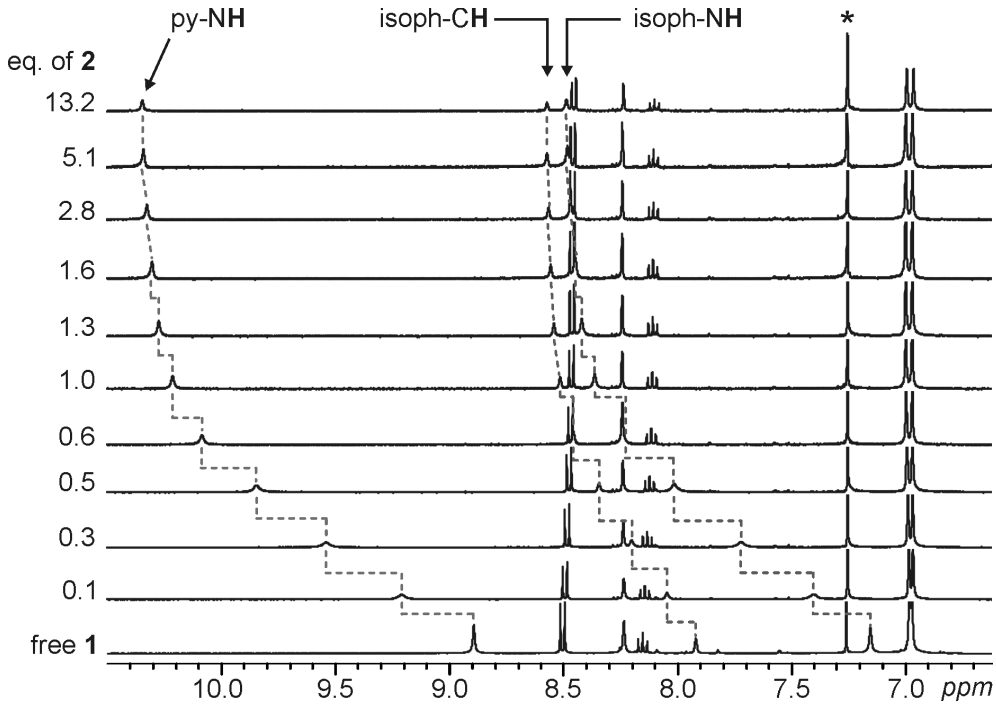

Figure 3.50: ^{1}H NMR titration of **1a** with **2** ($CDCl_3$, 298 K). The wheel's amide NH signals undergo significant complexation-induced low-field shifts. Also, the inner isophthaloyl C−H experiences low-field shifts due to the presence of the axle in the wheel's cavity.

wheel's walls. These complexation-induced shifts clearly confirm that the axle binds inside the wheel cavity by hydrogen bond formation between the wheel's amide NH hydrogen atoms and the axle's carbonyl oxygen atoms. Axle **4** can be used as a control to confirm the threaded geometry of the pseudorotaxanes under study: the two bulky trityl groups prevent slipping of this axle into the cavity so that either no or very different NMR signal shifts are expected. For this axle, only very minor shifts ($\Delta\delta < 0.1$ ppm) of the wheel's amide NH hydrogen atoms are observed. Also, the axle NCH_2 and NCH_3 protons do not shift during the titration. These results thus indicate the axle to be only weakly bound—if at all—at the macrocycle periphery outside the cavity. From the curvature of the titration curve (ESI‡), the binding constant was determined by nonlinear curve fitting based on eqn (3.12) and a 1:1 binding model.[530] In this equation, δ_{obs} is

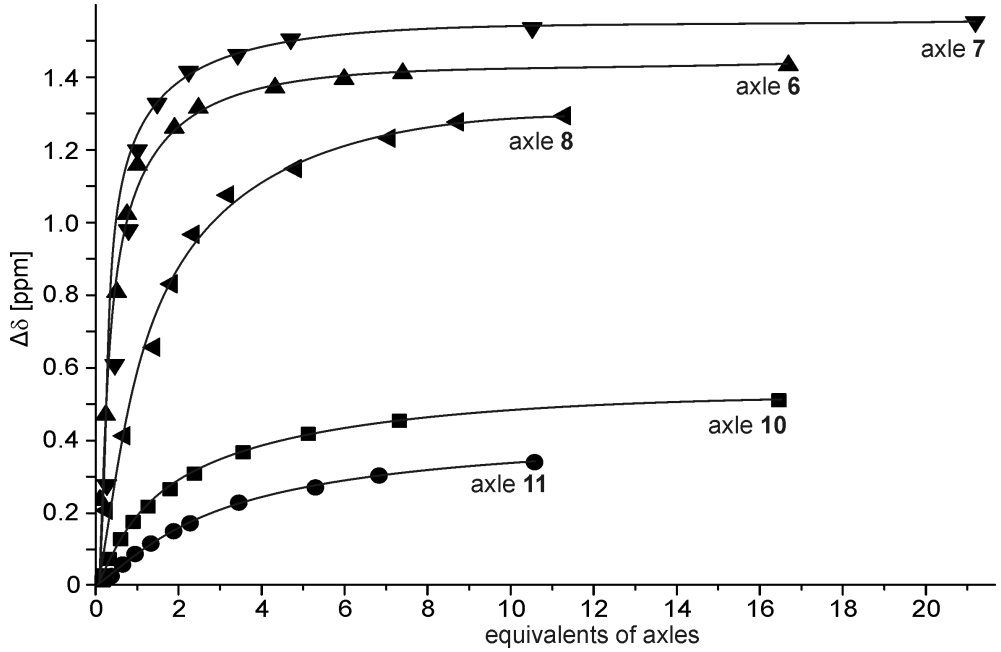

Figure 3.51: Shifts of the pyridine dicarboxamide NH signal of 1a during titrations with aryl-substituted axles **6**, **7**, **8**, **10** and **11** ($CDCl_3$, 298 K).

the observed shift of the py-NH signals of the macrocycle at each titration step as a function of the initial concentrations of macrocycle $[M]_0$ and guest $[G]_0$. δ_0 is the chemical shift of the free macrocycle and $\Delta\delta_{\max}$ is the difference between the theoretical signal shift at 100 % complexation and δ_0.

$$\delta_{\text{obs}} = \delta_0 + \frac{\Delta\delta_{\max}}{2[M]_0}\left[\frac{1}{K_{\text{a}}} + [M]_0 + [G]_0 - \sqrt{\left(\frac{1}{K_a} + [M]_0 + [G]_0\right)^2 - 4[M]_0[G]_0}\right] \tag{3.12}$$

$$c = nk_{\text{a}}[M]_0 \tag{3.13}$$

The same procedure was carried out for pseudorotaxanes **3@1a**–**12@1a** and the titration curves for the series of aryl-substituted axle derivatives **6**–**8**, **10** and **11** are summarized in Fig. 3.51. The resulting binding data are listed in Table 3.11.

Table 3.11: Thermodynamic data obtained from the NMR titrations and ITC measurements with pseudorotaxanes formed from TLM **1a** and guests **2**–**12**. NMR titrations and ITC measurements were performed at 25 °C.

	Hammett	NMR titrations[a]		ITC experiments[a]			
Axle	constant σ	K_a[M^{-1}]	ΔG[kJ mol^{-1}][b]	K_a[M^{-1}]	ΔH[kJ mol^{-1}]	$-T\Delta S$[kJ mol^{-1}]	ΔG[kJ mol^{-1}][b]
2		4000 ± 400	-20.6 ± 0.3	3500 ± 400	-38.2 ± 2.0	18.0 ± 2.3	-20.2 ± 0.3
3		3800 ± 400	-20.4 ± 0.3	2300 ± 300	-14.5 ± 0.8	-4.7 ± 1.1	-19.2 ± 0.3
4				No binding observed			
5		610 ± 70	-15.9 ± 0.3	490 ± 50	-24.9 ± 1.3	9.5 ± 1.6	-15.4 ± 0.3
6	-0.27	460 ± 50	-15.2 ± 0.3	510 ± 60	-18.9 ± 1.0	3.4 ± 1.3	-15.5 ± 0.3
7	-0.20	380 ± 40	-14.7 ± 0.3	640 ± 70	-29.6 ± 1.5	13.6 ± 1.8	-16.0 ± 0.3
8	0.00	370 ± 40	-14.7 ± 0.3	350 ± 40	-22.9 ± 1.2	8.4 ± 1.5	-14.5 ± 0.3
9		280 ± 30	-14.0 ± 0.3	190 ± 20	-32.5 ± 1.7	19.5 ± 2.0	-13.0 ± 0.3
10	0.43	< 20	-7.4	90 ± 10	-19.8 ± 1.0	8.6 ± 1.3	-11.2 ± 0.3
11	0.78	< 10	-5.7	No binding observed in ITC experiments			
12				No binding observed			

[a] Since NMR and ITC are different methods with respect to optimal concentration regimes and the primary information obtained, some deviations of the data can be expected as discussed earlier by Sessler *et al.*[516]

[b] Calculated with $\Delta G = -RT \ln K_a$

Two conclusions can be drawn from the NMR titration data. (i) Axles with alkyl (**3**) or alkenyl groups (**2**) attached to the diamide carbonyl groups have the highest binding constants among the axles under study. With about 4000 M^{-1}, they are roughly one order of magnitude higher than the phenyl substituted axle **8**. This results in the binding free energies of **2** and **3** being higher by *ca.* 6 kJ mol^{-1} than that of **8**. (ii) In the series of aryl-substituted diamides, the binding constants depend significantly on the electronic nature caused by the *para*-substituent. While electron-withdrawing substituents reduce the binding free energies, electron-donating substituents increase them. The axles with the strongest electron-withdrawing groups (*e. g.* NO_2) exhibit only vanishingly small binding constants; no binding was observed for the pentafluorophenyl-substituted axle **12**. Consequently, template effects for rotaxane synthesis based on similar diamide–TLM binding motifs can be modulated by substituent effects affecting the hydrogen bond acceptor qualities of the axle carbonyl groups. Fig. 3.52 exemplarily shows the titration curves for the complexation of **2** and **8** to TLM **1a** as obtained from complementary ITC experiments. The determination of K_a, ΔH, ΔG, and ΔS is simultaneously possible in a single experiment so that all relevant thermodynamic binding parameters can be obtained.[531,532] An important parameter for ITC experiments of low affinity systems is the so-called Wiseman "c" value, which is the product of the total host concentration and the binding constant K_a (eqn (3.13)).[533] For $c < 10$, ITC experiments become challenging. In this equation, n is the number of binding sites in the receptor with $n = 1$ for the pseudorotaxanes under study here. One way to compensate for low affinity binding would be to increase the total concentration of the macrocycle. Unfortunately, the solubility of TLM **1a** limits this approach here. An earlier report[534] on alkali metal ion binding to crown ethers, however, confirmed that ITC measurements still provide reliable data even when c is small and the titration curves are not sigmoidal in shape provided that the following requirement is met: a sufficiently large part of the binding isotherm with sufficient signal-to-noise must be used for analysis. Also, the stoichiometry of the complex formed must be clear

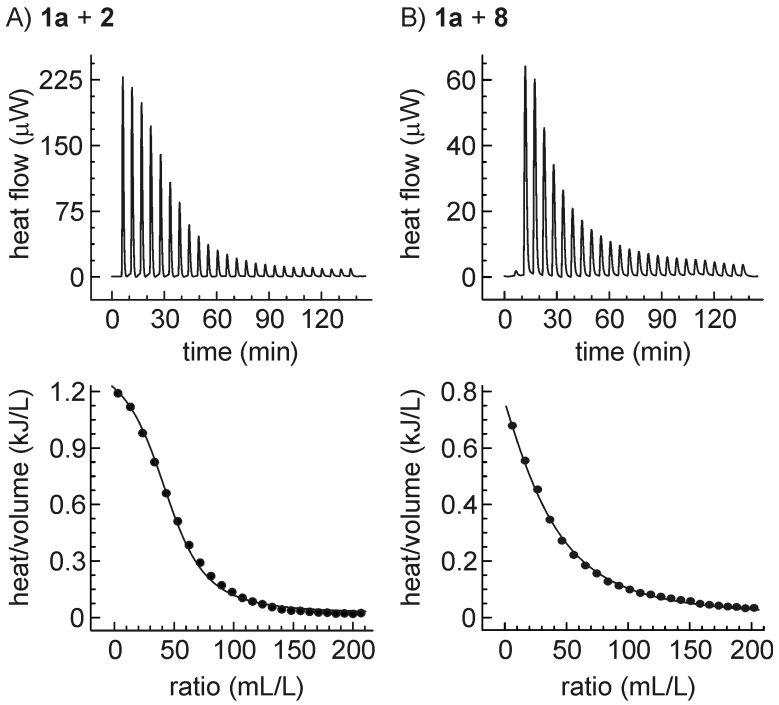

Figure 3.52: ITC experiments (heat flow *versus* time and heat/volume *versus* guest/TLM ratio; $CHCl_3$, 298 K) of (A) axle **2** and (B) axle **8** with TLM **1a**.

and the concentrations of both host and guest must be precisely known.

Making sure that these conditions are met, the binding free energies obtained from the ITC experiments (Table 1) agree well with those extracted from the NMR titrations within ±1.5 kJ mol^{-1} which corresponds to *ca.* 10 % of the total binding energies. Consequently, the conclusions drawn from the NMR data above are confirmed by the ITC data. Since the ITC experiments also provide binding enthalpies and binding entropies, a more detailed picture is obtained here. Axle **3** with the two long, flexible alkyl chains directly attached to the amide carbonyl groups has quite a low binding enthalpy, but a favorable positive binding entropy thus indicating the complexation to be significantly supported by entropic effects. In marked contrast, all axles that carry phenyl derivatives attached to the amide carbonyls, as well as axle **2** with the short alkenyl substituent, reveal approximately two times larger negative binding enthalpies, while all binding entropies are negative. Binding is clearly driven by enthalpy in these cases. Similar data

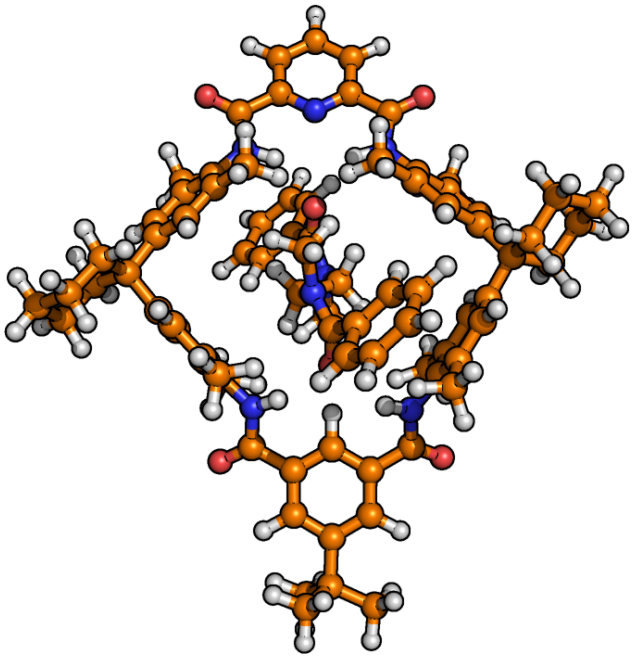

Figure 3.53: Structure of **8@1a** optimized at the B97-D level of theory with the TZVP basis set. For the calculated structures of the other aryl-substituted pseudorotaxanes, see ESI.‡

were obtained for monoamide binding in a related TLM.[183] We attribute the differences in binding entropies to solvent effects. The negative binding entropies for the aryl-substituted diamide axles are in line with the combination of two particles into one complex. The positive entropy for **3@1a** is then due to an overcompensation of this effect by differences in solvation.[535–538]

The substituent effects on the binding free energies have been investigated theoretically by density functional calculations at the B97-D/TZVP level. The structures of pseudorotaxanes with symmetrical aryl-substituted axles (**6@1a**–**8@1a** and **10@1a**–**12@1a**) were optimized starting from a geometry in which the diamide station was bound to the wheel by four (wheel)N−H···O=C(axle) hydrogen bonds. The optimized structure of **8@1a** is shown in Fig. 3.53 as a representative example. Hydrogen bond lengths and N−H···O angles are summarized in Table 3.12.

Table 3.12: Calculated hydrogen bond lengths and angles, adiabatic interaction energies ΔE_{adia}, energies ΔE_{CF} calculated for the conformational change of wheel and axle upon binding, and shared-electron number SEN for the series of pseudorotaxanes with symmetrically aryl-substituted axles (for definitions, see theoretical section). The four hydrogen bonds between axle are denoted "**py1/2**" for those in the pyridine dicarboxamide hemisphere and "**iso1/2**" for those in the isophthaloyl diamide hemisphere. "**py1**" and "**iso1**" diametrically oppose each other in the calculated structures

	N−H···O hydrogen bond lengths [Å]				N−H···O hydrogen bond angles [°]				ΔE_{adia}	ΔE_{CF}	SEN[a]
Axle	py1	py2	iso1	iso2	py1	py2	iso1	iso2	[kJ mol^{-1}]	[kJ mol^{-1}]	σ_{total}[e]
6	2.92	3.12	2.91	2.95	145.5	148.7	158.3	155.0	−194.4	−40.6	0.1206
7	3.03	2.99	3.15	3.11	146.0	146.9	162.7	149.2	−193.5	−28.7	0.0803
8	3.02	3.01	3.15	3.10	144.6	146.6	162.1	147.8	−182.1	−25.9	0.0770
10	3.04	3.08	3.15	3.09	140.3	144.6	160.1	147.3	−180.5	−28.2	0.0688
11	3.03	3.09	3.25	3.11	141.7	145.6	161.2	145.4	−178.4	−25.9	0.0626
12	3.10	4.37[b]	3.16	3.81[b]	133.3	154.7	146.5	163.0	−131.3	−35.7	0.0235

[a] The shared-electron numbers for the individual hydrogen bonds are given in the ESI.‡ [b] These N−O distances are too long to count as hydrogen bonds and likely do not contribute significantly to the binding.

The two hydrogen bonds formed to the pyridine dicarboxamide moiety are similar in length (3.01 and 3.02 Å) and somewhat shorter and likely somewhat stronger than the two hydrogen bonds formed with the isophthaloyldiamide group (3.15 and 3.10 Å). All four distances are nevertheless in the expected range (see Table 3.12). Thus, the tilt of the axle carbonyl group is more pronounced in the isophthaloyldiamide hemisphere of the complex as indicated also by the larger differences in N−H···O hydrogen bond angles on that side of the pseudorotaxane. In addition, also the angles are within the expected range. The other calculated structures do not deviate much from these values with one exception. The most weakly bound pseudorotaxane, *i.e.* the pentafluorophenyl-substituted axle **12**, forms only two hydrogen bonds. For the **py2** and **iso2** hydrogen bonds (Table 3.12), the N−O distances are 3.81 and 4.37 Å so we can safely assume these do not contribute significantly to the binding.

In order to study the substituent effects on the binding energies theoretically, the adiabatic interaction energies ΔE_{adia} were calculated according to eqn (3.14), in which E_{total} is the total energy calculated for the complex, E_{relaxed} the total energies of the two components in their conformationally relaxed geometries and ΔE_{BSSE} the basis set superposition error. The absolute values given in Table 3.12 are much higher than the experimental data. This, however, does not come as a surprise,[183] because the calculations do not involve competition of the axle with the solvent for binding inside the cavity of the TLM. More relevant are the substituent-dependent differences, which follow the same trend as the experimental values. More electron-donating axle substituents result in higher binding energies, because they increase the donor strengths of the axle carbonyl oxygen atoms and thus improve their hydrogen-bond acceptor qualities. Upon binding, both the wheel and the axle rearrange with respect to their con- formations to some extent in order to mutually accommodate the binding partner. The ΔE_{CF} values in Table 3.12 (eqn (3.15)) provide an estimate of the rearrangement energy necessary to bring the wheel and axles from their relaxed conformations into the structure which they finally have in the complex. With values between −25 and

-40 kJ mol^{-1}, these rearrangement energies are quite substantial.

$$\Delta E_{\text{adia}} = E_{\text{total}}^{\text{complex}} - E_{\text{relaxed}}^{\text{wheel}} - E_{\text{relaxed}}^{\text{axle}} - \Delta E_{\text{BSSE}} \tag{3.14}$$

$$\Delta E_{\text{CF}} = (E_{\text{relaxed}}^{\text{wheel}} - E_{\text{unrelaxed}}^{\text{wheel}}) + (E_{\text{relaxed}}^{\text{axle}} - E_{\text{unrelaxed}}^{\text{axle}}) \tag{3.15}$$

$$\Delta E_{\text{SEN}} = m \cdot \sigma_{HA} + b \tag{3.16}$$

Finally, the trend in substituent effects is also supported by the shared-electron numbers (SEN) for the hydrogen bonds between axles and wheels (also, see ESI‡). The SEN provides a semi-quantitative measure of the hydrogen bond strengths, because the linear relationship in eqn (3.16) exists, in which σ_{HA} represents the two-center shared electron number of a hydrogen bond and ΔE_{SEN} its binding energy. Even if one does not determine the slope and intercept, which differ with acceptor atom and the combination of functional and basis set, trends can easily be determined from the SEN values. From the data given in Table 3.12, the trend to stronger binding with more electron-donating substituents is clearly visible.

Conclusions

In conclusion, the choice of the substituents at the diamide axle changes the binding properties in several ways and can thus be utilized to fine-tune the binding properties. First, the alkyl- and alkenyl-substituted diamides bind with binding constants higher than the aryl-substituted axles by an order of magnitude. Second, the binding is driven by enthalpic effects, if the axle carries substituents with π-systems attached to the amide carbonyl groups. Only the formation of pseudorotaxane **3@1a** with alkyl chains at the carbonyl carbon atoms is due to positive binding entropies. Third, within the series of differently substituted aryl diamides, the electronic substituent effects are important for the formation of pseudorotaxanes. Electron-withdrawing substituents diminish the binding constants as compared to electron-donating substituents. The trends of binding energies thus follow the Hammett substituent parameters.

The experimental and theoretical results nicely agree with respect to the electronic substituent effects and thus have an impact on the design of template

effects for rotaxane synthesis. For example, it would be advantageous to elongate the axles for stopper attachment through ether linkages at the phenyl-C(4) rather than using esters or amides. Ethers would enhance the templating ability, while esters or amides would almost lead to the loss of the noncovalent connections between wheel and axle during rotaxane formation.

Our study complements an earlier study by Jeong *et al.*[508] who reported substituent effects on the ability of TLMs to bind the same diamide station. The changes found in our study are not as drastic as those reported by Jeong and coworkers, but they are still substantial. Furthermore, our binding data lends support to a recent theoretical study.[184] Even though a slightly different TLM was used for the calculated binding data, the trends are well confirmed in our study by experiment.

The present report is one of few which directly compare binding data from NMR titrations with ITC results and theoretical calculations. The pseudorotaxanes under study exhibit binding constants at the lower end of the ITC dynamic range, which is roughly between $10^2\ \mathrm{M}^{-1} < K_a < 10^7\ \mathrm{M}^{-1}$, and thus belong to the low-affinity systems, which do not fulfill the broadly accepted requirement that Wiseman's c value should be larger than 10. Nevertheless, the data obtained from both methods reveals quite good agreement. In line with a previous report on alkali metal ion/crown ether binding,[534] we conclude that these low-affinity systems can be studied by isothermal titration calorimetry. On the one hand, the combination of both methods is advantageous, because they overlap in yielding binding free energies, which can be directly compared and—in the case of good agreement—provides more confidence in the data. On the other hand, both methods contribute their individual share to the understanding of complex formation. While structural information can be extracted from NMR experiments, ITC measurements directly provide binding enthalpies and binding entropies. Otherwise, the determination of these two values would require the much higher effort of temperature-dependent NMR titrations.

Experimental section

General methods Reagents were purchased from Aldrich, ACROS or Fluka and used without further purification. TLMs **1a,b** were synthesized according to literature procedures.[519] The acid chloride for the synthesis of guest **4** was obtained from the corresponding triphenyl acetic acid by reaction with oxalyl chloride and a few drops of dry DMF in CH_2Cl_2. After a clear solution formed while stirring the reaction mixture at r.t., the solvents were evaporated under reduced pressure and the residue was used without further purification. All other acid chlorides were commercially available and used as purchased. Yields refer to chromatographically and spectroscopically homogeneous materials. Solvents were dried and distilled prior to use by usual laboratory methods. Thin-layer chromatography (TLC) was performed on precoated silica gel 60/F254 plates (Merck KGaA). Silica gel (0.04–0.063 mm; Merck) was used for column chromatography.

NMR spectroscopy and NMR titrations ^{1}H (400 MHz), ^{19}F (376 MHz) and ^{13}C (100 MHz) spectra were obtained on a Bruker ECX 400 instrument at 298 K. All chemical shifts are reported in ppm with signals of $CHCl_3$ (7.26 ppm (^{1}H) and 77.0 ppm (^{13}C)) or CCl_3F (0 ppm (^{19}F)) taken as internal standards; coupling constants are in Hz. The following abbreviations were used to indicate NMR multiplicities: s (singlet), d (doublet), t (triplet), q (quartet), m (multiplet), br (broad). Titration experiments were carried out in $CDCl_3$ at 25 ℃ on a Bruker ECX 400 instrument. Solutions of **1a** ($c = 5$ mM, 0.6 mL) were placed in NMR tubes and treated with various amounts of the guests **2**–**12** ($c = 50$ mM). After each injection, a ^{1}H NMR spectrum was recorded immediately. The true guest concentrations in the solution under study were determined by integration of the signals for the wheel versus the integration of the signals for guest protons. The binding constants were determined based on 1:1 binding model by fitting the experimental data with eqn (3.12). Nonlinear curve fitting was achieved with the tools implemented in *IgorPro* (Wavemetrics Inc., Lake Oswego, Oregon/USA).

Mass spectrometry Samples were measured on an Agilent 6210 ESI-TOF, Agilent Technologies, Santa Clara, CA, USA, with methanol as the spray solvent. The solvent flow rate was adjusted to 4 μL min^{-1} and the spray voltage set to 4 kV. The drying gas flow rate was adjusted to 15 psi (1 bar). All other parameters were optimized for a maximum abundance of the $[M + Na]^+$ ions.

Isothermal titration calorimetry (ITC) Titration experiments were carried out in $CHCl_3$ at 298 K on a TAM III microcalorimeter (Waters GmbH, TA Instruments, Eschborn, Germany). In a typical experiment, an 800 μL solution of 1a was placed in the sample cell at a concentration of 2 mM, and 250 μL of one of the guests **2**–**12** were in the injection syringe at a concentration of 40 mM in the same solvent. The titration schedule consisted of 25 consecutive injections of 8μL with a 5 min interval between injections. Heats of dilution, measured by titration of the guest into the sample cell with blank solvent, were subtracted from each data set. All solutions were degassed prior to titration. Titrations were repeated twice. The data were analyzed using the instrumental internal software package and fitted with a one-site binding model.

General procedure for the synthesis of the diamide guests (2–8, 10–12) Under argon, *N,N'*-dimethylethylenediamine (300 mg, 3.4 mmol) was dissolved in 30 mL CH_2Cl_2 and treated with 1.5 mL NEt_3. A solution of acid chloride (7.0 mmol) in 20 mL CH_2Cl_2 was slowly added and the resulting solution was stirred at r.t. for 18 h. The solvent was then evaporated and the products were isolated by column chromatography (silica gel, pure CH_2Cl_2 to CH_2Cl_2–acetone 2 : 1 or pure EtOAc).

Synthesis of the diamide guest (9)

Under argon, *N,N'*-dimethylethylenediamine (300 mg, 3.4 mmol) was dissolved in 30 mL CH_2Cl_2 and treated with 1.5 mL NEt_3. A solution of 4-methoxybenzoyl chloride (2.72 mmol) in 10 mL CH_2Cl_2 was slowly added and the resulting solution was stirred at r.t. for 4 h. After that, a solution of 4-trifluoromethylbenzoyl

chloride (2.72 mmol) in 10 mL CH_2Cl_2 was again slowly added and the resulting solution was left stirring at r.t. for another 14 h. The solvent was then evaporated and the product was isolated by column chromatography (preparative TLC, silica gel, CH_2Cl_2–EtOAc 1:1).

***N,N'*-(Ethane-1,2-diyl)bis(*N*-methylacrylamide) 2**

Yellow oil (0.33 g, 50 %); R_f = 0.34 (EtOAc); ^{1}H NMR (400 MHz, $CDCl_3$): δ = 3.03, 3.04, 3.12 (3 s, 6H; NCH_3), 3.51–3.62 (3 s, 4H; NCH_2), 5.63–5.68 (m, 2H; CH=CH_2),6.26–6.35 (m, 2H; CH=CH_2), 6.46–6.65 ppm (m, 2H; CH=CH_2); ^{13}C NMR (100 MHz, $CDCl_3$): δ = 34.2, 36.1, 37.4 (CH_3), 45.1, 47.3, 47.6 (CH_2), 127.0, 127.2, 127.8, 127.9, 128.4, 128.7 (CH_2, CH), 166.8 ppm (C=O); ESIMS: m/z (%): 219.1 (100) $[M+Na]^+$; HRMS (ESI$^+$): m/z calcd for $C_{26}H_{48}N_2O_2Na^+$: 219.1104 $[M + Na]^+$; found: 219.1107 (Δ = 1.4 ppm).

***N,N'*-(Ethane-1,2-diyl)bis(*N*-methylundec-10-enamide) 3**

Yellow oil (0.95 g, 67 %); R_f = 0.12 (CH_2Cl_2), 0.98 (CH_2Cl_2–acetone 2 : 1); ^{1}H NMR (400 MHz, $CDCl_3$): δ = 1.34 (br, 16H; CH_2), 1.39–1.44 (m, 4H; CH_2), 1.53–1.62 (m, 4H; CH_2), 2.06 (q, ^{3}J = 7.3 Hz, 4H; CH_2), 2.29 (m, 4H; CH_2), 2.96, 3.06, 3.08 (3 s, 6H; NCH_3), 3.54, 3.57, 3.60 (3 s, 4H; NCH_2), 4.91–5.02 (m, 4H; CH=CH_2), 5.77–5.87 ppm (m, 2H; CH=CH_2); ^{13}C NMR (100 MHz, $CDCl_3$): δ = 25.1, 27.5, 29.0, 29.2, 29.4, 29.5, 29.6, 33.9, 35.7, 44.6 (CH_2, CH_3), 114.2 (CH_2), 139.3 (CH), 173.6 ppm (C=O); ESIMS: m/z (%): 443.4 (100) $[M+Na]^+$; HRMS (ESI$^+$): m/z calcd for $C_{26}H_{48}N_2O_2Na^+$: 443.3608 $[M + Na]^+$; found: 443.3605 (Δ = -0.7 ppm).

***N,N'*-(Ethane-1,2-diyl)bis(*N*-methyl-2,2,2-triphenylacetamide) 4**

White powder (1.13 g, 53 %); R_f = 0.10 (CH_2Cl_2), 0.95 (CH_2Cl_2–acetone 2 : 1); ^{1}H NMR (400 MHz, $CDCl_3$): δ = 2.42 (s, 6H; NCH_3), 3.62 (s, 4H; NCH_2), 7.19–7.31 ppm (m, 30H; ArH); ^{13}C NMR (100 MHz, $CDCl_3$): δ = 38.5 (CH_3), 53.4 (CH_2), 67.3 (C_q), 126.6, 127.7, 130.1 (Ar−CH), 142.8 (Ar−C_q), 173.0 ppm

(C=O); ESIMS: m/z (%): 651.3 (100) $[M + Na]^+$; HRMS (ESI$^+$): m/z calcd for $C_{44}H_{40}N_2O_2Na^+$: 651.2982 $[M + Na]^+$; found: 651.2986 (Δ = 0.6 ppm).

***N,N'*-(Ethane-1,2-diyl)bis(*N*-methylnaphthamide) 5**

White powder (0.62 g, 46 %); R_f = 0.79 (CH_2Cl_2–acetone 2 : 1); ^{1}H NMR (400 MHz, $CDCl_3$): δ = 3.16 (br, 6H; NCH_3), 3.97 (br, 4H; NCH_2), 7.47–7.49 (m, 6H; ArH), 7.78–7.91 ppm (m, 8H; ArH); ^{13}C NMR (100 MHz, $CDCl_3$): δ = 37.8 (CH_3), 44.4 (CH_2), 67.3 (C_q), 112.1, 124.0, 126.4, 126.5, 126.8, 127.6, 128.0, 128.2, 132.5, 133.4 (Ar−CH, Ar−C_q), 171.8 ppm (C=O); ESIMS: m/z (%): 419.2 (100) $[M + Na]^+$; HRMS (ESI$^+$): m/z calcd for $C_{26}H_{24}N_2O_2Na^+$: 419.1730 $[M + Na]^+$; found: 419.1736 (Δ = 1.4 ppm).

***N,N'*-(Ethane-1,2-diyl)bis(4-methoxy-*N*-methylbenzamide) 6**

White powder (1.16 g, 96 %); R_f = 0.78 (CH_2Cl_2–acetone 2 : 1); ^{1}H NMR (400 MHz, $CDCl_3$): δ = 2.75–3.04 (br m, 6H; NCH_3), 3.39–3.80 (br m, 10H; NCH_2, OCH_3), 6.79 (d, ^{3}J = 6.3 Hz, 4H; ArH), 7.28–7.38 ppm (m, 4H; ArH); ^{13}C NMR (100 MHz, $CDCl_3$): δ = 37.8, 55.1 (CH_3), 44.3 (CH_2), 113.3, 128.6 (Ar−CH), 128.2, 160.3 (Ar−C_q), 171.6 ppm (C=O); ESIMS: m/z (%): 379.2 (100) $[M + Na]^+$; HRMS (ESI$^+$): m/z calcd for $C_{20}H_{24}N_2O_4Na^+$: 379.1634 $[M + Na]^+$; found: 379.1641 (Δ = 1.9 ppm).

***N,N'*-(Ethane-1,2-diyl)bis(4-(*t*-butyl)-*N*-methylbenzamide) 7**

White powder (1.22 g, 88 %); R_f = 0.81 (CH_2Cl_2–acetone 2 : 1); ^{1}H NMR (400 MHz, $CDCl_3$): δ = 1.29 (s, 18H; *t*Bu-H), 2.77–3.09 (br m, 6H; NCH_3), 3.60–3.87 (br m, 4H; NCH_2), 7.31–7.39 ppm (m, 10H; ArH); ^{13}C NMR (100 MHz, $CDCl_3$): δ = 31.1, 34.7 (CH_3), 37.9 (C_q), 44.4 (CH_2), 125.1, 126.7 (Ar−CH), 133.3, 152.6 (Ar−C_q), 172.0 ppm (C=O); ESIMS: m/z (%): 431.3 (100) $[M + Na]^+$; HRMS (ESI$^+$): m/z calcd for $C_{26}H_{36}N_2O_2Na^+$: 431.2675 $[M + Na]^+$; found: 431.2687 (Δ = 2.8 ppm).

***N,N'*-(Ethane-1,2-diyl)bis(*N*-methylbenzamide) 8**

White powder (0.89 g, 88 %); R_f = 0.73 (CH_2Cl_2–acetone 2 : 1); ^{1}H NMR (400 MHz, $CDCl_3$): δ = 2.58–3.08 (br m, 6H; NCH_3), 3.22–3.77 (br m, 4H; NCH_2), 7.06–7.26 ppm (m, 10H; ArH); ^{13}C NMR (100 MHz, $CDCl_3$): δ = 37.4 (CH_3), 44.0 (CH_2), 126.4, 127.9, 129.0 (Ar−CH), 135.9 (Ar−C_q), 171.5 ppm (C=O); ESIMS: m/z (%): 319.1 (100) $[M+Na]^+$; HRMS (ESI$^+$): m/z calcd for $C_{18}H_{20}N_2O_2Na^+$: 319.1417 $[M+Na]^+$; found: 319.1423 (Δ = 1.9 ppm).

4-Methoxy-*N*-methyl-*N*-(2-(*N*-methyl-4-(trifluoromethyl)-benzamido) ethyl)benzamide 9

White powder (0.41 g, 31 %); R_f = 0.48 (CH_2Cl_2−EtOAc 1 : 1); ^{1}H NMR (400 MHz, $CDCl_3$): δ = 3.08–3.15 (br m, 6H; NCH_3), 3.80–3.92 (br m, 7H; NCH_2, OCH_3), 6.87 (d, ^{3}J = 7.8 Hz, 2H; ArH), 7.37 (d, ^{3}J = 7.8 Hz, 2H; ArH), 7.51 (d, ^{3}J = 8.1 Hz, 2H; ArH), 7.64 ppm (d, ^{3}J = 8.1 Hz, 2H; ArH); ^{13}C NMR (100 MHz, $CDCl_3$): δ = 37.8, 55.0 (CH_3), 44.4 (CH_2), 113.4, 125.3, 126.9, 128.7 (Ar−CH), 122.3, 128.1, 139.7, 141.1, 160.3 (C_q, Ar−C_q), 170.4, 171.2 ppm (CvO); ^{19}F NMR (376 MHz, $CDCl_3$): δ = −62.8 ppm (s, 6F; CF_3); ESIMS: m/z (%): 417.1 (100) $[M+Na]^+$; HRMS (ESI$^+$): m/z calcd for $C_{20}H_{21}F_3N_2O_3Na^+$: 417.1402 $[M+Na]^+$; found: 417.1413 (Δ = 2.6 ppm).

***N,N'*-(Ethane-1,2-diyl)bis(*N*-methyl-4-(trifluoromethyl)-benzamide) 10**

White powder (1.37 g, 93 %); R_f = 0.69 (CH_2Cl_2–acetone 2 : 1); ^{1}H NMR (400 MHz, $CDCl_3$): δ = 3.06 (br s, 6H; NCH_3), 3.90 (br s, 4H; NCH_2), 7.48 (d, ^{3}J = 8.2 Hz, 4H; ArH), 7.61 ppm (d,^{3}J = 7.9 Hz, 4H; ArH); ^{13}C NMR (100 MHz, $CDCl_3$): δ = 37.7 (CH_3), 44.7 (CH_2), 125.5, 127.1 (Ar−CH), 122.9, 124.5, 139.8 (C_q, Ar−C_q), 170.7 ppm (C=O); ^{19}F NMR (376 MHz, $CDCl_3$): δ = −62.8 ppm (s, 6F; CF_3); ESIMS: m/z (%): 455.1 (100) $[M+Na]^+$; HRMS (ESI$^+$): m/z calcd for $C_{20}H_{18}F_6N_2O_2Na^+$: 455.1170 $[M+Na]^+$; found: 455.1153 (Δ = −3.7 ppm).

***N,N'*-(Ethane-1,2-diyl)bis(*N*-methyl-4-nitrobenzamide) 11**

Yellow powder (1.16 g, 89 %); R_f = 0.65 (CH_2Cl_2–acetone 2 : 1); ^{1}H NMR (400 MHz, $CDCl_3$): δ = 3.01 (br s, 6H; NCH_3), 3.89 (br s, 4H; NCH_2), 7.50 (d, ^{3}J = 8.9 Hz, 4H; ArH), 8.16 ppm (d, ^{3}J = 8.9 Hz, 4H; ArH); ^{13}C NMR (100 MHz, $CDCl_3$): δ = 37.6 (CH_3), 44.7 (CH_2), 123.7, 127.6 (Ar−CH), 142.3, 148.1 (Ar−C_q), 169.7 ppm (C=O); ESIMS: m/z (%): 409.1 (100) $[M + Na]^+$; HRMS (ESI^+): m/z calcd for $C_{18}H_{18}N_4O_6Na^+$: 409.1124 $[M + Na]^+$; found: 409.1133 (Δ = 2.2 ppm).

***N,N'*-(Ethane-1,2-diyl)bis(pentafluoro-*N*-methylbenzamide) 12**

Orange powder (1.49 g, 92 %); R_f = 0.14 (CH_2Cl_2); ^{1}H NMR (400 MHz, $CDCl_3$): δ = 3.04 (br s, 6H; NCH_3), 3.87 ppm (br s, 4H; NCH_2); ^{13}C NMR (100 MHz, $CDCl_3$): δ = 36.6 (CH_3), 44.8 (CH_2), 111.1, 136.4, 138.9, 140.7, 141.5, 144.0 (Ar−C_q), 159.2 ppm (C=O); ^{19}F NMR (376 MHz, $CDCl_3$): δ = −159.4 (m, 4F; ArF), −151.4 (m, 2F; ArF), −141.9 ppm (m, 4F; ArF); ESIMS: m/z (%): 499.1 (100) $[M + Na]^+$; HRMS (ESI^+): m/z calcd for $C_{18}H_{10}F_{10}N_2O_2Na^+$: 499.0475 $[M + Na]^+$; found: 499.0497 (Δ = 4.4 ppm).

Crystallographic section

Colorless crystals of **2@1b** and **8@1b** were obtained by diffusion of ether into a saturated chloroform solution of host and guest. The structural analysis was performed using Bruker-Nonius Kappa Apex II diffractometer with graphite-monochromatized Cu-Kα (λ = 1.54183 Å) radiation at 173 K for **2@1b** and Bruker-Nonius Kappa Apex II diffractometer with graphite-monochromatized Mo-Kα (λ = 0.71073 Å) radiation at 123 K for **8@1b**. Collect software[539] was used for the data measurement and DENZO-SMN[540] for the processing. The structures were solved by charge flipping method with SUPERFLIP[541] and refined by full-matrix least-squares methods using the WinGX-software,[542] which utilizes the SHELXL-97 module.[543] Multi-scan absorption correction was done by SADABS2008.[544] All C−H hydrogen positions were calculated using a riding

atom model with $U_{\mathrm{H}} = 1.2 \times U_{\mathrm{C}}$. All non-H atoms were refined anisotropically. Crystal data for **2@1b** (CCDC-853879): colorless blocks, $0.15 \times 0.20 \times 0.25$ mm, FW = 1691.08, $C_{82}H_{100}N_6O_6Cl_{12}$, triclinic, space group $P\bar{1}$, a = 13.087(3) Å, b = 13.192(2) Å, c = 14.620(3) Å, α = 103.23(2)°, β = 107.21(3)°, γ = 108.81(2)°, V = 2131(1) Å^3, Z = 1, D_c = 1.318 g cm^{-3}, $F000$ = 886, μ = 3.998 mm^{-1}, T = 173(2) K, $2\theta_{\max}$ = 63.31°, 6843 independent reflections, 5265 with $I_o > 2\sigma(I_o)$, R_{int} = 0.1111, 485 parameters, 0 restraints, GoF = 1.038, R = 0.0758 [$I_o > 2\sigma(I_o)$], wR = 0.2160 (all reflections), $0.692 < \Delta\rho < -0.501$ eÅ^3.
Crystal data for **8@1b** (CCDC-853880): colorless blocks, $0.10 \times 0.15 \times 0.35$ mm, FW = 1552.46, $C_{88}H_{102}N_6O_6Cl_6$, monoclinic, space group $C2/c$, a = 25.976(5) Å, b = 19.610(4) Å, c = 19.930(4) Å, β = 126.21(3)°, V = 8191(3) Å^3, Z = 4, D_c = 1.259 g cm^{-3}, $F000$ = 3288, μ = 0.266 mm^{-1}, T = 123(2) K, $2\theta_{\max}$ = 25°, 7156 independent reflections, 4611 with $I_o > 2\sigma(I_o)$, R_{int} = 0.1102, 480 parameters, 0 restraints, GoF = 1.046, R = 0.0695 [$I_o > 2\sigma(I_o)$], wR = 0.1742 (all reflections), $0.380 < \Delta\rho < -0.478$ eÅ^3.

Theoretical section

The structure of all complexes were optimized using density functional theory (DFT) combined with the resolution of identity technique (RI).[545] The TZVP basis set was applied in combination with the general gradient approximated type functional B97-D with dispersion correction developed by Grimme.[198,199,546] All calculations were performed using the TURBOMOLE 6.0 program package.[399,547] The obtained complex interaction energies were counterpoise-corrected by the method introduced by Boys and Bernardi.[548] According to the supramolecular approach, the adiabatic complex interaction energies ΔE_{ad} can be calculated by subtracting the energies of the relaxed wheel E_{rel}(wheel) and axle E_{rel}(guest) as well as the BSSE contributions to the total cluster energy E_{tot}(complex) as given in eqn (3.14). Because of complex formation, the conformation of the molecules changes. The energy ΔE_{CF} related to this conformational

change does not directly contribute to the hydrogen bond energies. Therefore, ΔE_{CF} was calculated according to eqn (3.15). We also carried out the computation of the two-center shared electron number (SEN).[399,547] The determination of the two-center shared electron number is based on the population analysis by Davidson.[549] A linear relationship (eqn (3.16)) exists between the two-center shared-electron number of a hydrogen bond σ_{HA} and its binding energy which allows an estimation of the bond strength. Therefore, the slope m and the axis intercept b of eqn (3.16) need to be determined, because they depend on the acceptor atom of the hydrogen bonds and the combination of functional and basis set. It is well known that this procedure works for a broad variety of chemical applications concerning hydrogen bonds.[185,550] To get qualitative results on the bonding strength, a comparison of the two center shared electron number σ_{HA} is sufficient.

Acknowledgment

This research has been funded by the Deutsche Forschungsgemeinschaft (SFB 765 and grant KI-768/7-1), the German Academic Exchange Service (DAAD), the Finnish Academy (KR proj. no. 130629, 122350, 140718) and the Fonds der Chemischen Industrie (FCI). L.K. and E.V.D. are deeply indebted to the Studienstiftung des deutschen Volkes (German National Academic Foundation) for doctoral scholarships. We thank Antti Senf, B.Sc. for synthesizing the wheel used in this study and Dr. Christian Ortmann (Waters GmbH) for help with the interpretation of the ITC experiments.

3.4.2 Substitution Effect and Effect of Axle's Flexibility at (Pseudo-)Rotaxanes

Friedrich Malberg[†], Jan Gerit Brandenburg[†], Werner Reckien[†], Oldamur Hollóczki[†], Stefan Grimme[†,⋆] and Barbara Kirchner[†,⋆]

Malberg, F.; Brandenburg, J. G.; Reckien, W.; Hollóczki, O.; Grimme, S.; Kirchner, B. *Beilstein J. Org. Chem.* **2014**, accepted

Own contributions to this manuscript:

- Static quantum chemical calculations
- Frequency calculations
- Interpretation of data
- Writing of the manuscript

[†] *Mulliken Center for Theoretical Chemistry, Institut für Physikalische und Theoretische Chemie, Universität Bonn, Beringstr. 4, D-53115 Bonn, Germany. E-mail: bkirchner@thch.uni-bonn.de, grimme@thch.uni-bonn.de*

Abstract This study investigates the effect of substitution with different functional groups and of molecular flexibility by changing within the axle from a single C−C bond to a double C=C bond. Therefore, we present static quantum chemical calculations at the dispersion corrected density functional level (DFT-D3) for several Leigh-type rotaxanes. The calculated crystal structure is in close agreement with the experimental X-ray data. Compared to a stiffer axle, a more flexible one results in a stronger binding by 1-3 kcal/mol. Alterations of the binding energy in the range of 5 kcal/mol could be achieved by substitution with different functional groups. The hydrogen bond geometry between the isophtalic unit and the carbonyl oxygen atoms of the axle exhibited distances in the range of 2.1 to 2.4 Å for six contact points, which shows that not solely but to a large amount the circumstances in the investigated rotaxanes are governed by hydrogen bonding. Moreover, the complex with the more flexible axle is usually more unsymmetrical than the one with the stiff axle. The opposite is observed for the experimentally investigated axle with the four phenyl stoppers. Furthermore, we considered an implicit continuum solvation model and found that the complex binding is weakened by approximately 10 kcal/mol, and hydrogen bonds are slightly shortened (up to 0.2 Å).

Introduction

Rotaxanes are prototypes for molecular machines and molecular switches,[551–553] being mechanically interlocked molecules consisting of a macrocycle, called "wheel", threaded on a linear chain, termed "axle", see Figure 3.54 for examples. Typically, the axle has at least one recognition site — often hydrogen bond donors or acceptors[554,555] — for the wheel, because most rotaxanes are obtained from template synthesis.[138,429] Bulky stopper groups at the ends of the axle prevent dethreading. Rotaxanes without their stopper groups are often referred to as pseudorotaxanes. It is implicitly assumed that these functionalities have no further influence on the electronic structure of the axle, hence neither on the axle-wheel interaction.

Applications of rotaxanes are many-fold, for example there is an interest in understanding the motions carried out by both entities with respect to each other. This can lead to molecular machines via pirouetting,[556] or molecular shuttles[152,557] via shifting the axle back and forth within the wheel. The Stoddart group synthesized the first rotaxane-based molecular shuttle in 1991.[154] It consisted of a tetracationic wheel, which was able to move back and forth between two identical hydroquinol stations. These symmetrically surrounded a polyether axle, which was terminated at the ends by large triisopropylsilyl stoppers.[154] Other rotaxane systems were also studied. For instance, Leigh and coworkers synthesized several rotaxane shuttles and switches in the last years.[175] Many of these rotaxanes are based on a benzylic amide macrocycle with isophtalamide units building up twofold hydrogen bonds to an acceptor axle. The Schalley group often used a similar hydrogen bond motif for the design of molecular shuttles with the Vögtle-Hunter tetralactam macrocycle next to several other combinations.[140,558,559]

Fernandes *et al.* recently published a further interesting application of rotaxanes.[560,561] The axle consisted of a peptide, which can be released from the wheel by the according reaction, thus allowing the rotaxane to function as a high-precision delivery system. The authors introduced a system, which — in contrast to the first generation of these kinds of rotaxanes — showed water solubility and contained appropriate locations for substitutions in order to improve its properties.[560]

Theoretical investigations on rotaxanes accompanied or even preceded experimental work frequently, thus showing that theory offers many viable tools for the understanding and the development of rotaxanes. Zerbetto *et al.* showed that the shuttling motion can be separated from the other degrees of freedom, and that the effective coordinate of the motion can be described as a double-minimum potential.[176] The co-conformer stability for rotaxane based molecular shuttles was investigated by means of molecular modeling.[179] The Peyerimhoff group has carried out an *in-depth* study of the rotaxane formation.[137] A later

study investigated the shuttling motion of the wheel as a one-dimensional translation, together with the influence of the Kohn–Sham frontier orbitals of wheel and axle upon conductivity and electron tunneling along the rotaxane.[177] A quantum chemical shuttling motion study of rotaxane-based molecular switching devices has revealed how the modification of the redox states of both entities results in changes of the computational energy profile.[178] The formation in gas phase of α-cyclodextrin-based [3]pseudorotaxanes was studied by means of density functional calculations.[562] Molecular mechanics calculations were used for a free energy calculation of an α-cyclodextrin rotaxane system and for the investigation of low-barrier molecular rotary motors with rotaxane architecture.[181] The co-conformational selectivity of two dibenzo-[24]crown-8 macrocycles to ammonia binding sites in a [3]rotaxane,[180] and the hydrogen bonding strength in polymeric urethane rotaxanes in a mean-field model[563] were investigated by semiempirical methods. In our groups we investigated the main binding motif for rotaxane systems of Vögtle-,[167,182–184] Schalley-,[182,183,564] and Leigh-type.[184] We performed an energetic and vibrational analysis for the twofold hydrogen bonds in order to understand the binding pattern.[167] A close relationship between the strength of the hydrogen bond and the charge of the acceptor oxygen was detected.[166] Substitution with electron withdrawing groups weakens the twofold hydrogen bond, whereas substitution with electron donating groups led to an increase of interaction energy. In the vibrational spectra, the red shift for both the C=O stretching mode and the N–H stretching mode was correlated to the binding energies of the hydrogen bonds.[184] Compared with single hydrogen bonds, the twofold hydrogen bonds showed shorter red shifts for the N–H stretching modes but larger red shifts for the C=O stretching mode.[184] Different density functionals, including one functional with an empirical correction for dispersion interaction, for the treatment of such rotaxane complexes were studied. We compared these density functional theory (DFT) results with Møller-Plesset second-order perturbation theory (MP2) calculations.[182] The contribution of the London dispersion interaction to the total interaction energy in gas phase is of the same magnitude as

the hydrogen bonding interaction (about −14 kcal/mol).

The molecular functionality of rotaxanes is solely based on the interplay of different noncovalent interactions between the axle and the wheel. Therefore, the understanding of these (mostly) attractive forces is crucial for the development of the field. Also, by understanding how one can modify or even tune the axle-wheel interplay, rotaxanes for different purposes can be designed enhancing the applicability of such materials. This study aims to understand rotaxanes with respect to its noncovalent interactions on the molecular level and to contribute to a more rational design of new molecular machines. For this purpose we investigated the energetics by substitution the rotaxanes with different functional groups and by changing the degree of molecular flexibility.

Computational methodologies

For all compounds, the structures were fully optimized without any symmetry constrains. Density functional theory (DFT) with the gradient-corrected meta-functional TPSS combined with the resolution of identity technique (RI) and the def2-TZVP basis set were applied[196,399] together with the dispersion correction D3.[200,565] This level of theory is abbreviated as TPSS-D3/def2-TZVP. All molecular calculations were performed using the TURBOMOLE 6.4 program package.[399] The convergence criterion for the geometry optimization was set to 10^{-4} atomic units for the norm of the Cartesian gradient. The SCF-convergence was set to 10^{-6} atomic units. The adiabatic complex interaction energies ΔE^{int} were calculated according to the supramolecular approach by subtracting the energies of the relaxed monomers $E^{\text{relax}}_{\text{wheel}}$, $E^{\text{relax}}_{\text{guest}}$ from the total complex energy E^{tot}.[79,566]

$$\Delta E^{\text{int}} = E^{\text{tot}} - E^{\text{relax}}_{\text{wheel}} - E^{\text{relax}}_{\text{guest}} \tag{3.17}$$

Interaction energies were counterpoise-corrected by the procedure introduced by Boys and Bernardi. The basis set superposition error (BSSE) does not exceed 3 kcal/mol (about 5 % of ΔE^{int}) for any of the complexes calculated. In order to confirm the nature of the stationary point obtained, we performed an analytical

frequency analyses with the aoforce module[567–569] resulting in only positive values for the minima.

As a first approximation to solvation, we applied the conductor-like screening model (COSMO).[209] This is a continuum solvation model, where the solute molecule forms a cavity within the dielectric continuum of permittivity ε that represents the solvent and which neglects the cavitation and solute-solvent dispersion term. For ε we choose 4.806 which is the value of Chloroform. The distance of solvents to van der Waals radii of the atom (here standard values were chosen) was set to 1.3 Å. The Hammett parameters are taken from Ref. [515].

Computational Details for Periodic Calculation

The periodic calculations were carried out by the Vienna Ab initio Simulation Package VASP 5.3.[570,571] We utilized the GGA functional PBE[572] in combination with a projector-augmented plane wave basis set (PAW)[203,573] with energy cutoff of 1000 eV. The Brillouin zone was sampled with a Γ-centered $2 \times 1 \times 1$ k-mesh. The crystal including cell parameters was fully optimized (including cell parameters) until all forces were below 0.005 eV/Å. The PBE functional was corrected for missing nonlocal correlation interactions via the atom-pairwise London dispersion correction D3 in the Becke-Johnson damping scheme.[200,565] A single (isolated) dimer was optimized with the same technical setup in a large unit cell with minimum intermolecular atom-atom distance of 16 Å. This method combination provides reliable results for both the gas phase and the solid state as shown in a number of publications by us[574–576] and other groups.[571,577]

Structures under study

The hereby considered pseudorotaxanes (Figure 3.54) consist of an amide axle inside the cavity of a macrocycle, which contains two isophtalamide units. One kind of the investigated axles is a fumaramide derivative with a C=C double bond and two connected amide groups (labeled as Leigh-type-DB, **DB** throughout the article),[143,552] and the other kind is a succinic amide derivative with a

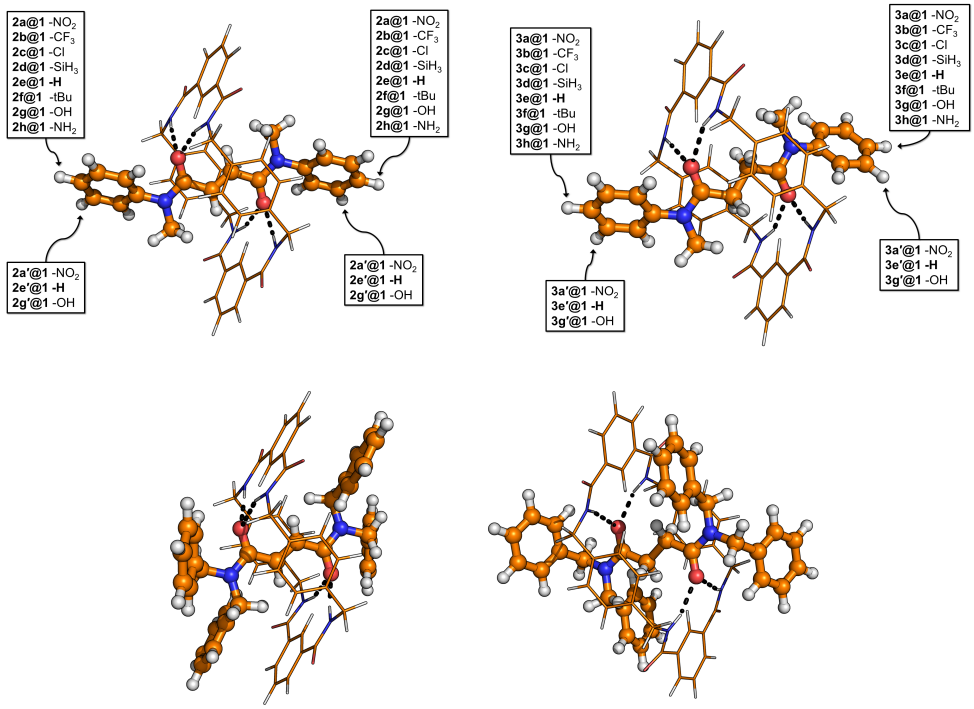

Figure 3.54: Chemical structure of the investigated systems. Left: Double bond within the axle; Right: Single bond within the axle. Red marks oxygen atoms, blue nitrogen atoms, orange carbon atom and hydrogen atoms are given in white. The labeling according to the substitution is given in bold letters. Structures below will be denoted **4@1** (left) and **5@1** (right).

C−C single bond, and two connected amide groups (labeled as Leigh-type-SB (**SB** throughout the article). Due to the aforementioned structure of the wheel and the axle, and since the wheel-O=C$\cdots$NH-axle type interplay is prohibited by the substitution of the corresponding hydrogen atoms by either a methyl group (Figure 3.54 top) or a benzyl group (Figure 3.54 bottom), only four hydrogen bonds can be formed between the subunits, via wheel-NH$\cdots$O=C-axle interactions. At the two different axles with single and double bond, the phenyl groups of the axle will be substituted symmetrically in order to investigate the substitution effect. Moreover, the influence of the axle's flexibility, see Figure 3.54 upper part, will be investigated. The rotaxanes with di-phenyl groups are analyzed in order to allow comparison to experimental data.

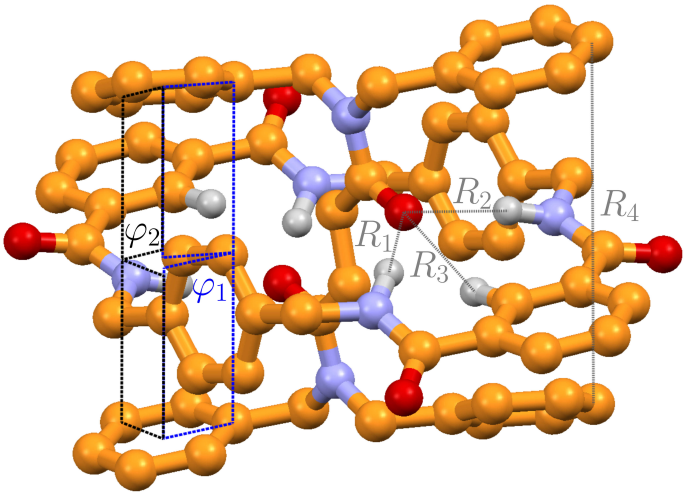

Figure 3.55: Molecular geometry of one rotaxane optimized in periodic boundaries at the PBE-D3/1000 eV level. Hydrogen atoms are omitted for clarity. Some intramolecular distances and angles are highlighted.

Results

Crystal structure The fully optimized crystal structure agrees very well with the experimental X-ray structure, see Table 3.13. The unit cell volume (Vol) is smaller than the experimental value by only 1.7 %. Typical thermal cell expansions (from calculated 0 K to measured 100 K) are 2 – 3 %. A recent study showed that PBE-D3 (with a large basis set) overestimates molecular sizes by approximately 1 %.[578] Therefore, the calculated cell volume is in a reasonable agreement with the experimental value when thermal expansion effects are considered in the comparison. The optimization is performed without symmetry constraints, and the correct space group (monoclinic) is reproduced, *i.e.* all cell angles differ by less than 0.3° from the X-ray structure.

Because the molecular structure is rather flexible, we observe interesting crystal packing effects. We compared the highlighted intramolecular distances and angles from experiment and theory in Figure 3.55. As a result, we exemplified the influence of noncovalent interactions. The distances R_1, R_2, and R_3 are significantly smaller in the crystal compared to the gas phase structure. The torsion

Table 3.13: Comparison of the X-ray structure of the rotaxane with the computed crystal and gas phase geometries. The structures are optimized at the PBE-D3/1000 eV level (TPSS-D3 with the def2-TZVP basis). The first block shows the cell parameters describing the intermolecular packing, whereas the second block highlights some intramolecular distances and angles (compare with Figure 3.55). Distances in parentheses denote the corresponding length to the heavy (nonhydrogen) atom.

	Reference	Crystal	Gas Phase	
	X-ray	PBE-D3	PBE-D3	TPSS-D3
a /Å	9.79	9.69	–	–
b /Å	16.16	16.16	–	–
c /Å	16.87	16.78	–	–
β /°	105.0	105.3	–	–
Vol /Å^3	2579	2535	–	–
R_1 /Å	2.01(2.98)	1.97(2.97)	2.11(3.10)	2.11(3.10)
R_2 /Å	2.24(3.16)	2.11(3.11)	2.30(3.28)	2.35(3.31)
R_3 /Å	2.31(3.13)	2.19(3.09)	2.25(3.28)	2.28(3.30)
R_4 /Å	8.24	8.19	9.25	9.11
φ_1 /°	−1.7	−1.2	−4.0	−2.2
φ_2 /°	5.16	4.4	−9.7	−7.0

angles ψ_1 and ψ_2 describe the relative tilting between the flexible phenyl rings, which differs by more than 10° between crystal and gas phase. All these geometrical data are very well reproduced by the PBE-D3/1000 eV calculations, see third column in Table 3.13. However, the gas phase calculations (5th and 6th column in Table 3.13) show that one has to be careful when comparing calculated gas phase structures with measured crystal geometries.

The calculated lattice energy (for one rotaxane, excluding phonon contributions) is with 77.7 kcal/mol quite large but in a reasonable range for a molecule

of this size. Recent benchmark studies showed that lattice energies on the PBE-D3/1000 eV level deviate by less than 9 % from (thermal back-corrected) experimental sublimation energies.[579] The excellent agreement of the utilized theoretical method with the X-ray experiment justifies its application in the following sections. Mostly for technical reasons we have chosen PBE-D3 in the solid state calculations but TPSS-D3 in the molecular treatments. According to many benchmark calculations (see *e. g.* Ref.[574,576,580]), both functionals perform very similar for noncovalent interaction (TPSS-D3 being even somewhat better for hydrogen bonding) which supports the above conclusion.

Table 3.14: Interaction energies E_{int} for the different pseudorotaxane systems, labeling see Figure 3.54. The first two columns list the substituents succeeded by their effects (mesomeric or inductive). The last line gives the values for the di-phenyl structures. In the last column the Hammett-parameters are given.

			E_{int} kcal/mol		E_{int} kcal/mol	σ
−I, −M	p-NO_2	**2a@1**	−41.2	**3a@1**	−43.1	0.78
−I	p-CF_3	**2b@1**	−42.4	**3b@1**	−44.9	0.54
−I,(+M)	p-Cl	**2c@1**	−43.0	**3c@1**	−45.4	0.23
+I,(−M)	p-SiH_3	**2d@1**	−44.1	**3d@1**	−45.9	0.10
−	p-H	**2e@1**	−44.7	**3e@1**	−46.5	0.00
+I	p-tBu	**2f@1**	−44.9	**3f@1**	−47.6	−0.20
−I, +M	p-OH	**2g@1**	−45.7	**3g@1**	−46.8	−0.37
−I, +M	p-NH_2	**2h@1**	−46.5	**3h@1**	−48.4	−0.66
−I, −M	m-NO_2	**2a′@1**	−43.7	**3a′@1**	−45.5	0.71
−I, +M	m-OH	**2g′@1**	−45.1	**3g′@1**	−47.5	0.12
	p-2Ph	**4@1**	−56.1	**5@1**	−58.7	−

Substitution effect The interaction energies in Table 3.14 show that the more flexible axle (**SB**) binds stronger to the wheel than the less flexible ethylene-containing axle (**DB**) for all pseudorotaxanes studied. The difference between the substituted **DB** and **SB** amounts to 1-3 kcal/mol. Substituents with $-M/-I$ effect bind more weakly than those with $+M/+I$ effect, which fits neatly to the fact that the axle in this investigated system accepts the hydrogen bond and therefore prefers electrons to be shifted towards the functional group. Interestingly, the substitution effects seem to be almost additive, *i.e.*, for both the **SB** and the **DB** structure changes in the energy range of 5 kcal/mol can be obtained with the appropriate functional group, compare for example **2a@1** to **2h@1** and **3a@1** to **3h@1**.

A qualitative insight of the varying binding situation can be gained from the electrostatic potential shown for six rotaxanes in Figure 3.56. The electron withdrawing groups reduce the hydrogen bond accepting character of the oxygen atoms (see reduced red color and increase in blue color of **2a@1** in Figure 3.56 compared to **2e@1**), the π-electron donating groups, on the other hand, increase the hydrogen bond accepting character (see more pronounced red areas and less pronounced blue color of **2f@1** in Figure 3.56 compared to **2e@1**).

In order to understand the origin of the different binding energies, we consider the most direct interaction between axle and wheel, namely the hydrogen bond accepted by the axle and donated from the wheel, as possible influence. Since the wheel and the axle are symmetrical, and there are two recognition sites between axle and wheel, the latter sites resemble each other very much in geometrical parameters. Thus, we only consider one binding site (isophtalic unit) with its hydrogen bonds. Note, that the hydrogen bond in the **DB** systems are more symmetrical than in **SB** systems. As the choice of the binding site is sort of arbitrary, we always choose the one with the shortest N–H$\cdots$O distance. The full data can be found in the supporting information.

The hydrogen bonds listed in Table 3.15 fall in the range of 2.1 to 2.4 Å, and their angles range from 150 to 180 degrees. The hydrogen bonds are only roughly

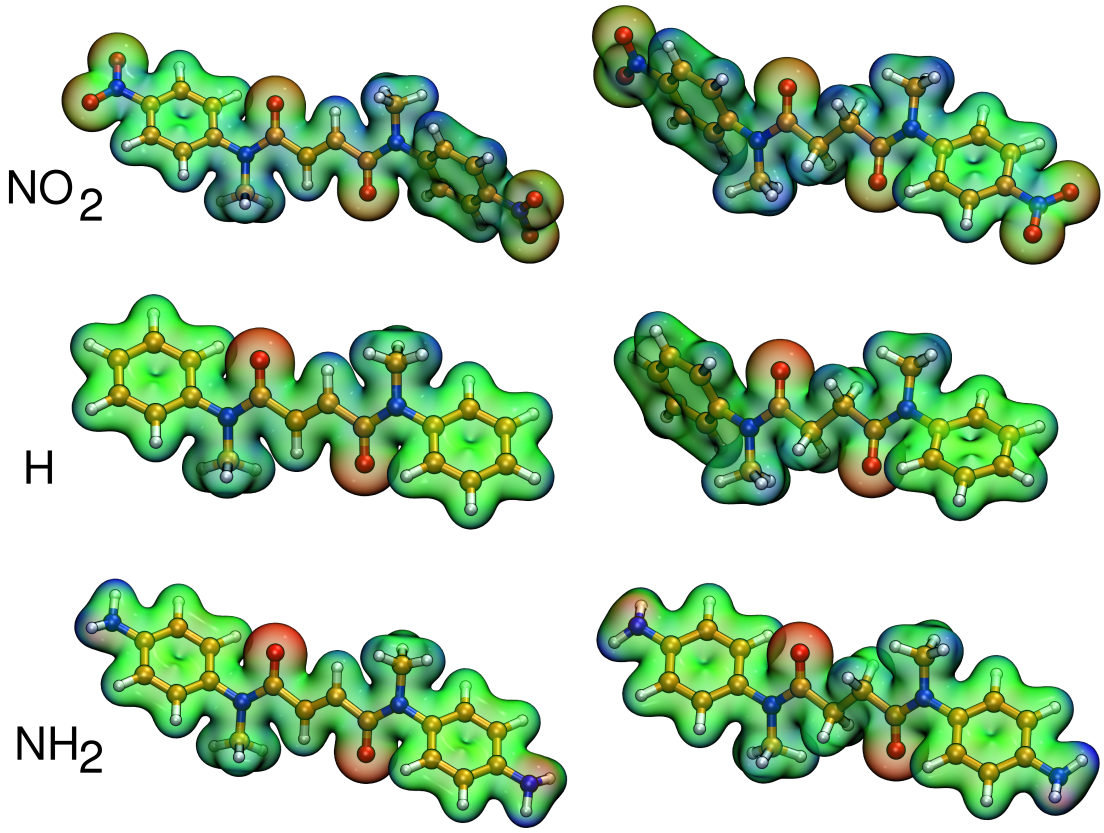

Figure 3.56: Electrostatic potential for the complexes **2a@1** (top left), **2e@1** (middle left), **2h@1** (lower left) and **3a@1** (top right), **3e@1** (middle right), **3h@1**. (lower right)

correlated to the strength of the interaction between axle and wheel, *i.e.*, the variations within different substitutions are too small to discuss them within the error of the method. However, a general shortening of the hydrogen bonds with increasing energies is visible, compare (*e. g.*, **2a@1**, **2e@1** and **2h@1**). Moreover, there are more symmetrical hydrogen bonding situations in the middle of the listed data in Table 3.15, *e. g.* **2e@1**). Furthermore, there is a significant difference (0.1-0.2 Å) between **SB** and **DB**. Considering these two(three)-fold hydrogen bonds, **SB** is less symmetric indicated by the shorter short N–H$\cdots$O bond and the longer long N–H$\cdots$O bond compared to **DB**. The di-phenyl rotaxanes exhibit the opposite trend, the shortest and longest hydrogen bond is given in **4@1**. The given energy trend is maintained, the longest N–H$\cdots$O bond in

Table 3.15: Hydrogen bond distances in Å for the different pseudorotaxane systems, for labeling see Figure 3.55. The second and third last lines show the substitution at the meta-position.

		R_1	R_2	R_3		R_1	R_2	R_3
p-NO_2	**2a@1**	2.24	2.40	2.29	**3a@1**	2.18	2.42	2.26
p-CF_3	**2b@1**	2.21	2.38	2.27	**3b@1**	2.16	2.43	2.24
p-Cl	**2c@1**	2.23	2.29	2.26	**3c@1**	2.15	2.35	2.22
p-SiH_3	**2d@1**	2.17	2.35	2.22	**3d@1**	2.15	2.34	2.21
p-H	**2e@1**	2.21	2.22	2.20	**3e@1**	2.14	2.33	2.20
p-tBu	**2f@1**	2.21	2.27	2.24	**3f@1**	2.11	2.39	2.20
p-OH	**2g@1**	2.08	2.18	2.34	**3g@1**	2.14	2.30	2.19
p-NH_2	**2h@1**	2.15	2.22	2.17	**3h@1**	2.11	2.34	2.18
m-NO_2	**2a′@1**	2.23	2.44	2.32	**3a′@1**	2.14	2.63	2.31
m-OH	**2g′@1**	2.26	2.22	2.22	**3g′@1**	2.13	2.38	2.22
p-2Ph	**4@1**	2.04	2.50	2.27	**5@1**	2.11	2.35	2.28

4@1 is much longer (2.5 Å) than other long N–H$\cdots$O bonds. This also shows the importance of such stopper groups for the interactions within the rotaxanes, as they have notable electronic influence. Thus, their role is not necessarily restricted to the mere mechanical prevention of the axle's dethreading which was also witnessed for diketopiperazine-based amide rotaxanes.[163]

In table 3.14 also the Hammett σ parameters are given. These substituent parameters[515] are the difference of the pKa values of substituted and nonsubstituted benzoic acids, they can be correlated with the interaction energies resulting in good correlation coefficients of 0.9880 (**DB**) and 0.9596 (**SB**) if the para-positions are considered only, see Figure 3.57. This fitted linear regression curve are reading:

$$\text{DB}: \; y = 3.7075 \text{ kcal/mol} \cdot \sigma - 44.255 \text{ kcal/mol} \tag{3.18}$$

$$\text{SB}: \; y = 3.3739 \text{ kcal/mol} \cdot \sigma - 46.25 \text{ kcal/mol} \tag{3.19}$$

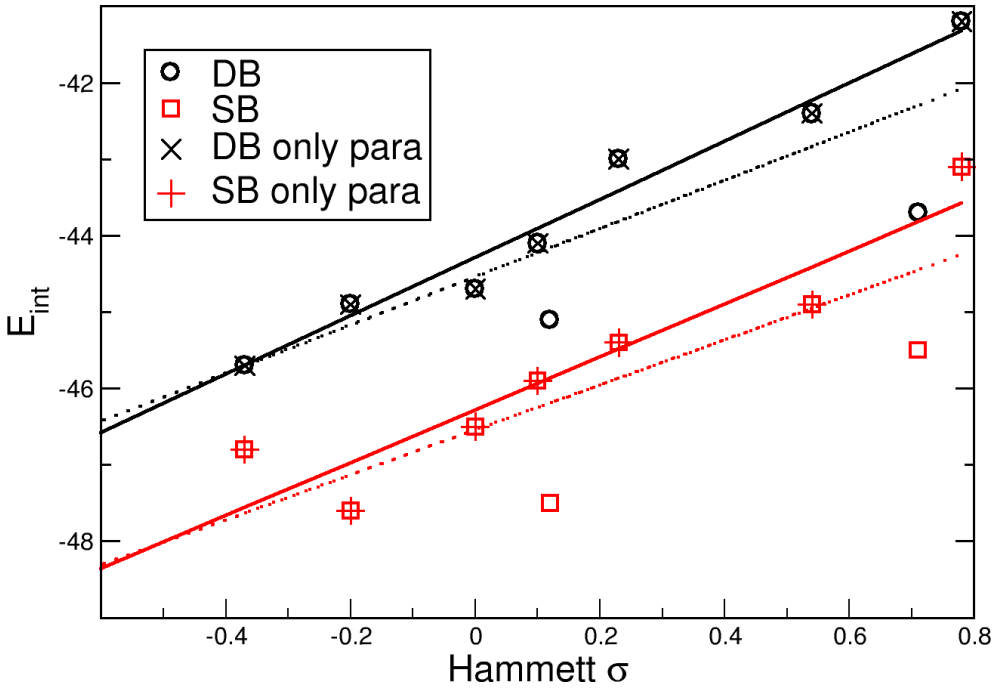

Figure 3.57: Interaction energies plotted against the Hammett σ parameters. The values are given in table 3.14. Black curves: **DB** and red curves: **SB**. The solid lines are fits to all energies of the para-substitution only, the dotted lines are linear regressions to all interaction energies.

Equations 3.18 and 3.19 can be used to estimate the contributions of different substituents given the σ-values are provided.

Solvent effects As expected, the presence of the solvent decreases the binding energy by 11-14 kcal/mol, see Table 3.16. Even though the trends in the difference between single and double bond binding energy is constantly 1-4 kcal/mol. By comparison of the total energies of the complex, separated wheel, and axle, this can be assigned to the stabilization of the complex and wheel by approximately 20 kcal/mol, whereas the axle is only stabilized by 10 kcal/mol.

In the following, we focus on the hydrogen bonded systems and repeat the previously described distances (Table 3.15) for the corresponding solvated systems in Table 3.17. Again the distances roughly follow the trend that with increasing binding energy the distances are shorter. The hydrogen bonding situation in the

Table 3.16: Interaction energies E_{int} for the different pseudorotaxane systems applying a solvent model, labeling see Figure 3.54. The first two columns list the substituents succeeded by their effects (mesomeric or inductive) as in Table 3.14.

			E_{int} kcal/mol		E_{int} kcal/mol
−I, −M	p-NO_2	**2a@1**	−29.6	**3a@1**	−31.0
−	p-H	**2e@1**	−32.4	**3e@1**	−33.8
−I, +M	p-NH_2	**2h@1**	−33.7	**3h@1**	−35.1
	p-2Ph	**4@1**	−42.1	**5@1**	−45.6

Table 3.17: Hydrogen bond geometry in Å for the different pseudorotaxane systems with solvent model, labeling see Figure 3.55. The second and third last lines show the substitution at the meta-position.

		R_1	R_2	R_3		R_1	R_2	R_3
p-NO_2	**2a@1**	2.19	2.41	2.30	**3a@1**	2.12	2.47	2.27
p-H	**2e@1**	2.11	2.16	2.16	**3e@1**	2.12	2.28	2.19
p-NH_2	**2h@1**	2.08	2.14	2.13	**3h@1**	2.09	2.18	2.14
p-2Ph	**4@1**	2.02	2.43	2.20	**5@1**	2.07	2.27	2.23

complexes with single bond is still less symmetrical, but the shorter N-H$\cdots$O bond is for the solvated not shorter than in the **DB** complexes. Typically, the distances in the solvated complexes are shorter up to 0.16 Å compared to the unsolvated systems. Considering the reduced binding energies, this is unusual. Comparing different intra- and intermolecular bonds, it appears that this arrangement of shorter and thus stronger hydrogen bonds stems from a more bowed axle with respect to the wheel.

Conclusion

We investigated several rotaxanes by static quantum chemical calculations in order to gain insight into the interplay of different noncovalent interactions. Therefore, we studied the substitution of the rotaxanes with different functional groups and the degree of molecular flexibility by changing within the axle from a single C-C bond to a double C=C bond.

In order to assess the methodology used, we calculated the crystal structure and found a very good agreement with the experiment. For instance, deviations of the unit cell volume were less than 2%. However, care has to be taken when comparing results calculated in the gas phase with those obtained in the condensed phase due to nonlocal crystal packing effects.

The computed DFT-D3 formation energies of the noncovalently bound rotaxanes in the gas phase range from about -41 to -58 kcal/mol which is typical for supramolecular complexes of this size.[575] For the investigated modified axles we found that – as expected – a more flexible axle binds stronger than the stiffer axle. Exchanging a double with a single bond leads to an increase of absolute value in binding energy of 1-3 kcal/mol. Alterations of the binding energy in the range of 5 kcal/mol could be achieved for substitution with different functional groups. Thus, it is possible to modulate the rotaxane binding by changing different chemical parts in the region of 1-5 kcal/mol, which should show an influence of the inter-related motion as well. We also investigated the hydrogen bond geometry between the isophtalic unit and the carbonyl oxygen atoms of the axle and found distances in the range of 2.1 to 2.4 Å for 6 contact points. This shows that to a large amount the interactions in the investigated rotaxanes are governed by hydrogen bonding. On the one hand, the single bound complex usually is less symmetric in exhibiting one short and one long N-H$\cdots$O bond than the double bond containing complex. On the other hand, the opposite is observed for the experimentally investigated axle with the four phenyl stoppers. One might assume that the terminal groups play a minor role in the interplay within the rotaxane and serve only to prevent the axle mechanically from de-

threading. However, we clearly demonstrated the importance of such rotaxanes parts as the stopper groups also for intra-molecular interactions of the rotaxanes.

Considering an implicit solvent model (COSMO), the complex binding is weakened by approximately 10 kcal/mol. This is due to the fact that the individual parts of the rotaxane are differently stabilized in the solvent. Thus, the axle is less stabilized than the wheel and the complex. Interestingly, we observed slightly shortened (up to 0.2 Å) hydrogen bonds for all investigated systems. This goes along together with a more tilted axle in the solvent.

In future, we plan to explicitly study the different motions within such complex systems. The main focus is on the influence of simple chemical differences such as substitution or dealkylation.

Acknowledgment

We would like to thank the DFG in the framework of the collaborative research center SFB 624 “Templates” at the University of Bonn for the funding of this research. Furthermore, the financial support of the DFG project KI 768/7-1 is gratefully acknowledged. Finally, the authors would like to add personal thanks to Christoph A. Schalley for helpful discussions and Barbara Intemann for correcting the manuscript.

4 Conclusion and Outlook

Two complex systems, namely ionic liquids and supramolecular structures called rotaxanes, were studied applying multiscalar molecular methods. The ionic liquids were investigated by means of *ab initio* and classical molecular dynamics, in order to dynamically probe their complex interactions in the bulk and gas phase as well as at the liquid-vacuum interface. Further, different population analysis were performed on geometry optimized structures to scan for charge transfer effects. For the rotaxanes, as they are large host-guest complexes and thus computationally demanding, static quantum chemical calculations were used to study alterations in their complex binding patterns through substitution effects. Additionally, solvation effects were probed by explicitly including solvent molecules as well as by utilizing an implicit solvent model.

- Comparison between the gas phase and the bulk phase of 1-ethyl-3-methylimidazolium ethylsulfate from *ab initio* molecular dynamics simulations at 400 K revealed, that conformations observed in the gas phase resemble only conformations in the bulk phase where the polar group of the anions coordinates via hydrogen bonding to the most acidic hydrogen atom of the cation. Additional interactions between cation and anion are not present in the gas phase. In the bulk phase, interactions via hydrogen bonding to the rear hydrogen atoms are present as well. Additionally, interactions between the apolar part of the anion and the imidazolium ring were found, which are mainly caused by dispersion interactions.

- Investigation of the temperature dependency of the main conformation found for this ionic liquid in the gas phase, showed a change in the coordina-

tion of the anion to the cation with increasing temperature. At room temperature, a mixed coordination of the terminal and bridging oxygen atoms of the anion and the most acidic hydrogen atom of the cation is present. At 400 K, the structural change occurs, shifting the bridging oxygen atom to further distances and at 600 K only interactions via the terminal oxygen atoms are observed. This shift was identified as a shift from a bulk phase-like to a more free, gas phase-like coordination and thus being a crucial part of the evaporation process of this ionic liquid. Dynamical investigations of the two possible conformations present in imidazolium-based ionic liquids, namely in-plane and on-top conformation, pointed to an enhanced hydrogen bonding affinity during the structural change. Furthermore, additional weak interactions between the side chain of the anion and the imidazolium ring were observed from the dynamical investigations, revealing an important role of dispersion interactions during the evaporation process.

The struture of ionic liquids at the liquid-vacuum interface, the influence of the interface on the molecular structure and the morphology in the bulk phase was investigated by means of classical molecular dynamics utilizing a force field especially developed for ionic liquids.

- Varying the alkyl chain length of 1-ethyl-3-methylimidazolium n-alkylsulfates (n = 2, 4, 6 and 8) revealed a linear relation between the molecular structure and the morphology of the polar and nonpolar domains present in imidazolium-based ionic liquids. At the surface, the alkyl chain of the anion points towards the vacuum, while the imidazolium ring adopts orientations parallel to the surface. Comparison of calculated surface tensions and the size of the polar and nonpolar domains to experimental data showed good agreements. In addition, the weak dispersion interaction between the alkyl chain of the anion and the imidazolium ring of the cation was found to be well represented by the applied force field.

- For pyrrolidinium-based ionic liquids, the segregation into polar and nonpolar domains was observed as well. Increasing the size of the anion only

influenced the characteristic size of the polar domain, while the morphology of the nonpolar domain was independent of the anion. As for the imidazolium-based ionic liquids, the surface is mainly composed of alkyl chains pointing towards the vacuum. The presence of the interface leads to a strong organization of the region close to the interface and it was found that the polar regions are more structured than the nonpolar domains.

In ionic liquids, a shortage of ion pairing was suggested, which is in contradiction to the sole ion pair found in the gas phase.

- Based on the information gained from the *ab initio* molecular dynamics simulations of the gas phase of 1-ethyl-3-methylimidazolium ethylsulfate, where a structural rearrangement from a bulk-phase like ion pair to a gas phase-like ion pair with increasing temperature occurs, an en route formation of ion pairs from the bulk to the surface has been suggested. With the aid of classical molecular dynamics simulations, applying the same force field, which was shown to be able to reproduce the molecular structure as well as to describe the surface of ionic liquids properly, a qualitative picture of the formation of an ion pair at the surface as well as the departure of this ion pair into the gas phase was gained for 1-ethyl-3-methylimidazolium ethylsulfate. From this qualitative picture, a four step evaporation mechanism has been proposed, which involves the diffusion of ions from bulk to surface, where they remain until a well-defined ion pair is formed, which leads to the departure from the surface into the vacuum.

- The relationship between ion pairing and charge transfer in ionic liquids was investigated. It was found, that charge transfer has a dramatic effect on the ion pairing behavior of ionic liquids. From static quantum chemical calculations, large charge transfer values were found for a series of ionic liquids, which are in good agreement with the general charge alteration used in force fields applied to ionic liquids. The decrease of charges in ionic liquids affects largely the ionicity, which is used to describe the ion pairing in

ionic liquids, and especially their interpretation. Thus, ion pairing in the bulk phase of ionic liquids seems less important than thought before, as the ionicity values need to be scaled according to the charge transfer values. In addition, structural effects were investigated by charge alteration of a solute NaCl ion pair within an ionic liquid. The increase of the solute charge favored the formation of ion pairs in ionic liquids making the solvent shell of the solute somehow static, while the decrease of the solute charge, which can be understood as charge transfer between the solvent and the solute, increased the dynamical behavior of the ionic liquid, making it more fluid. These findings are in good agreement with the general findings that the computed dynamical properties, *e. g.* viscosity, are described more accurately if the charge of ionic liquids is downscaled.

In the future, the proposed evaporation mechanism should be investigated in more details, for example, by developing a procedure to calculate the free energy of an ion pair leaving the surface or by extending the idea to other ionic liquids, which are known to be volatile and thereby confirming its validity. Furthermore, the investigation of the charge transfer effect on ion pairing can be extended to include the first solvent shell of ionic liquids utilizing the cluster ansatz and by increasing the number of possible conformations, therefore statistical events, increasing the accuracy of the charge transfer values and the hence scaled ionicity values.

The substitution effect of axles binding to different wheels, the Vögtle-type and the Leigh-type, has been investigated by static quantum chemical calculations.

- For the Vögtle-type pseudorotaxanes, experimental and theoretical data show that the substitution on the diamide axle changes the binding properties in several ways. First, the alkyl- and alkenyl-substituted axles bind with higher binding constants than aryl-substituted axles by an order of magnitude. Second, the binding is driven by enthalpic effects if the axle carries substituents with π-systems attached, only the formation of the alkyl-substituted pseudorotaxane is driven by positive binding entropies.

Third, within the series of different aryl-substituted diamide axles, the electronic substitution effects are important for the formation of pseudorotaxanes. Electron-withdrawing substituents diminish the binding constants compared to electron-donating substituents and the trends of the binding energies follow the Hammett substituent parameters.

- For the Leigh-type pseudorotaxanes, the substitution effects of different functional groups and the degree of molecular flexibility by changing the axles double C=C bond to a single C−C bond was studied. It was shown that a more flexible axle binds stronger than a more stiff one, thus changing from the double C=C bond to a single C−C bond the binding energy increased slightly. Alternating the substituent leads to a maximum increase of the binding energy by ∼10 %. Thus, it is possible to modulate the pseudorotaxane binding by the same amount. Stoppers on the axle, which are attributed a minor role in the binding of pseudorotaxanes, showed an influence on intramolecular interactions, as the trend of hydrogen bonding symmetry observed for the single and double bonded systems is reversed in their presence. Probing solvent effects by an implicit solvent model (COSMO) showed weakened complex binding for all systems, as the different parts of the system, axle and wheel, are differently stabilized by the surrounded solvent.

In the future, the solvent effects on pseudorotaxanes could be investigated by explicit solvent models like *ab initio* molecular dynamics and classical molecular dynamics. In addition, longer axles could be investigated, which have more than one docking station for the wheel, in order to study the different motions within these complex systems.

To summarize, the results presented in this work show that the utilization of a multiscale approach to investigate complex systems and their interactions is the right choice. Dynamical processes can be investigated in details by applying *ab initio* molecular dynamics and classical molecular dynamics. As shown for ionic liquids, the combination of both dynamical methods can be used to gain insights

into very complex processes, like the evaporation of these liquids. Furthermore, static quantum chemical calculations can be used to probe individual interactions present in complex systems, increasing the understanding of these systems, as shown for both rotaxanes and ionic liquids. The comprehension of the possible interactions in complex systems can further help to tune them for specific tasks as well as to improve the accuracy of empirical methods.

List of Figures

1.1 Chemical structures of common cations and anions in ionic liquids. 2
1.2 Methylation of an imidazolium cation at the C2 position. 4
1.3 Segregation of an ionic liquid into polar and nonpolar domains. . 12
1.4 Schematic illustration of a rotaxane. 15
1.5 Representation of Vögtle/Schalley-type and Leigh-type rotaxanes. 16
1.6 Representation of a twofold hydrogen bond in rotaxanes. 17
1.7 Schematic illustration of two important motions present in rotaxanes with two docking stations. 18

2.1 Definition of the in-plane and on-top conformation for imidazolium-based ionic liquids. 43

3.1 Labeling of 1-ethyl-3-methylimidazolium ethylsulfate used in this communication. 49
3.2 Comparison of the power spectrum obtained for one ion pair and for the bulk phase. 50
3.3 Spatial distribution function of atoms from the anion around the cation for one ion pair and for the bulk phase. 52
3.4 Adoptive labeling of 1-ethyl-3-methylimidazolium ethylsulfate used throughout the article. 59
3.5 Distance distribution functions and radial distribution functions of certain atoms in 1-ethyl-3-methylimidazolium ethylsulfate. 62

3.6 Combined distribution functions of distance distribution functions between certain atoms. 64
3.7 Spatial distribution functions of atoms from the anion around the cation. 65
3.8 Comparison of power spectra at three different temperatures. . . . 68
3.9 Illustrations of the in-plane, on-top and multiple interaction conformation. 70
3.10 Definition of in-plane and on-top conformation for imidazolium-based ionic liquids. 71
3.11 Boundaries for the in-plane conformation and on-top conformation. 72
3.12 Histogram and comparison of the occupation of both in-plane and on-top conformations. 73
3.13 Continuous correlation functions of the in-plane and on-top conformation. 75
3.14 Combined distribution function and continuous correlation function of the on-top conformation *via* the terminal carbon atom of the anion. 76
3.15 Comparison of distance distribution function to the free energy surface of this distance. 78
3.16 Adopted nomenclature for the studied 1-ethyl-3-methylimidazolium alkylsulfate ionic liquids. 88
3.17 Snapshots of simulation boxes, using a coloring code to identify polar and nonpolar domains in the ionic liquids. 90
3.18 Cation-anion site–site radial distribution functions. 93
3.19 Spatial distribution functions of the oxygen atoms and the terminal atom of the anion around the cation. 94
3.20 Static structure factors of representative atoms of the polar and nonpolar regions. 95

3.21 Number density profiles of 1-ethyl-3-methylimidazolium ethylsulfate and 1-ethyl-3-methylimidazolium octylsulfate. 98
3.22 Snapshots of the simulation boxes of 1-ethyl-3-methylimidazolium ethylsulfate and 1-ethyl-3-methylimidazolium octylsulfate. 99
3.23 Orientational ordering parameter of 1-ethyl-3-methylimidazolium ethylsulfate and 1-ethyl-3-methylimidazolium octylsulfate. 101
3.24 Variation of the charge density and electrostatic potential for 1-ethyl-3-methylimidazolium ethylsulfate and 1-ethyl-3-methylimidazolium octylsulfate. 102
3.25 Tangential radial distribution functions of individual regions for several representative pairs of atoms in the interfacial and bulk regions. 104
3.26 Surface tension profiles for 1-ethyl-3-methylimidazolium ethylsulfate across the direction normal of the interface and long-range correction to the surface tension for 1-ethyl-3-methylimidazolium octylsulfate. 106
3.27 Adopted nomenclature for the three pyrrolidinium-based ionic liquids. 115
3.28 Electrostatic potential mapped onto an isoelectronic density surface. 118
3.29 Snapshots of simulation boxes using a coloring code to identify polar and nonpolar domains in the ionic liquids. 119
3.30 Site–site radial distribution functions between several representative atoms of the cations and anions. 120
3.31 Static structure factors of representative atoms of the polar and nonpolar domains. 123
3.32 Number density profiles of the three pyrrolidinium-based ionic liquids. 124
3.33 Snapshots of the simulation boxes, representing high-charged and low-charged regions. 125

3.34 Orientational ordering parameter of the three pyrrolidinium-based ionic liquids. 127
3.35 Charge density profiles and electrostatic potential of the three pyrrolidinium-based ionic liquids. 129
3.36 Tangential radial distribution functions of individual regions for several representative pairs of atoms in the interfacial and bulk regions. 131
3.37 Surface tension profiles for 1-butyl-1-methylpyrrolidinium triflate across the direction normal of the interface and long-range correction to the surface tension for 1-butyl-1-methylpyrrolidinium bis(trifluoromethanesulfonyl)imide. 133
3.38 Schematic of the multistep mechanism for the complex evaporation of ionic liquids. 139
3.39 Histogram of neighboring counter-ions. 140
3.40 Combined distribution functions of the displacement and lifetime of next neighbors for the bulk and the surface region. 142
3.41 Histogram of the average distance between several points in anion and cation. 143
3.42 Reaction between charged species in ionic liquids. 149
3.43 Studied ionic liquids and their abbreviations 151
3.44 Example of the simulation boxes. 152
3.45 Labeling of 1-butyl-3-methylimidazolium cation. 153
3.46 Development of the sodium–chloride distance over time in three simulations. 159
3.47 Snapshot of sodium chloride solvation shell. 160
3.48 Pseudo-spatial distribution of the imidazolium cation's ring hydrogen atoms and the bromide anions around the sodium chloride ion pair. 160
3.49 Ortep plots of crystal structures of two pseudorotaxanes, their crystal packing and space filling representations. 173

3.50 ^{1}H NMR titration of an pseudorotaxane. 175
3.51 Shifts of the pyridine dicarboxamide NH signal. 176
3.52 Isothermal titration calorimetry experiments of two pseudorotaxanes. 179
3.53 Optimized structure of one pseudorotaxane. 180
3.54 Chemical structure of the investigated pseudorotaxanes. 199
3.55 Optimized molecular geometry of one rotaxane. 200
3.56 Electrostatic potential for different rotaxane complexes. 204
3.57 Interaction energies plotted against the Hammett parameters. . . 206

List of Tables

3.1 Comparison of important calculation parameters for the three investigated systems. 61

3.2 Length scales of polar and nonpolar domains. 96

3.3 Surface tension for the studied ionic liquids using different operational expressions. 105

3.4 Length scales of polar and nonpolar domains in pyrrolidinium-based ionic liquids. 121

3.5 Surface tension for the studied ionic liquids using different operational expressions. 132

3.6 Calculated absolute charges on the ions within a single ion pair and their recalculated ionicity values. 154

3.7 Characteristic distances in the simulations of a single sodium chloride ion pair in 1-butyl-3-methylimidazolium bromide with different charges on sodium and chloride. 158

3.8 Free energy barrier and free energy of dissociation of the sodium chloride ion pair with different charges on sodium and chloride. . . 161

3.9 Characteristic distances of a single sodium chloride in 1-butyl-3-methylimidazolium bromide with different sizes of the sodium anion. 162

3.10 Free energy barrier and free energy of dissociation of the sodium chloride ion pair with different sizes of the sodium anion. 163

3.11 Thermodynamic data obtained from NMR titrations and isothermal titration calorimetry measurements. 177

3.12 Calculated hydrogen bond lengths and angles, adiabatic interaction energies, conformation change energies of wheel and axle upon binding, and shared electron number for the same pseudorotaxanes. 181
3.13 Comparison of the X-ray structure of the rotaxane with the computed crystal and gas phase geometries. 201
3.14 Interaction energies for the different pseudorotaxane systems. . . . 202
3.15 Hydrogen bond distances for the different pseudorotaxane systems. 205
3.16 Interaction energies for the different pseudorotaxane systems applying a solvent model. 207
3.17 Hydrogen bond geometry for the different pseudorotaxane systems with solvent model. 207

Bibliography

[1] Rogers, R. D.; Seddon, K. R. *Science* **2003**, *302*, 792–793.

[2] Brennecke, J. F.; Rogers, R. D.; Seddon, K. R. *Ionic liquids IV. Not just solvents anymore.*; American Chemical Society, 2007.

[3] Plechkova, N. V.; Seddon, K. R. *Chem. Soc. Rev.* **2008**, *37*, 123–150.

[4] Wasserscheid, P.; Welton, T. *Ionic liquids in Synthesis, Second Edition*; Wiley Online Library, 2008; Vol. 7.

[5] Welton, T. *Chem. Rev.* **1999**, *99*, 2071–2084.

[6] Wasserscheid, P.; Keim, W. *Angew. Chem. Int. Ed.* **2000**, *39*, 3772–3789.

[7] Sheldon, R. *Chem. Commun.* **2001**, 2399–2407.

[8] Blanchard, L. A.; Hancu, D.; Beckman, E. J.; Brennecke, J. F. *Nature* **1999**, *399*, 28–29.

[9] Almantariotis, D.; Stevanovic, S.; Fandiño, O.; Pensado, A. S.; Pádua, A. A. H.; Coxam, J.-Y.; Costa Gomes, M. F. *J. Phys. Chem. B* **2012**, *116*, 7728–7738.

[10] Almantariotis, D.; Gefflaut, T.; Pádua, A. A. H.; Coxam, J.-Y.; Costa Gomes, M. F. *J. Phys. Chem. B* **2010**, *114*, 3608–3617.

[11] Deng, Y.; Morrissey, S.; Gathergood, N.; Delort, A.-M.; Husson, P.; Costa Gomes, M. *ChemSusChem* **2010**, *3*, 377–385.

[12] Anthony, J. L.; Anderson, J. L.; Maginn, E. J.; Brennecke, J. F. *J. Phys. Chem. B* **2005**, *109*, 6366–6374.

[13] Heintz, A. *J. Chem. Thermodyn.* **2005**, *37*, 525–535.

[14] Mokrushin, V.; Assenbaum, D.; Paape, N.; Gerhard, D.; Mokrushina, L.; Wasserscheid, P.; Arlt, W.; Kistenmacher, H.; Neuendorf, S.; Göke, V. *Chem. Eng. Technol.* **2010**, *33*, 63–73.

[15] Lei, Z.; Arlt, W.; Wasserscheid, P. *Fluid Phase Equilib.* **2006**, *241*, 290–299.

[16] Li, R.; Xing, H.; Yang, Q.; Zhao, X.; Su, B.; Bao, Z.; Yang, Y.; Ren, Q. *Industrial & Engineering Chemistry Research* **2012**, *51*, 8588–8597.

[17] Zhao, W.; He, G.; Nie, F.; Zhang, L.; Feng, H.; Liu, H. *J. Membr. Sci.* **2012**, *411–412*, 73–80.

[18] Jiménez, A. E.; Bermúdez, M. D. *Tribol. Lett.* **2007**, *26*, 53–60.

[19] Palacio, M.; Bhushan, B. *Tribol. Lett.* **2010**, *40*, 247–268.

[20] Bayley, P. M.; Best, A. S.; MacFarlane, D. R.; Forsyth, M. *ChemPhysChem* **2011**, *12*, 823–827.

[21] Lane, G. H.; Best, A. S.; MacFarlane, D. R.; Forsyth, M.; Bayley, P. M.; Hollenkamp, A. F. *Electrochim. Acta* **2010**, *55*, 8947–8952.

[22] Simons, T. J.; Torriero, A. A. J.; Howlett, P. C.; MacFarlane, D. R.; Forsyth, M. *Electrochem. Commun.* **2012**, *18*, 119–122.

[23] Visser, A. E.; Swatloski, R. P.; Reichert, W. M.; Mayton, R.; Sheff, S.; Wierzbicki, A.; Davis Jr., J. H.; Rogers, R. D. *Chem. Commun.* **2001**, *1*, 135–136.

[24] Bates, E. D.; Mayton, R. D.; Ntai, I.; Davis Jr., J. H. *J. Am. Chem. Soc.* **2002**, *124*, 926–927.

[25] Visser, A. E.; Swatloski, R. P.; Reichert, W. M.; Mayton, R.; Sheff, S.; Wierzbicki, A.; Davis Jr., J. H.; Rogers, R. D. *Environ. Sci. Technol.* **2002**, *36*, 2523–2529.

[26] H. Davis, J., Jr *Chem. Lett.* **2004**, *33*, 1072–1077.

[27] Deng, Y.; Besse-Hoggan, P.; Sancelme, M.; Delort, A.-M.; Husson, P.; Costa Gomes, M. F. *J. Hazard. Mater.* **2011**, *198*, 165–174.

[28] Zahn, S.; Uhlig, F.; Thar, J.; Spickermann, C.; Kirchner, B. *Angew. Chem. Int. Ed.* **2008**, *47*, 3639–3641.

[29] Zahn, S.; Kirchner, B. *J. Phys. Chem. A* **2008**, *112*, 8430–8435.

[30] Pensado, A. S.; Brehm, M.; Thar, J.; Seitsonen, A. P.; Kirchner, B. *ChemPhysChem* **2012**, *13*, 1845–1853.

[31] Grimme, S.; Hujo, W.; Kirchner, B. *Phys. Chem. Chem. Phys.* **2012**, *14*, 4875–4883.

[32] Seddon, K. R.; Stark, A.; Torres, M.-J. *Pure Appl. Chem.* **2000**, *72*, 2275–2287.

[33] Bernard, U. L.; Izgorodina, E. I.; MacFarlane, D. R. *J. Phys. Chem. C* **2010**, *114*, 20472–20478.

[34] Hunt, P. A. *J. Phys. Chem. B* **2007**, *111*, 4844–4853.

[35] Li, H.; Ibrahim, M.; Agberemi, I.; Kobrak, M. N. *J. Chem. Phys.* **2008**, *129*, 124507.

[36] Tsuzuki, S.; Tokuda, H.; Hayamizu, K.; Watanabe, M. *J. Phys. Chem. B* **2005**, *109*, 16474–16481.

[37] Tsuzuki, S.; Tokuda, H.; Mikami, M. *Phys. Chem. Chem. Phys.* **2007**, *9*, 4780–4784.

[38] Zahn, S.; Bruns, G.; Thar, J.; Kirchner, B. *Phys. Chem. Chem. Phys.* **2008**, *10*, 6921–6924.

[39] Izgorodina, E. I. *Phys. Chem. Chem. Phys.* **2011**, *13*, 4189–4207.

[40] Lehmann, S. B. C.; Roatsch, M.; Schöppke, M.; Kirchner, B. *Phys. Chem. Chem. Phys.* **2010**, *12*, 7473–7486.

[41] Kempter, V.; Kirchner, B. *J. Mol. Struct. (Theochem)* **2010**, *972*, 22–34.

[42] Leys, J.; Rajesch, R. N.; Menon, P. C.; Glorieux, C.; Longuemart, S.; Nockemann, P.; Pellens, M.; Binnemans, K. *J. Chem. Phys.* **2010**, *133*, 034503.

[43] Abdul-Sada, A. K.; Greenway, A. M.; Hitchcock, P. B.; Mohammed, T. J.; Seddon, K. R.; Zora, J. A. *J. Chem. Soc., Chem. Commun.* **1986**, *24*, 1753–1754.

[44] Izgorodina, E. I.; MacFarlane, D. R. *J. Phys. Chem. B* **2011**, *115*, 14659–14667.

[45] Goswami, M.; Arunan, E. *Phys. Chem. Chem. Phys.* **2009**, *11*, 8974–8383.

[46] Pimentel, G. C.; McCleallan, A. L. *The Hydrogen Bond*; W. H. Freeman and Co.: San Francisco, 1960.

[47] Gardas, R. L.; Costa, H. F.; Freire, M. G.; Carvalho, P. J.; Marrucho, I. M.; Fonseca, I. M. A.; Ferreira, A. G. M.; Coutinho, J. A. P. *J. Chem. Eng. Data* **2008**, *53*, 805–811.

[48] Sánchez, L. G.; Espel, J. R.; Onink, F.; Meindersma, G. W.; de Haan, A. B. *J. Chem. Eng. Data* **2009**, *54*, 2803–2812.

[49] Castner Jr., E. W.; Wishart, J. F. *J. Chem. Phys.* **2010**, *132*, 120901.

[50] Siedlecka, E. M.; Czerwicka, M.; Stolte, S.; Stepnowski, P. *Curr. Org. Chem.* **2011**, *15*, 1974–1991.

[51] Bonhôte, P.; Dias, A.-P.; Papageorgiou, N.; Kalyanasundaram, K.; Grätzel, M. *Inorg. Chem.* **1996**, *35*, 1168–1178.

[52] Fumino, K.; Wulf, A.; Ludwig, R. *Phys. Chem. Chem. Phys.* **2009**, *11*, 8790–8794.

[53] Fumino, K.; Peppel, T.; Geppert-Rybczyńska, M.; Zaitsau, D. H.; Lehmann, J. K.; Verevkin, S. P.; Köckerling, M.; Ludwig, R. *Phys. Chem. Chem. Phys.* **2011**, *13*, 14064–14075.

[54] Fumino, K.; Wulf, A.; Ludwig, R. *Angew. Chem. Int. Ed.* **2008**, *47*, 8731–8734.

[55] Wulf, A.; Fumino, K.; Ludwig, R. *Angew. Chem. Int. Ed.* **2010**, *49*, 449–453.

[56] Noack, K.; Schulz, P. S.; Paape, N.; Kiefer, J.; Wasserscheid, P.; Leipertz, A. *Phys. Chem. Chem. Phys.* **2010**, *12*, 14153–14161.

[57] Nockemann, P.; Thijs, B.; Driesen, K.; Janssen, C. R.; Van Hecke, K.; Van Meervelt, L.; Koßmann, S.; Kirchner, B.; Binnemans, K. *J. Phys. Chem. B* **2007**, *111*, 5254–5263.

[58] Welton, T. *Green Chem.* **2011**, *13*, 225–225.

[59] Earle, M. J.; Esperança, J. M. S. S.; Gilea, M. A.; Canongia Lopes, J. N.; Rebelo, L. P. N.; Magee, J. W.; Seddon, K. R.; Widegren, J. A. *Nature* **2006**, *439*, 831–834.

[60] Rebelo, L. P. N.; Canongia Lopes, J. N.; Esperança, J. M. S. S.; Filipe, E. *J. Phys. Chem. B* **2005**, *109*, 6040–6043.

[61] Zaitsau, D. H.; Kabo, G. J.; Strechan, A. A.; Paulechka, Y. U.; Tschersich, A.; Verevkin, S. P.; Heintz, A. *J. Phys. Chem. A* **2006**, *110*, 7303–7306.

[62] Strasser, D.; Goulay, F.; Kelkar, M. S.; Maginn, E. J.; Leone, S. R. *J. Phys. Chem. A* **2007**, *111*, 3191–3195.

[63] Kelkar, M. S.; Maginn, E. J. *J. Phys. Chem. B* **2007**, *111*, 9424–9427.

[64] Armstrong, J. P.; Hurst, C.; Jones, R. G.; Licence, P.; Lovelock, K. R. J.; Satterley, C. J.; Villar-Garcia, I. J. *Phys. Chem. Chem. Phys.* **2007**, *9*, 982–990.

[65] Leal, J. a. P.; Esperança, J. M. S. S.; Minas da Piedade, M. E.; Canongia Lopes, J. N.; Rebelo, L. P. N.; Seddon, K. R. *J. Phys. Chem. A* **2007**, *111*, 6176–6182.

[66] Akai, N.; Kawai, A.; Shibuya, K. *Chem. Lett.* **2008**, *37*, 256–257.

[67] Akai, N.; Parazs, D.; Kawai, A.; Shibuya, K. *J. Phys. Chem. B* **2009**, *113*, 4756–4762.

[68] Fumino, K.; Wulf, A.; Verevkin, S. P.; Heintz, A.; Ludwig, R. *Chem. Phys. Chem.* **2010**, *11*, 1623–1626.

[69] Lovelock, K. R. J.; Deyko, A.; Licence, P.; Jones, R. G. *Phys. Chem. Chem. Phys.* **2010**, *12*, 8893–8901.

[70] Esperança, J. M. S. S.; Canongia Lopes, J. N.; Tariq, M.; Santos, L. M. N. B. F.; Magee, J. W.; Rebelo, L. P. N. *J. Chem. Eng. Data* **2010**, *55*, 3–12.

[71] Chambreau, S. D.; Boatz, J. A.; Vaghjiani, G. L.; Koh, C.; Kostko, O.; Golan, A.; Leone, S. R. *J. Phys. Chem. A* **2012**, *116*, 5867–5876.

[72] Ahmed, E.; Breternitz, J.; Groh, M. F.; Ruck, M. *CrystEngComm* **2012**, *14*, 4874–4885.

[73] Santos, L. M. N. B. F.; Canongia Lopes, J. N.; Coutinho, J. a. A. P.; Esperança, J. M. S. S.; Gomes, L. R.; Marrucho, I. M.; Rebelo, L. P. N. *J. Am. Chem. Soc.* **2007**, *129*, 284–285, PMID: 17212402.

[74] Rocha, M. A. A.; Lima, C. F. R. A. C.; Gomes, L. R.; Schröder, B.; Coutinho, J. a. A. P.; Marrucho, I. M.; Esperança, J. M. S. S.; Rebelo, L. P. N.; Shimizu, K.; Canongia Lopes, J. N.; Santos, L. M. N. B. F. *J. Phys. Chem. B* **2011**, *115*, 10919–10926.

[75] Morrow, T. I.; Maginn, E. J. *J. Phys. Chem. B* **2002**, *106*, 12807–12813.

[76] Deyko, A.; Lovelock, K. R. J.; Corfield, J.-A.; Taylor, A. W.; Gooden, P. N.; Villar-Garcia, I. J.; Licence, P.; Jones, R. G.; Krasovskiy, V. G.; Chernikova, E. A.; Kustov, L. M. *Phys. Chem. Chem. Phys.* **2009**, *11*, 8544–8555.

[77] Luo, H.; Baker, G. A.; Dai, S. *J. Phys. Chem. B* **2008**, *112*, 10077–10081.

[78] Santos, L. M.; Spencer S. Lima, L. M.; Lima, C. F.; Magalhães, F. a. D.; Torres, M. C.; Schröder, B.; Ribeiro da Silva, M. A. V. *J. Chem. Thermodyn.* **2011**, *43*, 834–843.

[79] Koßmann, S.; Thar, J.; Kirchner, B.; Hunt, P. A.; Welton, T. *J. Chem. Phys.* **2006**, *124*, 174506.

[80] Ballone, P.; Pinilla, C.; Kohanoff, J.; Del Pópolo, M. G. *J. Phys. Chem. B* **2007**, *111*, 4938–4950.

[81] Hallett, J. P.; Liotta, C. L.; Ranieri, G.; Welton, T. *J. Org. Chem.* **2009**, *74*, 1864–1868.

[82] Lui, M. Y.; Crowhurst, L.; Hallett, J. P.; Hunt, P. A.; Niedermeyer, H.; Welton, T. *Chem. Sci.* **2011**, *2*, 1491–1496.

[83] Lovelock, K. R. J. *Phys. Chem. Chem. Phys.* **2012**, *14*, 5071–5089.

[84] Endres, F. *Phys. Chem. Chem. Phys.* **2012**, *14*, 5008–5009.

[85] Jiménez, A. E.; Bermúdez, M. D. *Tribol. Lett.* **2009**, *33*, 111–126.

[86] Jiménez, A. E.; Bermúdez, M. D. *Tribol. Lett.* **2010**, *37*, 431–443.

[87] Jiménez, A. E.; Bermúdez, M. D. *Tribol. Lett.* **2010**, *40*, 237–246.

[88] Mehnert, C. P.; Mozeleski, E. J.; Cook, R. A. *Chem. Commun.* **2002**, 3010–3011.

[89] Köhler, R.; Restolho, J.; Krastev, R.; Shimizu, K.; Canongia Lopes, J. N.; Saramago, B. *J. Phys. Chem. Lett.* **2011**, *2*, 1551–1555.

[90] Riisager, A.; Fehrmann, R.; Haumann, M.; Wasserscheid, P. *Top. Catal.* **2006**, *40*, 91–102.

[91] Riisager, A.; Fehrmann, R.; Haumann, M.; Wasserscheid, P. *Eur. J. Inorg. Chem.* **2006**, *2006*, 695–706.

[92] Dupont, J.; Scholten, J. D. *Chem. Soc. Rev.* **2010**, *39*, 1780–1804.

[93] Wender, H.; Gonçalves, R. V.; Feil, A. F.; Migowski, P.; Poletto, F. S.; Pohlmann, A. R.; Dupont, J.; Teixeira, S. R. *J. Phys. Chem. C* **2011**, *115*, 16362–16367.

[94] Torimoto, T.; Tsuda, T.; Okazaki, K.-i.; Kuwabata, S. *Adv. Mater.* **2010**, *22*, 1196–1221.

[95] Lockett, V.; Sedev, R.; Bassell, C.; Ralston, J. *Phys. Chem. Chem. Phys.* **2008**, *10*, 1330–1335.

[96] Bowers, J.; Vergara-Gutierrez, M. C.; Webster, J. R. P. *J. Power Sources* **2004**, *20*, 309–312.

[97] Ridings, C.; Lockett, V.; Andersson, G. *Phys. Chem. Chem. Phys.* **2011**, *13*, 17177–17184.

[98] Hammer, T.; Reichelt, M.; Morgner, H. *Phys. Chem. Chem. Phys.* **2010**, *12*, 11070–11080.

[99] Martinez, I. S.; Santos, C.; Baldelli, S. *ChemPhysChem* **2012**, *13*, 1818–1824.

[100] Santos, C. S.; Baldelli, S. *Chem. Soc. Rev.* **2010**, *39*, 2136–2145.

[101] Lynden-Bell, R. M.; Del Pópolo, M. *Phys. Chem. Chem. Phys.* **2006**, *8*, 949–954.

[102] Bhargava, B. L.; Balasubramanian, S. *J. Am. Chem. Soc.* **2006**, *128*, 10073–10078.

[103] Jiang, W.; Wang, Y.; Yan, T.; Voth, G. A. *J. Phys. Chem. C* **2008**, *112*, 1132–1139.

[104] Pensado, A. S.; Malfreyt, P.; Pádua, A. A. H. *J. Phys. Chem. B* **2009**, *113*, 14708–14718.

[105] Wang, Y.; Voth, G. A. *J. Am. Chem. Soc.* **2005**, *127*, 12192–12193.

[106] Canongia Lopes, J. N. A.; Pd́ua, A. A. H. *J. Phys. Chem. B* **2006**, *110*, 3330–3335.

[107] Triolo, A.; Russina, O.; Bleif, H.-J.; Di Cola, E. *J. Phys. Chem. B* **2007**, *111*, 4641–4644.

[108] Russina, O.; Gontrani, L.; Fazio, B.; Lombardo, D.; Triolo, A.; Caminiti, R. *Chem. Phys. Lett.* **2010**, *493*, 259–262.

[109] Triolo, A.; Russina, O.; Fazio, B.; Triolo, R.; Di Cola, E. *Chem. Phys. Lett.* **2008**, *457*, 362–365.

[110] Russina, O.; Triolo, A.; Gontrani, L.; Caminiti, R.; Xiao, D.; Hines Jr., L. G.; Bartsch, R. A.; Quitevis, E. L.; Plechkova, N.; Seddon, K. R. *J. Phys.: Condens. Matter* **2009**, *21*, 424121.

[111] Russina, O.; Triolo, A.; Gontrani, L.; Caminiti, R. *J. Phys. Chem. Lett.* **2012**, *3*, 27–33.

[112] Russina, O.; Lo Celso, F.; Di Michiel, M.; Passerini, S.; Appetecchi, G. B.; Castiglione, F.; Mele, A.; Caminiti, R.; Triolo, A. *Faraday Discuss.* **2013**, *167*, 499–513.

[113] Pereiro, A. B.; Pastoriza-Gallego, M. J.; Shimizu, K.; Marrucho, I. M.; Canongia Lopes, J. N.; Piñeiro, M. M.; Rebelo, L. P. N. *J. Phys. Chem. B* **2013**, *117*, 10826–10833.

[114] Weber, H.; Hollóczki, O.; Pensado, A. S.; Kirchner, B. *J. Chem. Phys.* **2013**, *139*, 084502.

[115] Marcus, Y.; Hefter, G. *Chem. Rev.* **2006**, *106*, 4585–4621.

[116] Brüssel, M.; Brehm, M.; Pensado, A. S.; Malberg, F.; Ramzan, M.; Stark, A.; Kirchner, B. *Phys. Chem. Chem. Phys.* **2012**, *14*, 13204–13215.

[117] Hardacre, C.; Holbrey, J. D.; McMath, S. J.; Bowron, D. T.; Soper, A. K. *J. Chem. Phys.* **2003**, *118*, 273–278.

[118] Hardacre, C.; Holbrey, J. D.; Nieuwenhuyzen, M.; Youngs, T. G. A. *Acc. Chem. Res.* **2007**, *40*, 1146–1155.

[119] Bühl, M.; Chaumont, A.; Schurhammer, R.; Wipff, G. *J. Phys. Chem. B* **2005**, *109*, 18591–18599.

[120] Matthews, R. P.; Welton, T.; Hunt, P. A. *Phys. Chem. Chem. Phys.* **2014**, *16*, 3238–3253.

[121] Zhao, W.; Leroy, F.; Heggen, B.; Zahn, S.; Kirchner, B.; Balasubramanian, S.; Müller-Plathe, F. *J. Am. Chem. Soc.* **2009**, *131*, 15825–15833.

[122] Tokuda, H.; Hayamizu, K.; Ishii, K.; Susan, M. A. B. H.; Watanabe, M. *J. Phys. Chem. B* **2004**, *108*, 16593–16600.

[123] Tokuda, H.; Hayamizu, K.; Ishii, K.; Susan, M. A. B. H.; Watanabe, M. *J. Phys. Chem. B* **2005**, *109*, 6103–6110.

[124] Tokuda, H.; Tsuzuki, S.; Susan, M. A. B. H.; Hayamizu, K.; Watanabe, M. *J. Phys. Chem. B* **2006**, *110*, 19593–19600.

[125] Ueno, K.; Tokuda, H.; Watanabe, M. *Phys. Chem. Chem. Phys.* **2010**, *12*, 1649–1658.

[126] Angell, C. A.; Ansari, Y.; Zhao, Z. *Faraday Discuss.* **2012**, *154*, 9–27.

[127] Walden, P. *Z. Physik. Chem.* **1906**, *55*, 207.

[128] Angell, C. A.; Byrne, N.; Belieres, J.-P. *Acc. Chem. Res.* **2007**, *40*, 1228–1236.

[129] MacFarlane, D. R.; Forsyth, M.; Izgorodina, E. I.; Abbott, A. P.; Annat, G.; Fraser, K. *Phys. Chem. Chem. Phys.* **2009**, *11*, 4962–4967.

[130] Youngs, T. G. A.; Hardacre, C. *ChemPhysChem* **2008**, *9*, 1548–1558.

[131] Schill, G. *Rotaxanes and Knots*; Academic Press: New York, 1971.

[132] Sauvage, J. P., Dietrich-Buchecker, C., Eds. *Molecular Catenanes, Rotaxanes, and Knots*; Wiley-VCH: Weinheim, 1999.

[133] Altieri, A.; Gatti, F. G.; Kay, E. R.; Leigh, D. A.; Martel, D.; Paolucci, F.; Slawin, A. M. Z.; Wong, J. K. Y. *J. Am. Chem. Soc.* **2003**, *125*, 8644–8654.

[134] Linnartz, P.; Bitter, S.; Schalley, C. *Eur. J. Org. Chem.* **2003**, *2003*, 4819–4829.

[135] Brouwer, A. M.; Fazio, S. M.; Frochot, C.; Gatti, F. G.; Leigh, D. A.; Wong, J. K. Y.; Wurpel, G. W. H. *Pure Appl. Chem.* **2003**, *75*, 1055–1060.

[136] Tseng, H.-R.; Vignon, S. A.; Celestre, P. C.; Perkins, J.; Jeppesen, J. O.; Di Fabio, A.; Ballardini, R.; Gandolfi, M. T.; Venturi, M.; Balzani, V.; Stoddart, J. F. *Chem. Eur. J.* **2004**, *10*, 155–172.

[137] Schalley, C. A.; Reckien, W.; Peyerimhoff, S.; Baytekin, B.; Vögtle, F. *Chem. Eur. J.* **2004**, *10*, 4777–4789.

[138] Schalley, C. A.; Weilandt, T.; Brüggemann, J.; Vögtle, F. In *Templates in Chemistry I*; Schalley, C., Vögtle, F., Dötz, K., Eds.; Topics in Current Chemistry; Springer Berlin Heidelberg, 2004; Vol. 248; pp 141–200.

[139] Keaveney, C. M.; Leigh, D. A. *Angew. Chem. Int. Ed.* **2004**, *43*, 1222–1224.

[140] Ghosh, P.; Federwisch, G.; Kogej, M.; Schalley, C. A.; Haase, D.; Saak, W.; Lützen, A.; Gschwind, R. M. *Org. Biomol. Chem.* **2005**, *3*, 2691–2700.

[141] Leigh, D. A.; Morales, M. A. F.; Pérez, E. M.; Wong, J. K. Y.; Saiz, C. G.; Slawin, A. M. Z.; Carmichael, A. J.; Haddleton, D. M.; Brouwer, A. M.; Buma, W. J.; Wurpel, G. W. H.; León, S.; Zerbetto, F. *Angew. Chem. Int. Ed.* **2005**, *44*, 3062–3067.

[142] Moonen, N. N. P.; Flood, A. H.; Fernández, J. M.; Stoddart, J. F. In *Molecular Machines*; Kelly, T., Ed.; Topics in Current Chemistry; Springer Berlin Heidelberg, 2005; Vol. 262; pp 99–132.

[143] Kay, E. R.; Leigh, D. A. In *Molecular Machines*; Kelly, T., Ed.; Topics in Current Chemistry; Springer Berlin Heidelberg, 2005; Vol. 262; pp 133–177.

[144] Marlin, D. S.; González Cabrera, D.; Leigh, D. A.; Slawin, A. M. Z. *Angew. Chem. Int. Ed.* **2006**, *45*, 1385–1390.

[145] Vickers, M. S.; Beer, P. D. *Chem. Soc. Rev.* **2007**, *36*, 211–225.

[146] Haussmann, P. C.; Khan, S. I.; Stoddart, J. F. *J. Org. Chem.* **2007**, *72*, 6708–6713.

[147] Baytekin, B.; Zhu, S. S.; Brusilowskij, B.; Illigen, J.; Ranta, J.; Huuskonen, J.; Russo, L.; Rissanen, K.; Kaufmann, L.; Schalley, C. A. *Chem. Eur. J.* **2008**, *14*, 10012–10028.

[148] Fioravanti, G.; Haraszkiewicz, N.; Kay, E. R.; Mendoza, S. M.; Bruno, C.; Marcaccio, M.; Wiering, P. G.; Paolucci, F.; Rudolf, P.; Brouwer, A. M.; Leigh, D. A. *J. Am. Chem. Soc.* **2008**, *130*, 2593–2601.

[149] Umehara, T.; Kawai, H.; Fujiwara, K.; Suzuki, T. *J. Am. Chem. Soc.* **2008**, *130*, 13981–13988.

[150] von Delius, M.; Geertsema, E. M.; Leigh, D. A. *Nature Chem.* **2010**, *2*, 96–101.

[151] von Delius, M.; Leigh, D. A. *Chem. Soc. Rev.* **2011**, *40*, 3656–3676.

[152] Barrell, M. J.; Leigh, D. A.; Lusby, P. J.; Slawin, A. M. Z. *Angew. Chem. Int. Ed.* **2008**, *47*, 8036–8039.

[153] Barrell, M. J.; Campaña, A. G.; von Delius, M.; Geertsema, E. M.; Leigh, D. A. *Angew. Chem. Int. Ed.* **2011**, *50*, 285–290.

[154] Anelli, P. L.; Spencer, N.; Stoddart, J. F. *J. Am. Chem. Soc.* **1991**, *113*, 5131–5133.

[155] Leigh, D. A.; Thomson, A. R. *Org. Lett.* **2006**, *8*, 5377–5379.

[156] Berná, J.; Bottari, G.; Leigh, D. A.; Pérez, E. M. *Pure Appl. Chem.* **2007**, *79*, 39–54.

[157] Crowley, J. D.; Leigh, D. A.; Lusby, P. J.; McBurney, R. T.; Perret-Aebi, L.-E.; Petzold, C.; Slawin, A. M. Z.; Symes, M. D. *J. Am. Chem. Soc.* **2007**, *129*, 15085–15090.

[158] Goldup, S. M.; Leigh, D. A.; Lusby, P. J.; McBurney, R. T.; Slawin, A. M. Z. *Angew. Chem. Int. Ed.* **2008**, *47*, 3381–3384.

[159] Leigh, D. A.; Thomson, A. R. *Tetrahedron* **2008**, *64*, 8411–8416, 2007 Tetrahedron Prize for Creativity in Organic Chemistry. Synthetic NanoSystems and NanoMachinery. Professor Sir Fraser Stoddart.

[160] Altieri, A.; Aucagne, V.; Carrillo, R.; Clarkson, G. J.; D'Souza, D. M.; Dunnett, J. A.; Leigh, D. A.; Mullen, K. M. *Chem. Sci.* **2011**, *2*, 1922–1928.

[161] Schalley, C. A.; Beizai, K.; Vögtle, F. *Acc. Chem. Res.* **2001**, *34*, 465–476, PMID: 11412083.

[162] Ghosh, P.; Mermagen, O.; Schalley, C. A. *Chem. Commun.* **2002**, 2628–2629.

[163] Dzyuba, E. V.; Kaufmann, L.; Löw, N. L.; Meyer, A. K.; Winkler, H. D. F.; Rissanen, K.; Schalley, C. A. *Org. Lett.* **2011**, *13*, 4838–4841.

[164] Hunter, C. A. *J. Am. Chem. Soc.* **1992**, *114*, 5303–5311.

[165] Vögtle, F.; Dünnwald, T.; Schmidt, T. *Acc. Chem. Res.* **1996**, *29*, 451–460.

[166] Reckien, W.; Peyerimhoff, S. D. *J. Phys. Chem. A* **2003**, *107*, 9634–9640.

[167] Reckien, W.; Kirchner, B.; Peyerimhoff, S. D. *J. Phys. Chem. A* **2006**, *110*, 12963–12970.

[168] Linke, M.; Chambron, J.-C.; Heitz, V.; Sauvage, J.-P.; Semetey, V. *Chem. Commun.* **1998**, 2469–2470.

[169] Raehm, L.; Kern, J.-M.; Sauvage, J.-P. *Chem. Eur. J.* **1999**, *5*, 3310–3317.

[170] Kern, J.-M.; Raehm, L.; Sauvage, J.-P.; Divisia-Blohorn, B.; Vidal, P.-L. *Inorg. Chem.* **2000**, *39*, 1555–1560.

[171] Létinois-Halbes, U.; Hanss, D.; Beierle, J. M.; Collin, J.-P.; Sauvage, J.-P. *Org. Lett.* **2005**, *7*, 5753–5756.

[172] Collin, J.-P.; Durola, F.; Mobian, P.; Sauvage, J.-P. *Eur. J. Inorg. Chem.* **2007**, *2007*, 2420–2425.

[173] Durot, S.; Reviriego, F.; Sauvage, J.-P. *Dalton Trans.* **2010**, *39*, 10557–10570.

[174] Periyasamy, G.; Sour, A.; Collin, J.-P.; Sauvage, J.-P.; Remacle, F. *J. Phys. Chem. B* **2009**, *113*, 6219–6229.

[175] Baggerman, J.; Haraszkiewicz, N.; Wiering, P. G.; Fioravanti, G.; Marcaccio, M.; Paolucci, F.; Kay, E. R.; Leigh, D. A.; Brouwer, A. M. *Chem. Eur. J.* **2013**, *19*, 5566–5577.

[176] Leigh, D. A.; Troisi, A.; Zerbetto, F. *Angew. Chem. Int. Ed.* **2000**, *39*, 350–353.

[177] Deng, W.-Q.; Muller, R. P.; Goddard III, W. A. *J. Am. Chem. Soc.* **2004**, *126*, 13562–13563.

[178] Hirva, P.; Haukka, M.; Pakkanen, T. A. *J. Mol. Model.* **2008**, *14*, 879–886.

[179] Altieri, A.; Bottari, G.; Dehez, F.; Leigh, D. A.; Wong, J. K. Y.; Zerbetto, F. *Angew. Chem. Int. Ed.* **2003**, *42*, 2296–2300.

[180] Zheng, X.; Sohlberg, K. *J. Phys. Chem. A* **2006**, *110*, 11862–11869.

[181] Ben Shir, I.; Sasmal, S.; Mejuch, T.; Sinha, M. K.; Kapon, M.; Keinan, E. *J. Org. Chem.* **2008**, *73*, 8772–8779.

[182] Reckien, W.; Spickermann, C.; Eggers, M.; Kirchner, B. *Chem. Phys.* **2008**, *343*, 186–199, Theoretical Spectroscopy and its Impact on Experiment - (in honour of Sigrid D. Peyerimhoff).

[183] Spickermann, C.; Felder, T.; Schalley, C.; Kirchner, B. *Chem. Eur. J.* **2008**, *14*, 1216–1227.

[184] Kirchner, B.; Spickermann, C.; Reckien, W.; Schalley, C. A. *J. Am. Chem. Soc.* **2010**, *132*, 484–494.

[185] Thar, J.; Kirchner, B. *J. Phys. Chem. A* **2006**, *110*, 4229–4237.

[186] The Nobel Prize in Chemistry 2013 - Advanced Information. *Nobelprize.org*, Nobel Media AB 2013. Web. 1 Apr 2014; `http://www.nobelprize.org/nobel_prizes/chemistry/laureates/2013/advanced.html`.

[187] Abrol, R.; Kirchner, B.; Vrabec, J. *Multiscale Molecular Methods in Applied Chemistry*; Springer, 2011; Vol. 307.

[188] Szabo, A.; Ostlund, N. S. *Modern quantum chemistry: introduction to advanced electronic structure theory*; Courier Dover Publications, 2012.

[189] Jensen, F. *Introduction to computational chemistry*; John Wiley & Sons, 2007.

[190] Parr, R. G.; Yang, W. *Density-functional theory of atoms and molecules*; Oxford university press, 1989; Vol. 16.

[191] Koch, W.; Holthausen, M. C. *A chemist's guide to density functional theory*; 2001; Vol. 2.

[192] Hohenberg, P.; Kohn, W. *Phys. Rev.* **1964**, *136*, B864–B871.

[193] Kohn, W.; Sham, L. J. *Phys. Rev.* **1965**, *137*, A1697–A1705.

[194] Kohn, W.; Sham, L. J. *Phys. Rev.* **1965**, *140*, A1133–A1138.

[195] Vosko, S. H.; Wilk, L.; Nusair, M. *Can. J. Phys.* **1980**, *58*, 1200–1211.

[196] Becke, A. D. *Phys. Rev. A* **1988**, *38*, 3098–3100.

[197] Lee, C.; Yang, W.; Parr, R. G. *Phys. Rev. B* **1988**, *37*, 785–789.

[198] Grimme, S. *J. Comput. Chem.* **2004**, *25*, 1463–1473.

[199] Grimme, S. *J. Comput. Chem.* **2006**, *27*, 1787–1799.

[200] Grimme, S.; Antony, J.; Ehrlich, S.; Krieg, H. *J. Chem. Phys.* **2010**, *132*, 154104.

[201] Lippert, G.; Hutter, J.; Parrinello, M. *Mol. Phys.* **1997**, *92*, 477–487.

[202] Lippert, G.; Hutter, J.; Parrinello, M. *Theor. Chim. Acta* **1999**, *103*, 124–140.

[203] Blöchl, P. *Phys. Rev. B* **1994**, *50*, 17953–17979.

[204] Goedecker, S.; Teter, M.; Hutter, J. *Phys. Rev. B* **1996**, *54*, 1703–1710.

[205] Hartwigsen, C.; Goedecker, S.; Hutter, J. *Phys. Rev. B* **1998**, *58*, 3641–3662.

[206] VandeVondele, J.; Krack, M.; Mohamed, F.; Parrinello, M.; Chassaing, T.; Hutter, J. *Comput. Phys. Comm.* **2005**, *167*, 103–128.

[207] Hermansson, K.; Knuts, S.; Lindgren, J. *J. Chem. Phys.* **1991**, *95*, 7486–7496.

[208] Eggenberger, R.; Gerber, S.; Huber, H.; Searles, D.; Welker, M. *J. Chem. Phys.* **1992**, *97*, 5898–5904.

[209] Klamt, A.; Schüürmann, G. *J. Chem. Soc. Perkin Trans.* **1993**, *2*, 799–805.

[210] Marx, D.; Hutter, J. *Ab initio molecular dynamics: basic theory and advanced methods*; Cambridge University Press, 2009.

[211] Jorgensen, W. L.; Maxwell, D. S.; Tirado-Rives, J. *J. Am. Chem. Soc.* **1996**, *118*, 11225–11236.

[212] Cornell, W. D.; Cieplak, P.; Bayly, C. I.; Gould, I. R.; Merz, K. M.; Ferguson, D. M.; Spellmeyer, D. C.; Fox, T.; Caldwell, J. W.; Kollman, P. A. *J. Am. Chem. Soc.* **1995**, *117*, 5179–5197.

[213] Wang, J.; Wolf, R. M.; Caldwell, J. W.; Kollman, P. A.; Case, D. A. *J. Comput. Chem.* **2004**, *25*, 1157–1174.

[214] Leach, A. R. *Molecular modelling: principles and applications*; Pearson Education, 2001.

[215] Lorentz, H. A. *Ann. Phys. (Berlin)* **1881**, *248*, 127–136.

[216] Berthelot, D. *C. R. Hebd. Seances Acad. Sci.* **1898**, *126*, 1703–1855.

[217] Mulliken, R. S. *J. Chem. Phys.* **1955**, *23*, 1833–1840.

[218] Mulliken, R. S. *J. Chem. Phys.* **1955**, *23*, 1841–1846.

[219] Mulliken, R. S. *J. Chem. Phys.* **1955**, *23*, 2338–2342.

[220] Mulliken, R. S. *J. Chem. Phys.* **1955**, *23*, 2343–2346.

[221] Mulliken, R. S. *J. Chem. Phys.* **1962**, *36*, 3428–3439.

[222] Löwdin, P.-O. *Adv. Quantum Chem.* **1970**, *5*, 185.

[223] Bader, R. F. W. *Atoms in Molecules*; Wiley Online Library, 1990.

[224] Reed, A. E.; Weinstock, R. B.; Weinhold, F. *J. Chem. Phys.* **1985**, *83*, 735–746.

[225] Bayly, C. I.; Cieplak, P.; Cornell, W.; Kollman, P. A. *J. Phys. Chem.* **1993**, *97*, 10269–10280.

[226] Blöchl, P. E. *J. Chem. Phys.* **1995**, *103*, 7422–7428.

[227] Kirchner, B. In *Ionic Liquids*; Kirchner, B., Ed.; Springer Berlin / Heidelberg: Top. Curr. Chem., 2009; Vol. 290.

[228] Maginn, E. J. *J. Phys.: Condens. Matter* **2009**, *21*, 373101.

[229] Cadena, C.; Zhao, Q.; Snurr, R. Q.; Maginn, E. J. *J. Phys. Chem. B* **2006**, *110*, 2821–2832.

[230] Cadena, C.; Maginn, E. J. *J. Phys. Chem. B* **2006**, *110*, 18026–18039.

[231] Brehm, M.; Kirchner, B. *J. Chem. Inf. Model.* **2011**, *51*, 2007–2023.

[232] Kiefer, J.; Fries, J.; Leipertz, A. *Appl. Spectrosc.* **2007**, *61*, 1306–1311.

[233] Dhumal, N. R.; Kim, H. J.; Kiefer, J. *J. Phys. Chem. A* **2011**, *115*, 3551–3558.

[234] Fumino, K.; Wulf, A.; Ludwig, R. *Angew. Chem. Int. Ed.* **2008**, *47*, 3830–3834.

[235] Wulf, A.; Fumino, K.; Ludwig, R.; Taday, P. F. *ChemPhysChem* **2010**, *11*, 349–353.

[236] Fumino, K.; Wulf, A.; Verevkin, S. P.; Heintz, A.; Ludwig, R. *ChemPhysChem* **2010**, *11*, 1623–1626.

[237] Sarangi, S. S.; Reddy, S. K.; Balasubramanian, S. *J. Phys. Chem. B* **2011**, *115*, 1874–1880.

[238] Thar, J.; Brehm, M.; Seitsonen, A. P.; Kirchner, B. *J. Phys. Chem. B* **2009**, *113*, 15129–15132, PMID: 19852454.

[239] Rai, N.; Maginn, E. J. *J. Phys. Chem. Lett.* **2011**, *2*, 1439–1443.

[240] Santos, C. S.; Baldelli, S. *J. Phys. Chem. B* **2009**, *113*, 923–933.

[241] Maier, F.; Cremer, T.; Kolbeck, C.; Lovelock, K. R. J.; Paape, N.; Schulz, P. S.; Wasserscheid, P.; Steinrück, H.-P. *Phys. Chem. Chem. Phys.* **2010**, *12*, 1905–1915.

[242] Kirchner, B. In *Ionic Liquids*; Kirchner, B., Ed.; Topics in Current Chemistry; Springer Berlin / Heidelberg, 2009; Vol. 290; pp 213–262.

[243] Dai, Q.; Menzies, D. B.; MacFarlane, D. R.; Batten, S. R.; Forsyth, S.; Spiccia, L.; Cheng, Y. B.; Forsyth, M. *C. R. Chim.* **2006**, *9*, 617–621.

[244] Kuang, D.; Wang, P.; Ito, S.; Zakeeruddin, S. M.; Grätzel, M. *J. Am. Chem. Soc.* **2006**, *128*, 7732–7733.

[245] Oda, T.; Tanaka, S.; Hayase, S. *Sol. Energ. Mat. Sol. C.* **2006**, *90*, 2696–2709.

[246] Wei, D. *Int. J. Mol. Sci.* **2010**, *11*, 1103–1113.

[247] Podgoršek, A.; Salas, G.; Campbell, P. S.; Santini, C. C.; Pádua, A. A. H.; Costa Gomes, M. F.; Fenet, B.; Chauvin, Y. *J. Phys. Chem. B* **2011**, *115*, 12150–9.

[248] Campbell, P. S.; Santini, C. C.; Chauvin, Y. *Chim. Oggi* **2010**, *28*, 36–39.

[249] Campbell, P. S.; Podgoršek, A.; Gutel, T.; Santini, C. C.; Pádua, A. A. H.; Costa Gomes, M. F.; Bayard, F.; Fenet, B.; Chauvin, Y. *J. Phys. Chem. B* **2010**, *114*, 8156–8165.

[250] Hahn, F. E.; Jahnke, M. C. *Angew. Chem. Int. Ed.* **2008**, *47*, 3122–3172.

[251] Arduengo, A. J.; Bertrand, G. *Chem. Rev.* **2009**, *109*, 3209–3210, PMID: 19642638.

[252] Melaimi, M.; Soleilhavoup, M.; Bertrand, G. *Angew. Chem. Int. Ed.* **2010**, *49*, 8810–8849.

[253] Hollóczki, O.; Gerhard, D.; Massone, K.; Szarvas, L.; Németh, B.; Veszprémi, T.; Nyulászi, L. *New J. Chem.* **2010**, *34*, 3004–3009.

[254] Kelemen, Z.; Hollóczki, O.; Nagy, J.; Nyulászi, L. *Org. Biomol. Chem.* **2011**, *9*, 5362–5364.

[255] Rodríguez, H.; Gurau, G.; Holbrey, J. D.; Rogers, R. D. *Chem. Commun.* **2011**, *47*, 3222–3224.

[256] Brehm, M.; Weber, H.; Pensado, A. S.; Stark, A.; Kirchner, B. *Phys. Chem. Chem. Phys.* **2012**, *14*, 5030–5044.

[257] Hollóczki, O.; Nyulászi, L. *Carbenes from Ionic Liquids*; Topics in Current Chemistry; Springer Berlin Heidelberg, 2013; pp 1–24.

[258] Hollóczki, O.; Firaha, D. S.; Friedrich, J.; Brehm, M.; Cybik, R.; Wild, M.; Stark, A.; Kirchner, B. *J. Phys. Chem. B* **2013**, *117*, 5898–5907.

[259] Malberg, F.; Pensado, A. S.; Kirchner, B. *Phys. Chem. Chem. Phys.* **2012**, *14*, 12079–12082.

[260] Domańska, U.; Laskowska, M. *J. Solution Chem.* **2008**, *37*, 1271–1287.

[261] Blesic, M.; Swadzba-Kwasny, M.; Belhocine, T.; Gunaratne, H. Q. N.; Canongia Lopes, J. N.; Costa Gomes, M. F.; Pádua, A. A. H.; Seddon, K. R.; Rebelo, L. P. N. *Phys. Chem. Chem. Phys.* **2009**, *11*, 8939–8948.

[262] Zhang, Z.-H.; Tan, Z.-C.; Sun, L.-X.; Jia-Zhen, Y.; Lv, X.-C.; Shi, Q. *Thermochim. Acta* **2006**, *447*, 141–146.

[263] Fernández, A.; Torrecilla, J.; García, J.; Rodríguez, F. *J. Chem. Eng. Data* **2007**, *52*, 1979–1983.

[264] Ficke, L. E.; Rodriguez, H.; Brennecke, J. F. *J. Chem. Eng. Data* **2008**, *53*, 2112–2119.

[265] Paulechka, Y. U.; Kabo, A. G.; Blokhin, A. V.; Kabo, G. J.; Shevelyova, M. P. *J. Chem. Eng. Data* **2010**, *55*, 2719–2724.

[266] Paulechka, Y. U. *J. Phys. Chem. Ref. Data* **2010**, *39*, 033108.

[267] Nieto de Castro, C. A.; Langa, E.; Morais, A. L.; Matos Lopes, M. L.; Lourenço, M. J. V.; Santos, F. J. V.; Santos, M. S. C. S.; Canongia Lopes, J. N.; Veiga, H. I. M.; Macatrão, M.; Esperança, J. M. S. S.; Marques, C. S.; Rebelo, L. P. N.; Afonso, C. A. M. *Fluid Phase Equilib.* **2010**, *294*, 157–179.

[268] Jacquemin, J.; Husson, P.; Pádua, A. A. H.; Majer, V. *Green Chem.* **2006**, *8*, 172–180.

[269] Gómez, E.; González, B.; Calvar, N.; Tojo, E.; Domínguez, Á. *J. Chem. Eng. Data* **2006**, *51*, 2096–2102.

[270] CP2k developers group (GNU General Public License) see http://cp2k.berlios.de/index.html.

[271] VandeVondele, J.; Hutter, J. *J. Chem. Phys.* **2007**, *127*, 114105.

[272] Nosé, S. *J. Chem. Phys.* **1984**, *81*, 511.

[273] Nosé, S. *Mol. Phys.* **1984**, *52*, 255–268.

[274] Martyna, G. J.; Klein, M. L.; Tuckerman, M. *J. Chem. Phys.* **1992**, *97*, 2635–2643.

[275] Brüssel, M.; Di Dio, P. J.; Muñiz, K.; Kirchner, B. *Int. J. Mol. Sci.* **2011**, *12*, 1389–1409.

[276] Sprik, M.; Ciccotti, G. *J. Chem. Phys.* **1998**, *109*, 7737–7744.

[277] Humphrey, W.; Dalke, A.; Schulten, K. *J. Mol. Graphics Modell.* **1996**, *14*, 33–38.

[278] Stone, J. An Efficient Library for Parallel Ray Tracing and Animation. 1995.

[279] Grace, (c) 1996-2008 Grace Development Team, see http://plasma-gate.weizmann.ac.il/Grace.

[280] Wolfram Research, Inc., Mathematica, Version 8.0, Champaign, IL (2010).

[281] Wendler, K.; Brehm, M.; Malberg, F.; Kirchner, B.; Delle Site, L. *J. Chem. Theory Comput.* **2012**, *8*, 1570–1579.

[282] Thomas, M.; Brehm, M.; Fligg, R.; Vöhringer, P.; Kirchner, B. *Phys. Chem. Chem. Phys.* **2013**, *15*, 6608–6622.

[283] Paredes, X.; Fernández, J.; Pádua, A. A. H.; Malfreyt, P.; Malberg, F.; Kirchner, B.; Pensado, A. S. *J. Phys. Chem. B* **2012**, *116*, 14159–14170.

[284] Hallett, J. P.; Welton, T. *Chem. Rev.* **2011**, *111*, 3508–3576.

[285] Campbell, P. S.; Santini, C. C.; Bouchu, D.; Fenet, B.; Philippot, K.; Chaudret, B.; Pádua, A. A. H.; Chauvin, Y. *Phys. Chem. Chem. Phys.* **2010**, *12*, 4217–4223.

[286] Salas, G.; Podgoršek, A.; Campbell, P. S.; Santini, C. C.; Pádua, A. A. H.; Costa Gomes, M. F.; Philippot, K.; Chaudret, B.; Turmine, M. *Phys. Chem. Chem. Phys.* **2011**, *13*, 13527–13536.

[287] Prechtl, M. H. G.; Campbell, P. S.; Scholten, J. D.; Fraser, G. B.; Machado, G.; Santini, C. C.; Dupont, J.; Chauvin, Y. *Nanoscale* **2010**, *2*, 2601–2606.

[288] Gutel, T.; Santini, C. C.; Philippot, K.; Pádua, A.; Pelzer, K.; Chaudret, B.; Chauvin, Y.; Basset, J.-M. *J. Mater. Chem.* **2009**, *19*, 3624–3631.

[289] Pereiro, A. B.; Deive, F. J.; Esperança, J. M. S. S.; Rodríguez, A. *Fluid Phase Equilib.* **2010**, *294*, 49–53.

[290] Holbrey, J. D.; Reichert, W. M.; Swatloski, R.; Broker, G. A.; Pitner, W. R.; Seddon, K. R.; Rogers, R. D. *Green Chem.* **2002**, *4*, 407–413.

[291] Costa, A. J. L.; Esperança, J. M. S. S.; Marrucho, I. M.; Rebelo, L. P. N. *J. Chem. Eng. Data* **2011**, *56*, 3433–3441.

[292] Gaciño, F. M.; Regueira, T.; Lugo, L.; Comuñas, M. J. P.; Fernández, J. *J. Chem. Eng. Data* **2011**, *56*, 4984–4999.

[293] Wilfred, C. D.; Kiat, C. F.; Man, Z.; Bustam, M. A.; Mutalib, M. I. M.; Phak, C. Z. *Fuel Process. Technol.* **2012**, *93*, 85–89.

[294] Pereiro, A. B.; Deive, F. J.; Esperança, J. M. S. S.; Rodríguez, A. *Fluid Phase Equilib.* **2010**, *291*, 13–17.

[295] Canongia Lopes, J. N.; Pádua, A. A. H.; Shimizu, K. *J. Phys. Chem. B* **2008**, *112*, 5039–5046.

[296] Canongia Lopes, J. N.; Deschamps, J.; Pádua, A. A. H. *J. Phys. Chem. B* **2004**, *108*, 2038–2047.

[297] Todorov, I. T.; Smith, W.; Trachenko, K.; Dove, M. T. *J. Mater. Chem.* **2006**, *16*, 1911–1918.

[298] Gloor, G. J.; Jackson, G.; Blas, F. J.; de Miguel, E. *J. Chem. Phys.* **2005**, *123*, 134703.

[299] Irving, J. H.; Kirkwood, J. G. *J. Chem. Phys.* **1950**, *18*, 817–829.

[300] Kirkwood, J. G.; Buff, F. P. *J. Chem. Phys.* **1949**, *17*, 338–343.

[301] Pensado, A. S.; Costa Gomes, M. F.; Canongia Lopes, J. N.; Malfreyt, P.; Pádua, A. A. H. *Phys. Chem. Chem. Phys.* **2011**, *13*, 13518–13526.

[302] Pensado, A. S.; Pádua, A. A. H.; Costa Gomes, M. F. *J. Phys. Chem. B* **2011**, *115*, 3942–3948.

[303] Pádua, A. A. H.; Costa Gomes, M. F.; Canongia Lopes, J. N. A. *Acc. Chem. Res.* **2007**, *40*, 1087–1096.

[304] Bodo, E.; Gontrani, L.; Caminiti, R.; Plechkova, N. V.; Seddon, K. R.; Triolo, A. *J. Phys. Chem. B* **2010**, *114*, 16398–16407.

[305] Macchiagodena, M.; Gontrani, L.; Ramondo, F.; Triolo, A.; Caminiti, R. *J. Chem. Phys.* **2011**, *134*, 114521.

[306] Shimizu, K.; Almantariotis, D.; Costa Gomes, M. F.; Pádua, A. A. H.; Canongia Lopes, J. N. *J. Phys. Chem. B* **2010**, *114*, 3592–3600.

[307] Bresme, F.; González-Melchor, M.; Alejandre, J. *J. Phys.: Condens. Matter* **2005**, *17*, S3301–S3307.

[308] Biscay, F.; Ghoufi, A.; Goujon, F.; Lachet, V.; Malfreyt, P. *J. Chem. Phys.* **2009**, *130*, 184710.

[309] Biscay, F.; Ghoufi, A.; Lachet, V.; Malfreyt, P. *J. Phys. Chem. C* **2011**, *115*, 8670–8683.

[310] Neyt, J.-C.; Wender, A.; Lachet, V.; Malfreyt, P. *J. Phys. Chem. C* **2012**, *116*, 10563–10572.

[311] Ghoufi, A.; Goujon, F.; Lachet, V.; Malfreyt, P. *J. Chem. Phys.* **2008**, *128*, 154716.

[312] Restolho, J.; Serro, A. P.; Mata, J. L.; Saramago, B. *J. Chem. Eng. Data* **2009**, *54*, 950–955.

[313] Yang, J.-Z.; Lu, X.-M.; Gui, J.-S.; Xu, W.-G. *Green Chem.* **2004**, *6*, 541–543.

[314] Wandschneider, A.; Lehmann, J. K.; Heintz, A. *J. Chem. Eng. Data* **2008**, *53*, 596–599.

[315] Fernández, A.; García, J.; Torrecilla, J. S.; Oliet, M.; Rodríguez, F. *J. Chem. Eng. Data* **2008**, *53*, 1518–1522.

[316] Hasse, B.; Lehmann, J.; Assenbaum, D.; Wasserscheid, P.; Leipertz, A.; Fröba, A. P. *J. Chem. Eng. Data* **2009**, *54*, 2576–2583.

[317] Tariq, M.; Freire, M. G.; Saramago, B.; Coutinho, J. a. A. P.; Canongia Lopes, J. N.; Rebelo, L. P. N. *Chem. Soc. Rev.* **2012**, *41*, 829–868.

[318] Weingarth, D.; Czekaj, I.; Fei, Z.; Foelske-Schmitz, A.; Dyson, P. J.; Wokaun, A.; Kötz, R. *J. Electrochem. Soc.* **2012**, *159*, H611–H615.

[319] Weingarth, D.; Foelske-Schmitz, A.; Kötz, R. *J. Power Sources* **2013**, *225*, 84–88.

[320] Holbrey, J. D.; Seddon, K. R. *J. Chem. Soc., Dalton Trans.* **1999**, 2133–2140.

[321] Vila, J.; Varela, L. M.; Cabeza, O. *Electrochim. Acta* **2007**, *52*, 7413–7417.

[322] Blesic, M.; Canongia Lopes, J. N.; Costa Gomes, M. F.; Rebelo, L. P. N. *Phys. Chem. Chem. Phys.* **2010**, *12*, 9685–9692.

[323] Canongia Lopes, J. N.; Costa Gomes, M. F.; Pádua, A. A. H. *J. Phys. Chem. B* **2006**, *110*, 16816–16818.

[324] Wender, H.; Andreazza, M. L.; Correia, R. R. B.; Teixeira, S. R.; Dupont, J. *Nanoscale* **2011**, *3*, 1240–1245.

[325] MacFarlane, D. R.; Pringle, J. M.; Howlett, P. C.; Forsyth, M. *Phys. Chem. Chem. Phys.* **2010**, *12*, 1659–1669.

[326] Janiczek, P.; Kalb, R. S.; Thonhauser, G.; Gamse, T. *Sep. Purif. Technol.* **2012**, *97*, 20–25.

[327] Althuluth, M.; Kroon, M. C.; Peters, C. J. *Industrial & Engineering Chemistry Research* **2012**, *51*, 16709–16712.

[328] Tietze, A. A.; Heimer, P.; Stark, A.; Imhof, D. *Molecules* **2012**, *17*, 4158–4185.

[329] Borgel, V.; Markevich, E.; Aurbach, D.; Semrau, G.; M., S. *J. Power Sources* **2009**, *189*, 331–336.

[330] Hayyan, M.; Mjalli, F. S.; Hashim, M. A.; AlNashef, I. M.; Mei, T. X. *J. Ind. Eng. Chem.* **2013**, *19*, 106–112.

[331] O'Mahony, A. M.; Silvester, D. S.; Aldous, L.; Hardacre, C.; Compton, R. G. *J. Chem. Eng. Data* **2008**, *53*, 2884–2891.

[332] Santos, C. S.; Murthy, N. S.; Baker, G. A.; Castner Jr., E. W. *J. Chem. Phys.* **2011**, *134*, 121101.

[333] Li, S.; Bañuelos, J. L.; Guo, J.; Anovitz, L.; Rother, G.; Shaw, R. W.; Hillesheim, P. C.; Dai, S.; Baker, G. A.; Cummings, P. T. *J. Phys. Chem. Lett.* **2012**, *3*, 125–130.

[334] Men, S.; Lovelock, K. R. J.; Licence, P. *Phys. Chem. Chem. Phys.* **2011**, *13*, 15244–15255.

[335] Men, S.; Hurisso, B. B.; Lovelock, K. R. J.; Licence, P. *Phys. Chem. Chem. Phys.* **2012**, *14*, 5229–5238.

[336] Lovelock, K. R. J.; Kolbeck, C.; Cremer, T.; Paape, N.; Schulz, P. S.; Wasserscheid, P.; Maier, F.; Steinrück, H.-P. *J. Phys. Chem. B* **2009**, *113*, 2854–2864.

[337] Reinmöller, M.; Ulbrich, A.; Ikari, T.; Preiß, J.; Höfft, O.; Endres, F.; Krischok, S.; Beenken, W. J. D. *Phys. Chem. Chem. Phys.* **2011**, *13*, 19526–19533.

[338] Macchiagodena, M.; Ramondo, F.; Triolo, A.; Gontrani, L.; Caminiti, R. *J. Phys. Chem. B* **2012**, *116*, 13448–13458.

[339] Canongia Lopes, J. N.; Pádua, A. A. H. *Theor. Chem. Acc.* **2012**, *131*, 1–11.

[340] Russina, O.; Triolo, A. *Faraday Discuss.* **2012**, *154*, 97–109.

[341] Triolo, A.; Russina, O.; Caminiti, R.; Shirota, H.; Lee, H. Y.; Santos, C. S.; Murthy, N. S.; Castner Jr., E. W. *Chem. Commun.* **2012**, *48*, 4959–4961.

[342] Bowron, D. T.; D'Agostino, C.; Gladden, L. F.; Hardacre, C.; Holbrey, J. D.; Lagunas, M. C.; McGregor, J.; Mantle, M. D.; Mullan, C. L.; Youngs, T. G. A. *J. Phys. Chem. B* **2010**, *114*, 7760–7768.

[343] Deetlefs, M.; Hardacre, C.; Nieuwenhuyzen, M.; Pádua, A. A. H.; Sheppard, O.; Soper, A. K. *J. Phys. Chem. B* **2006**, *110*, 12055–12061.

[344] Hardacre, C.; Holbrey, J. D.; Mullan, C. L.; Nieuwenhuyzen, M.; Youngs, T. G. A.; Bowron, D. T. *J. Phys. Chem. B* **2008**, *112*, 8049–8056.

[345] Hardacre, C.; Holbrey, J. D.; Mullan, C. L.; Youngs, T. G. A.; Bowron, D. T. *J. Chem. Phys.* **2010**, *133*, 074510.

[346] Annapureddy, H. V. R.; Kashyap, H. K.; De Biase, P. M.; Margulis, C. J. *J. Phys. Chem. B* **2010**, *114*, 16838–16846.

[347] Kashyap, H. K.; Hettige, J. J.; Annapureddy, H. V. R.; Margulis, C. J. *Chem. Commun.* **2012**, *48*, 5103–5105.

[348] Kashyap, H. K.; Santos, C. S.; Annapureddy, H. V. R.; Murthy, N. S.; Margulis, C. J.; Castner Jr, E. W. *Faraday Discuss.* **2012**, *154*, 133–143.

[349] Kashyap, H. K.; Santos, C. S.; Daly, R. P.; Hettige, J. J.; Murthy, N. S.; Shirota, H.; Castner Jr., E. W.; Margulis, C. J. *J. Phys. Chem. B* **2013**, *117*, 1130–1135.

[350] Lockett, V.; Sedev, R.; Harmer, S.; Ralston, J.; Horne, M.; Rodopoulos, T. *Phys. Chem. Chem. Phys.* **2010**, *12*, 13816–13827.

[351] Aliaga, C.; Baker, G. A.; Baldelli, S. *J. Phys. Chem. B* **2008**, *112*, 1676–1684.

[352] Perez-Blanco, M. E.; Maginn, E. J. *J. Phys. Chem. B* **2010**, *114*, 11827–11837.

[353] Guo, M.; Lu, B. C.-Y. *J. Chem. Phys.* **1998**, *109*, 1134–1140.

[354] Fletcher, S. I.; Sillars, F. B.; Hudson, N. E.; Hall, P. J. *J. Chem. Eng. Data* **2010**, *55*, 778–782.

[355] Kolbeck, C.; Lehmann, J.; Lovelock, K. R. J.; Cremer, T.; Paape, N.; Wasserscheid, P.; Fröba, A. P.; Maier, F.; Steinrück, H.-P. *J. Phys. Chem. B* **2010**, *114*, 17025–17036.

[356] Jin, H.; O'Hare, B.; Dong, J.; Arzhantsev, S.; Baker, G. A.; Wishart, J. F.; Benesi, A. J.; Maroncelli, M. *J. Phys. Chem. B* **2008**, *112*, 81–92.

[357] Shamsipur, M.; Beigi, A. A. M.; Teymouri, M.; Pourmortazavi, S. M.; Irandoust, M. *J. Mol. Liq.* **2010**, *157*, 43–50.

[358] Carvalho, P. J.; Neves, C. M. S. S.; Coutinho, J. a. A. P. *J. Chem. Eng. Data* **2010**, *55*, 3807–3812.

[359] Oliveira, M. B.; Domínguez-Pérez, M.; Freire, M. G.; Llovell, F.; Cabeza, O.; Lopes-da Silva, J. A.; Vega, L. F.; Coutinho, J. A. P. *J. Phys. Chem. B* **2012**, *116*, 12133–12141.

[360] Malberg, F.; Brehm, M.; Hollóczki, O.; Pensado, A. S.; Kirchner, B. *Phys. Chem. Chem. Phys.* **2013**, *15*, 18424–18436.

[361] Zahn, S.; Thar, J.; Kirchner, B. *J. Chem. Phys.* **2010**, *132*, 124506.

[362] Zhang, Y.; Maginn, E. J. *Phys. Chem. Chem. Phys.* **2012**, *14*, 12157–12164.

[363] Brak, K.; Jacobsen, E. N. *Angew. Chem. Int. Ed.* **2013**, *52*, 534–561.

[364] Lacour, J.; Moraleda, D. *Chem. Comm.* **2009**, 7073–7089.

[365] Briere, J.-F.; Oudeyer, S.; Dalla, V.; Levacher, V. *Chem. Soc. Rev.* **2012**, *41*, 1696–1707.

[366] Macchioni, A. *Chem. Rev.* **2005**, *105*, 2039–2074.

[367] Winstein, S.; Clippinger, E.; Fainberg, A. H.; Heck, R.; Robinson, G. C. *J. Am. Chem. Soc.* **1956**, *78*, 328–335.

[368] Fuoss, R. M.; Kraus, C. A. *J. Am. Chem. Soc.* **1935**, *57*, 1–4.

[369] Mayer, U. *Coord. Chem. Rev.* **1976**, *21*, 159–179.

[370] Collins, K. D. *Biophys. Chem.* **2012**, *167*, 43–59.

[371] Rogers, R. D.; Seddon, K. R.; Volkov, S. *Green Industrial Applications of Ionic Liquids*; Kluwer Academic Publishers, Dodrecht, 2002.

[372] Welton, T. *Coord. Chem. Rev.* **2004**, *248*, 2459–2477.

[373] Armand, M.; Endres, F.; MacFarlane, D. R.; Ohno, H.; Scrosati, B. *Nature Materials* **2009**, *8*, 621–629.

[374] Galinski, M.; Lewandowski, A.; Stepniak, I. *Electrochim. Acta* **2006**, *51*, 5567–5580.

[375] Liu, H.; Liu, Y.; Li, J. *Phys. Chem. Chem. Phys.* **2010**, *12*, 1685–1697.

[376] Shiddiky, M. J. A.; Torriero, A. A. J. *Biosens. Bioelectr.* **2011**, *26*, 1775–1787.

[377] Quartarone, E.; Mustarelli, P. *Chem. Soc. Rev.* **2011**, *40*, 2525–2540.

[378] Gorlov, M.; Kloo, L. *Dalton Trans.* **2008**, 2655–2666.

[379] Chen, Z.; Li, F.; Yang, H.; Yi, T.; Huang, C. *ChemPhysChem* **2007**, *8*, 1293–1297.

[380] Mishra, A.; Fischer, M. K. R.; Bäuerle, P. *Angew. Chem. Int. Ed.* **2009**, *48*, 2474–2499.

[381] Zakeeruddin, S. M.; Grätzel, M. *Adv. Func. Mat.* **2009**, *19*, 2187–2202.

[382] Angell, C. A.; Xu, W.; Yoshizawa, M.; Hayashi, A.; Belieres, J.-P.; Lucas, P.; Videa, M.; Zhao, Z.-F.; Ueno, K.; Ansari, Y.; Thomson, J.; Gervasio, D. In *Electrochemical Aspects of Ionic Liquids, 2nd ed.*; Ohno, H., Ed.; John Wiley and sons, 2011.

[383] Niedermeyer, H.; Ashworth, C.; Brandt, A.; Welton, T.; Hunt, P. A. *Phys. Chem. Chem. Phys.* **2013**, *15*, 11566–11578.

[384] Hollóczki, O.; Nyulászi, L. *Org. Biomol. Chem.* **2011**, *9*, 2634–2640.

[385] *Faraday Discuss.* **2012**, *154*, 439–464.

[386] Thomas, M.; Brehm, M.; Hollóczki, O.; Kirchner, B. *Chem. Eur. J.* **2014**, *20*, 1622–1629.

[387] Lynden-Bell, R. M. *Phys. Chem. Chem. Phys.* **2010**, *12*, 1733–1740.

[388] Yoshizawa, M.; Xu, W.; Angell, C. A. *J. Am. Chem. Soc.* **2003**, *125*, 15411–15419.

[389] Sieffert, N.; Wipff, G. *J. Phys. Chem. B* **2007**, *111*, 7253–7266.

[390] Bagh, F. S. G.; Mjalli, F. S.; Hashim, M. A.; Hadj-Kali, M. K. O.; AlNashef, I. M. *Ind. Eng. Chem. Res.* **2013**, *52*, 11488–11493.

[391] Hunt, P. A.; Kirchner, B.; Welton, T. *Chem. Eur. J.* **2006**, *12*, 6762–6775.

[392] Hunt, P. A.; Gould, I. R.; Kirchner, B. *Aust. J. Chem.* **2007**, *60*, 9–14.

[393] Skarmoutsos, I.; Dellis, D.; Matthews, R. P.; Welton, T.; Hunt, P. A. *J. Phys. Chem. B* **2012**, *116*, 4921–4933.

[394] Kohagen, M.; Brehm, M.; Lingscheid, Y.; Giernoth, R.; Sangoro, J.; Kremer, F.; Naumov, S.; Iacob, C.; Kärger, J.; Valiullin, R.; Kirchner, B. *J. Phys. Chem. B* **2011**, *115*, 15280–15288.

[395] Lungwitz, R.; Spange, S. *New J. Chem.* **2008**, *32*, 392–294.

[396] Kohagen, M.; Brehm, M.; Thar, J.; Zhao, W.; Müller-Plathe, F.; Kirchner, B. *J. Phys. Chem. B* **2011**, *115*, 693–702.

[397] Müller-Plathe, F.; van Gunsteren, W. F. *J. Chem. Phys.* **1995**, *103*, 4745–4756.

[398] Klamt, A. *J. Phys. Chem.* **1995**, *99*, 2224–2235.

[399] Ahlrichs, R.; Bär, M.; Häser, M.; Horn, H.; Kölmel, C. *Chem. Phys. Lett.* **1989**, *162*, 165–169.

[400] AIMAll (Version 13.05.06), Todd A. Keith, TK Gristmill Software, Overland Park KS, USA, 2013, `(aim.tkgristmill.com)`.

[401] Ahlrichs, R.; Ehrhardt, C. *Chem. Unser. Z.* **1985**, *19*, 120–124.

[402] Plimpton, S. *J. Comp. Phys.* **1995**, *117*, 1–19.

[403] LAMMPS WWW site:, `http://lammps.sandia.gov`.

[404] Canongia Lopes, J. N.; Pádua, A. A. H. *J. Phys. Chem. B* **2006**, *110*, 19586–19592.

[405] Åqvist, J. *J. Phys. Chem.* **1990**, *94*, 8021.

[406] Spohr, H. V.; Patey, G. N. *J. Chem. Phys.* **2008**, *129*, 064517.

[407] Spohr, H. V.; Patey, G. N. *J. Chem. Phys.* **2010**, *132*, 154504.

[408] Canongia Lopes, J. N. *Mol. Phys.* **1999**, *96*, 1649–1658.

[409] Lehn, J.-M. *Supramolecular Chemistry - Concepts and Perspectives*; Wiley-VCH, 1996.

[410] Gerbeleu, N. V.; Arion, V. B.; Burgess, J. *Template Synthesis of Macrocyclic Compounds*; Wiley-VCH, 1999.

[411] Diederich, F., Stang, P. J., Eds. *Templated organic synthesis*; Wiley-VCH, 2000.

[412] Schliwa, M., Ed. *Molecular Motors*; Wiley-VCH, 2003.

[413] Balzani, V.; Credi, A.; Venturi, M. *Molecular Devices and Machines. A Journey into the Nano World*; Wiley-VCH, 2003.

[414] Steed, J. W.; Turner, D. R.; Wallace, K. *Core concepts in supramolecular chemistry and nanochemistry*; Wiley-VCH, 2007.

[415] Balzani, V.; Credi, A.; Venturi, M. *Molecular devices and machines: concepts and perspectives for the nanoworld*; Wiley-VCH, 2008.

[416] Diederich, F., Stang, P. J., Tykwinski, R. R., Eds. *Modern supramolecular chemistry: strategies for macrocycle synthesis*; Wiley-VCH, 2008.

[417] Steed, J. W.; Atwood, J. L. *Supramolecular chemistry*; Wiley, 2009.

[418] Ariga, K., Nalwa, H. S., Eds. *Bottom-up Nanofabrication: Supramolecules, Self-Assemblies and Organized Films*; American Scientific Pub., 2009.

[419] Sauvage, J.-P., Gaspard, P., Eds. *From Non-Covalent Assemblies to Molecular Machines*; Wiley-VCH, 2010.

[420] Sauvage, J.-P. *Acc. Chem. Res.* **1998**, *31*, 611–619.

[421] Blanco, M.-J.; Jiménez, M. C.; Chambron, J.-C.; Heitz, V.; Linke, M.; Sauvage, J.-P. *Chem. Soc. Rev.* **1999**, *28*, 293–305.

[422] Balzani, V.; Credi, A.; Raymo, F. M.; Stoddart, J. F. *Angew. Chem. Int. Ed.* **2000**, *39*, 3348–3391.

[423] Ballardini, R.; Balzani, V.; Credi, A.; Gandolfi, M. T.; Venturi, M. *Acc. Chem. Res.* **2001**, *34*, 445–455.

[424] Harada, A. *Acc. Chem. Res.* **2001**, *34*, 456–464.

[425] Collin, J.-P.; Dietrich-Buchecker, C.; Gaviña, P.; Jimenez-Molero, M. C.; Sauvage, J.-P. *Acc. Chem. Res.* **2001**, *34*, 477–487.

[426] Clemente-León, M.; Credi, A.; Martínez-Díaz, M. V.; Mingotaud, C.; Stoddart, J. F. *Adv. Mater.* **2006**, *18*, 1291–1296.

[427] Balzani, V.; Credi, A.; Silvi, S.; Venturi, M. *Chem. Soc. Rev.* **2006**, *35*, 1135–1149.

[428] Credi, A. *Angew. Chem. Int. Ed.* **2007**, *46*, 5472–5475.

[429] Kay, E. R.; Leigh, D. A.; Zerbetto, F. *Angew. Chem. Int. Ed.* **2007**, *46*, 72–191.

[430] Mateo-Alonso, A.; Guldi, D. M.; Paolucci, F.; Prato, M. *Angew. Chem. Int. Ed.* **2007**, *46*, 8120–8126.

[431] Champin, B.; Mobian, P.; Sauvage, J.-P. *Chem. Soc. Rev.* **2007**, *36*, 358–366.

[432] Bonnet, S.; Collin, J.-P. *Chem. Soc. Rev.* **2008**, *37*, 1207–1217.

[433] Silvi, S.; Venturi, M.; Credi, A. *J. Mater. Chem.* **2009**, *19*, 2279–2294.

[434] Bodis, P.; Panman, M. R.; Bakker, B. H.; Mateo-Alonso, A.; Prato, M.; Buma, W. J.; Brouwer, A. M.; Kay, E. R.; Leigh, D. A.; Woutersen, S. *Acc. Chem. Res.* **2009**, *42*, 1462–1469.

[435] Dietrich-Buchecker, C. O.; Sauvage, J. P. *Chem. Rev.* **1987**, *87*, 795–810.

[436] Anderson, S.; Anderson, H. L.; Sanders, J. K. M. *Acc. Chem. Res.* **1993**, *26*, 469–475.

[437] Chambron, J.-C.; Collin, J.-P.; Heitz, V.; Jouvenot, D.; Kern, J.-M.; Mobian, P.; Pomeranc, D.; Sauvage, J.-P. *Eur. J. Org. Chem.* **2004**, 1627–1638.

[438] Ammann, M.; Rang, A.; Schalley, C. A.; Bäuerle, P. *Eur. J. Org. Chem.* **2006**, 1940–1948.

[439] Hutin, M.; Schalley, C. A.; Bernardinelli, G.; Nitschke, J. R. *Chem. Eur. J.* **2006**, *12*, 4069–4076.

[440] Bäuerle, P.; Ammann, M.; Wilde, M.; Götz, G.; Mena-Osteritz, E.; Rang, A.; Schalley, C. A. *Angew. Chem. Int. Ed.* **2007**, *46*, 363–368.

[441] Yamashita, K.-i.; Kawano, M.; Fujita, M. *J. Am. Chem. Soc.* **2007**, *129*, 1850–1851.

[442] Meyer, C. D.; Joiner, C. S.; Stoddart, J. F. *Chem. Soc. Rev.* **2007**, *36*, 1705–1723.

[443] Crowley, J. D.; Goldup, S. M.; Lee, A.-L.; Leigh, D. A.; McBurney, R. T. *Chem. Soc. Rev.* **2009**, *38*, 1530–1541.

[444] Faiz, J. A.; Heitz, V.; Sauvage, J.-P. *Chem. Soc. Rev.* **2009**, *38*, 422–442.

[445] Collin, J.-P.; Durola, F.; Heitz, V.; Reviriego, F.; Sauvage, J.-P.; Trolez, Y. *Angew. Chem. Int. Ed.* **2010**, *49*, 10172–10175.

[446] Clever, G. H.; Shionoya, M. *Chem. Eur. J.* **2010**, *16*, 11792–11796.

[447] Megiatto Jr., J. D.; Schuster, D. I.; Abwandner, S.; de Miguel, G.; Guldi, D. M. *J. Am. Chem. Soc.* **2010**, *132*, 3847–3861.

[448] Hänni, K. D.; Leigh, D. A. *Chem. Soc. Rev.* **2010**, *39*, 1240–1251.

[449] Guo, J.; Mayers, P. C.; Breault, G. A.; Hunter, C. A. *Nature Chem.* **2010**, *2*, 218–222.

[450] Amabilino, D. B.; Stoddart, J. F.; Williams, D. J. *Chem. Mater.* **1994**, *6*, 1159–1167.

[451] Amabilino, D. B.; Stoddart, J. F. *Chem. Rev.* **1995**, *95*, 2725–2828.

[452] Glink, P. T.; Stoddart, J. F. *Pure Appl. Chem.* **2009**, *70*, 419–424.

[453] Nepogodiev, S. A.; Stoddart, J. F. *Chem. Rev.* **1998**, *98*, 1959–1976.

[454] Lee, J. W.; Samal, S.; Selvapalam, N.; Kim, H.-J.; Kim, K. *Acc. Chem. Res.* **2003**, *36*, 621–630.

[455] Kim, K.; Selvapalam, N.; Ko, Y. H.; Park, K. M.; Kim, D.; Kim, J. *Chem. Soc. Rev.* **2007**, *36*, 267–279.

[456] Dichtel, W. R.; Miljanić, O. v.; Zhang, W.; Spruell, J. M.; Patel, K.; Aprahamian, I.; Heath, J. R.; Stoddartt, J. F. *Acc. Chem. Res.* **2008**, *41*, 1750–1761.

[457] Griffiths, K. E.; Stoddart, J. F. *Pure Appl. Chem.* **2009**, *80*, 485–506.

[458] Isaacs, L. *Chem. Commun.* **2009**, 619–629.

[459] Appel, E. A.; Biedermann, F.; Rauwald, U.; Jones, S. T.; Zayed, J. M.; Scherman, O. A. *J. Am. Chem. Soc.* **2010**, *132*, 14251–14260.

[460] Zhang, M.; Zhu, K.; Huang, F. *Chem. Commun.* **2010**, *46*, 8131–8141.

[461] Au-Yeung, H. Y.; Pantoş, G. D.; Sanders, J. K. M. *Angew. Chem. Int. Ed.* **2010**, *49*, 5331–5334.

[462] Cougnon, F. B. L.; Au-Yeung, H. Y.; Pantoş, G. D.; Sanders, J. K. M. *J. Am. Chem. Soc.* **2011**, *133*, 3198–3207.

[463] Fang, L.; Basu, S.; Sue, C.-H.; Fahrenbach, A. C.; Stoddart, J. F. *J. Am. Chem. Soc.* **2011**, *133*, 396–399.

[464] Biedermann, F.; Rauwald, U.; Zayed, J. M.; Scherman, O. A. *Chem. Sci.* **2011**, *2*, 279–286.

[465] Niu, Z.; Huang, F.; Gibson, H. W. *J. Am. Chem. Soc.* **2011**, *133*, 2836–2839.

[466] Hunter, C. A. *J. Chem. Soc., Chem. Commun.* **1991**, 749–751.

[467] Vögtle, F.; Meier, S.; Hoss, R. *Angew. Chem. Int. Ed.* **1992**, *31*, 1619–1622.

[468] Ottens-Hildebrandt, S.; Meier, S.; Schmidt, W.; Vögtle, F. *Angew. Chem. Int. Ed.* **1994**, *33*, 1767–1770.

[469] Kim, K. *Chem. Soc. Rev.* **2002**, *31*, 96–107.

[470] Jiang, W.; Winkler, H. D. F.; Schalley, C. A. *J. Am. Chem. Soc.* **2008**, *130*, 13852–13853.

[471] Jiang, W.; Schalley, C. A. *Proc. Natl. Acad. Sci. U.S.A.* **2009**, *106*, 10425–10429.

[472] Stoddart, J. F. *Chem. Soc. Rev.* **2009**, *38*, 1802–1820.

[473] Lee, C.-F.; Leigh, D. A.; Pritchard, R. G.; Schultz, D.; Teat, S. J.; Timco, G. A.; Winpenny, R. E. P. *Nature* **2009**, *458*, 314–318.

[474] Jiang, W.; Schäfer, A.; Mohr, P. C.; Schalley, C. A. *J. Am. Chem. Soc.* **2010**, *132*, 2309–2320.

[475] Jiang, W.; Schalley, C. A. *Beilstein J. Org. Chem.* **2010**, *6*.

[476] Fang, L.; Olson, M. A.; Benítez, D.; Tkatchouk, E.; Goddard III, W. A.; Stoddart, J. F. *Chem. Soc. Rev.* **2010**, *39*, 17–29.

[477] Ma, X.; Tian, H. *Chem. Soc. Rev.* **2010**, *39*, 70–80.

[478] Hübner, G. M.; Gläser, J.; Seel, C.; Vögtle, F. *Angew. Chem. Int. Ed.* **1999**, *38*, 383–386.

[479] Schalley, C. A.; Silva, G.; Nising, C.-F.; Linnartz, P. *Helv. Chim. Acta* **2002**, *85*, 1578–1596.

[480] Beer, P. D.; Sambrook, M. R.; Curiel, D. *Chem. Commun.* **2006**, 2105–2117.

[481] Lankshear, M. D.; Beer, P. D. *Acc. Chem. Res.* **2007**, *40*, 657–668.

[482] Mullen, K. M.; Beer, P. D. *Chem. Soc. Rev.* **2009**, *38*, 1701–1713.

[483] Chmielewski, M. J.; Davis, J. J.; Beer, P. D. *Org. Biomol. Chem.* **2009**, *7*, 415–424.

[484] Gong, H.-Y.; Rambo, B. M.; Karnas, E.; Lynch, V. M.; Sessler, J. L. *Nature Chem.* **2010**, *2*, 406–409.

[485] Serpell, C. J.; Cookson, J.; Thompson, A. L.; Beer, P. D. *Chem. Sci.* **2011**, *2*, 494–500.

[486] Evans, N. H.; Serpell, C. J.; Beer, P. D. *Angew. Chem. Int. Ed.* **2011**, *50*, 2507–2510.

[487] Gasa, T. B.; Valente, C.; Stoddart, J. F. *Chem. Soc. Rev.* **2011**, *40*, 57–78.

[488] Badjić, J. D.; Nelson, A.; Cantrill, S. J.; Turnbull, W. B.; Stoddart, J. F. *Acc. Chem. Res.* **2005**, *38*, 723–732.

[489] Jiang, W.; Han, M.; Zhang, H.-Y.; Zhang, Z.-J.; Liu, Y. *Chem. Eur. J.* **2009**, *15*, 9938–9945.

[490] Chen, C.-F. *Chem. Commun.* **2011**, *47*, 1674–1688.

[491] Mammen, M.; Choi, S.-K.; Whitesides, G. M. *Angew. Chem. Int. Ed.* **1998**, *37*, 2754–2794.

[492] Mulder, A.; Huskens, J.; Reinhoudt, D. N. *Org. Biomol. Chem.* **2004**, *2*, 3409–3424.

[493] Kiessling, L. L.; Gestwicki, J. E.; Strong, L. E. *Angew. Chem. Int. Ed.* **2006**, *45*, 2348–2368.

[494] Reczek, J. J.; Kennedy, A. A.; Halbert, B. T.; Urbach, A. R. *J. Am. Chem. Soc.* **2009**, *131*, 2408–2415.

[495] Johnson, J. R.; Fu, N.; Arunkumar, E.; Leevy, W. M.; Gammon, S. T.; Piwnica-Worms, D.; Smith, B. D. *Angew. Chem. Int. Ed.* **2007**, *46*, 5528–5531.

[496] Gassensmith, J. J.; Arunkumar, E.; Barr, L.; Baumes, J. M.; DiVittorio, K. M.; Johnson, J. R.; Noll, B. C.; Smith, B. D. *J. Am. Chem. Soc.* **2007**, *129*, 15054–15059.

[497] Gassensmith, J. J.; Baumes, J. M.; Smith, B. D. *Chem. Commun.* **2009**, 6329–6338.

[498] Baumes, J. M.; Gassensmith, J. J.; Giblin, J.; Lee, J.-J.; White, A. G.; Culligan, W. J.; Leevy, W. M.; Kuno, M.; Smith, B. D. *Nature Chem.* **2010**, *2*, 1025–1030.

[499] Herrmann, U.; Jonischkeit, T.; Bargon, J.; Hahn, U.; Li, Q.-Y.; Schalley, C. A.; Vogel, E.; Vögtle, F. *Anal. Bioanal. Chem.* **2002**, *372*, 611–614.

[500] Bargon, J. et al. *Sensor. Actuat. B-Chem.* **2003**, *95*, 6–19.

[501] Kleefisch, G.; Kreutz, C.; Bargon, J.; Silva, G.; Schalley, C. A. *Sensors* **2004**, *4*, 136–146.

[502] Kossev, I.; Reckien, W.; Kirchner, B.; Felder, T.; Nieger, M.; Schalley, C. A.; Vögtle, F.; Sokolowski, M. *Adv. Funct. Mater.* **2007**, *17*, 513–519.

[503] Kossev, I.; Reckien, W.; Felder, T.; Kishan, M. R.; Schalley, C. A.; Sokolowski, M. *J. Phys. Chem. C* **2009**, *113*, 12870–12877.

[504] Kossev, I.; Felder, T.; Schalley, C. A.; Vögtle, F.; Sokolowski, M. In *Physics and Engineering of New Materials*; Cat, D., Pucci, A., Wandelt, K., Eds.; Springer Proceedings in Physics; Springer Berlin Heidelberg, 2009; Vol. 127; pp 235–245.

[505] Affeld, A.; Hübner, G. M.; Seel, C.; Schalley, C. A. *Eur. J. Org. Chem.* **2001**, 2877–2890.

[506] Felder, T.; Schalley, C. A. *Angew. Chem. Int. Ed.* **2003**, *42*, 2258–2260.

[507] Linnartz, P.; Schalley, C. A. *Supramol. Chem.* **2004**, *16*, 263–267.

[508] Chang, S.-Y.; Kim, H. S.; Chang, K.-J.; Jeong, K.-S. *Org. Lett.* **2004**, *6*, 181–184.

[509] Jorgensen, W. L.; Pranata, J. *J. Am. Chem. Soc.* **1990**, *112*, 2008–2010.

[510] Jeong, K. S.; Tjivikua, T.; Rebek Jr., J. *J. Am. Chem. Soc.* **1990**, *112*, 3215–3217.

[511] Pranata, J.; Wierschke, S. G.; Jorgensen, W. L. *J. Am. Chem. Soc.* **1991**, *113*, 2810–2819.

[512] Murray, T. J.; Zimmerman, S. C. *J. Am. Chem. Soc.* **1992**, *114*, 4010–4011.

[513] Johnston, A. G.; Leigh, D. A.; Pritchard, R. J.; Deegan, M. D. *Angew. Chem. Int. Ed.* **1995**, *34*, 1209–1212.

[514] Johnston, A. G.; Leigh, D. A.; Nezhat, L.; Smart, J. P.; Deegan, M. D. *Angew. Chem. Int. Ed.* **1995**, *34*, 1212–1216.

[515] Hansch, C.; Leo, A.; Taft, R. W. *Chem. Rev.* **1991**, *91*, 165–195.

[516] Sessler, J. L.; Gross, D. E.; Cho, W.-S.; Lynch, V. M.; Schmidtchen, F. P.; Bates, G. W.; Light, M. E.; Gale, P. A. *J. Am. Chem. Soc.* **2006**, *128*, 12281–12288.

[517] Gross, D. E.; Schmidtchen, F. P.; Antonius, W.; Gale, P. A.; Lynch, V. M.; Sessler, J. L. *Chem. Eur. J.* **2008**, *14*, 7822–7827.

[518] Hornung, J.; Fankhauser, D.; Shirtcliff, L. D.; Praetorius, A.; Schweizer, W. B.; Diederich, F. *Chem. Eur. J.* **2011**, *17*, 12362–12371.

[519] Braun, O.; Hünten, A.; Vögtle, F. *J. Prakt. Chem./Chem.-Ztg* **1999**, *341*, 542–547.

[520] Carver, F. J.; Hunter, C. A.; Shannon, R. J. *J. Chem. Soc., Chem. Commun.* **1994**, 1277–1280.

[521] Hunter, C. A.; Shannon, R. J. *Chem. Commun.* **1996**, 1361–1362.

[522] Adams, H.; Carver, F. J.; Hunter, C. A.; Osborne, N. J. *Chem. Commun.* **1996**, 2529–2530.

[523] Allott, C.; Adams, H.; Hunter, C. A.; Thomas, J. A.; Bernad Jr., P. L.; Rotger, C. *Chem. Commun.* **1998**, 2449–2450.

[524] Zhu, S. S.; Nieger, M.; Daniels, J.; Felder, T.; Kossev, I.; Schmidt, T.; Sokolowski, M.; Vögtle, F.; Schalley, C. A. *Chem. Eur. J.* **2009**, *15*, 5040–5046.

[525] Löw, N. L.; Dzyuba, E. V.; Brusilowskij, B.; Kaufmann, L.; Franzmann, E.; Maison, W.; Brandt, E.; Aicher, D.; Wiehe, A.; Schalley, C. A. *Beilstein J. Org. Chem.* **2012**, *8*, 234–245.

[526] Ottens-Hildebrandt, S.; Nieger, M.; Rissanen, K.; Rouvinen, J.; Meier, S.; Harder, G.; Vögtle, F. *J. Chem. Soc., Chem. Commun.* **1995**, 777–778.

[527] Reuter, C.; Seel, C.; Nieger, M.; Vögtle, F. *Helv. Chim. Acta* **2000**, *83*, 630–640.

[528] Mohry, A.; Vögtle, F.; Nieger, M.; Hupfer, H. *Chirality* **2000**, *12*, 76–83.

[529] Li, X.-Y.; Illigen, J.; Nieger, M.; Michel, S.; Schalley, C. A. *Chem. Eur. J.* **2003**, *9*, 1332–1347.

[530] Hirose, K. In *Analytical Methods in Supramolecular Chemistry*; Schalley, C. A., Ed.; Wiley-VCH, 2007; pp 17–54.

[531] Schmidtchen, F. P. In *Analytical Methods in Supramolecular Chemistry*; Schalley, C., Ed.; Wiley-VCH, 2007; pp 55–78.

[532] Holdgate, G. A. *BioTechniques* **2001**, *31*, 164–168.

[533] Wiseman, T.; Williston, S.; Brandts, J. F.; Lin, L. N. *Anal. Biochem.* **1989**, *179*, 131–137.

[534] Turnbull, W. B.; Daranas, A. H. *J. Am. Chem. Soc.* **2003**, *125*, 14859–14866.

[535] Kang, J. M.; Rebek, J. *Nature* **1996**, *382*, 239–241.

[536] Parac, T. N.; Caulder, D. L.; Raymond, K. N. *J. Am. Chem. Soc.* **1998**, *120*, 8003–8004.

[537] Hosseini, A.; Taylor, S.; Accorsi, G.; Armaroli, N.; Reed, C. A.; Boyd, P. D. W. *J. Am. Chem. Soc.* **2006**, *128*, 15903–15913.

[538] Houk, K. N.; Leach, A. G.; Kim, S. P.; Zhang, X. *Angew. Chem. Int. Ed.* **2003**, *42*, 4872–4897.

[539] Hooft, R. W. W. *Delft, The Netherlands* **1998**,

[540] Otwinowski, Z.; Minor, W. *Macromolecular Crystallography, Pt A* **1997**, *276*, 307–326.

[541] Palatinus, L.; Chapuis, G. *J. Appl. Crystallogr.* **2007**, *40*, 786–790.

[542] Farrugia, L. J. *J. Appl. Crystallogr.* **1999**, *32*, 837–838.

[543] Sheldrick, G. SHELXL-97 – A program for the Refinement of Crystal Structures, University of Göttingen, Germany, 1997.

[544] Sheldrick, G. SADABS, Version 2008/2; University of Göttingen: Göttingen, Germany, 2008.

[545] Eichkorn, K.; Treutler, O.; Öhm, H.; Häser, M.; Ahlrichs, R. *Chem. Phys. Lett.* **1995**, *240*, 283–289.

[546] Schäfer, A.; Huber, C.; Ahlrichs, R. *J. Chem. Phys.* **1994**, *100*, 5829.

[547] TURBOMOLE, University of Karlsruhe and Forschungszentrum Karlsruhe GmbH, see http://www.turbomole.com. 1989-2010.

[548] Boys, S. F.; Bernardi, F. *Mol. Phys.* **1970**, *19*, 553–566.

[549] Davidson, E. R. *J. Chem. Phys.* **1967**, *46*, 3320–3324.

[550] Wendler, K.; Thar, J.; Zahn, S.; Kirchner, B. *J. Phys. Chem. A* **2010**, *114*, 9529–9536.

[551] Schalley (ed.), C. A. *Analytical Methods in Supramolecular Chemistry, 2nd edition*; Wiley-VCH,: Weinheim/Germany, 2012.

[552] Rijs, A. M.; Crews, B. O.; de Vries, M. S.; Hannam, J. S.; Leigh, D. A.; Fanti, M.; Zerbetto, F.; Buma, W. J. *Angew. Chem. Int. Ed.* **2008**, *47*, 3174–3179.

[553] Christen, H. F., Vögtle, F., Eds. *Organische Chemie*; Band III; Otto Salle Verlag: Frankfurt am Main, 1994.

[554] Jäger, R.; Vögtle, F. *Angew. Chem. Int. Ed.* **1997**, *36*, 930–944.

[555] Leigh, D. A.; Murphy, A.; Smart, J. P.; Slawin, A. M. Z. *Angew. Chem. Int. Ed.* **1997**, *36*, 728–732.

[556] Hancock, L. M.; Beer, P. D. *Chem. Commun.* **2011**, *47*, 6012–6014.

[557] Panman, M. R.; Bodis, P.; Shaw, D. J.; Bakker, B. H.; Newton, A. C.; Kay, E. R.; Leigh, D. A.; Buma, W. J.; Brouwer, A. M.; Woutersen, S. *Phys. Chem. Chem. Phys.* **2012**, *14*, 1865–1875.

[558] Jiang, W.; Nowosinski, K.; Löw, N. L.; Dzyuba, E. V.; Klautzsch, F.; Schäfer, A.; Huuskonen, J.; Rissanen, K.; Schalley, C. A. *J. Am. Chem. Soc.* **2012**, *134*, 1860–1868.

[559] Talotta, C.; Gaeta, C.; Qi, Z.; Schalley, C. A.; Neri, P. *Angew. Chem. Int. Ed.* **2013**, *52*, 7437–7441.

[560] Fernandes, A.; Viterisi, A.; Aucagne, V.; Leigh, D. A.; Papot, S. *Chem. Commun.* **2012**, *48*, 2083–2085.

[561] Lewandowski, B.; De Bo, G.; Ward, J. W.; Papmeyer, M.; Kuschel, S.; Aldegunde, M. J.; Gramlich, P. M. E.; Heckmann, D.; Goldup, S. M.; D'Souza, D. M.; Fernandes, A. E.; Leigh, D. A. *Science* **2013**, *339*, 189–193.

[562] Yu, Y.; Cai, W.; Chipot, C.; Sun, T.; Shao, X. *J. Phys. Chem. B* **2008**, *112*, 5268–5271.

[563] Marand, E.; Hu, Q.; Gibson, H. W.; Veytsman, B. *Macromolecules* **1996**, *29*, 2555.

[564] Kaufmann, L.; Dzyuba, E. V.; Malberg, F.; Löw, N. L.; Groschke, M.; Brusilowskij, B.; Huuskonen, J.; Rissanen, K.; Kirchner, B.; Schalley, C. A. *Org. Biomol. Chem.* **2012**, *10*, 5954–5964.

[565] Grimme, S.; Ehrlich, S.; Goerigk, L. *J. Comput. Chem.* **2011**, *32*, 1456–1465.

[566] Kirchner, B.; Reiher, M. *J. Am. Chem. Soc.* **2002**, *124*, 6206–6215.

[567] Deglmann, P.; Furche, F.; Ahlrichs, R. *Phys. Lett.* **2002**, *362*, 511–518.

[568] Deglmann, P.; Furche, F. *J. Chem. Phys.* **2002**, *117*, 9535–9538.

[569] Deglmann, P.; May, K.; Furche, F.; Ahlrichs, R. *Chem. Phys. Lett.* **2004**, *384*, 103–107.

[570] Kresse, G.; Furthmüller, J. *Comput. Mat. Sci.* **1996**, *6*, 15–50.

[571] Bucko, T.; Hafner, J.; Lebegue, S.; Angyan, J. G. *J. Phys. Chem. A* **2010**, *114*, 11814–11824.

[572] Perdew, J. P.; Burke, K.; Ernzerhof, M. *Phys. Rev. Lett.* **1996**, *77*, 3865–3868.

[573] Kresse, G.; Joubert, D. *Phys. Rev. B* **1999**, *59*, 1758–1775.

[574] Goerigk, L.; Grimme, S. *Phys. Chem. Chem. Phys.* **2011**, *13*, 6670–6688.

[575] Grimme, S. *Chem. Eur. J.* **2012**, *18*, 9955–9964.

[576] Brandenburg, J. G.; Grimme, S. *Theor. Chem. Acc.* **2013**, *132*, 1399.

[577] Burns, L. A.; Vazquez-Mayagoitia, A.; Sumpter, B. G.; Sherrill, C. D. *J. Chem. Phys.* **2011**, *134*, 084107.

[578] Grimme, S.; Steinmetz, M. *Phys. Chem. Chem. Phys* **2013**, *15*, 16031–16042.

[579] Brandenburg, J. G.; Grimme, S. *Top. Curr. Chem.* **2013**,

[580] Moellmann, J.; Grimme, S. *Organometallics* **2013**, *32*, 3784–3787.

Acknowledgment

The content of this thesis has been researched in the group of Prof. Dr. Barbara Kirchner at the University of Leipzig and at the University of Bonn from November 2010 to April 2014. It has only been possible due to the support by many people, who I would like to acknowledge here.

First of all, I would like to thank Prof. Dr. Barbara Kirchner for giving me the opportunity to join her research group, providing me with such interesting state of the art topics and thus, making this thesis possible. Furthermore, I am very grateful to Dr. Alfonso S. Pensado for many helpful discussions and numerous comments during my work. In addition, I would like to thank Prof. Dr. Margarida Costa Gomes for accepting to be a reviewer of this thesis.

I would like to express my gratitude to all members (and former members) of the Kirchner group for the pleasing atmosphere at work and for the many scientific and nonscientific discussions we had. Concerning the analysis of the trajectories, I would like to thank Dr. Martin Brehm for developing `Travis`, Martin Thomas for special implementations, and both for maintaining the program. I would further like to acknowledge Dr. Matthias Kudra at the University of Leipzig and Jens Mekelburger at the University of Bonn for maintaining the computers of the Kirchner group.

Special thanks go to Dr. Alfonso S. Pensado, Henry Weber, Martin Thomas, Dr. Werner Reckien and Dr. Marina Macchiagodena for proof-reading of and esthetic input on this thesis.

Finally, I would like to thank my parents, my brothers, and my friends for the support, for motivational comments and for making life easier during this thesis.

List of Publications

Related to and Published prior to the Thesis

(1) L. Kaufmann, E. V. Dzyuba, F. Malberg, N. L. Löw, M. Groschke, B. Brusilowskij, J. Huuskonen, K. Rissanen, B. Kirchner, C. A. Schalley, *"Substituent effects on axle binding in amide pseudorotaxanes: comparison of NMR titration and ITC data with DFT calculations"*, Org. Biomol. Chem. **2012**, *10*, 5954–5964. (see subsection 3.4.1)

(2) F. Malberg, A. S. Pensado, B. Kirchner, *"The Bulk and the Gas Phase of Ionic Liquids: Dispersion Interaction makes the Difference."*, Phys. Chem. Chem. Phys. **2012**, *14*, 12079–12082. (see subsection 3.1.1)

(3) X. Paredes, J. Fernández, A. A. H. Pádua, P. Malfreyt, F. Malberg, B. Kirchner, A. S. Pensado, *"Using Molecular Simulation to Understand the Structure of $[C_2C_1im]^+$ Alkylsulfate Ionic Liquids: Bulk and Liquid-Vapor Interfaces"*, J. Phys. Chem. B **2012**, *116*, 14159–14170. (see subsection 3.2.1)

(4) F. Malberg, M. Brehm, O. Hollóczki, A. S. Pensado, B. Kirchner, *"Understanding the evaporation of ionic liquids using the example of 1-ethyl-3-methylimidazolium ethylsulfate"*, Phys. Chem. Chem. Phys. **2013**, *15*, 18424–18436. (see subsection 3.1.2)

(5) X. Paredes, J. Fernández, A. A. H. Pádua, P. Malfreyt, F. Malberg, B. Kirchner, A. S. Pensado, *"Bulk and Liquid-Vapor Interface of Pyrrolidinium-Based Ionic Liquids: A Molecular Simulation Study"*, J. Phys. Chem. B **2014**, *118*, 731–742. (see subsection 3.2.2)

(6) F. Malberg, J. G. Brandenburg, W. Reckien,O. Hollóczki, S. Grimme, B. Kirchner, *"Substitution effect and effect of axle's flexibility at (pseudo-)rotaxanes"*, Beilstein J. Org. Chem. **2014**, accepted. (see subsection 3.4.2)

(7) O. Hollóczki, F. Malberg, T. Welton, B. Kirchner, *"On the Origin of Ionicity in Ionic liquids. Ion Pairing versus Charge Transfer"*, Phys. Chem. Chem. Phys. **2014**, submitted. (see subsection 3.3.2)

(8) F. Malberg, O. Hollóczki, M. Thomas, A. S. Pensado, B. Kirchner, *"En Route Formation of Ion Pairs at the Ionic Liquid-Vacuum Interface"*, ChemPhysChem **2014**, submitted. (see subsection 3.3.1)

Unrelated to the Thesis

(1) K. Wendler, M. Brehm, F. Malberg, B. Kirchner, L. Delle Site, *"Short time dynamics of ionic liquids in AIMD based power spectra"*, J. Chem. Theory Comput. **2012**, *8 (5)*, 341–344.

(2) M. Brüssel, M. Brehm, A. S. Pensado, F. Malberg, M. Ramzan, A. Stark, B. Kirchner, *"On the ideality of binary mixtures of ionic liquids"*, Phys. Chem. Chem. Phys. **2012**, *14*, 13204–13215.

(3) A. S. Pensado, F. Malberg, M. F. Costa Gomes, A. A. H. Pádua, J. Fernández, B. Kirchner, *"Interactions and structure of ionic liquids on graphene and carbon nanotubes surfaces"*, RSC Adv. **2014**, *4*, 18017–18024.

Statement of Authorship

I, Friedrich Malberg, hereby declare that I am the sole author of this thesis. The ideas and work of others, whether published or unpublished, have been fully acknowledged and referenced in my thesis.

Bonn, May 5, 2014

Friedrich Malberg